Variability in the Engineering Properties of Open-Graded Aggregate Backfills: A Large-Scale Direct Shear Round-Robin Study

PUBLICATION NO. FHWA-HRT-23-046

JULY 2023

U.S. Department of Transportation
Federal Highway Administration

Research, Development, and Technology
Turner-Fairbank Highway Research Center
6300 Georgetown Pike
McLean, VA 22101-2296

FOREWORD

Open-graded aggregates (OGAs) are a common civil engineering material used in the construction of roads and bridges. Their unit weight and shear strength are important parameters that transportation agencies must consider during design, yet little is known about the variability of those parameters. To address this gap, the Federal Highway Administration initiated a round-robin study in which six laboratories tested three commonly used OGAs from five different quarries for gradation, density, and shear strength using large-scale direct shear devices.

This report presents and analyzes the results from this interlaboratory study and discusses the sensitivity of the physical and mechanical parameters for OGAs. The results of this study should assist State and local transportation agencies, design consultants, contractors, and researchers in determining appropriate design parameters and understanding their reliability.

Jean Nehme, Ph.D., P.E.
Director, Office of Infrastructure
Research and Development

TECHNICAL REPORT DOCUMENTATION PAGE

1. Report No. FHWA-HRT-23-046	2. Government Accession No.	3. Recipient's Catalog No.
4. Title and Subtitle Variability in the Engineering Properties of Open-Graded Aggregate Backfills: A Large-Scale Direct Shear Round-Robin Study		5. Report Date July 2023 6. Performing Organization Code
7. Author(s) Jennifer E. Nicks (ORCID: 0000-0001-7230-3578), Michael T. Adams (ORCID: 0000-0003-2358-4128), Nicholas Culbreth (ORCID: 0000-0003-0434-230X), and Thomas Gebrenegus (ORCID: 0000-0002-5742-6411)		8. Performing Organization Report No.
9. Performing Organization Name and Address Office of Infrastructure R&D FHWA Research, Development and Technology 6300 Georgetown Pike McLean, VA 22101		10. Work Unit No. 11. Contract or Grant No. 693JJ320F000160/693JJ319D000057
12. Sponsoring Agency Name and Address Office of Research, Development, and Technology Federal Highway Administration 6300 Georgetown Pike McLean, VA 22101-2296		13. Type of Report and Period Final Report; February 2019– July 2023 14. Sponsoring Agency Code HRDI-40
15. Supplementary Notes The contracting officer's representative was Michael T. Adams (HRDI-10; 0000-0003-2358-4128).		

16. Abstract

Open-graded aggregates (OGAs) are a common type of structural backfill used to build a variety of transportation earthworks. Therefore, the Federal Highway Administration (FHWA) has made a concerted effort over the past decade to better understand and quantify the strength-deformation characteristics of OGAs through large-scale direct shear (LSDS) testing performed on a wide variety of stone sizes. However, all of this testing was performed using a single type of LSDS device, primarily conducted by a single laboratory technician, with OGAs generally obtained from a single quarry. To address these limitations and better understand the variability expected for OGAs across the country, FHWA initiated a round-robin study that included sieve, maximum and minimum density, and LSDS tests. In the study, six laboratories tested three stone size classifications (No. 57, No. 68, and No. 8) from five quarries with different mineralogy, meaning 90 OGAs were evaluated. Ottawa 20-30 sand was also included as standard soil for comparison. A statistical analysis of all the data for key geotechnical design parameters was then performed to determine mean values, standard deviations, coefficients of variation, and suggested statistical distribution types. This report details the testing program; results from all the laboratory tests performed and from the statistical analyses, including the sensitivity of engineering properties to different factors; and the impact on design, with suggested values for preliminary design provided.

17. Key Words	18. Distribution Statement
Open-graded aggregates, structural backfill, large-scale direct shear, coefficient of variation, friction angle, dilation angle, shear strength, dry unit weight	No restrictions. No restrictions. This document is available to the public through the National Technical Information Service, Springfield, VA 22161. http://www.ntis.gov

19. Security Classif. (of this report)	20. Security Classif. (of this page)	21. No. of Pages	22. Price
Unclassified	Unclassified	257	N/A

Form DOT F 1700.7 (8-72) Reproduction of completed page authorized

SI* (MODERN METRIC) CONVERSION FACTORS

APPROXIMATE CONVERSIONS TO SI UNITS

Symbol	When You Know	Multiply By	To Find	Symbol
		LENGTH		
in	inches	25.4	millimeters	mm
ft	feet	0.305	meters	m
yd	yards	0.914	meters	m
mi	miles	1.61	kilometers	km
		AREA		
in^2	square inches	645.2	square millimeters	mm^2
ft^2	square feet	0.093	square meters	m^2
yd^2	square yard	0.836	square meters	m^2
ac	acres	0.405	hectares	ha
mi^2	square miles	2.59	square kilometers	km^2
		VOLUME		
fl oz	fluid ounces	29.57	milliliters	mL
gal	gallons	3.785	liters	L
ft^3	cubic feet	0.028	cubic meters	m^3
yd^3	cubic yards	0.765	cubic meters	m^3
	NOTE: volumes greater than 1,000 L shall be shown in m^3			
		MASS		
oz	ounces	28.35	grams	g
lb	pounds	0.454	kilograms	kg
T	short tons (2,000 lb)	0.907	megagrams (or "metric ton")	Mg (or "t")
		TEMPERATURE (exact degrees)		
°F	Fahrenheit	5 (F-32)/9 or (F-32)/1.8	Celsius	°C
		ILLUMINATION		
fc	foot-candles	10.76	lux	lx
fl	foot-Lamberts	3.426	$candela/m^2$	cd/m^2
		FORCE and PRESSURE or STRESS		
lbf	poundforce	4.45	newtons	N
lbf/in^2	poundforce per square inch	6.89	kilopascals	kPa

APPROXIMATE CONVERSIONS FROM SI UNITS

Symbol	When You Know	Multiply By	To Find	Symbol
		LENGTH		
mm	millimeters	0.039	inches	in
m	meters	3.28	feet	ft
m	meters	1.09	yards	yd
km	kilometers	0.621	miles	mi
		AREA		
mm^2	square millimeters	0.0016	square inches	in^2
m^2	square meters	10.764	square feet	ft^2
m^2	square meters	1.195	square yards	yd^2
ha	hectares	2.47	acres	ac
km^2	square kilometers	0.386	square miles	mi^2
		VOLUME		
mL	milliliters	0.034	fluid ounces	fl oz
L	liters	0.264	gallons	gal
m^3	cubic meters	35.314	cubic feet	ft^3
m^3	cubic meters	1.307	cubic yards	yd^3
		MASS		
g	grams	0.035	ounces	oz
kg	kilograms	2.202	pounds	lb
Mg (or "t")	megagrams (or "metric ton")	1.103	short tons (2,000 lb)	T
		TEMPERATURE (exact degrees)		
°C	Celsius	1.8C+32	Fahrenheit	°F
		ILLUMINATION		
lx	lux	0.0929	foot-candles	fc
cd/m^2	candela/m2	0.2919	foot-Lamberts	fl
		FORCE and PRESSURE or STRESS		
N	newtons	2.225	poundforce	lbf
kPa	kilopascals	0.145	poundforce per square inch	lbf/in^2

*SI is the symbol for International System of Units. Appropriate rounding should be made to comply with Section 4 of ASTM E380. (Revised March 2003)

TABLE OF CONTENTS

LIST OF FIGURES

LIST OF TABLES

LIST OF ABBREVIATIONS

AASHTO	American Association of State Highway and Transportation Officials
AD	Anderson-Darling
AIMS2	Aggregate Imaging Measurement System 2
ANOVA	analysis of variance
AR	acceptable range
ASTM	American Society for Testing and Materials
BA	basalt
COV	coefficient of variation
DI	diabase
DS	direct shear
FHWA	Federal Highway Administration
F&E	flat and elongated
GA	gradient angularity
GG	granite-gneiss
K-S	Kolmogorov-Smirnov
L.A.	Los Angeles
LI	limestone
LRFD	load and resistance factor design
LSDS	large-scale direct shear
LVDT	linear variable differential transformer
OGA	open-graded aggregate
OS-20-30	Ottawa 20-30 sand
RD	relative density
SI	siltstone
SP	sphericity
TFHRC	Turner-Fairbank Highway Research Center
TX	texture
ZDA	zero dilation angle
95RD	95 percent relative density

LIST OF SYMBOLS

Δh	change in horizontal displacement
Δt	sampling frequency
Δv_{max}	maximum change in vertical displacement
$\varepsilon_{h,peak}$	horizontal strain at peak shear
$\varepsilon_{h,peak,5psi}$	horizontal strain at peak shear at 5-psi target applied normal stress
$\varepsilon_{h,peak,10psi}$	horizontal strain at peak shear at 10-psi target applied normal stress
$\varepsilon_{h,peak,15psi}$	horizontal strain at peak shear at 15-psi target applied normal stress
$\varepsilon_{h,peak,30psi}$	horizontal strain at peak shear at 30-psi target applied normal stress
γ	unit weight of the aggregates
γ_{d95}	dry unit weight at 95 percent relative density
γ_{dmax}	maximum dry unit weight
γ_{dmin}	minimum dry unit weight
σ_h	lateral earth pressure
σ_n	applied normal stress
τ	shear strength
$\tau_{initial}$	initial shear stress values before the shear phase
$\tau_{peak,5psi}$	peak shear stress at 5-psi target applied normal stress
$\tau_{peak,10psi}$	peak shear stress at 10-psi target applied normal stress
$\tau_{peak,15psi}$	peak shear stress at 15-psi target applied normal stress
$\tau_{peak,30psi}$	peak shear stress at 30-psi target applied normal stress
τ_r	residual shear stress at 20 percent horizonal strain
ϕ	friction angle
ϕ_{cv}	constant volume friction angle
$\phi_{cv,fixed}$	constant volume friction angle under fixed upper shear box conditions
$\phi_{cv,mobile}$	constant volume friction angle under mobile upper shear box conditions
ϕ_s	secant, or peak friction angle
$\phi_{s,5psi}$	secant, or peak friction angle at 5-psi target applied normal stress
$\phi_{s,10psi}$	secant, or peak friction angle at 10-psi target applied normal stress
$\phi_{s,15psi}$	secant, or peak friction angle at 15-psi target applied normal stress
$\phi_{s,30psi}$	secant, or peak friction angle at 30-psi target applied normal stress
ϕ_t	tangent friction angle
$\phi_{t,r}$	residual tangent friction angle
ψ	dilation angle
ψ_{max}	maximum dilation angle
$\psi_{max,5psi}$	maximum dilation angle at 5-psi target applied normal stress
$\psi_{max,10psi}$	maximum dilation angle at 10-psi target applied normal stress
$\psi_{max,15psi}$	maximum dilation angle at 15-psi target applied normal stress
$\psi_{max,30psi}$	maximum dilation angle at 30-psi target applied normal stress
B_I	breakage index
c_a	apparent cohesion
D_{85}	particle diameter at which 85 percent of the sample is finer, by mass
d_{max}	maximum grain size
EH	horizontal earth pressure load

EV	vertical pressure from dead load of earth fill
Gsb	bulk dry specific gravity
H_0	null hypothesis
H_1	alternative hypothesis
K_a	active earth pressure coefficient
K_u	kurtosis
L	length of particle
n	number of samples or points
s	standard deviation
S	thickness of particle
S_k	skewness
W	histogram's optimal bin width
W_i	initial (i.e., as-received) percentage retained for each sieve size evaluated
W_f	final (i.e., post-shear) percentage retained for each sieve size evaluated
$\bar{x}$	mean
Z	standard normal variable
z	depth

CHAPTER 1. INTRODUCTION

Open-graded aggregates (OGAs) are a common type of structural backfill used to build a variety of transportation earthworks (e.g., retaining walls, embankments, and bridge abutments) (figure 1). Early application of OGAs began in the 1950s as surface courses for asphalt pavements (Kandhal and Mallick 1999). The use of OGAs in transportation construction is still evolving with applications related to pavement bases and subbases, portland cement pervious concrete, and structural backfills (Mallick et al. 2000; Nicks et al. 2015; Tao and Abu-Farsakh 2008; Tyson and Tayabji 2012; Younger et al. 1994). OGAs are most often produced from the blasting of rock in quarries. The blasted rock is then crushed and sorted into aggregates of different sizes per the material specifications for a project.

OGAs are classified per the American Association of State Highway and Transportation Officials (AASHTO) M 43-05 *Standard Specification for Sizes of Aggregate for Road and Bridge Construction* (AASHTO 2018a). The maximum grain size (d_{max}) under the AASHTO M 43–05 specification ranges from 0.375 to 4 inches, although for most structural backfill applications, d_{max} is limited to 1.5 inches (AASHTO 2018a). Because of their relatively large void ratios and limited amounts of fine content, OGAs have excellent drainage characteristics, low frost-heave potential, easy placement during construction, quick quality assurance for compaction, and relatively lower unit weight compared to conventional, well-graded backfills.

Source: FHWA.

Figure 1. Photo. OGAs as structural backfill in a geosynthetic reinforced soil abutment.

Over the past decade, the Federal Highway Administration (FHWA) has made a concerted effort to better understand and quantify the engineering properties of OGAs. Strength-deformation characteristics, such as shear strength (τ) (i.e., friction angle) and dilation behavior (i.e., dilation

angle), which were assessed using large-scale laboratory testing devices, were of primary interest (Nicks and Adams 2013; Nicks et al. 2015; Gebrenegus et al. 2015; Gebrenegus et al. 2017; Nicks et al. 2021). For large-scale direct shear (LSDS) testing in particular, all of the testing conducted by FHWA was performed on a single type of LSDS device (figure 2) in FHWA's Geotechnical Laboratory at the Turner-Fairbank Highway Research Center (TFHRC). In addition, the OGAs evaluated, ranging from an AASHTO No. 5 to an AASHTO No. 10, largely came from a single source with identical mineralogy.

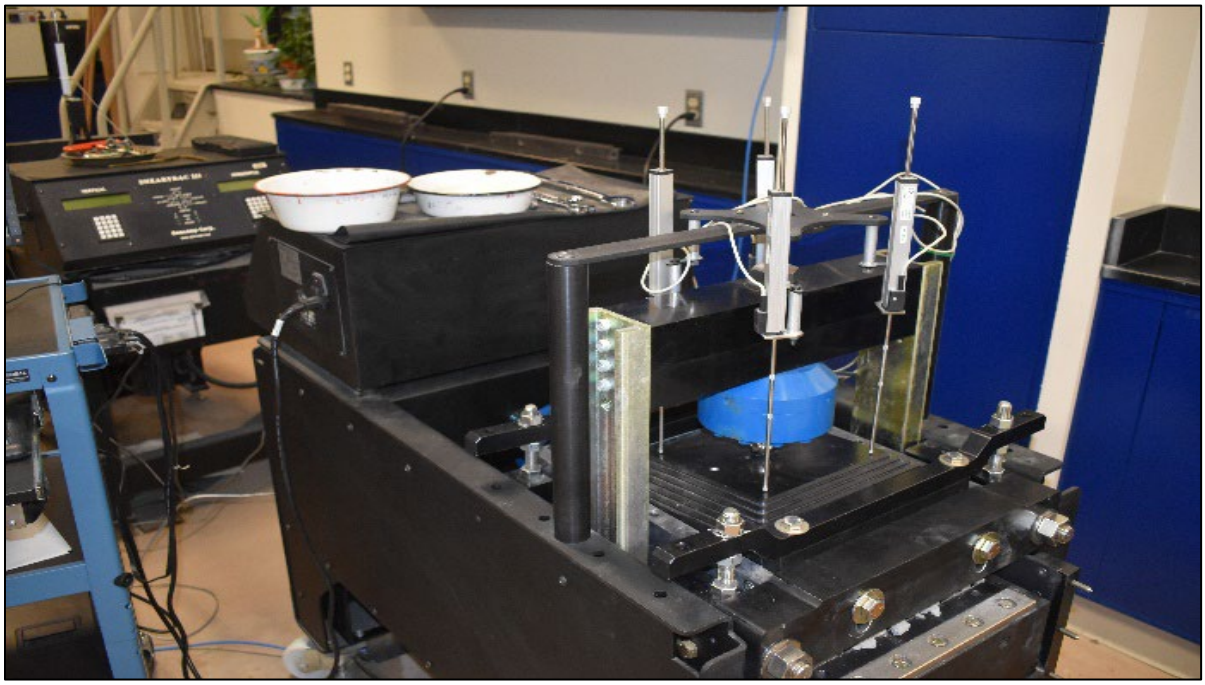

Source: FHWA.

Figure 2. Photo. LSDS devices at TFHRC.

To address the limitations in previous FHWA studies, including use of a single type of LSDS device, limited OGA rock types, and a single laboratory technician conducting the tests, FHWA initiated an interlaboratory, round-robin study. The purpose of this study was to evaluate the variability of engineering properties for three common OGA gradations (i.e., No. 57, No. 68, and No. 8). TFHRC and five other laboratories in the United States with LSDS devices were included in the study. Each laboratory was sent three OGA gradations obtained from five different quarries. Each quarry had different geologic conditions and mineralogy (i.e., basalt (BA), diabase (DI), granite-gneiss (GG), limestone (LI), and siltstone (SI)). Each laboratory therefore tested 15 different OGAs; for 6 laboratories, a total of 90 OGAs were evaluated in this study.

Each laboratory measured the as-received gradation of each OGA; minimum and maximum dry unit weights; secant, tangent, residual, and constant volume friction angles; apparent cohesion (c_a); and maximum dilation angles. A statistical analysis of all the relevant data was also performed to determine mean ($\bar{x}$) values, standard deviations (s), and coefficients of variation (COV). The associated statistical distributions for the key engineering parameters were also determined.

The results of this interlaboratory study can be used by designers to assess more reasonable values for geotechnical designs, by agencies to update or develop relevant material specifications, and by contractors to select structural backfills for a project. Additionally, researchers can use the results to evaluate the reliability of various design methods and calibrate load and resistance factors in the framework of load and resistance factor design (LRFD). The results may also lay the foundation for the development of new test standards and specifications for LSDS testing of structural backfills like OGAs by organizations like AASHTO and ASTM International.

BACKGROUND

The engineering properties of construction materials like soils and aggregates play a large role in the design of transportation earthworks. These properties impact calculations related to lateral earth pressure (σ_h), nominal bearing resistance, settlement, lateral deformation, and more. Therefore, using appropriate input values for geotechnical design parameters such as friction angle, cohesion, and unit weight is of utmost importance. Oftentimes, in the absence of testing, preliminary, or default, values for these parameters are used. For example, a typical default value of 34 degrees is frequently specified by designers for the friction angle of any soil or aggregate used as a structural backfill. Another alternative for coarse-grained materials is to perform conventional testing on a reduced size sample, prepared either through scalping or a parallel gradation technique. In either case (i.e., using a default value or using a scalped sample), the tradeoff is that the actual strength of the coarse-grained soils (e.g., OGAs) could be underestimated, and/or the dominant behaviors of such materials during shear, such as crushing, rearrangement or interlocking, and dilation may not be captured.

The introduction of LSDS devices in geotechnical laboratory testing addresses many of these concerns. However, even with larger devices, other uncertainties arise in measuring design properties. For example, no existing industry standards (i.e., AASHTO, ASTM) specify the "correct" configuration of a LSDS device (e.g., fixity of the stationary box, connection between the platen and the normal load, application of load), and no noted differences in the associated test procedures, which were initially developed for soils, exist (e.g., gap size, strain rate). Since no common industry standard controls the device configuration and test procedure, their influence on the sample behavior during shear, and thus the measured parameters, is not well known.

A conservative design is generally associated with high construction costs or, at the very least, an underestimation of in-service performance. The discussion in the following paragraphs demonstrates wide variations in engineering properties of OGAs illustrating how unrealistic default values could be if applied blindly. For example, previous work by FHWA suggested that an estimate of 40 degrees for the friction angle may be more appropriate for OGAs (Nicks et al. 2015) compared to the conventional default value of 34 degrees; this difference represents a nearly 30 percent decrease in computed σ_h values.

Engineering Properties of Structural Backfills

Since soils (and rocks) are naturally occurring materials, their fundamental behavior is not as well understood or as straightforward as manmade materials. Manmade materials like steel or concrete can be engineered to specifically suit design requirements. To combat this issue for

most transportation earthworks, and to achieve a more desired behavior, structural backfills are often used as an alternative to the native material at a site. These backfills can be better controlled and have better engineering properties.

Common structural backfills include well-graded materials and OGAs. Well-graded backfills are recommended for applications such as mechanically stabilized earth walls (Berg et al. 2009), whereas OGAs for geotechnical infrastructure applications were introduced only recently in FHWA guidance for geosynthetic reinforced soil abutments and integrated bridge systems (Adams et al. 2011). The key physical and strength-deformation characteristics of structural backfills, such as unit weight and τ, are thought to largely depend on the gradation (e.g., maximum aggregate size, uniformity, fines content), saturation level, shape (e.g., angularity, sphericity (SP), texture (TX), durability (e.g., abrasion resistance, soundness), and mineralogy of the material.

While all structural backfills are commonly assumed to be free draining, and thus will not result in a buildup of hydrostatic pressures against the back of retaining walls (Gomez et al. 2014), the unit weight and shear strength may still be impacted by the presence of water. The maximum dry unit weight of structural backfills is measured using a Standard/Modified Proctor test (AASHTO T 99/AASHTO T 180) for well-graded aggregates and a vibratory table test (ASTM D4253/ASTM D4254) for OGAs (AASHTO 2018a, AASHTO 2018b, ASTM 2016b, and ASTM 2016c). Well-graded aggregates naturally result in higher unit weights than OGAs. For example, based on standard Proctor tests for 16 well-graded aggregates commonly used in Virginia, maximum dry unit weights ranged from 131.8 to 155.8 lb/ft^3 (Hossain and Lane 2015). In contrast, maximum dry unit weights of 101.3 to 115.9 lb/ft^3 have been reported by Nicks et al. (2015) and Nicks et al. (2018) for OGAs.

Shear strength is traditionally determined through triaxial tests (ASTM D7181) and/or direct shear (DS) tests (ASTM D3080) (ASTM 2011b, ASTM 2011a). For structural backfills, large-scale versions of the test devices are required. Focusing solely on LSDS tests of structural backfills, tangent friction angles (ϕ_t) up to 54 degrees for well-graded aggregates used in geosynthetic reinforced soil applications, have been reported (Adams and Nicks 2018; Abu-Hejleh et al. 2000). The strength of OGAs is similar, with reported friction angles ranging from 37 to 58 degrees (Nicks and Adams 2013; Nicks et al. 2015; Nicks et al. 2021; Stallings 2020; Abu-Farsakh et al. 2020). These results indicate that structural backfills are stronger than the conservative default value of 34 degrees commonly used in preliminary design calculations.

Regardless of the backfill type and the methods to measure their engineering properties, large uncertainties in these properties can result from many disparate sources. According to Phoon and Kulhawy (1999), three primary sources of uncertainty exist: inherent variability, measurement error, and transformation uncertainty. Of particular interest to this study is measurement error, and, to some degree, the inherent variability in blasting and sampling of the aggregate stockpile. Variability in measurements is related to equipment, procedure(s), operator(s), and random testing effects related to inaccuracies and error; an interlaboratory study is one approach to quantify measurement errors. Examples related to the variability of physical properties and characteristics and the τ of soils and aggregates are presented in the following subsections.

Variability of Physical Properties and Characteristics

The physical properties and characteristics of interest in this study were unit weight (i.e., density), aggregate shape factors, and abrasion resistance. Limited studies are available in the literature on the variability of these physical properties (Yoshimi and Tohno 1973; Hamidi et al. 2013; Ganji 2019; Gates et al. 2011; Cuelho et al. 2007; Hossain et al. 2007). Therefore, the variabilities often reported by the standard test procedures can serve as a guide for assessing the $\bar{x}$, s, COV, and acceptable range (AR) of values for the applicable parameter (table 1).

Table 1. Reported variabilities of select physical properties and characteristics.

Parameter	Soil Type	Variability Between Laboratories				Reference
		$\bar{x}$	S	COV (%)	AR	
Minimum dry unit weight	Poorly graded sand	97.54 lb/ft^3	2.63 lb/ft^3	2.70	7.3 lb/ft^3	D4254 (ASTM 2016c)
Maximum dry unit weight		116.9 lb/ft^3	1.8 lb/ft^3	1.54	5.1 lb/ft^3	D4253 (ASTM 2016b)
Angularity	Gravel (0.5 inches)	2777.9	119.3	4.3	12.2%	Gates et al. (2011)
SP		0.69	0.0133	1.9	7.4%	Gates et al. (2011)
TX		233.6	16.3	7.0	20.0%	Gates et al. (2011)
Micro-Deval$^+$ abrasion resistance	—	5%	0.5%	10	28%	T 327-12 (AASHTO 2020)
L.A. abrasion resistance		21%	1.11%	5.3	15%	
	—	—	—	6.4	18.1%	C535 (ASTM 2016a)

—Not specified.
$^+$Statistics provided are for the lowest and highest aggregate abrasion loss reported in AASHTO T 327 (AASHTO 2020b).

Variability of Shear Strength

The mechanical properties of interest in this study were τ (i.e., friction angle and c_a) and maximum dilation angle. Several researchers have investigated the sources of τ variability, as measured through DS testing. Some of the investigated sources of variability include the size and shape of the specimen (Cerato and Lutenegger 2006; Bareither et al. 2008b; Wu et al. 2008; Dadkhah et al. 2010; Sobol et al. 2015; Altaf et al. 2016), the gap size between the upper and lower shear boxes (Kim et al. 2012), and the shear displacement rate (Mamo and Dey 2014). All these studies were based on sand samples except for the study by Sobol et al. (2015), where recycled concrete aggregates were tested.

On the effect of specimen size, Cerato and Lutenegger (2006) found that the measured friction angles generally decreased with an increase in box size; friction angles were up to 10 degrees

higher in a 2.4-inch (60 mm) box than in a 12-inch (305 mm) box. Bareither et al. (2008a) also reported a decrease in friction angle with an increase in specimen size, but the effect was much smaller; an average tangent friction angle of 42.6 degrees was obtained for the 2.5 inch (64 mm) square box compared to a 40.5-degree angle for the 12-inch (305 mm) square box. The effect of specimen/box shape on friction angles was reported by Altaf et al. (2016) who found that using a circular shear box resulted in friction angles 2 to 3 degrees higher compared to a square shear box. To evaluate the effect of gap size between the upper and lower DS boxes, Kim et al. (2012) performed tests using seven types of sand at six different gap sizes ranging from 0.008 inch (0.2 mm) to 0.16 inch (4.0 mm). The results of this study indicated that the peak shear strength generally decreased with an increase in opening size due to outflow of the sands between the gap. On the effect of shear displacement rate, Mamo and Dey (2014) investigated the influence of different strain rates (i.e., 0.0014, 0.0069, and 0.035 percent lateral displacement per second) for sand specimens prepared at 70 percent and 85 percent relative densities (RDs). The tangent friction angle increased slightly with an increase in strain rate; from 42.5 to 46.5 degrees at 70 percent RD and from 44.8 to 48.2 degrees at 85 percent RD.

There have been limited round-robin studies to quantify the variability of shear strength parameters and, to a lesser degree, deformation behavior of granular materials (Converse 1952; Bareither et al. 2008b). In the work reported by Converse (1952), seven laboratories performed stress- and strain-controlled DS tests on Ottawa 20-30 sand (OS-20-30) in loose and dense states; the findings from only the strain-controlled DS tests from three laboratories are presented herein. For the dense sands, the measured peak friction angles ranged from 29.3 to 43.2 degrees, with an average of 36.1 degrees and a COV of 19.1 percent; for sands tested in the loose state, peak friction angles were lower, ranging from 23.8 to 32.0 degrees, with an average and COV of 27.5 degrees and 14.9 percent, respectively. Residual (i.e., ultimate) friction angles were also computed for OS-20-30, and COVs of 18.6 and 21.9 percent were reported for the loose and dense states, respectively. Converse (1952) suggested that the variability in the measured friction angles was associated with the details of the equipment and procedures, such as loading methods and rates, shear box dimensions, specimen thickness, and the gap size between shear boxes. The work eventually led to the development of a standard test method for DS testing of soils (i.e., ASTM D3080) (ASTM 2011a).

The interlaboratory study conducted by Bareither et al. (2008b) included 10 laboratories. Each laboratory performed inundated DS testing on four homogeneous granular backfill materials. All the materials were classified as poorly graded (i.e., open-graded) sands. Eight of the shear boxes were circular and two were square. The results from this study showed variability in the Mohr-Coulomb failure envelopes and the resulting tangent friction angles (with COVs ranging from 8.6 to 15.3 percent). This study also reported a wide variation in volume change behavior (i.e., dilation and contraction) among the laboratories; however, the dilation angles were not quantified. Based on the results presented in this study, interlaboratory variability was also observed through the dilation angle, the maximum vertical strain at peak shear stress, and the horizontal strain where the maximum contraction of the sample occurred. The same sources of variability discussed earlier, including sample thickness, gap size, and displacement rate, along with differences in the frequency of data collection, attributed to the variability of strength-deformation behavior in their interlaboratory study.

Greco (2016) provided a theoretical basis to evaluate uncertainties and variabilities in cohesion and friction coefficient values as measured through DS testing and included an extensive

literature review documenting reported values by other researchers. In Greco's literature review, the COV for the friction coefficient (and thus friction angle) was reported to be between 10 and 20 percent for a wide range of soils—from clays to rock fills. The reported COV for cohesion was between 20 and 60 percent. The variabilities for both strength parameters were generally considered inherent due to variations resulting simply from the magnitude of normal stress applied during DS testing but were also partially attributed to measurement error.

In order to have a comprehensive understanding of the variability due to measurement error, interlaboratory studies should include and document different configurations of DS devices so their influence can be analyzed. Configurations of interest include the connection between the normal load and the loading platen, the connection between the loading platen and the upper shear box, the mobility of the upper box relative to the specimen during shear, and so on. The following subsections highlight some of these variations in DS testing and DS device configurations.

DS Testing

A DS test is commonly used to determine the shear strength and dilation behavior of soils and aggregates. Despite its limitations in having a predetermined horizontal failure plane and nonhomogeneous stress state, DS tests are popular in practice due to their operational simplicity and the wide spectrum of geomaterials that they can test without the need for highly specialized personnel (Taylor 1953; Shibuya et al. 1997; Cerato and Lutenegger 2006). DS tests have been in use for nearly three quarters of a century, and their history for engineering applications is well documented by Matthews (1988).

DS Devices

Shibuya et al. (1997) and Kim et al. (2012) reviewed the types of DS devices that have been used since the 1950s and classified them into three different types (i.e., types A, B, and C), based on the configuration of the upper box, loading platen, and ram (figure 3). In type A, devised by Skempton and Bishop (1950), the top platen is connected to the loading ram with a hinge or ball bearing and is independent of the mobile upper shear box. Type B, devised by Jewell and Wroth (1987), is like type A except for the fixity of the top platen with respect to the loading ram and the mobile upper shear box. In type C, the upper shear box is fixed and independent of the top platen, which is fixed to the loading ram.

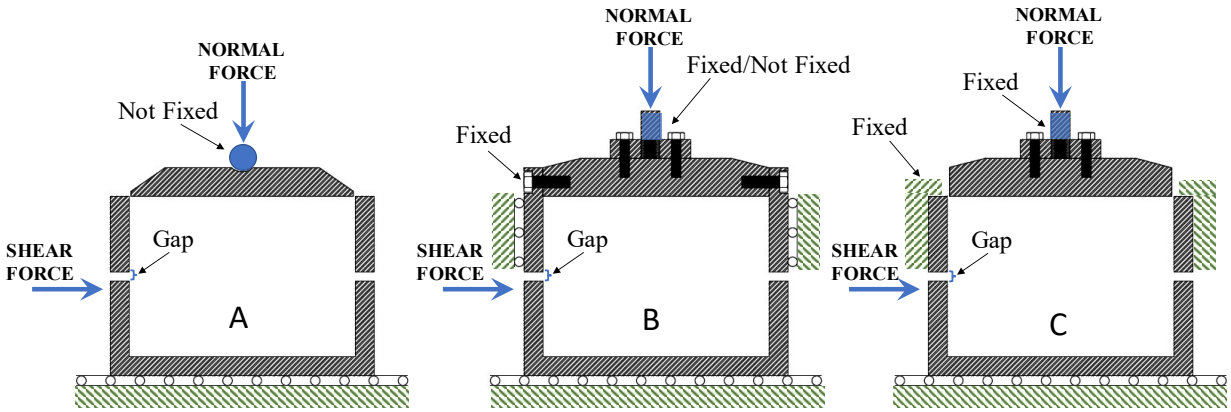

Source: FHWA.

Figure 3. Illustration. Basic types of DS boxes, as described by Shibuya et al. (1997).

ASTM D3080 includes the following requirements, which dictate the size of the DS device relative to the size of the soil sample being tested (ASTM 2011a):

- The sample width or diameter must be at least 2 inches (50.8 mm).
- The minimum sample thickness must be approximately 0.5 inches (12.7 mm) but no less than six times the maximum particle size (d_{max}).
- The minimum sample width or diameter to thickness ratio must be 2 to 1.
- The width of the specimen must be at least 10 times d_{max}.

DS Test Procedures

DS testing is commonly performed per ASTM D3080 or AASHTO T 236 (ASTM 2011a; AASHTO 2018). Both test procedures determine the consolidated drained shear strength of a soil in DS by deforming the specimen along a predesignated horizontal shear plane between the two shear box halves. However, some differences between the two standards related to shearing, inundation, gap size, and data collection frequency exist. For example, the ASTM method is performed in single shear with optional inundation, whereas the AASHTO method may be performed in either single shear or in double shear under inundation. Another difference is that the tests in ASTM are displacement controlled, whereas in the AASHTO method, stress-controlled tests are also allowed. For simplicity, only ASTM D3080 is further discussed in this report (ASTM 2011a).

Note that DS tests were originally developed to test soils; therefore, the impact of the associated test procedures within ASTM D3080 for structural backfills, such as OGAs, has not been fully evaluated, but modifications to the test procedure have been noted by FHWA in the past (Nicks et al. 2015). Regardless of the soil or aggregate being tested, the primary test procedures that can impact the results of DS testing include the following: the compaction level of the specimen; the filling of the shear box with water; the time allotted for the consolidation stage; the gap size

between the two shear box halves; the selection of the shear displacement rate; and the frequency of data collection.

REPORT OVERVIEW

Given the limited work performed on OGAs and whether the variability found for soils is accurate for these structural backfills, this FHWA round-robin study is timely and will aid in a better understanding of the behavior of OGAs during shear in different LSDS devices and the resulting variability of their engineering properties. The information and key findings from this study serve to assist owners in selecting reliable design parameters when OGAs are specified for a project. The chapters in this report are organized as follows:

- Chapter 2 describes the test program, including the materials, sampling methods, and laboratory tests and associated procedures followed as part of the round-robin study.

- Chapter 3 provides all of the test results defining the physical properties and characteristics (e.g., particle size, particle breakage, dry unit weight, bulk dry specific gravity, shape factors, and abrasion resistance and durability) and the strength-deformation characteristics (e.g., friction and dilation angles) of the OGAs evaluated; results from the standard OS-20-30 are also presented as a baseline for comparison. Basic statistics such as $\bar{x}$, s, and COV are presented for each parameter evaluated.

- Chapter 4 presents the in-depth analysis of the results, including the determination of parameter distribution types through histograms, normal probability plots, and a goodness-of-fit test; an investigation into the impact of stone size, mineralogy, and laboratory on the results through analysis of variance (ANOVA); and insights into the influence various LSDS device characteristics and procedures have on the results. Given the analysis, implications to geotechnical practice are also presented.

- Chapter 5 summarizes the main conclusions and key findings from the study. Lessons learned from setting up a round-robin study and the subsequent data analysis are also presented, along with future research plans.

- Appendixes A–E are provided to deliver all the results for each OGA tested by each laboratory (i.e., round-robin test instructions, pre- and post-shear sieve data, AIMS2 and LSDS data), along with additional information and steps to detail the analysis presented in chapter 4.

CHAPTER 2. TEST PROGRAM

This chapter provides details on the test program employed in this study. It includes the materials selected, the sampling procedures for those materials, the various laboratory tests performed to determine the physical characteristics and shear strength of the materials, and key details of the six independent laboratories participating in this round-robin study. Differences between the test devices used by the laboratories are noted.

MATERIALS

The materials included in the interlaboratory round-robin study were OGAs; however, OS-20-30 was also included as a standard soil for a comparison of the results between the different laboratories.

OS-20-30

OS-20-30 is a standard sand per ASTM C778; it is a naturally rounded, poorly graded silica sand mined from the areas of Ottawa, IL and Le Sueur, MN. As the name suggests, OS-20-30 has a gradation that predominantly passes a No. 20 sieve but is retained on a No. 30 sieve (table 2) (ASTM 2017). Bags of OS-20-30 were procured and delivered by the supplier directly to each laboratory for testing.

Table 2. ASTM C778 OS-20-30 gradation requirements (ASTM 2017).

Sieve	Particle Size (inches)	Percent Passing
No. 16	0.046	100
No. 20	0.033	85–100
No. 30	0.024	0–5

OGAs

Three types of OGAs meeting the AASHTO M 43-05 specifications were selected for this study: No. 57, No. 68, and No. 8 (table 3) (AASHTO 2018a). These specific OGA classifications were chosen to span the range of the AASHTO M 43-05 gradations more commonly used in geotechnical applications (AASHTO 2018a). Since quarries around the country vary in geology, five different rock types for each OGA gradation were evaluated in this study, all obtained from different quarries in Virginia. These rock types included BA, DI, GG, LI, and SI, which represent the entire spectrum of geologic rock formations, including igneous, metamorphic, and sedimentary rocks. The five selected rock types (figure 4) were verified through petrographic analysis performed by the Aggregate and Petrography Laboratory at TFHRC following modified ASTM C295 procedures (ASTM 2018).

Table 3. Selected AASHTO M 43-05 stone size designations (AASHTO 2018a).

Sieve	Particle Size (inches)	Percent Passing		
		No. 57	No. 68	No. 8
1.5 inches	1.5	100	—	—
1 inch	1.0	95–100	100	—
3/4 inch	0.75	—	90–100	—
1/2 inch	0.50	25–60	—	100
3/8 inch	0.375	—	30–65	85–100
No. 4	0.187	0–10	5–25	10–30
No. 8	0.093	0–5	0–10	0–10
No. 16	0.046	—	0–5	0–5

—Not specified.

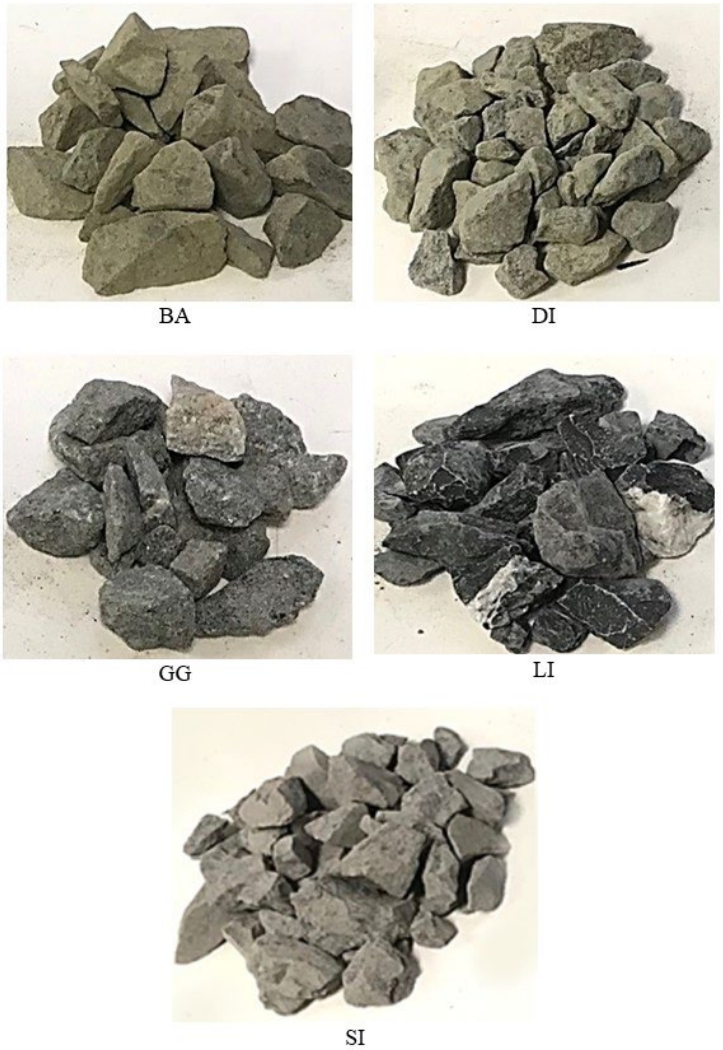

Source: FHWA.

Figure 4. Photos. Rock types for the OGAs evaluated.

The total number of OGAs tested by each laboratory was 15 (i.e., 3 OGA stone size classifications, each with 5 different rock types). Nomenclature was established for each combination of aggregate and rock type (see table 4). The identity of the participating laboratories is withheld in this report; instead, each of the six laboratories included in this round-robin study was assigned an alphanumeric designation (i.e., L01, L02, L03, L04, L05, and L06), which was incorporated at the end of the sample IDs shown in table 4 (e.g., No. 57-BA-L01). This study resulted in a total number of 90 samples tested.

Table 4. OGA sample nomenclature.

Stone Size	Rock Type	Sample ID
No. 57	Basalt	No. 57-BA
	Diabase	No. 57-DI
	Granite-Gneiss	No. 57-GG
	Limestone	No. 57-LI
	Siltstone	No. 57-SI
No. 68	Basalt	No. 68-BA
	Diabase	No. 68-DI
	Granite-Gneiss	No. 68-GG
	Limestone	No. 68-LI
	Siltstone	No. 68-SI
No. 8	Basalt	No. 8-BA
	Diabase	No. 8-DI
	Granite-Gneiss	No. 8-GG
	Limestone	No. 8-LI
	Siltstone	No. 8-SI

OGA Sampling

Each OGA was first delivered in 5-ton stockpiles to TFHRC. To ensure consistency among the OGA samples delivered to and tested by each laboratory, a procedure was established to randomly collect samples from the bottom, middle, and top layers of the stockpiles. Four 5-gal buckets were filled for each laboratory (figure 5). On average, approximately 275 lb of each OGA were sent to each laboratory for testing. As will be discussed in the Initial Sieve Testing section later in this chapter, each laboratory performed a sieve analysis on the as-received samples. The variation in these initial gradations will be noted in chapter 3.

Source: FHWA.

Figure 5. Photo. Stockpile of aggregates at TFHRC for random sampling.

LABORATORY TESTING

Six commercial and research laboratories participated in the round-robin study. Six is the minimum number required for interlaboratory studies per ASTM C802; this number allows for a reasonable evaluation of reproducibility for a given construction material test method (ASTM 2014).

Sequence of Round-Robin Testing

Six rounds of testing were conducted in this study. The sequence of materials sent to each laboratory is shown in table 5. The OGAs were selected for the first five rounds because the primary objective of the study was to define the variability of their physical properties and characteristics and shear strength. The last round (i.e., round 6) was specifically selected to further evaluate the test devices in each laboratory using a standard soil (i.e., OS-20-30).

Table 5. Round-robin test order.

Round No.	Soil Type	Rock Type
1	OGA	DI
2	OGA	LI
3	OGA	GG
4	OGA	BA
5	OGA	SI
6	OS-20-30	Quartz

Sequence of Laboratory Testing

OGA testing for this study included the following in sequential order: sieve testing on the as-received materials; minimum and maximum density testing; LSDS testing; and post-shear sieve testing. While not included in the interlaboratory study, FHWA also separately characterized the shape (i.e., angularity, SP, percentage of flat and elongated (F&E) particles, and TX) and abrasion resistance for each rock type using the aggregate image measurement system 2 (AIMS2) and the Micro-Deval devices at TFHRC, respectively. For the OS-20-30, only LSDS testing was performed by each laboratory; however, FHWA performed all other applicable tests (e.g., sieve analysis, minimum and maximum density testing, and AIMS2).

Sample Preparation

FHWA developed a protocol and set of instructions for consistent preparation of each OGA test sample by each laboratory (appendix A). The basic steps for each laboratory included first oven drying all four buckets received for each OGA sample at 212 °F and then blending and separating the oven-dried OGAs to appropriate test sizes using a quartering method as per AASHTO T 248—Method B (AASHTO 2014).

Initial Sieve Testing

Dry sieving was performed on the as-received samples per ASTM C136 (2019). This action facilitated a comparison with the AASHTO M 43-05 gradation specifications for a given sample. It also allowed for an analysis of the range and variability in OGA gradations meeting the specification as well as an evaluation of the impact of gradation (i.e., stone size) on the strength-deformation characteristics of OGAs. In addition, the gradation curves provided the aggregate size in which 85 percent of the material is smaller (D_{85}); D_{85} is used by FHWA to define the gap size between the upper and lower shear boxes in LSDS testing (Nicks and Adams 2013).

Minimum and Maximum Density Testing

The minimum dry unit weight (γ_{dmin}) and maximum dry unit weight (γ_{dmax}) for each OGA sample were determined using Method A of ASTM D4254-16 and Method 1A of ASTM D4253-16 (vibratory table method), respectively (ASTM 2016c, ASTM 2016b). As allowed by the ASTM D4253-16 standard (ASTM 2016b), all but one of the laboratories performed the maximum density tests using a shake table. L05 used a universal testing machine as the platform instead. Most of the laboratories (i.e., L01, L03, L04, and L06) conducted the maximum density tests at a

frequency of 60 Hz for a duration of 8 min such that the mold had a double amplitude of vertical vibration of 0.013 inch. L05 cycled at 50 Hz with a peak-to-peak amplitude of 0.019 inches, and L02 did not characterize or report the frequency or amplitude used in their testing. The results of these tests allowed for the determination of the dry unit weight at 95 percent relative density (γ_{d95}) for each OGA sample (equation 1); γ_{d95} was specified as the target dry unit weight for LSDS testing.

$$95RD = \frac{\gamma_{dmax}(\gamma_{d95} - \gamma_{dmin})}{\gamma_{d95}(\gamma_{dmax} - \gamma_{dmin})} \quad (1)$$

Where *95RD* denotes 95 percent relative density.

LSDS Testing

LSDS tests were performed per ASTM D3080 (2011) to determine the secant (ϕ_s), tangent (ϕ_t), residual tangent ($\phi_{t,r}$), and constant volume (ϕ_{cv}) friction angles, along with the maximum dilation angles (ψ_{max}) and c_a for each sample type. The following testing conditions were specified:

- All shear tests were performed under dry conditions (i.e., no saturation of the samples).
- Placement of the OGAs in the shear box required compaction to *95RD* for each sample.
- A constant shear rate of 0.015 inch/min was maintained throughout the test for all samples.
- The gap between the upper and lower boxes was set at D_{85} for each sample.
- The applied normal stress (σ_n) values were 5, 10, 15, and 30 psi to cover the typical stress ranges for most geotechnical applications where OGAs are used.
- The end point for termination of each LSDS test was set at 20 percent horizontal strain (e.g., 2.4 inches for a 12-inch square box).

Each laboratory included in the round-robin study had a different type of LSDS device. The configurations for each device are presented in table 6 with the corresponding schematics shown in figure 6. Key differences between the LSDS devices included the mobility of the upper shear box, the connection between the loading platen and the normal load, the shear box dimensions, the number of linear variable differential transformers (LVDTs) to measure vertical deformations, the method of load application for normal and shear loads, and the capacity of the load cells used to measure the loads (table 6). Other differences not necessarily related to the LSDS device itself included the sample dimensions for testing and the frequency of data collection for load and displacement.

Table 6. LSDS device and testing configurations.

Lab ID and Type[+]	LSDS Specimen Shape	Upper Shear Box Mobility	Base of Top Platen/ Spacer	Connection Between Loading Platen and Normal Load	Nominal Bottom Shear Box Dimensions (inch × inch × inch)*	Nominal Specimen Dimensions (inch × inch × inch)*	Number of Vertical LVDTs[++]	Normal Load Application and Capacity (kips)	Horizontal Load Application and Capacity (kips)	Typical Time Step for Data Collection (s)
L01 (C)	Square	Mobile	Smooth	Fixed	12 × 12 × 12	12 × 12 × 6	4	Micro stepper motor (50.0)	Micro stepper motor (50.0)	16
L02 (C/R)	Square	Fixed	Grooved	Not fixed	12 × 12 × 8	12 × 12 × 7	3	Airbag/ Hydraulic** (14.4/20.0)	Hydraulic (12.5)	24
L03 (C)	Square	Mobile	Grooved	Not fixed	15 × 12 × 6	12 × 12 × 6	2	Dead weight/ Airbag*** (20.0)	Step motor system (20.0)	80^
L04 (C)	Square	Mobile	Textured	Fixed	12 × 12 × 7.5	12 × 12 × 6	1	Hydraulic (20.0)	Hydraulic (12.0)	200^
L05 (R)	Circular	Fixed	Smooth	Fixed	12 × 8	12 × 7.5	1	Hydraulic (45.0)	Hydraulic (67.4)	1
L06 (R)	Square	Fixed	Smooth	Not fixed	12 × 12 × 8	12 × 12 × 7.5	4	Micro stepper motor (20.0)	Micro stepper motor (20.0)	40

[+]C = commercial; R = research.
*Interior dimensions shown as length × width × height (square specimen) or diameter × height (circular specimen).
[++]Results presented in the report represent averages of all LVDT measurements.
**Airbag for the DI OGAs; hydraulic loading for all other OGA rock types.
***Dead weight was used for 5 and 10 psi normal stresses; airbag was used for 15 and 30 psi normal stresses.
^Actual time step varied at different intervals throughout testing; representative value shown.

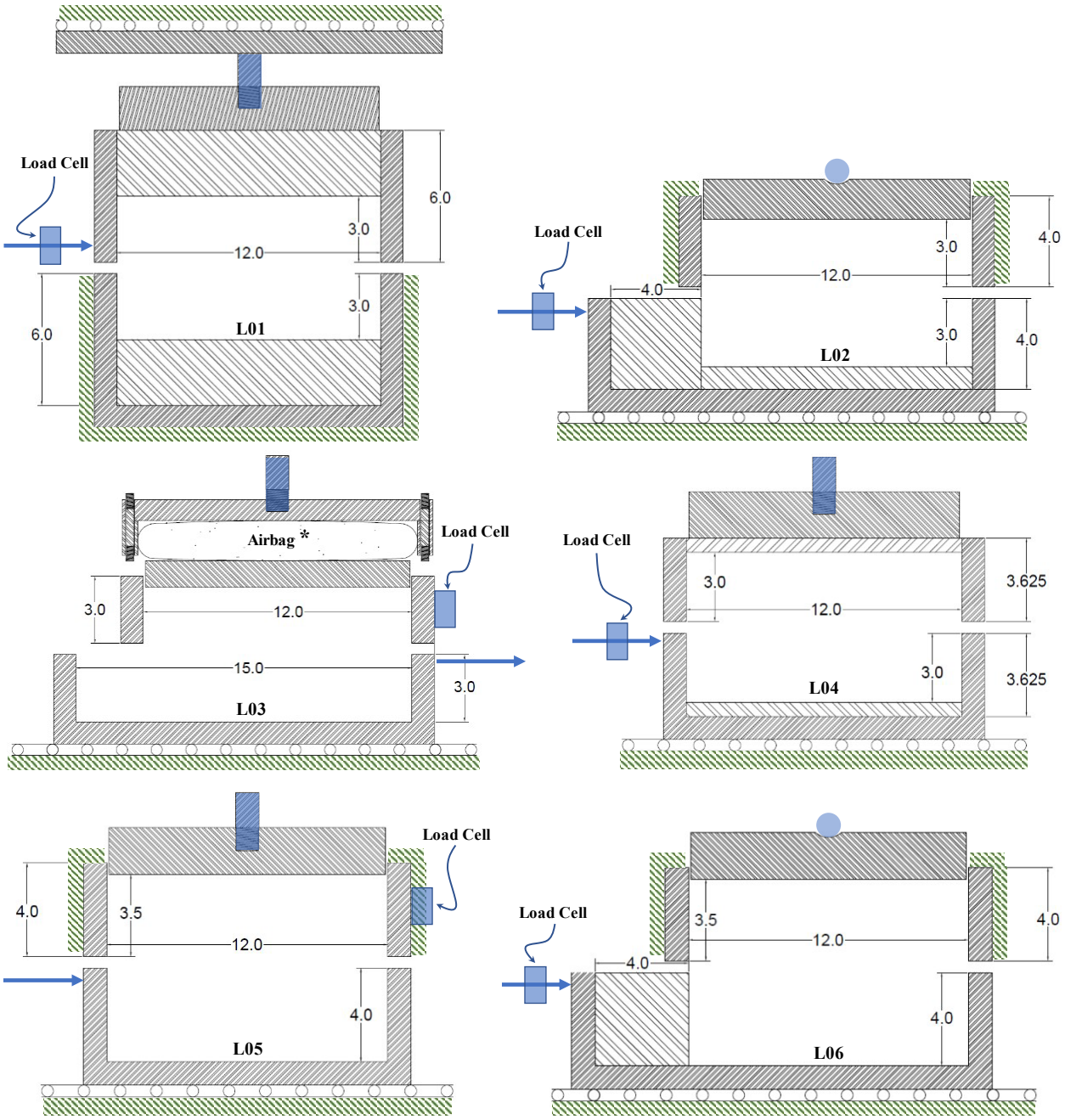

Source: FHWA.
*Dead weight for lower normal loads.

Figure 6. Schematics. LSDS device configurations for each laboratory with dimensions in inches.

Post-Shear Sieve Testing

After LSDS testing, dry sieve tests per ASTM C136 (2019) were again performed by each laboratory on each OGA sample. The sample for post-shear sieve testing was prepared by

blending the aggregates used for each of the four-point LSDS test series into a single pile and performing the same sample reduction procedure used previously. This sequence of events allowed for an evaluation of particle breakage after each OGA type was sheared to failure (i.e., 20 percent horizontal strain). While this information is not used in design, it does provide an indication of the strength of the aggregates and may allow for the evaluation of the differences between different LSDS devices.

AIMS2 Testing

The AIMS2 device at TFHRC was used to characterize the shape factors (e.g., angularity, SP, percentage of F&E particles, and TX) for each OGA rock type (i.e., BA, DI, GG, LI, and SI) and the OS-20-30. This testing was performed solely by FHWA. The shape factors of the materials tested should be independent of the laboratory and were not a key variable in the round-robin study. In addition, the variability of AIMS2 results has already been established as part of the development/refinement of the device, as research performed by Gates et al. (2011) explains (noted in chapter 1). AIMS2 testing was performed per AASHTO T 381 (2018e).

Micro-Deval Testing

Since different geologic sources were selected for this study, the abrasion resistance of each OGA rock type was evaluated solely by FHWA to determine their relative durability and the potential impact on τ. The quarries provided results of Los Angeles (L.A.) abrasion testing and magnesium sulfate soundness testing for the OGAs delivered (shown in chapter 3). To supplement those results, the abrasion resistance of each rock type (e.g., BA, DI, GG, LI, and SI) was also evaluated solely by FHWA using a Micro-Deval apparatus at TFHRC. Micro-Deval testing was performed in accordance with AASHTO T 327-12 (AASHTO 2020).

The Micro-Deval test is typically recommended as a test to measure the abrasion resistance of aggregate, while the L.A. abrasion test is better suited as an indirect measure of aggregate strength; the sulfate soundness test is widely used to predict the freeze-thaw durability of aggregates (Weyers et al. 2005). While not included in the round-robin study, the variability of abrasion resistance has already been established (noted in chapter 1).

CHAPTER 3. TEST RESULTS

This chapter presents the physical properties, characteristics, and shear strength of OS-20-30 and the three types of OGAs (No. 57, No. 68, and No. 8) tested in the round-robin study. Properties not tested by the participant laboratories in the round-robin study were either tested by the FHWA Geotechnical Laboratory or came from aggregate stockpile reports by the source quarries.

PHYSICAL PROPERTIES AND CHARACTERISTICS

The key physical properties and characteristics tested included particle size and dry unit weight as tested by the participant laboratories; the bulk dry specific gravity of each OGA as tested by the source quarries; and particle shape (e.g., angularity, SP, percentage of F&E particles, and TX), abrasion resistance, and durability as tested by FHWA and source quarries.

Particle Size

Each laboratory conducted dry sieving to characterize the size, uniformity, and variability of the as-received OGA gradations. In addition, dry sieving was conducted by each laboratory after each four-point LSDS test to roughly quantify the amount of breakage the OGAs experienced as a result of shearing to failure (i.e., 20 percent horizontal strain). Dry sieving of OS-20-30 was performed solely by FHWA before its delivery to each laboratory. Complete sieve analysis results are provided in appendix B.

As-Received Gradations

To illustrate the sieve analysis results, the as-received gradation curves for No. 57-LI, No. 68-LI, and No. 8-LI are presented in figure 7.

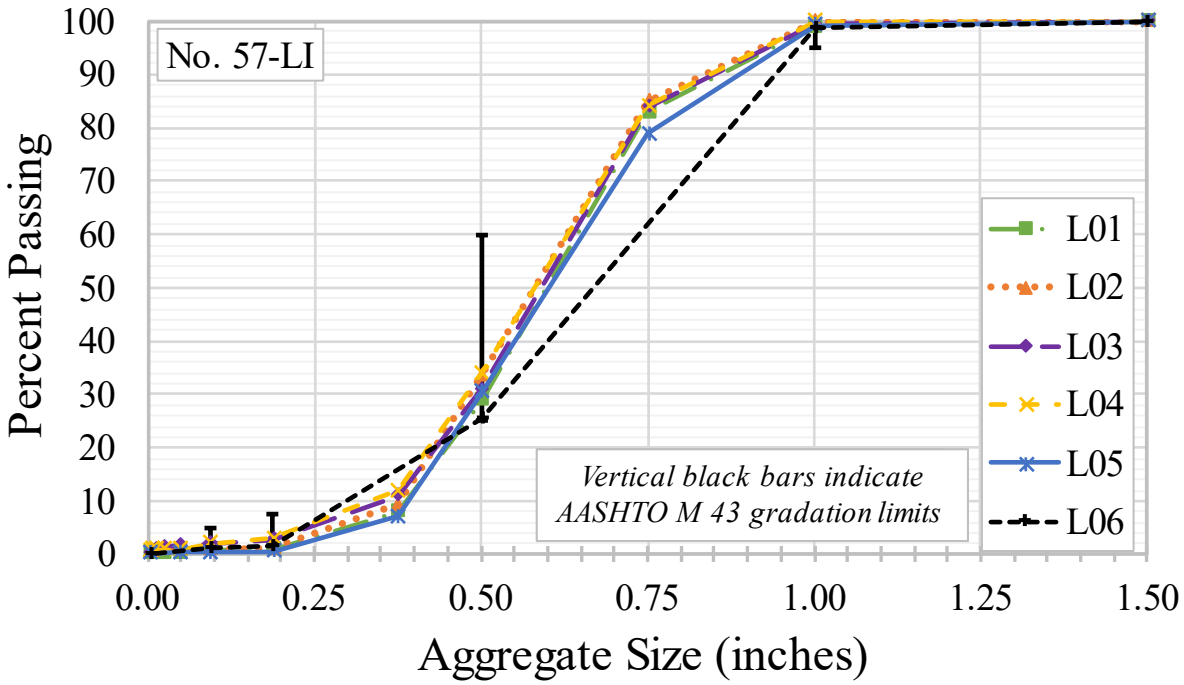

Source: FHWA.

A. No. 57-LI.

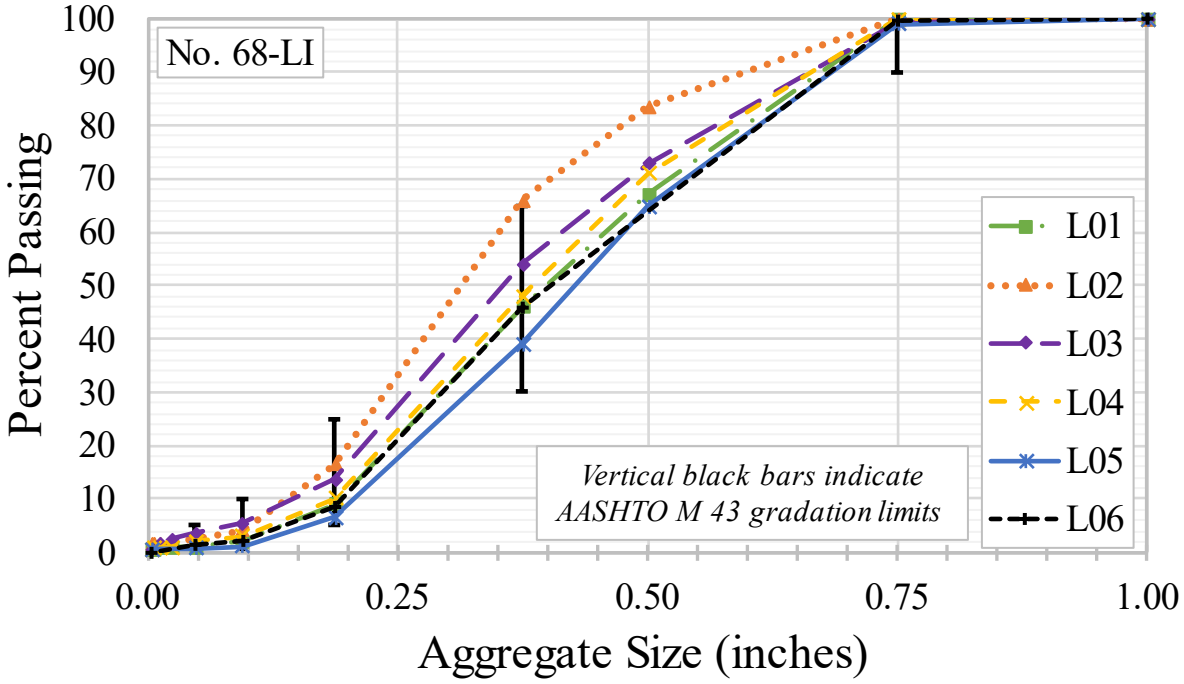

Source: FHWA.

B. No. 68-LI.

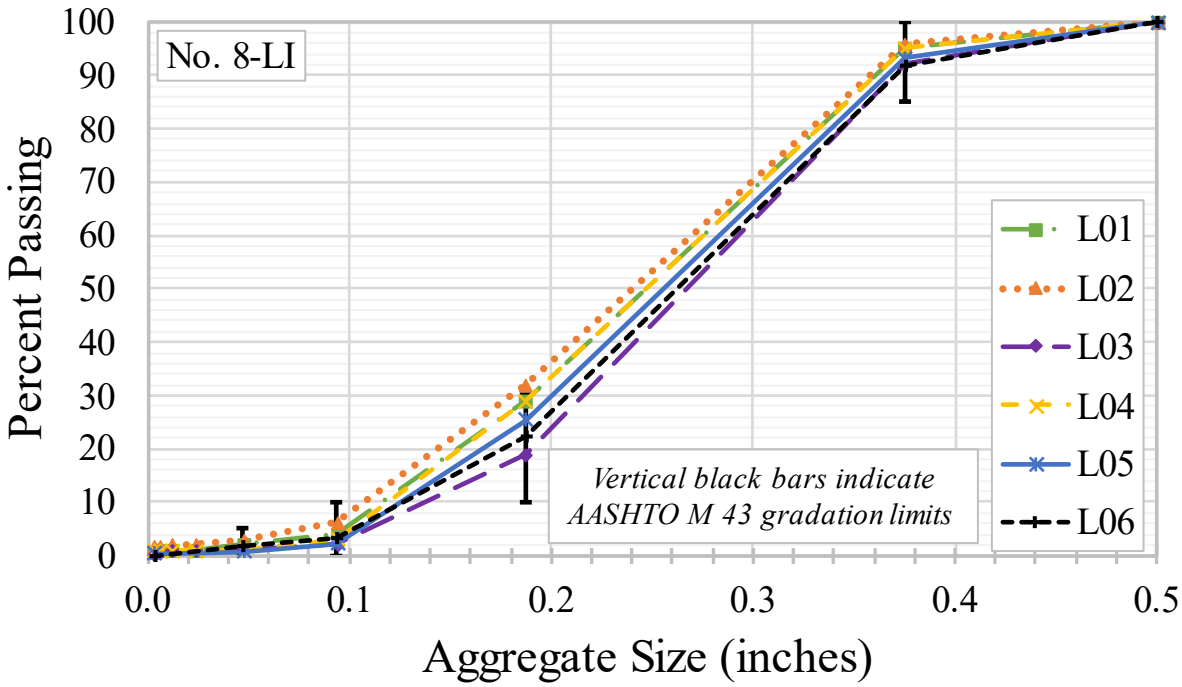

Source: FHWA.

C. No. 8-LI.

Figure 7. Charts. Gradation curves for the as-received LI OGAs.

Note that the AASHTO M 43-05 stone size limits are indicated by vertical bars on the charts at the appropriate sieve sizes for comparison. All laboratories, save L06, often included intermediate sieves not explicitly required to test for M 43-05 compliance. Nine of the fifteen OGAs tested were found by at least one laboratory to not comply with the M 43-05 stone size supplied by the source quarries (table 7), although the differences per sieve size was generally small (appendix B). The largest discrepancies were found for the GG and SI aggregates, whereby 18 of the 24 samples did not meet the specification which could suggest quarry practice resulted in the noncompliance.

The noted deviations in the as-received gradation results may also be in part due to variability in the stockpiles or due to FHWA packaging procedures when preparing samples from the initial 5-ton stockpiles delivered by the source quarries. In addition, natural segregation of the aggregates during delivery and specimen preparation by the participant laboratories could be another source of deviation. Regardless, the results presented in this chapter and the analyses in chapter 4 assume that each sample met the appropriate M 43-05 classification for reporting purposes (i.e., No. 57, No. 68, or No. 8). Any impacts resulting from noncompliance, however, were considered when evaluating the results of all subsequent testing.

Table 7. As-received gradation test results per AASHTO M 43-05 specifications.

Stone Size	Sample ID	L01	L02	L03	L04	L05	L06
No. 57	No. 57-BA	✓	✓	✓	✓	✓	✓
	No. 57-DI	✓	✓	✓	✓	✓	✓
	No. 57-GG	✓	×	×	×	✓	✓
	No. 57-LI	✓	✓	✓	✓	✓	✓
	No. 57-SI	✓	×	×	✓	✓	×
No. 68	No. 68-BA	✓	✓	✓	✓	✓	✓
	No. 68-DI	✓	✓	✓	×	×	✓
	No. 68-GG	✓	×	✓	✓	×	✓
	No. 68-LI	✓	×	✓	✓	✓	✓
	No. 68-SI	✓	✓	✓	✓	✓	✓
No. 8	No. 8-BA	✓	✓	×	✓	✓	×
	No. 8-DI	✓	✓	✓	✓	✓	✓
	No. 8-GG	✓	×	×	×	✓	×
	No. 8-LI	✓	×	✓	✓	✓	✓
	No. 8-SI	×	×	×	×	×	×

✓ = compliance with the specification; × = noncompliance with the specification.

Beyond testing simply for AASHTO M 43-05 compliance, the as-received sieving data were also used to determine relevant gradation parameters for each OGA, namely the D_{85}, or the particle size where 85 percent of particles are smaller (table 8).

Table 8. D_{85} (inch) for as-received OGAs.

Stone Size	Sample ID	L01	L02	L03	L04	L05	L06	$\bar{x}$	s	COV (%)
No. 57	No. 57-BA	0.73	0.78	0.72	0.75	0.87	0.88	0.79	0.07	8.9
	No. 57-DI	0.73	0.72	0.70	0.71	0.84	0.86	0.76	0.07	9.2
	No. 57-GG	0.84	0.73	0.85	0.80	0.87	0.90	0.83	0.06	7.2
	No. 57-LI	0.77	0.78	0.76	0.76	0.87	0.91	0.81	0.06	7.4
	No. 57-SI	0.75	0.86	0.66	0.81	0.85	0.84	0.80	0.08	10.0
	No. 57-Avg.	0.76	0.77	0.74	0.77	0.86	0.88	0.80	0.06	7.5
No. 68	No. 68-BA	0.73	0.65	0.64	0.63	0.66	0.68	0.67	0.04	6.0
	No. 68-DI	0.70	0.61	0.68	0.69	0.67	0.68	0.67	0.03	4.5
	No. 68-GG	0.60	0.61	0.66	0.63	0.63	0.66	0.63	0.02	3.2
	No. 68-LI	0.62	0.60	0.60	0.60	0.63	0.65	0.62	0.02	3.2
	No. 68-SI	0.66	0.65	0.61	0.67	0.66	0.68	0.66	0.02	3.0
	No. 68-Avg.	0.66	0.62	0.64	0.64	0.65	0.67	0.65	0.02	3.1
No. 8	No. 8-BA	0.37	0.36	0.43	0.36	0.36	0.37	0.38	0.03	7.9
	No. 8-DI	0.36	0.35	0.34	0.35	0.35	0.36	0.35	0.01	2.9
	No. 8-GG	0.39	0.37	0.40	0.40	0.37	0.37	0.38	0.02	5.3
	No. 8-LI	0.34	0.35	0.35	0.34	0.34	0.36	0.35	0.01	2.9
	No. 8-SI	0.37	0.35	0.36	0.35	0.36	0.37	0.36	0.01	2.8
	No. 8-Avg.	0.37	0.36	0.38	0.36	0.36	0.37	0.37	0.01	2.7

Avg. = average.

Figure 8 illustrates the variability of the D_{85} values presented in table 8. The D_{85} for each OGA sample was used to set the gap size between the upper and lower shear boxes during LSDS testing, hence its variability is of primary importance to this study. All laboratories found similar D_{85} values for the OGAs, indicating relatively uniform gradations among the laboratories (and thus gap sizes for LSDS testing). The largest variability in gradation occurred for the No. 57 OGAs, with an average COV of 7.5 percent. Sieve analysis for OS-20-30 was performed solely by FHWA, with a D_{85} (i.e., gap size) of 0.032 inches provided directly to each participant laboratory. Sieve analysis for the as-received OS-20-30 was not requested by the participant laboratories since the purpose was simply to evaluate differences in behavior due to the LSDS device and laboratory procedures using a standard soil.

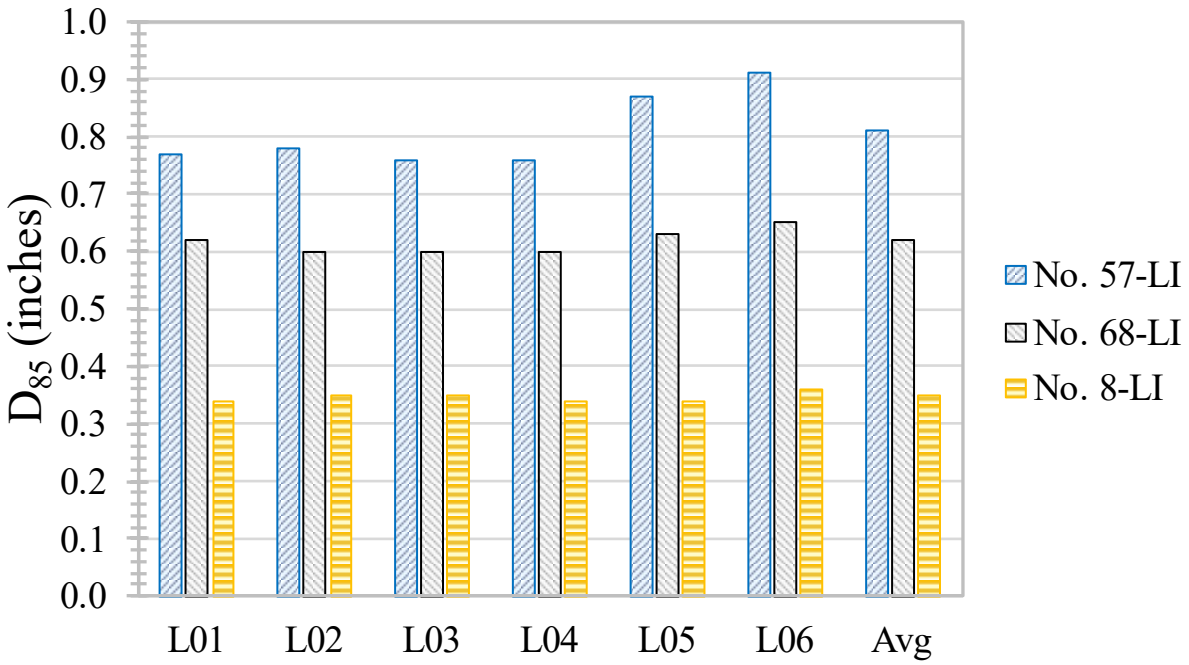

Source: FHWA.

Figure 8. Chart. D_{85} for LI OGAs.

Post-LSDS Gradations

For each OGA type tested, the sheared samples after LSDS testing under the four target normal stresses were then blended and sieved to determine the post-shear gradation (see appendix B). The change in the post-shear gradation was evaluated using the breakage index (B_I) described by Marsal (1967) (equation 2).

$$B_I = \sum [W_i - W_f] \quad (2)$$

Where W_i and W_f are the initial (i.e., as-received) and final (i.e., post-shear) percentages retained for each sieve size evaluated, respectively.

Only the positive changes in percent retained values were summed to determine the B_I for each sample (table 9).

Table 9. Breakage index (percent).

Stone Size	Sample ID	L01	L02	L03	L04	L05	L06	$\bar{x}$	*s*	COV (percent)
No. 57	No. 57-BA	10.0	9.3	4.3	7.0	1.6	0.4	5.4	4.0	74.1
	No. 57-DI	3.0	—	7.6	14.4	2.6	0.0	5.5	5.7	103.6
	No. 57-GG	8.1	14.8	7.0	6.0	6.0	0.0	7.0	4.8	68.6
	No. 57-LI	6.0	10.3	14.6	4.0	1.7	0.2	6.1	5.4	88.5
	No. 57-SI	5.9	21.5	10.2	9.1	9.5	1.4	9.6	6.7	69.8
	No. 57-Avg.	6.6	14.0	8.7	8.1	4.3	0.4	7.0	4.6	65.7
No. 68	No. 68-BA	7.3	6.4	10.5	2.0	7.7	3.7	6.3	3.0	47.6
	No. 68-DI	4.0	—	10.4	12.5	3.3	7.5	7.5	4.0	53.3
	No. 68-GG	4.2	3.1	13.7	13.0	15.3	0.1	8.2	6.5	79.3
	No. 68-LI	3.7	2.9	5.7	7.0	2.4	0.9	3.8	2.2	57.9
	No. 68-SI	4.0	15.3	6.5	7.0	3.8	0.6	6.2	5.0	80.6
	No. 68-Avg.	4.6	6.9	9.4	8.3	6.5	2.6	6.4	2.5	39.1
No. 8	No. 8-BA	9.3	4.6	17.8	13.7	2.3	4.6	8.7	6.0	69.0
	No. 8-DI	2.0	—	8.4	5.0	4.9	0.6	4.2	3.0	71.4
	No. 8-GG	3.2	2.4	3.0	11.2	5.6	9.1	5.8	3.6	62.1
	No. 8-LI	7.2	2.8	9.2	10.0	2.7	4.8	6.1	3.2	52.5
	No. 8-SI	3.0	8.4	4.0	7.5	2.2	4.4	4.9	2.5	51.0
	No. 8-Avg.	4.9	4.6	8.5	9.5	3.5	4.7	6.0	2.4	40.0

—Not measured/evaluated.

The highest B_I values were generally found by L03 and L04, whereas the lowest B_I values were generally found by L05 and L06. The largest variability in breakage occurred for the No. 57 OGAs, with an average COV of 65.7 percent. To illustrate the difference in breakage results, bar charts for the No. 57-LI, No. 68-LI, and No. 8-LI are presented in figure 9.

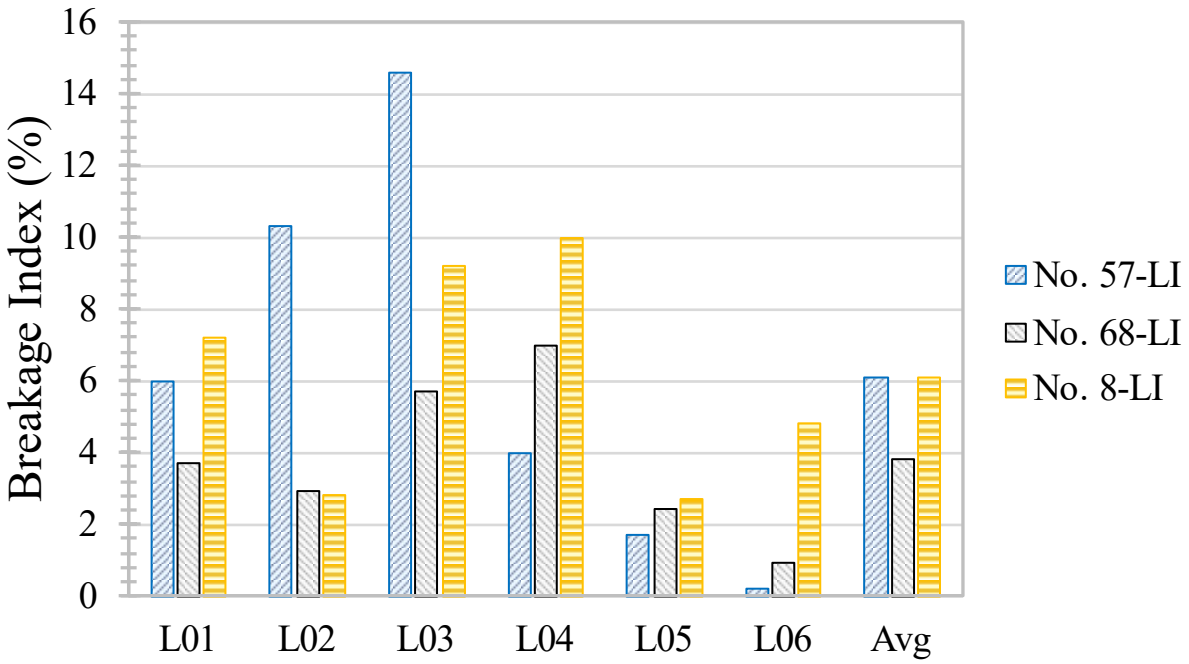

Source: FHWA.

Figure 9. Chart. Breakage index results for LI OGAs.

Dry Unit Weight

Participant laboratories were instructed to test the γ_{dmax} and γ_{dmin} of the OGAs per ASTM D4253 (ASTM 2016b) and D4254 (ASTM 2016c), respectively. The dry unit weight at 95 percent relative density (γ_{d95}) for each OGA was then calculated by the participating laboratories using equation 1 (chapter 2). The dry unit weight results were consistent across the laboratories for all OGAs for each particular rock type (table 10 through table 12).

Table 10. Dry unit weights for No. 57 OGAs.

Parameter	Sample ID	L01	L02	L03	L04	L05	L06	$\bar{x}$	s	COV (%)
γ_{dmin} (lb/ft^3)	No. 57-BA	96.8	98.4	97.1	97.0	93.6	98.3	96.9	1.7	1.8
	No. 57-DI	95.0	98.1	101.7	97.5	96.3	96.2	97.5	2.3	2.4
	No. 57-GG	89.0	92.6	90.7	89.5	84.3	89.4	89.3	2.8	3.1
	No. 57-LI	84.3	84.4	86.7	87.1	83.2	86.3	85.3	1.6	1.9
	No. 57-SI	90.6	87.8	89.1	88.3	87.7	88.3	88.6	1.1	1.2
	No. 57-Avg.	91.1	92.3	93.1	91.9	89.0	91.7	91.5	1.4	1.5
γ_{dmax} (lb/ft^3)	No. 57-BA	110.5	114.0	109.2	108.7	112.7	114.2	111.6	2.4	2.2
	No. 57-DI	106.7	110.9	110.9	110.8	110.8	110.4	110.1	1.7	1.5
	No. 57-GG	99.6	103.2	102.2	97.7	100.1	104.6	101.2	2.6	2.6
	No. 57-LI	97.3	99.4	98.6	96.3	101.7	99.7	98.8	1.9	1.9
	No. 57-SI	105.0	106.4	101.9	100.9	102.4	106.1	103.8	2.3	2.2
	No. 57-Avg.	103.8	106.8	104.6	102.9	105.5	107.0	105.1	1.6	1.5
γ_{d95} (lb/ft^3)	No. 57-BA	109.7	113.1	108.5	108.5	111.6	113.3	110.8	2.2	2.0
	No. 57-DI	106.0	110.2	110.4	110.1	110.0	109.6	109.4	1.7	1.6
	No. 57-GG	99.0	102.7	101.6	97.3	99.1	103.7	100.6	2.5	2.5
	No. 57-LI	96.6	98.5	97.9	95.8	100.5	98.9	98.0	1.7	1.7
	No. 57-SI	104.2	105.2	101.2	100.2	101.5	105.1	102.9	2.2	2.1
	No. 57-Avg.	103.1	105.9	103.9	102.4	104.5	106.1	104.3	1.5	1.4

Table 11. Dry unit weights for No. 68 OGAs.

Parameter	Aggregate	L01	L02	L03	L04	L05	L06	$\bar{x}$	s	COV (%)
γ_{dmin} (lb/ft^3)	No. 68-BA	100.1	97.0	100.8	99.1	98.2	101.8	99.5	1.8	1.8
	No. 68-DI	95.9	100.0	100.2	96.3	98.1	95.8	97.7	2.0	2.0
	No. 68-GG	86.6	94.5	88.5	89.7	89.2	90.6	89.9	2.6	2.9
	No. 68-LI	88.1	85.9	89.5	85.3	84.0	87.6	86.7	2.0	2.3
	No. 68-SI	93.6	89.2	92.5	89.3	88.4	90.6	90.6	2.1	2.3
	No. 68-Avg.	92.9	93.3	94.3	91.9	91.6	93.3	92.9	1.0	1.1
γ_{dmax} (lb/ft^3)	No. 68-BA	116.7	119.1	118.6	115.4	118.8	119.9	118.1	1.7	1.4
	No. 68-DI	112.3	115.7	111.2	110.6	111.1	112.7	112.3	1.9	1.7
	No. 68-GG	102.0	105.9	104.7	102.6	107.4	105.0	104.6	2.0	1.9
	No. 68-LI	98.7	103.4	102.1	100.0	104.9	104.4	102.3	2.5	2.4
	No. 68-SI	107.0	106.8	105.0	103.7	105.2	105.0	105.5	1.2	1.1
	No. 68-Avg.	107.3	110.2	108.3	106.5	109.5	109.4	108.5	1.4	1.3
γ_{d95} (lb/ft^3)	No. 68-BA	115.8	117.8	117.6	114.5	117.6	118.8	117.0	1.6	1.4
	No. 68-DI	111.5	114.8	110.6	109.8	110.4	111.7	111.5	1.8	1.6
	No. 68-GG	101.0	105.3	103.8	101.9	106.3	104.1	103.7	2.0	1.9
	No. 68-LI	98.1	102.3	101.4	99.2	103.6	103.4	101.3	2.3	2.3
	No. 68-SI	106.3	105.8	104.3	102.9	104.2	104.1	104.6	1.2	1.1
	No. 68 Avg.	106.5	109.2	107.5	105.7	108.4	108.4	107.6	1.3	1.2

Table 12. Dry unit weights for No. 8 OGAs.

Parameter	Aggregate	L01	L02	L03	L04	L05	L06	$\bar{x}$	s	COV (%)
γ_{dmin} (lb/ft^3)	No. 8-BA	94.6	94.4	94.3	91.8	93.1	96.8	94.2	1.7	1.8
	No. 8-DI	87.4	94.7	91.8	86.1	91.1	85.6	89.5	3.6	4.0
	No. 8-GG	87.3	95.2	88.7	85.7	87.4	88.1	88.7	3.3	3.7
	No. 8-LI	78.8	83.3	81.2	78.7	80.6	80.6	80.5	1.7	2.1
	No. 8-SI	88.0	85.1	85.2	84.8	84.8	85.6	85.6	1.2	1.4
	No. 8-Avg.	87.2	90.5	88.2	85.4	87.4	87.3	87.7	1.7	1.9
γ_{dmax} (lb/ft^3)	No. 8-BA	112.7	113.2	113.9	106.4	112.8	117.6	112.8	3.6	3.2
	No. 8-DI	103.7	105.9	106.5	102.8	107.0	106.1	105.3	1.7	1.6
	No. 8-GG	100.1	106.3	103.6	98.5	102.3	104.6	102.6	2.9	2.8
	No. 8-LI	96.5	100.3	98.9	96.8	102.7	100.8	99.3	2.4	2.4
	No. 8-SI	101.9	104.8	103.0	97.6	101.4	103.2	102.0	2.4	2.4
	No. 8 Avg.	103.0	106.1	105.2	100.4	105.2	106.5	104.4	2.3	2.2
γ_{d95} (lb/ft^3)	No. 8-BA	111.6	112.1	112.7	105.6	111.6	116.3	111.7	3.5	3.1
	No. 8-DI	102.5	105.2	105.7	102.0	106.1	104.8	104.4	1.7	1.6
	No. 8-GG	99.5	105.6	102.7	97.8	101.4	103.7	101.8	2.8	2.8
	No. 8-LI	95.4	99.3	97.8	95.7	101.4	99.5	98.2	2.3	2.3
	No. 8-SI	101.1	103.6	102.0	96.9	100.4	102.1	101.0	2.3	2.3
	No. 8 Avg.	102.0	105.2	104.2	99.6	104.2	105.3	103.4	2.2	2.1

This consistency indicates relatively uniform levels of target compaction (i.e., γ_{d95}) for LSDS testing; see figure 10 as an example. The target unit weight (i.e., γ_{d95}) for LSDS testing of OS-20-30 was provided to each laboratory based on density testing performed solely by FHWA; the γ_{d95} for OS-20-30 was 111.0 lb/ft^3, and the minimum and maximum dry densities for OS-20-30 were 98.9 and 111.7 lb/ft^3, respectively.

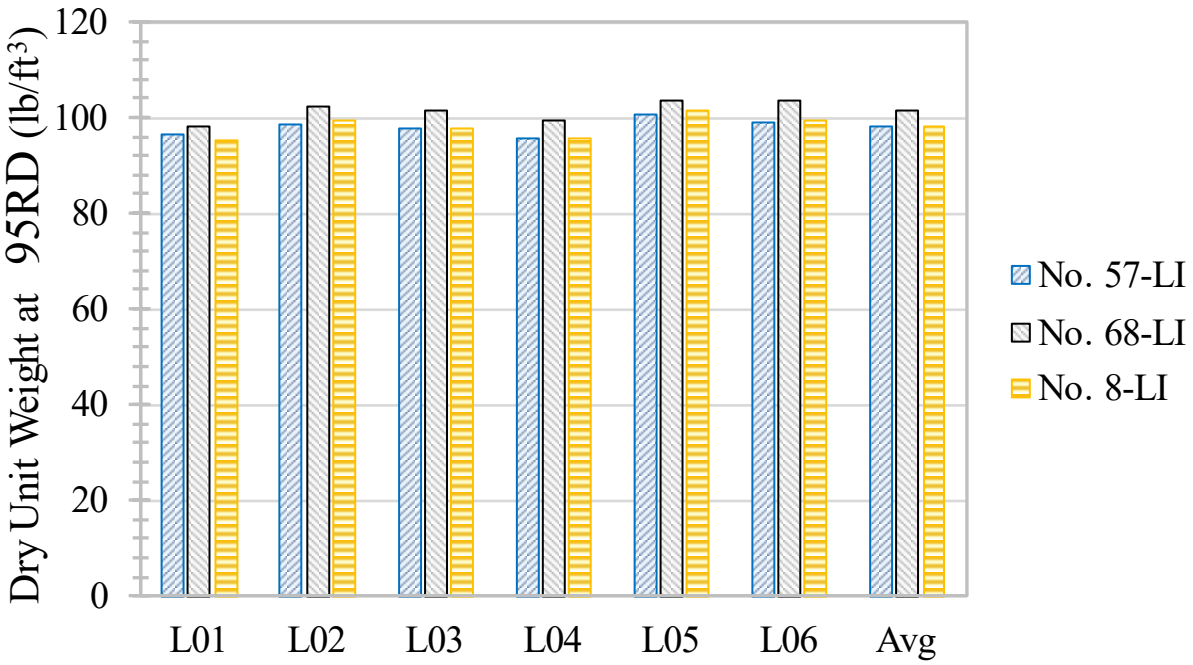

Source: FHWA.

Figure 10. Chart. γ_{d95} values for LI OGAs.

Bulk Dry Specific Gravity

The bulk dry specific gravity (*Gsb*) of each OGA was provided directly by the source quarries (table 13). The *Gsb* refers to the ratio of the dry unit weight of the aggregate to the weight of water of equal volume. The heaviest rock types were BA and DI, with average *Gsb* values of 2.922 and 2.923, respectively; GG was generally the lightest, with an average *Gsb* of 2.704.

Table 13. Reported bulk dry specific gravities for the OGAs.

Stone Size	Sample ID	*Gsb*
No. 57	No. 57-BA	2.923
	No. 57-DI	2.936
	No. 57-GG	2.685
	No. 57-LI	2.716
	No. 57-SI	2.737
No. 68	No. 68-BA	2.928
	No. 68-DI	2.908
	No. 68-GG	2.730
	No. 68-LI	2.722
	No. 68-SI	2.737
No. 8	No. 8-BA	2.914
	No. 8-DI	2.925
	No. 8-GG	2.697
	No. 8-LI	2.722
	No. 8-SI	2.727

Particle Characteristics

FHWA performed AIMS2 testing on each OGA sample to evaluate gradient angularity (GA), SP, F&E values, and TX. For OS-20-30, FHWA only performed AIMS2 GA testing. SP, F&E, and TX could not be evaluated for OS-20-30, per AASHTO T 381, due to the relatively fine particle size. Full AIMS2 results for each sample are provided in appendix C.

Angularity

The cumulative angularity for each sieve size was evaluated individually (appendix C). A stockpile approach was taken whereby the weighted average GA indexes were calculated by summing the individual angularity results per sieve multiplied by the percentage of material retained on that sieve. The weighted AIMS2 GA index results (table 14) show that all tested OGAs have low angularity (i.e., average GA index $\leq$ 3,300, per AASHTO R 91-18) (AASHTO 2018b). The AIMS2 results classified OS-20-30 as also having low angularity, although the weighted average GA index is an order of magnitude lower than the OGAs (table 14). The variability of angularity measurements per sample ID was not evaluated in the round-robin study; however, when all OGAs evaluated in this study were combined, the mean GA index was 3,069, with a COV of 3.7 percent.

Table 14. Summary of AIMS2 weighted averages for angularity.

Stone Size	Sample ID	Average GA Index	GA Classification
No. 57	No. 57-BA	2,948	Low
	No. 57-DI	2,957	Low
	No. 57-GG	2,934	Low
	No. 57-LI	3,177	Low
	No. 57-SI	3,031	Low
	No. 57-Avg.	3,009	Low
No. 68	No. 68-BA	2,956	Low
	No. 68-DI	2,936	Low
	No. 68-GG	3,158	Low
	No. 68-LI	3185	Low
	No. 68-SI	3147	Low
	No. 68-Avg.	3,076	Low
No. 8	No. 8-BA	3,131	Low
	No. 8-DI	2,922	Low
	No. 8-GG	3,147	Low
	No. 8-LI	3,209	Low
	No. 8-SI	3,192	Low
	No. 8-Avg.	3,120	Low
OS-20-30	OS-20-30	674	Low

Sphericity

AIMS2 SP testing was conducted in a similar fashion to angularity, resulting in weighted average SP indexes for each OGA (table 15). All OGAs were classified as having medium SP (i.e., average SP index between 0.3 and 0.7, per AASHTO R 91-18) (AASHTO 2018b). The variability of these SP measurements per sample ID was not evaluated in the round-robin study; however, when all OGAs evaluated in this study were combined, the mean SP index was 0.579, with a COV of 5 percent.

Table 15. Summary of AIMS2 weighted averages for SP.

Stone Size	Sample ID	Average SP Index	SP Classification
No. 57	No. 57-BA	0.568	Medium
	No. 57-DI	0.588	Medium
	No. 57-GG	0.607	Medium
	No. 57-LI	0.541	Medium
	No. 57-SI	0.595	Medium
	No. 57-Avg.	0.580	Medium
No. 68	No. 68-BA	0.626	Medium
	No. 68-DI	0.614	Medium
	No. 68-GG	0.577	Medium
	No. 68-LI	0.527	Medium
	No. 68-SI	0.612	Medium
	No. 68-Avg.	0.591	Medium
No. 8	No. 8-BA	0.556	Medium
	No. 8-DI	0.567	Medium
	No. 8-GG	0.576	Medium
	No. 8-LI	0.547	Medium
	No. 8-SI	0.580	Medium
	No. 8-Avg.	0.565	Medium

F&E Values

The F&E values refer to the ratio of particle length (*L*) to thickness (*S*). Table 16 provides the distribution of the F&E values for different *L*/*S* ratios; F&E values greater than 5:1 are indicative of an exceptionally elongated shape. The No. 8 OGAs had the highest average percentages for F&E values of 3:1, 4:1, and 5:1 (i.e., the least spherical) while No. 57 OGAs had the least. The DI and GG OGAs exhibited the least F&E of greater than 5:1 percent.

Table 16. Summary of AIMS2 weighted averages for F&E values.

Stone Size		Flat and Elongated Distribution (%)				
		L/S ≥ 1:1	L/S > 2:1	L/S > 3:1	L/S > 4:1	L/S > 5:1
No. 57	No. 57-BA	98.0	73.3	33.6	13.8	7.7
	No. 57-DI	96.8	79.6	42.3	16.9	3.6
	No. 57-GG	99.4	68.5	23.8	10.8	2.0
	No. 57-LI	96.9	80.9	38.6	16.6	7.2
	No. 57-SI	93.8	81.6	43.1	20.4	8.8
	No. 57-Avg.	97.0	76.8	36.3	15.7	5.9
No. 68	No. 68-BA	86.4	67.8	30.1	12.0	6.3
	No. 68-DI	94.2	85.6	43.8	16.8	4.7
	No. 68-GG	95.9	81.5	46.0	18.1	7.5
	No. 68-LI	90.1	87.6	66.5	32.9	11.6
	No. 68-SI	92.0	82.6	45.7	20.3	9.4
	No. 68-Avg.	91.7	81.0	46.4	20.0	7.9
No. 8	No. 8-BA	80.6	73.4	57.1	38.9	21.8
	No. 8-DI	82.6	78.3	49.1	22.0	9.3
	No. 8-GG	92.0	83.6	50.8	31.1	11.4
	No. 8-LI	74.2	67.8	50.1	31.8	19.9
	No. 8-SI	76.8	72.2	46.9	23.8	16.4
	No. 8-Avg.	81.2	75.1	50.8	29.5	15.8

Surface TX

AIMS2 surface roughness measurements and weighted average TX indexes were prepared for all OGAs (table 17). TX classifications ranged from medium (i.e., average TX index values between 260 and 550 per AASHTO R 91-18) to high (i.e., average TX index values between 550 and 1,000) roughness without an obvious trend associated with stone size. Mineralogy appeared to be a larger factor; SI OGAs had consistently lower (i.e., smoother) average TX index values, while GG OGAs had the highest roughness within each stone size. The variability of these TX measurements per sample ID was not evaluated in the round-robin study. However, when all OGAs evaluated in this study were combined, the mean TX index was 485, with a COV of 25.2 percent.

Table 17. Summary of AIMS2 weighted averages for texture.

Stone Size	Sample ID	Average TX Index	TX Classification
No. 57	No. 57-BA	335	Medium
	No. 57-DI	523	Medium
	No. 57-GG	633	High
	No. 57-LI	479	Medium
	No. 57-SI	261	Medium
	No. 57-Avg.	446	Medium
No. 68	No. 68-BA	483	Medium
	No. 68-DI	571	High
	No. 68-GG	628	High
	No. 68-LI	552	High
	No. 68-SI	336	Medium
	No. 68-Avg.	514	Medium
No. 8	No. 8-BA	518	Medium
	No. 8-DI	582	High
	No. 8-GG	630	High
	No. 8-LI	366	Medium
	No. 8-SI	372	Medium
	No. 8-Avg.	494	Medium

Abrasion Resistance and Durability

L.A. abrasion and magnesium sulfate soundness results were provided by the source quarries for the respective rock types delivered (table 18). In addition, Micro-Deval tests were performed by FHWA to further characterize the abrasion and impact resistance of the OGA rock types (table 18). SI OGAs saw the lowest percent mass loss during both Micro-Deval and L.A. abrasion testing. Conversely, GG experienced the highest mass loss during both abrasion tests. BA OGAs experienced the least percent mass loss after magnesium sulfate soundness tests, while GG had the highest mass loss. The combined results indicate that SI was the most durable rock type, while GG was the least. The variability of these abrasion resistance and durability measurements was not evaluated in the round-robin study; however, as reported in chapter 1, a COV of 5.3 to 10.0 percent may be expected for the Micro-Deval and L.A. Abrasion results.

Table 18. Durability results for the OGA rock types.

Rock Type	Percent Mass Loss		
	Micro-Deval	L.A. Abrasion*	Magnesium Sulfate Soundness*
BA	10.3	13.7**	0.40
DI	5.5	13.0	1.20
GG	11.2	36.0	1.30
LI	10.2	12.0	0.70
SI	5.3	12.0	0.50

*Data were provided by the quarries for each OGA delivered.
**Average value for the OGAs is reported; No. 8-BA and No. 68-BA = 14.0, whereas No. 57-BA = 13.0.

SHEAR STRENGTH AND DEFORMATION

The mechanical properties of soils and aggregates primarily relate to the strength and deformation characteristics during loading (Borowicka 1961). To this end, participant laboratories were instructed to conduct LSDS testing per ASTM D3080 (2011). All the samples were subject to four LSDS tests. The tests were performed at target applied normal stresses (σ_n) of 5, 10, 15, and 30 psi. The direct LSDS test outputs include normal load, shear load, horizontal displacement/strain, and vertical displacement/strain. From these measurements, the derived shear strength parameters include the following:

a. Secant (i.e., peak) friction angle (ϕ_s) at each target applied σ_n (e.g., secant, or peak friction angle at 5-psi target applied normal stress ($\phi_{s,5psi}$), secant, or peak friction angle at 10-psi target applied normal stress ($\phi_{s,10psi}$), secant, or peak friction angle at 15-psi target applied normal stress ($\phi_{s,15psi}$), secant, or peak friction angle at 30-psi target applied normal stress ($\phi_{s,30psi}$));

b. Tangent friction angle (ϕ_t) and c_a based on a linear Mohr-Coulomb failure envelope;

c. Residual tangent friction angle at 20 percent horizontal strain ($\phi_{t,r}$) based on a linear Mohr-Coulomb failure envelope;

d. Constant volume friction angle (ϕ_{cv}) based on the zero dilation angle approach. A detailed description of the data reduction approaches, and key definitions of the extracted strength parameters used in this report, are referenced in Nicks et al. (2015).

The τ of a soil/aggregate (equation 3) is a function of the σ_n, friction angle (ϕ), and cohesion value (c).

$$\tau = \sigma_n \tan\phi + c \tag{3}$$

The design requirements for a project, plus engineering judgment, will determine which friction angle to use to evaluate τ (e.g., secant, tangent, residual tangent, or constant volume). Friction angles are a function of interparticle sliding, crushing, rearrangement, and the dilation of the particles during shear (Rowe 1962); interlocking of the particles during shear has also been

found to contribute to friction angle (Guo and Su 2007). Many of these mechanisms can be captured by measuring the deformation behavior during LSDS testing (i.e., the vertical and horizontal displacement/strain). The vertical displacement during the shearing process typically indicates contraction (i.e., compression) of the specimen, followed by expansion of the specimen (i.e., dilation), until a general leveling off at large horizontal displacements.

Since all LSDS tests were performed under dry conditions (i.e., no saturation), total stress parameters are presented herein; however, effective stress parameters could also have been equivalently used because the pore water pressure was zero in all cases. Representative graphs illustrating the results of LSDS tests are presented in this section, including the baseline OS-20-30 and Nos. 57-, 68-, and 8-LI OGAs. All LSDS stress-strain and strain-strain plots are presented in appendix D.

In the data reduction and analysis of the LSDS results, note that no area corrections were applied to the reported results for normal and shear stresses since that was not standard practice among the participating laboratories. Corrections were also not applied for the shear or deformation resistance of the LSDS devices themselves since that also was not standard practice among the participating laboratories. The vertical strain results represent an average of all LVDT measurements, initialized to zero at the start of shear. For laboratories with only one LVDT (table 6), the results are presented directly as reported, initialized to zero at the start of shear. Positive values of vertical strain indicate compression whereas negative values indicate dilation. The shear stress was initialized to zero at the start of shear for each laboratory (see appendix D for those initial values post-consolidation, pre-shear). The impact of applying or not applying corrections to LSDS data was not evaluated in this study; however, the characteristic trends found through the results would remain similar regardless.

OS-20-30

The shear stress-horizontal strain curves for OS-20-30 are presented in figure 11; corresponding vertical-horizontal strain curves are shown in figure 12. Based on these results, the peak shear stress, horizontal strain at peak shear ($\varepsilon_{h,peak}$), secant, tangent, residual tangent, ϕ_{cv}, and maximum dilation angle were determined.

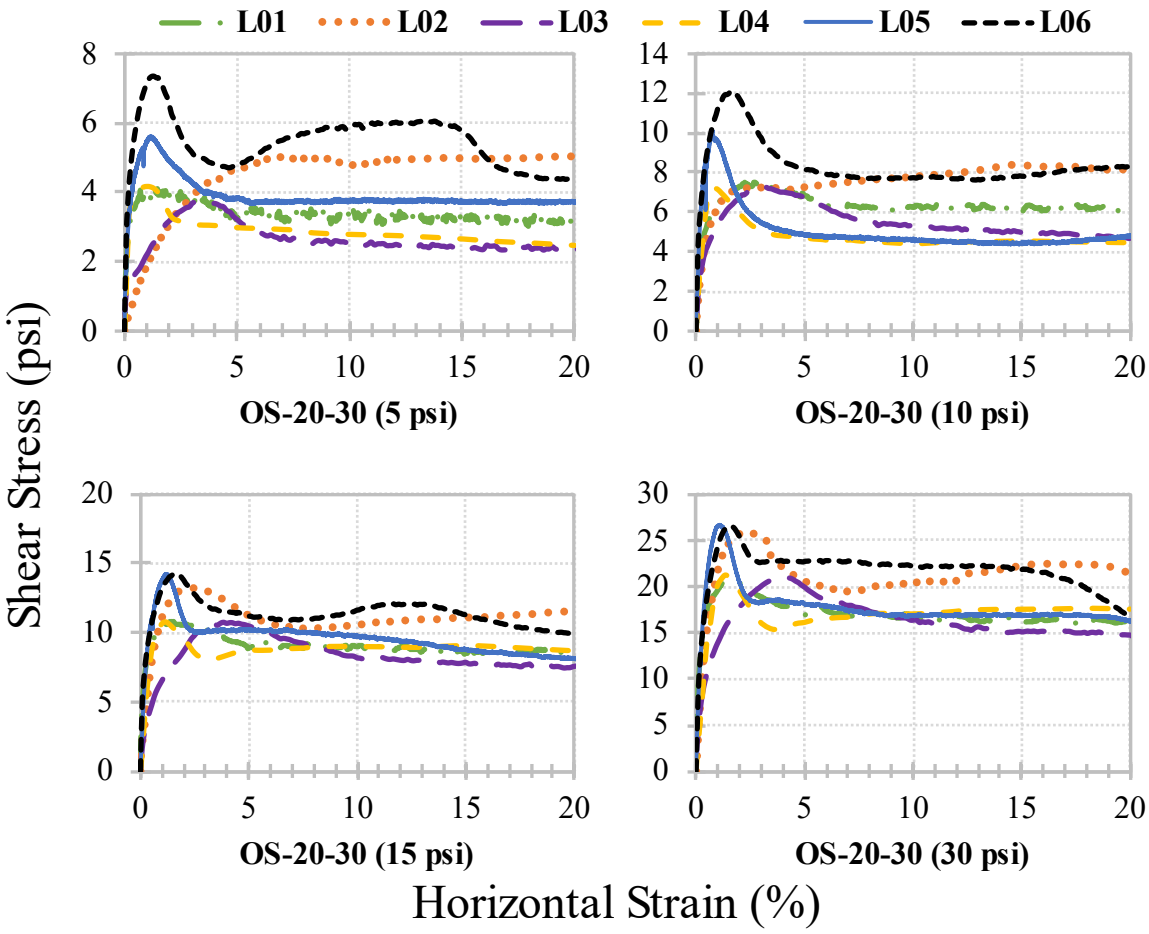

Source: FHWA.

Figure 11. Charts. Shear stress versus horizontal strain for OS-20-30.

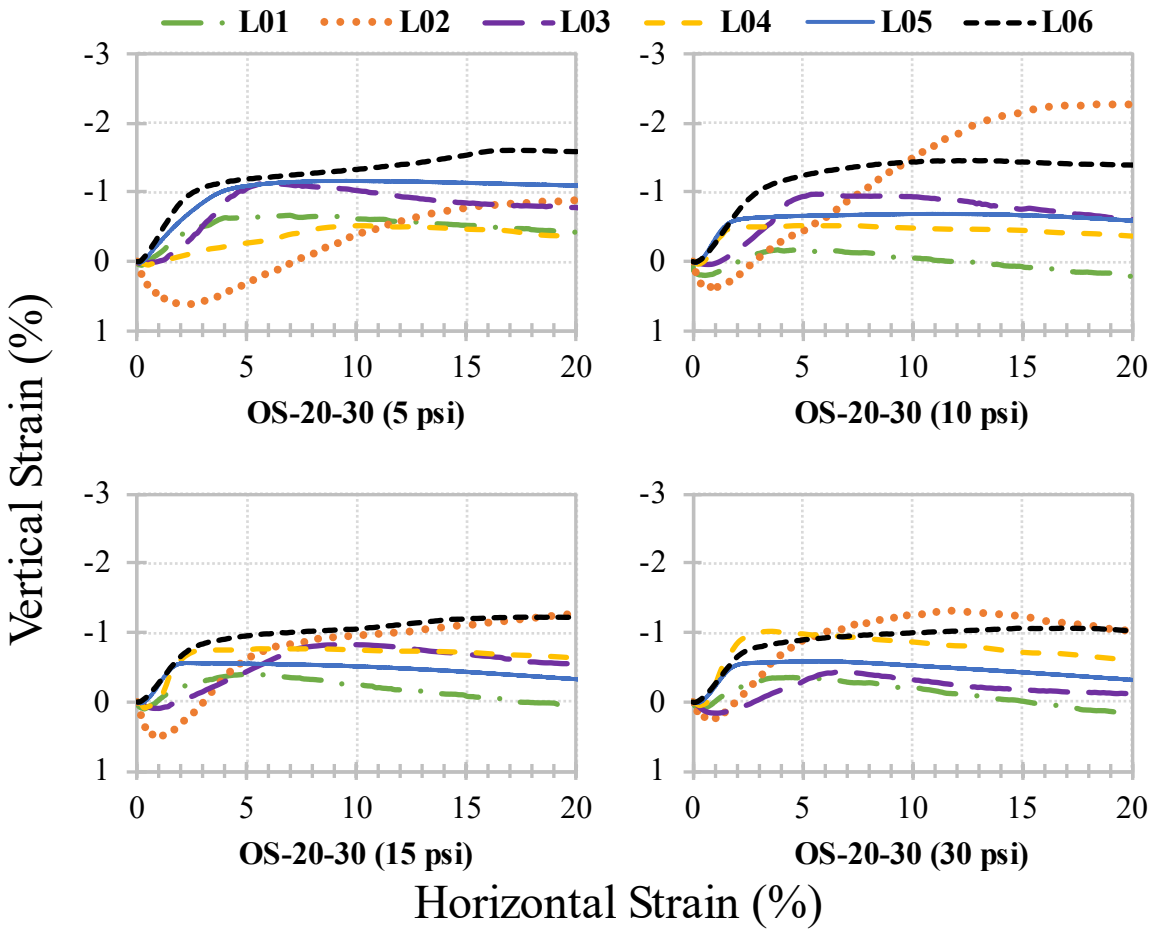

Source: FHWA.

Figure 12. Charts. Vertical strain versus horizontal strain for OS-20-30.

Peak Shear Stress

Classical results for a densely packed soil sample would show a sharp peak in shear stress followed by strain softening (Holtz and Kovacs 1981). This expected behavior was consistently seen in L04, L05, and L06 shear-strain curves (figure 11); however, not all results indicated this behavior. For example, although the target density for LSDS testing was the same for all laboratories (i.e., γ_{d95} = 111.0 lb/ft^3), the results from L02 at lower σ_n exhibited the behavior of a loosely packed sample whereby the shear stress continued to gradually increase with no shear softening (figure 11). Excluding L02's anomalously high values for $\varepsilon_{h,peak}$ at these lower normal stresses, the interlaboratory variability of $\varepsilon_{h,peak}$ was relatively large, with COVs of 50 percent or greater (table 19). In addition to differences in the characteristic shapes of the shear stress-horizontal strain curves, the magnitude of peak shear stresses (τ_{peak}) varied between these laboratories, with COVs decreasing with increasing σ_n, ranging from 26.0 to 12.7 percent (table 19).

Table 19. Peak shear parameters for OS-20-30.

Parameter		L01	L02	L03	L04	L05	L06	$\bar{x}$	s	COV (percent)
Peak Shear Stress (psi)	$\tau_{peak,5psi}$	4.1	5.0	3.7	4.2	5.6	7.3	5.0	1.3	26.0
	$\tau_{peak,10psi}$	7.5	8.4	7.3	7.2	10.1	12.1	8.8	2.0	22.7
	$\tau_{peak,15psi}$	10.8	13.3	10.7	10.8	14.2	14.3	12.4	1.8	14.5
	$\tau_{peak,30psi}$	20.6	25.9	21.0	21.2	26.7	26.6	23.7	3.0	12.7
Horizontal Strain at Peak Shear Stress (percent)	$\varepsilon_{h,peak,5psi}$	1.5	18.8	3.3	1.0	1.1	1.3	4.5	7.1	157.8
	$\varepsilon_{h,peak,10psi}$	2.2	14.7	3.2	0.8	0.8	1.6	3.9	5.4	138.5
	$\varepsilon_{h,peak,15psi}$	1.4	2.6	3.8	1.2	1.2	1.6	2.0	1.0	50.0
	$\varepsilon_{h,peak,30psi}$	1.4	2.5	4.0	1.3	1.1	1.5	2.0	1.1	55.0

$\varepsilon_{h,peak}$ = horizontal strain at peak shear.
$\varepsilon_{h,peak,5psi}$ = horizontal strain at peak shear at 5-psi target applied normal stress.
$\varepsilon_{h,peak,10psi}$ = horizontal strain at peak shear at 10-psi target applied normal stress.
$\varepsilon_{h,peak,15psi}$ = horizontal strain at peak shear at 15-psi target applied normal stress.
$\varepsilon_{h,peak,30psi}$ = horizontal strain at peak shear at 30-psi target applied normal stress.

Secant Friction Angle

The secant friction angle (ϕ_s) for each target σ_n was also calculated (table 20).

Table 20. Shear strength parameters for OS-20-30.

Parameter		L01	L02	L03	L04	L05	L06	$\bar{x}$	s	COV (percent)
Secant Friction Angle (degree)	$\phi_{s,5psi}$	39.4	45.3	36.8	39.8	48.3	55.8	44.2	7.1	16.1
	$\phi_{s,10psi}$	36.9	40.0	36.0	35.8	45.4	50.3	40.7	5.9	14.5
	$\phi_{s,15psi}$	35.8	41.5	35.6	35.7	43.5	43.6	39.3	4.0	10.2
	$\phi_{s,30psi}$	34.5	40.8	35.0	35.3	41.6	41.5	38.1	3.5	9.2
Mohr-Coulomb Parameters	c_a (psi)	0.9	0.5	0.4	0.5	1.6	3.7	1.3	1.3	100.0
	ϕ_t (deg)	33.4	40.3	34.6	34.5	40.0	37.1	36.7	3.0	8.2
	$\phi_{t,r}$ (deg)	29.2	36.5	26.2	29.7	28.4	31.1	30.2	3.5	11.6
Constant Volume Friction Angle (degree)	ϕ_{cv}	32.4	48.4	34.3	41.1	44.7	-0.7	33.4	17.8	53.3

As expected, all laboratories (excepting L02) saw a decrease in ϕ_s as the target σ_n increased from 5 psi to 30 psi (figure 13).

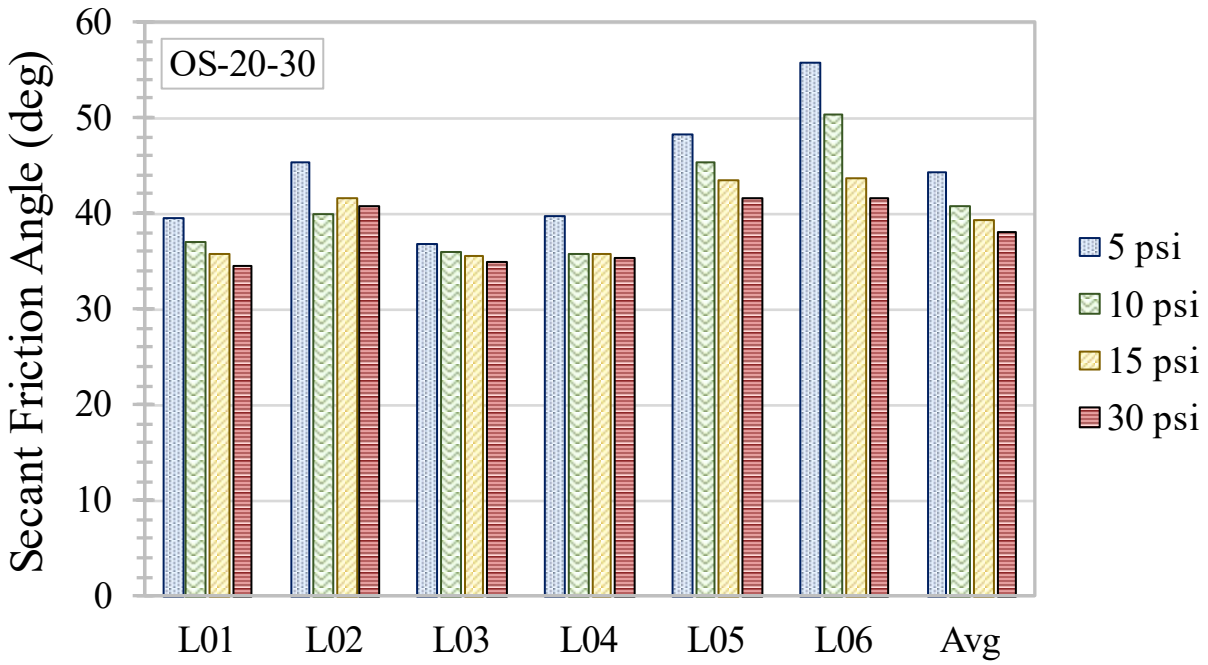

Source: FHWA.

Figure 13. Chart. Secant friction angles for OS-20-30.

The mean ($\bar{x}$), standard deviation (s), and COV between the laboratories were computed for each parameter (table 20). The variability of ϕ_s was lower than the variability of τ_{peak}, with COVs ranging from 9.2 to 16.1 percent.

Tangent Friction Angle

Tangent friction angle (ϕ_t) and c_a values, presented in table 20, were derived from the linear Mohr-Coulomb failure envelopes (figure 14). Regardless of the behavior during shear, the resulting ϕ_t had generally low variability, with a mean ϕ_t of 36.7 degrees and a COV of 8.2 percent. Ultimately, ϕ_t results were less variable than those of ϕ_s. Apparent cohesion (c_a) appeared in the assumed linear failure envelopes for all laboratories (table 20), despite OS-20-30 being cohesionless. Variability of c_a was high, with a mean of 1.3 psi and a COV of 100 percent. However, c_a would not be considered in design.

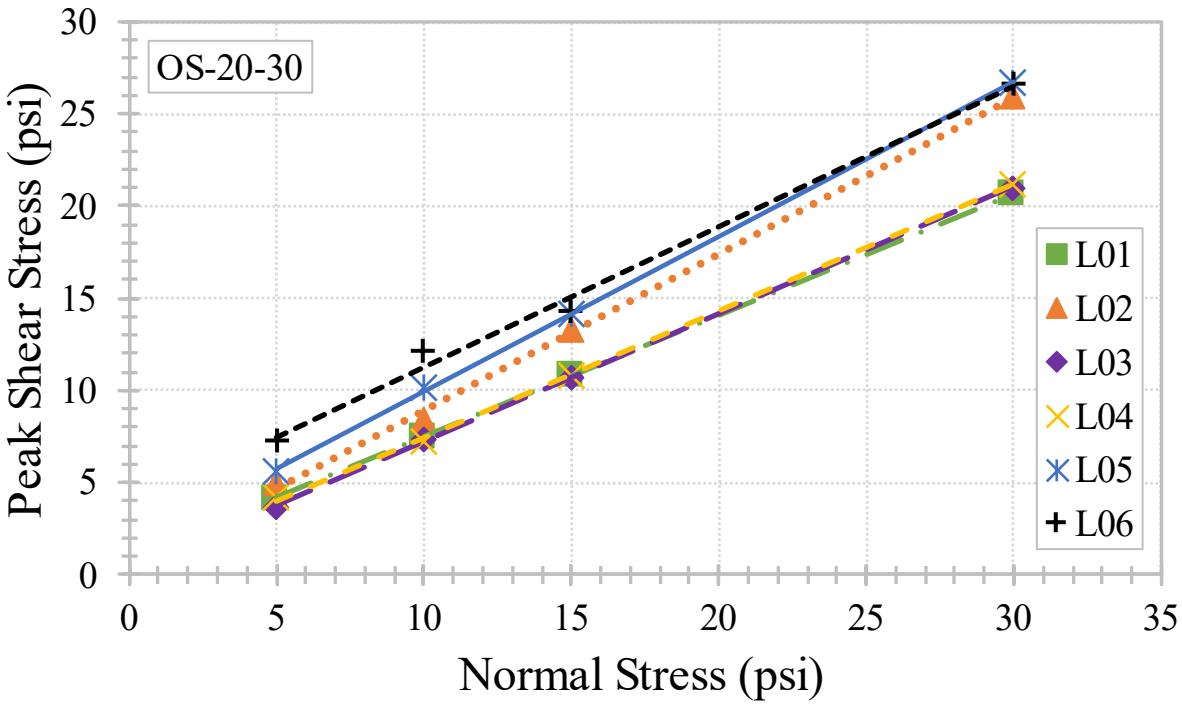

Source: FHWA.

Figure 14. Chart. Linear Mohr-Coulomb failure envelopes for OS-20-30.

Residual Friction Angle

Using the residual, or "fully softened," shear stresses (τ_r) (i.e., τ at 20-percent horizontal strain) to develop linear Mohr-Coulomb failure envelopes, the tangent of the residual friction angles ($\phi_{t,r}$) were calculated (table 20). In the case of $\phi_{t,r}$, all failure envelopes were force-fit to have zero cohesion. The mean $\phi_{t,r}$ was 30.2 degrees, with a COV of 11.6 percent.

Constant Volume Friction Angle

Another strength parameter evaluated was the constant volume friction angle (ϕ_{cv}) that corresponds to ϕ_s at zero dilation. Peak secant friction angles for each target σ_n were plotted against their corresponding maximum dilation angles (ψ_{max}); the y-intercept of the best-fit line through those plotted points is the ϕ_{cv} (table 20). Relatively large variability was found for this parameter, ranging from −0.7 to 48.4 degrees, with a mean ϕ_{cv} of 33.4 degrees and a COV of 53.3 percent.

Maximum Dilation Angle

As described in the preceding subsection, a key parameter needed to determine the ϕ_{cv} was the maximum dilation angle (ψ_{max}). Maximum dilation angles were calculated with the equation $\psi_{max} = tan^{-1}(\Delta v_{max}/\Delta h)$, where Δv_{max} and Δh are the maximum change in vertical displacement and the constant change in horizontal displacement, respectively. To ensure uniformity in determining Δv_{max} for a consistent Δh between the laboratories, differing "n-point" centered moving averages were used to analyze the data. This method of analysis was required because the sampling

frequency, or time step (Δt), for data collection varied widely between the laboratories (table 21). Centered moving averages targeting a 0.02-inch Δh were selected so that results from this study could be directly compared to previous FHWA work on characterizing OGAs (Nicks et al. 2015). It is worth noting that L04 had a particularly variable Δt that continuously increased during their tests. While the overall average Δh was 0.05 inches for L04, Δh was closer to the 0.02-inch target during the early stages of the test where maximum dilation typically occurred.

Table 21. Selection of *n*-point centered moving averages for ψ_{max} computation.

Laboratory ID	Δt^{+} (s)	Δh^{+} (inch)	Required *n*-point	Actual *n*-point	Actual *n*-point Δh (inch)
L01	16	0.004	6	7	0.024
L02	24	0.006	4.3	5	0.024
L03	80	0.02	2	1	0.02
L04	200	0.05	1.4	1	0.05
L05	1	0.00025	81	81	0.02
L06	40	0.01	3	3	0.02

[+]Typical values (table 6).

The vertical-horizontal strain curves (figure 12) and thus the computed maximum dilation angles (table 22), showed considerable variation in deformation behavior during shear. COVs for ψ_{max} ranged from 38.1 to 49.7 percent, with means ranging from 12.5 to 15.4 degrees.

Table 22. Maximum dilation angles for OS-20-30.

Parameter	L01	L02	L03	L04	L05	L06	$\bar{x}$	s	COV (percent)
$\psi_{max,5psi}$ (degree)	9.6	10.6	14.4	5.7	15.2	19.3	12.5	4.8	38.4
$\psi_{max,10psi}$ (degree)	5.9	14.3	15.6	21.8	18.4	16.4	15.4	5.3	34.4
$\psi_{max,15psi}$ (degree)	8.7	14.3	9.6	24.2	16.9	14.7	14.7	5.6	38.1
$\psi_{max,30psi}$ (degree)	7.7	19.6	4.9	24.2	15.3	15.0	14.5	7.2	49.7

In general, ψ_{max} is expected to decrease with increasing σ_n; however, all laboratories diverged from the expected trend to varying degrees (figure 15). This divergence may be due to issues with measuring vertical deformation that could also be impacted by the mobility and rigidity of the LSDS device, or due to issues with the data collection frequency.

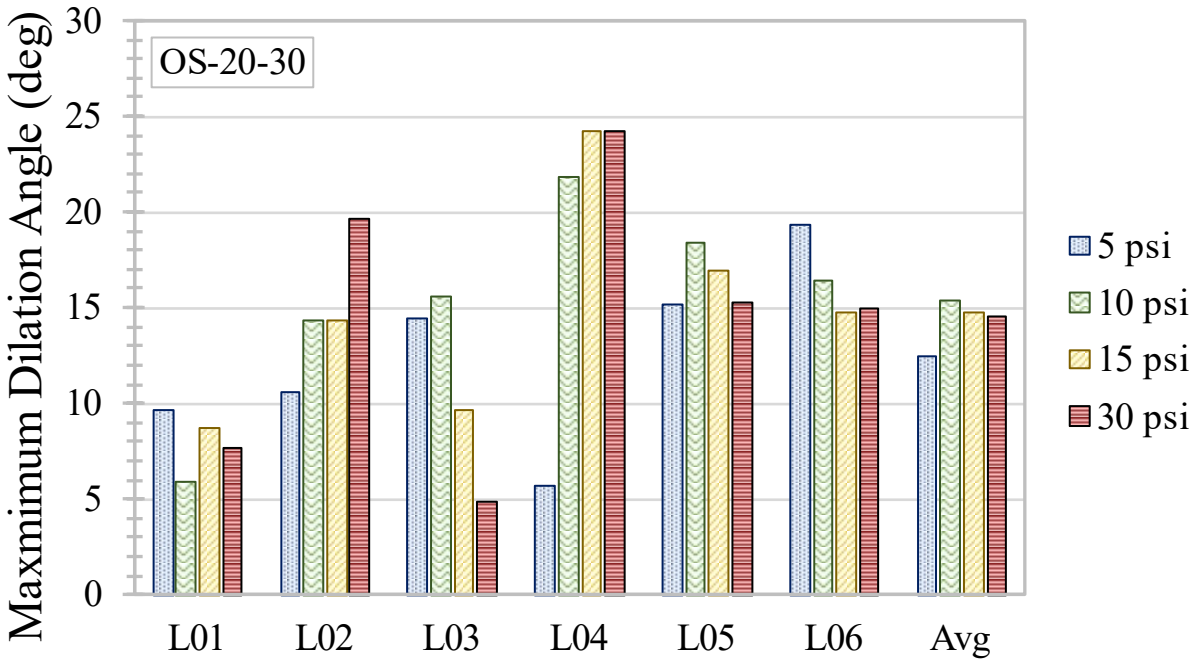

Source: FHWA.

Figure 15. Chart. Maximum dilation angle for OS-20-30.

No. 57 OGAs

The shear stress-horizontal strain curves and corresponding vertical-horizontal strain curves for the No. 57 OGAs are all presented in appendix D; No. 57-LI was selected as a representative sample (figure 16 and figure 17, respectively) to illustrate the main findings in this section. Recall that the vertical strain results presented represent an average of all LVDT measurements.

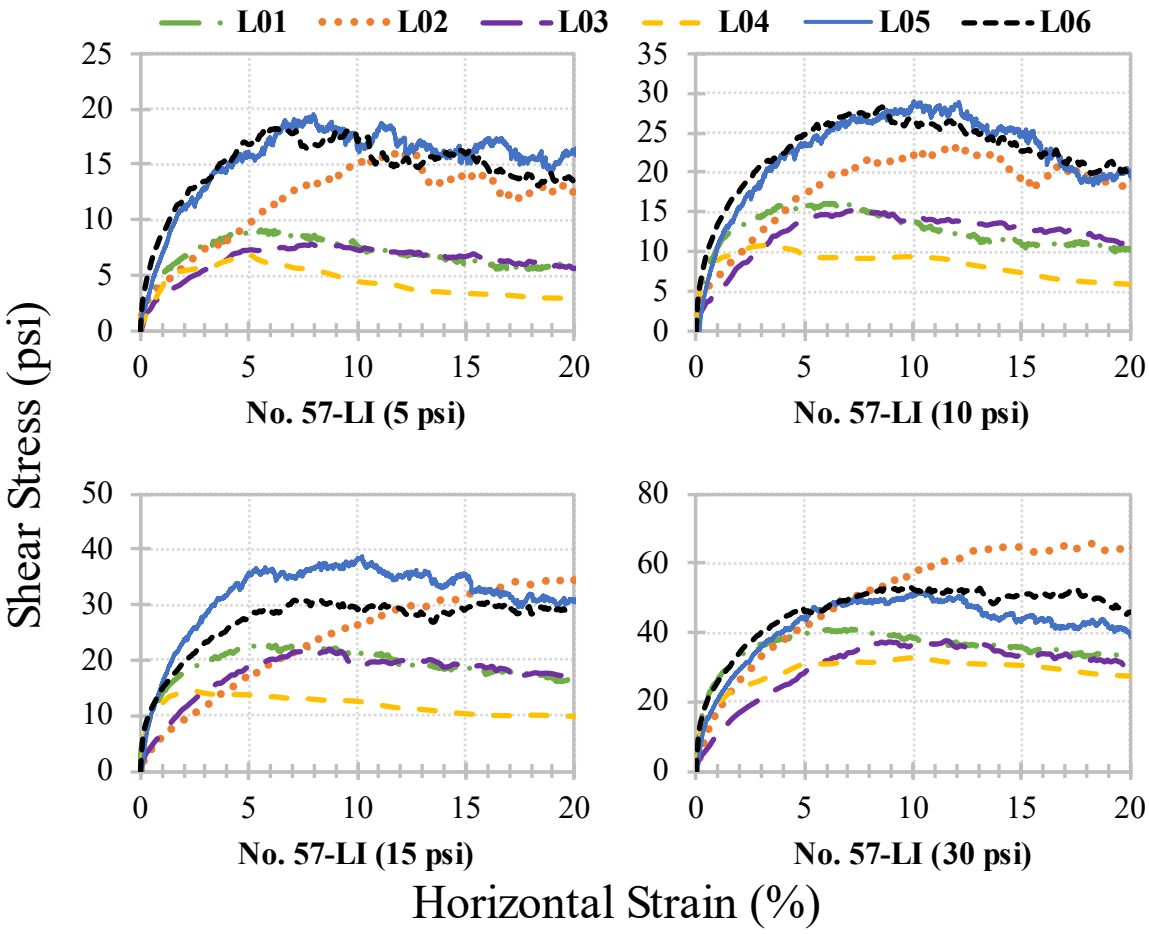

Source: FHWA.

Figure 16. Charts. Shear stress versus horizontal strain for No. 57-LI.

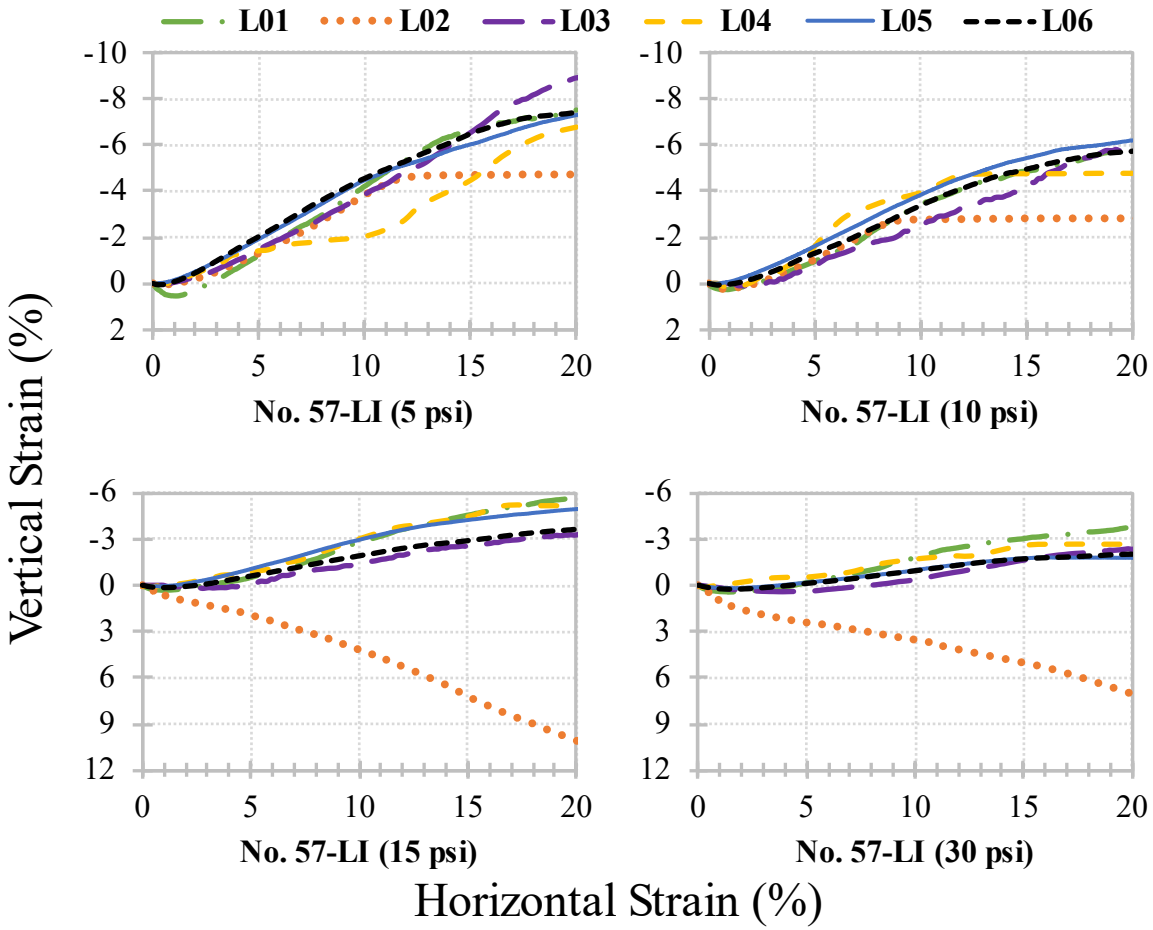

Source: FHWA.

Figure 17. Charts. Vertical strain versus horizontal strain for No. 57-LI.

Peak Shear Stress

The classical sharp peak in shear stress followed by strain softening that was observed in some OS-20-30 results (figure 11) is not well pronounced for the No. 57 samples (e.g., figure 16). COVs for τ_{peak} were also higher for No. 57 OGAs compared to OS-20-30, ranging from about 30 to 80 percent (table 23); increasing σ_n continued to correlate with lower COVs.

In addition, the location of τ_{peak} occurred at much larger horizontal strain ($\varepsilon_{h,peak}$) than with the OS-20-30. On average, $\varepsilon_{h,peak}$ ranged from 6.3 to 11.1 percent, with increasing $\varepsilon_{h,peak}$ as σ_n increased (table 23); interlaboratory COVs ranged from 33.3 to 78.5 percent (table 23).

Table 23. Peak shear stress parameters for No. 57 OGAs.

Parameter	Sample ID	L01	L02	L03	L04	L05	L06	$\bar{x}$	s	COV (%)
$\tau_{peak,5psi}$ (psi)	No. 57-BA	7.3	7.0	10.0	7.0	34.0	15.3	13.4	10.6	79.1
	No. 57-DI	9.7	16.1	7.4	5.8	19.9	13.7	12.1	5.4	44.6
	No. 57-GG	6.9	12.3	7.4	5.5	15.8	18.6	11.1	5.3	47.7
	No. 57-LI	9.3	16.1	7.8	6.9	19.6	18.2	13.0	5.6	43.1
	No. 57-SI	7.8	16.3	7.5	5.9	22.3	20.0	13.3	7.1	53.4
$\tau_{peak,10psi}$ (psi)	No. 57-BA	14.5	16.1	15.3	12.3	44.5	30.2	22.2	12.7	57.2
	No. 57-DI	16.9	24.3	15.5	11.5	37.6	28.4	22.4	9.7	43.3
	No. 57-GG	13.7	23.9	14.9	10.3	24.5	21.9	18.2	6.0	33.0
	No. 57-LI	16.1	23.4	15.3	10.8	29.0	28.3	20.5	7.5	36.6
	No. 57-SI	13.5	19.4	14.3	10.7	34.0	27.5	19.9	9.1	45.7
$\tau_{peak,15psi}$ (psi)	No. 57-BA	22.3	26.4	21.5	18.8	55.0	42.2	31.0	14.4	46.5
	No. 57-DI	23.0	35.8	21.6	16.7	38.9	33.5	28.3	9.0	31.8
	No. 57-GG	20.6	29.6	21.3	14.4	30.7	34.1	25.1	7.5	29.9
	No. 57-LI	22.9	34.9	22.0	14.4	38.8	30.8	27.3	9.1	33.3
	No. 57-SI	18.7	37.7	20.6	15.8	46.8	29.4	28.2	12.2	43.3
$\tau_{peak,30psi}$ (psi)	No. 57-BA	39.1	54.1	40.7	35.7	77.7	66.2	52.3	16.9	39.1
	No. 57-DI	41.9	61.8	38.6	30.7	60.7	64.6	49.7	14.4	41.9
	No. 57-GG	35.0	55.2	37.2	30.5	50.8	52.6	43.6	10.5	35.0
	No. 57-LI	41.0	65.6	37.5	32.6	51.7	53.1	46.9	12.2	41.0
	No. 57-SI	35.9	55.6	37.4	32.7	71.9	50.3	47.3	15.0	35.9
$\varepsilon_{h,peak,5psi}$ (%)	No. 57-BA	3.6	14.8	7.4	6.3	7.0	7.2	7.7	3.7	48.1
	No. 57-DI	3.3	12.5	5.8	2.1	7.2	7.1	6.3	3.7	58.7
	No. 57-GG	3.3	13.9	8.1	4.6	6.1	4.0	6.7	3.9	58.2
	No. 57-LI	5.2	11.7	7.9	5.0	8.0	6.2	7.3	2.5	34.2
	No. 57-SI	4.3	19.0	6.0	3.3	6.6	7.0	7.7	5.7	74.0
$\varepsilon_{h,peak,10psi}$ (%)	No. 57-BA	4.6	12.8	7.6	2.5	6.6	6.5	6.8	3.5	51.5
	No. 57-DI	4.7	9.7	9.9	2.9	8.2	6.8	7.0	2.8	40.0
	No. 57-GG	5.1	16.7	7.8	3.3	6.4	5.6	7.5	4.8	64.0
	No. 57-LI	5.9	12.1	7.3	3.3	10.1	8.6	7.9	3.1	39.2
	No. 57-SI	4.3	19.9	4.1	2.9	13.4	12.8	9.6	6.8	70.8
$\varepsilon_{h,peak,15psi}$ (%)	No. 57-BA	4.7	20.0	8.7	2.5	11.0	7.7	9.1	6.1	67.0
	No. 57-DI	6.3	19.9	8.3	2.5	9.3	7.3	8.9	5.9	66.3
	No. 57-GG	6.3	18.4	7.4	2.9	9.4	6.9	8.6	5.3	61.6
	No. 57-LI	7.3	19.8	8.7	2.5	10.2	7.1	9.3	5.8	62.4
	No. 57-SI	4.4	19.8	4.7	2.5	7.1	8.8	7.9	6.2	78.5
$\varepsilon_{h,peak,30psi}$ (%)	No. 57-BA	7.3	19.3	10.4	3.3	8.3	8.8	9.6	5.3	55.2
	No. 57-DI	8.2	13.2	7.9	3.8	10.9	6.8	8.5	3.3	38.8
	No. 57-GG	5.8	15.2	9.1	5.0	9.8	10.5	9.2	3.7	40.2
	No. 57-LI	7.6	18.2	11.5	10.0	10.3	8.8	11.1	3.7	33.3
	No. 57-SI	5.2	17.5	8.8	5.4	12.7	14.1	10.6	5.0	47.2

Each τ_{peak} and corresponding $\varepsilon_{h,peak}$ for the No. 57 OGAs are plotted in figure 18. Of further note is L02's distinct plateau in vertical strain for 5 and 10 psi, along with anomalous sample compression for 15 and 30 psi during the No. 57-LI tests, as seen in figure 17. Anomalous or potentially erroneous data such as these present an additional, and difficult to quantify, source of variability.

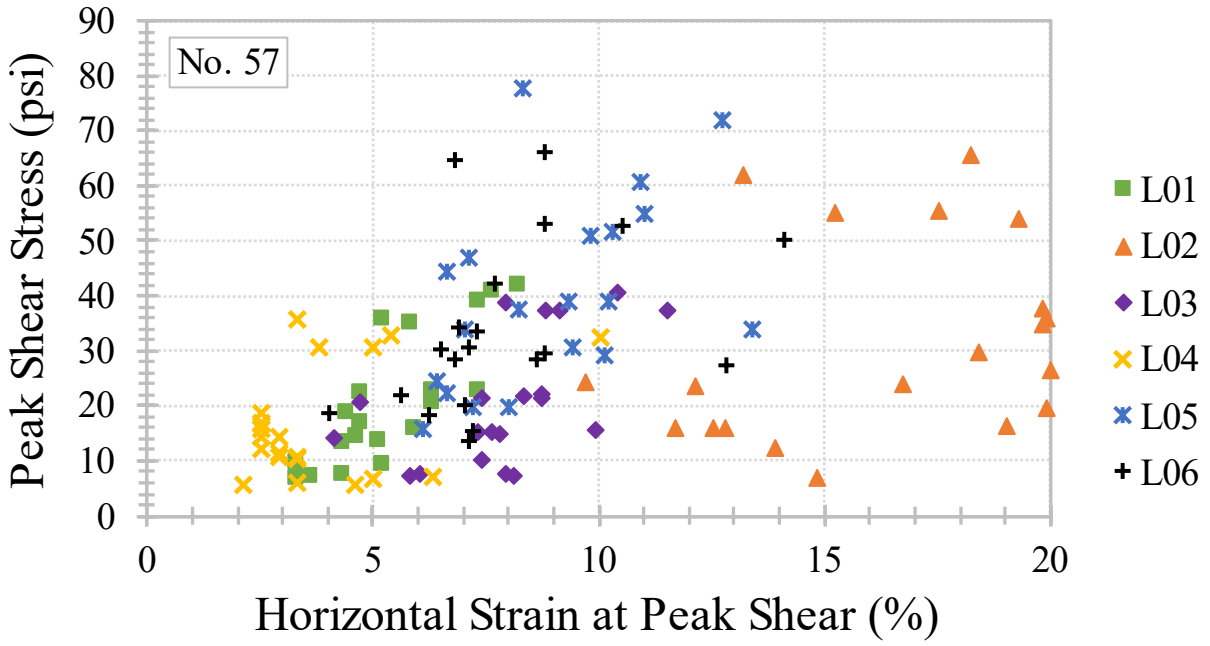

Source: FHWA.

Figure 18. Chart. Peak shear stress versus $\varepsilon_{h,peak}$ for No. 57 OGAs.

Secant Friction Angle

All laboratories, save L04, continued to show the expected trend of ϕ_s decreasing as σ_n increased for No. 57-LI (figure 19).

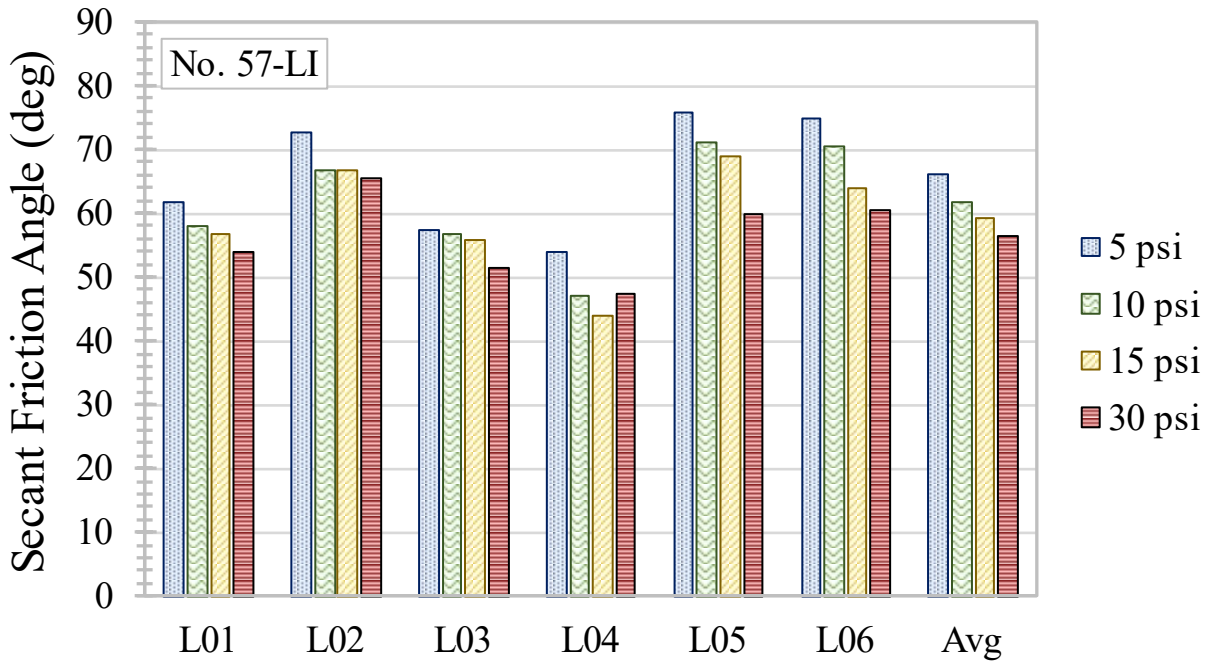

Source: FHWA.

Figure 19. Chart. Secant friction angles for No. 57-LI.

Across all No. 57 OGAs tested, average secant friction angles (ϕ_s) ranged from 54.5 to 66.0 degrees, with COVs ranging from 11.9 to 18.3 percent (table 24), dramatically lower than the variability of τ_{peak} (table 23).

Table 24. Shear strength parameters for No. 57 OGAs.

Parameter	Sample ID	L01	L02	L03	L04	L05	L06	$\bar{x}$	s	COV (percent)
$\phi_{s,5psi}$ (degree)	No. 57-BA	55.7	54.3	63.4	54.4	81.6	71.9	63.6	11.2	17.6
	No. 57-DI	62.7	72.7	55.8	49.4	75.9	69.9	64.4	10.3	16.0
	No. 57-GG	54.2	67.9	56.1	47.8	72.4	74.9	62.2	11.0	17.7
	No. 57-LI	61.6	72.8	57.4	54.0	75.7	74.7	66.0	9.5	14.4
	No. 57-SI	57.3	72.9	56.4	49.5	77.4	76.0	64.9	11.9	18.3
$\phi_{s,10psi}$ (degree)	No. 57-BA	55.5	58.1	56.9	50.8	77.3	71.7	61.7	10.4	16.9
	No. 57-DI	59.5	67.7	57.2	49.1	75.1	70.6	63.2	9.6	15.2
	No. 57-GG	53.8	67.3	56.2	45.7	67.8	65.5	59.4	8.9	15.0
	No. 57-LI	58.1	66.8	56.8	47.1	71.0	70.5	61.7	9.4	15.2
	No. 57-SI	53.4	62.8	55.0	46.9	73.6	70.0	60.3	10.3	17.1
$\phi_{s,15psi}$ (degree)	No. 57-BA	56.0	60.4	55.1	51.3	74.7	70.4	61.3	9.3	15.2
	No. 57-DI	56.9	67.3	55.3	48.1	68.9	65.9	60.4	8.2	13.6
	No. 57-GG	53.9	63.1	54.9	43.8	63.9	66.2	57.6	8.4	14.6
	No. 57-LI	56.8	66.7	55.7	43.8	68.8	64.0	59.3	9.2	15.5
	No. 57-SI	51.3	68.3	53.9	46.6	72.2	63.0	59.2	10.2	17.2
$\phi_{s,30psi}$ (degree)	No. 57-BA	52.5	61.0	53.6	50.0	68.9	65.6	58.6	7.7	13.1
	No. 57-DI	54.4	64.1	52.1	45.6	63.7	65.1	57.5	8.0	13.9
	No. 57-GG	49.4	61.5	51.1	45.4	59.5	60.3	54.5	6.8	12.5
	No. 57-LI	53.8	65.4	51.4	47.4	59.9	60.5	56.4	6.7	11.9
	No. 57-SI	50.1	61.7	51.3	47.5	67.4	59.2	56.2	7.8	13.9
c_a (psi)	No. 57-BA	1.9	-2.5	3.3	1.1	26.9	8.9	6.6	10.6	160.6
	No. 57-DI	3.8	6.9	2.4	1.5	16.8	5.4	6.1	5.6	91.8
	No. 57-GG	2.4	5.2	2.7	0.1	9.8	10.6	5.1	4.3	84.3
	No. 57-LI	3.4	4.8	3.1	0.4	16.1	12.3	6.7	6.1	91.0
	No. 57-SI	2.1	7.6	2.2	0.1	14.4	14.0	6.7	6.3	94.0
ϕ_t (degree)	No. 57-BA	51.5	62.1	51.2	49.2	59.9	63.1	56.2	6.2	11.0
	No. 57-DI	51.9	61.5	50.7	44.5	56.3	63.1	54.7	7.0	12.8
	No. 57-GG	47.9	59.1	49.5	45.0	54.0	54.7	51.7	5.2	10.1
	No. 57-LI	51.6	63.6	49.4	46.4	51.2	53.5	52.6	5.9	11.2
	No. 57-SI	48.4	58.6	49.8	47.2	63.0	50.0	52.8	6.4	12.1
ϕ_r (degree)	No. 57-BA	38.5	59.9	47.2	32.3	61.7	59.2	49.8	12.4	24.9
	No. 57-DI	41.3	64.5	46.2	30.4	56.5	55.7	49.1	12.3	25.1
	No. 57-GG	38.4	59.5	46.0	34.7	49.0	58.2	47.6	10.1	21.2
	No. 57-LI	47.9	65.2	46.6	39.8	56.9	59.0	52.6	9.4	17.9
	No. 57-SI	37.0	62.5	47.2	33.9	64.8	59.3	50.8	13.4	26.4
ϕ_{cv} (degree)	No. 57-BA	49.3	61.3	61.6	37.7	57.0	56.8	54.0	9.1	16.9
	No. 57-DI	38.2	—	65.8	44.2	54.8	55.0	51.6	10.7	20.7
	No. 57-GG	41.3	52.1	50.4	43.1	48.5	52.3	48.0	4.7	9.8
	No. 57-LI	20.7	65.9	46.8	47.0	47.0	51.7	46.5	14.6	31.4
	No. 57-SI	38.8	65.7	50.9	42.0	54.1	50.7	50.4	9.5	18.8

—Not measured/evaluated.

Tangent Friction Angle

Tangent friction angles (ϕ_t) and c_a values, presented in table 24, were derived from the linear Mohr-Coulomb failure envelopes (e.g., figure 20). Interlaboratory variability in ϕ_t was low for the No. 57 OGAs; COVs were between 10.1 and 12.8 percent (table 24). Although the COVs are similar to those found for OS-20-30, the magnitude of ϕ_t were 15° to 20° higher than the mean ϕ_t for OS-20-30 (table 20), ranging from 51.7 to 56.2 degrees, on average (table 24).

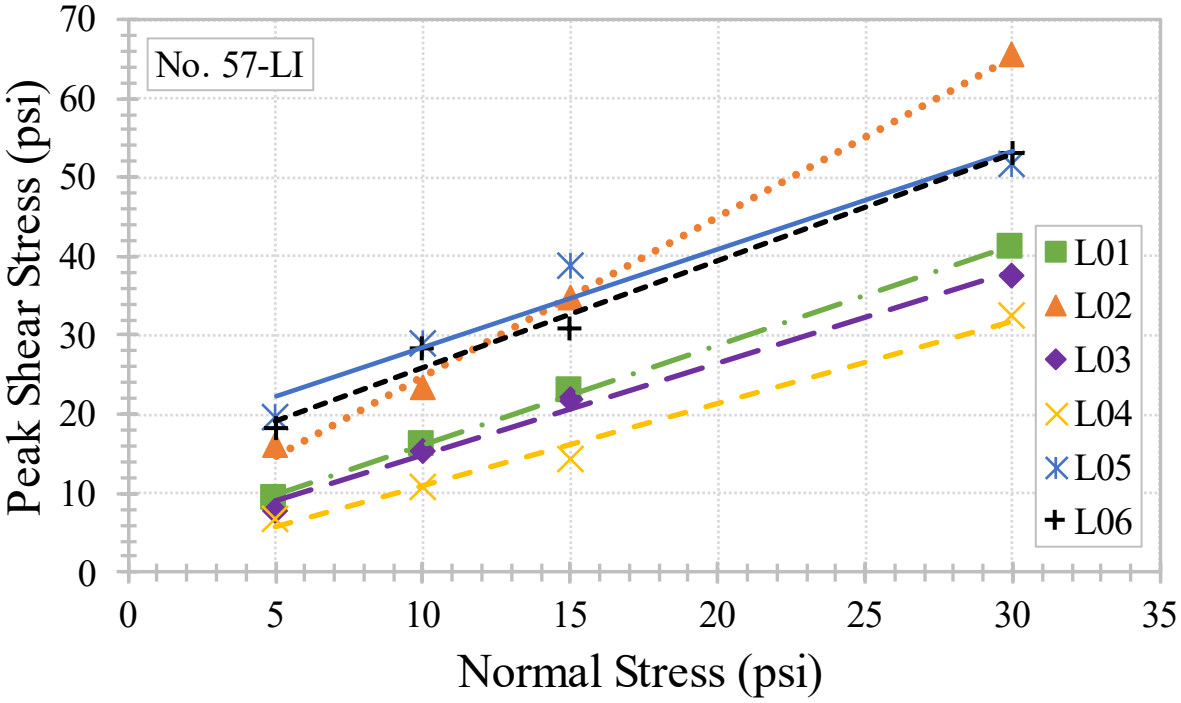

Source: FHWA.

Figure 20. Chart. Linear Mohr-Coulomb failure envelopes for No. 57-LI.

Residual Friction Angle

Average residual, tangent friction angles ($\phi_{t,r}$) ranged from 47.6 to 52.6 degrees; COVs ranged from 17.9 to 26.4 percent (table 24).

Constant Volume Friction Angle

Constant volume friction angles (ϕ_{cv}) ranged, on average, from 46.5 to 54.0 degrees (table 24). Variability in ϕ_{cv} for the No. 57 OGAs was generally greater than the other τ parameters, with COVs up to 31.4 percent (table 24). However, this range in variability is still markedly lower than the COV of 53.3 percent found for ϕ_{cv} in the OS-20-30 tests (table 20). Of note is that vertical displacement measurements were not measured by L02 in round one (i.e., DI); accordingly, ϕ_{cv} and ψ_{max} values from L02 for DI OGAs are not available for consideration.

Maximum Dilation Angle

Using the *n*-point centered moving average approach (table 21), ψ_{max} was computed for the No. 57 OGAs (table 25).

Table 25. Maximum dilation angles for No. 57 OGAs.

Parameter	Sample ID	L01	L02	L03	L04	L05	L06	$\bar{x}$	*s*	COV (percent)
$\psi_{max,5psi}$ (degree)	No. 57-BA	18.9	25.6	28.5	32.6	25.9	25.1	26.1	4.5	17.2
	No. 57-DI	26.7	—	19.4	35.8	24.4	21.2	25.5	6.4	25.1
	No. 57-GG	18.4	19.6	23.7	43.5	18.7	23.2	24.5	9.6	39.2
	No. 57-LI	20.5	18.0	21.1	20.7	19.4	20.0	20.0	1.1	5.5
	No. 57-SI	16.1	13.0	28.3	33.0	20.3	21.3	22.0	7.5	34.1
$\psi_{max,10psi}$ (degree)	No. 57-BA	23.3	3.5	28.5	28.8	25.0	20.8	21.7	9.4	43.3
	No. 57-DI	24.6	—	22.4	25.6	20.7	19.8	22.6	2.5	11.1
	No. 57-GG	16.4	18.4	36.2	24.7	15.9	17.2	21.5	7.9	36.7
	No. 57-LI	19.7	15.3	24.5	30.1	17.2	17.1	20.7	5.6	27.1
	No. 57-SI	15.2	15.2	28.3	29.2	16.4	13.4	19.6	7.1	36.2
$\psi_{max,15psi}$ (degree)	No. 57-BA	17.8	9.7	38.3	31.0	17.0	20.2	22.3	10.4	46.6
	No. 57-DI	23.2	—	23.8	19.3	15.5	16.5	19.7	3.8	19.3
	No. 57-GG	18.4	13.8	18.0	19.8	15.1	15.0	16.7	2.4	14.4
	No. 57-LI	19.3	0.0	22.6	17.7	15.1	10.8	14.3	8.0	55.9
	No. 57-SI	12.3	12.5	39.2	24.7	16.7	11.1	19.4	10.9	56.2
$\psi_{max,30psi}$ (degree)	No. 57-BA	15.1	8.4	26.1	24.7	15.6	15.0	17.5	6.7	38.3
	No. 57-DI	17.7	—	24.0	20.8	10.2	13.2	17.2	5.6	32.6
	No. 57-GG	11.8	11.4	12.7	13.5	8.4	7.8	10.9	2.3	21.1
	No. 57-LI	16.8	0.0	11.3	11.3	8.8	7.8	9.3	5.5	59.1
	No. 57-SI	10.1	11.0	20.7	22.8	11.6	7.4	13.9	6.3	45.3

—Not measured/evaluated.

Except for the results from L03 and L04, the expected downward trend of ψ_{max} with increasing σ_n was found (figure 21).

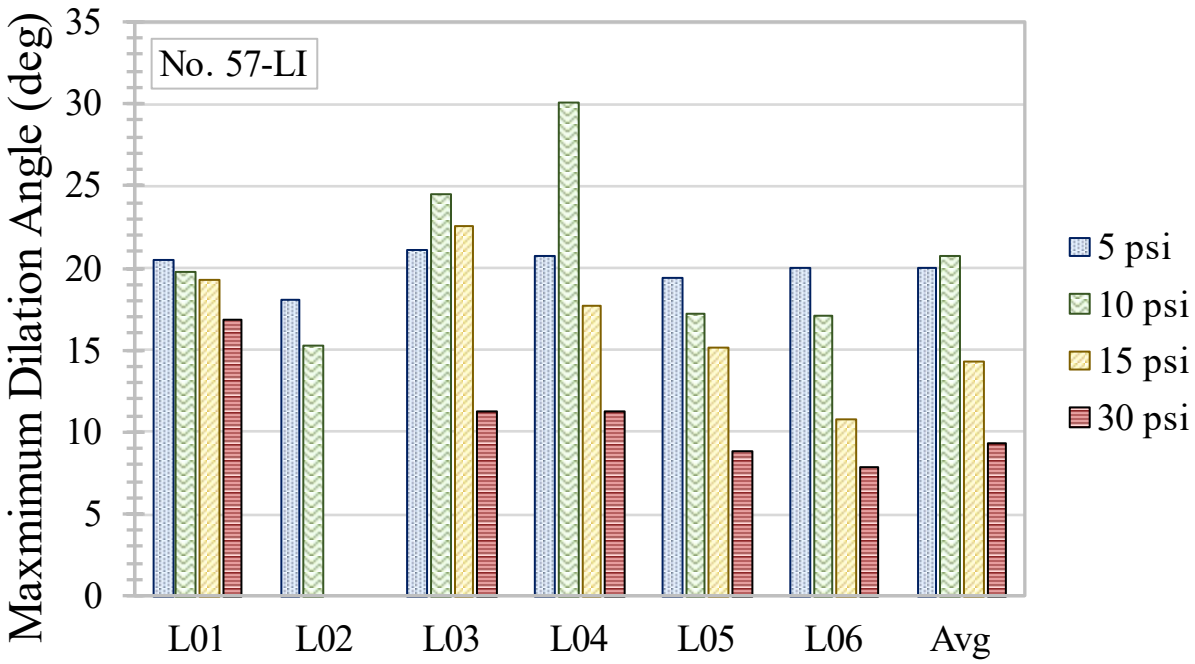

Source: FHWA.

Figure 21. Chart. Maximum dilation angle for No. 57-LI.

On average, ψ_{max} ranged from 9.3 to 26.1 degrees. COVs for ψ_{max} trended upward as σ_n increased, with the lowest COV of 5.5 percent at 5 psi and the highest of 59.1 percent at 30 psi (table 25).

No. 68 OGAs

The shear stress-horizontal strain curves and corresponding vertical-horizontal strain curves for the No. 68 OGAs are all presented in appendix D; No. 68-LI was selected as a representative sample (figure 22 and figure 23, respectively) to illustrate the main findings in this section. Recall that the vertical strain results presented represent an average of all LVDT measurements.

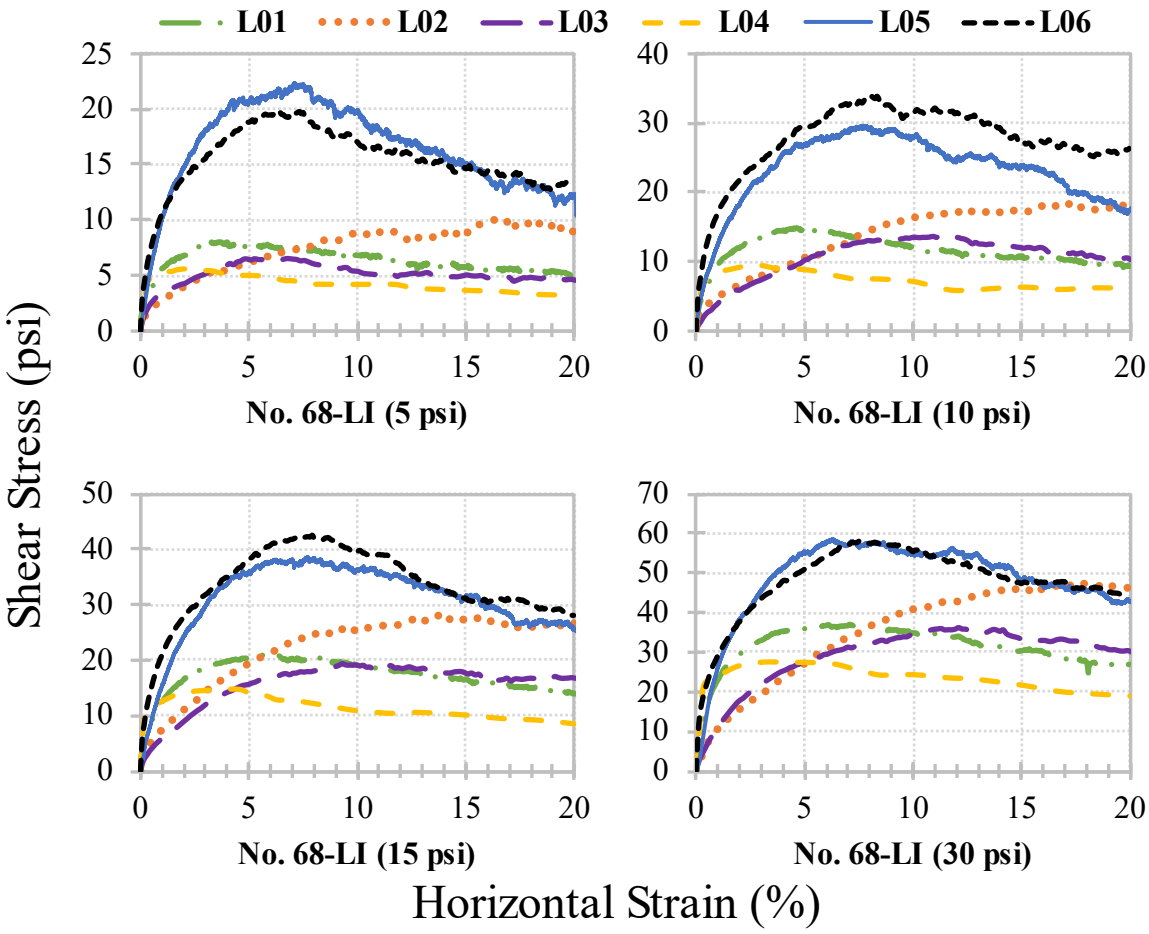

Source: FHWA.

Figure 22. Charts. Shear stress versus horizontal strain for No. 68-LI.

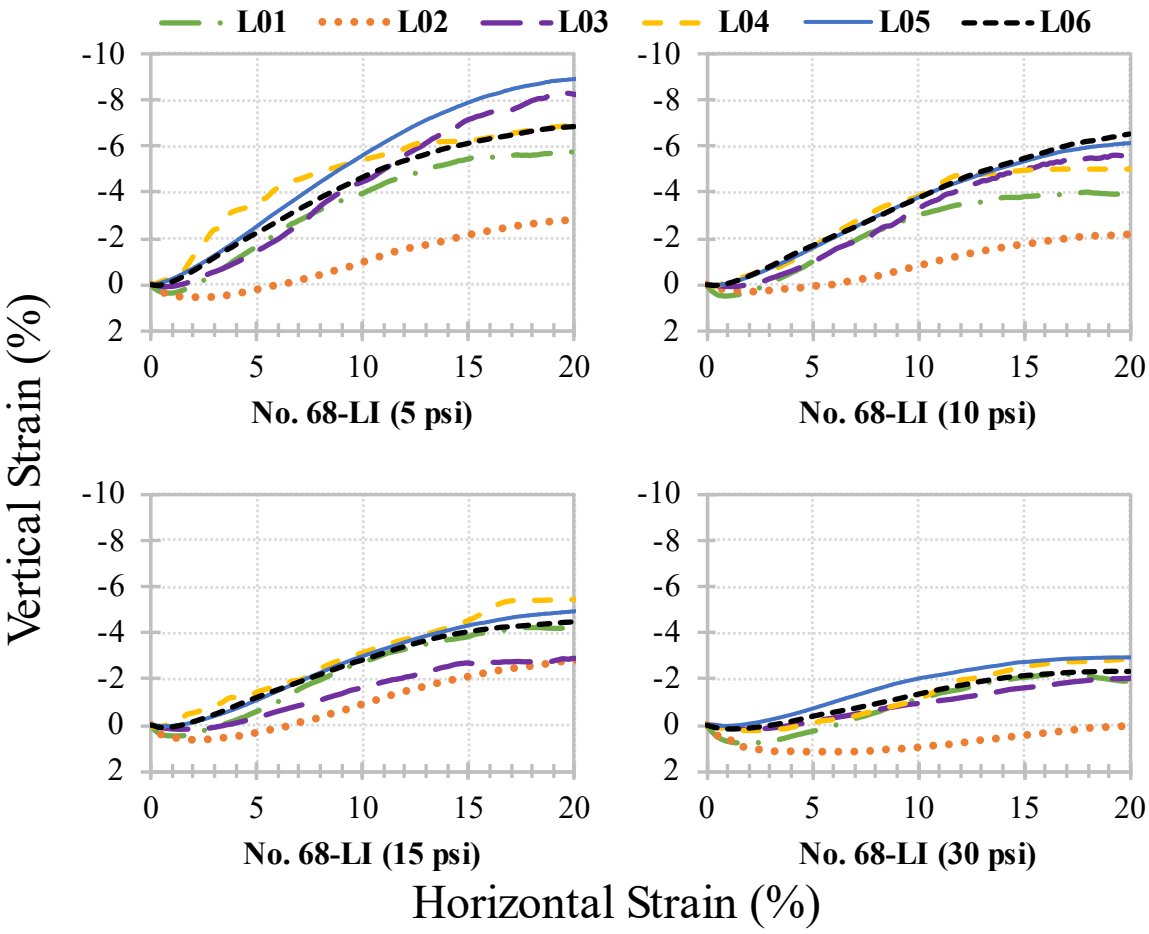

Source: FHWA.

Figure 23. Charts. Vertical strain versus horizontal strain for No. 68-LI.

Peak Shear Stress

Broadly, the stress-strain curves for No. 68 OGAs are smoother than those of the No. 57 OGAs (appendix D). Sharp shear peaks and post-peak strain softening are minimal, continuing to diverge from classical expectations for densely packed samples; each τ_{peak} and corresponding $\varepsilon_{h,peak}$ for all No. 68 samples are plotted in figure 24.

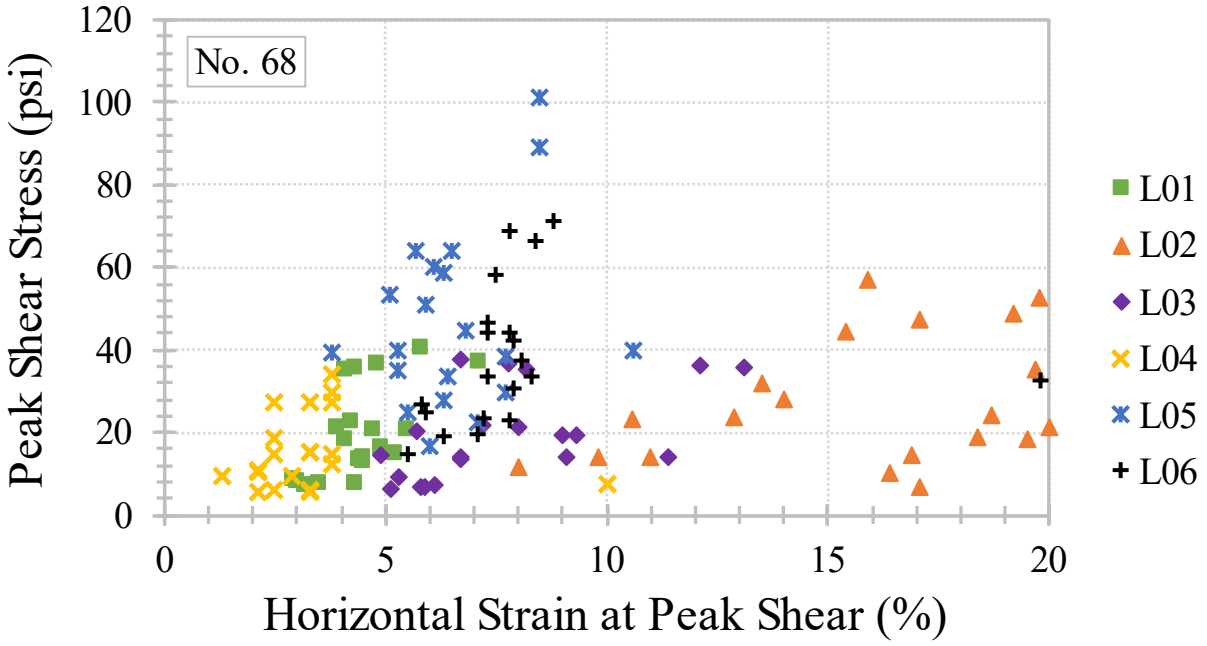

Source: FHWA.

Figure 24. Chart. Peak shear stress versus $\varepsilon_{h,peak}$ for No. 68 OGAs.

The No. 68 OGAs had a broad range of COVs for τ_{peak}, ranging from 27.9 to 84.6 percent (table 26). Similarly, COVs for $\varepsilon_{h,peak}$ ranged from 32.7 to 83.1 percent (table 26)—similar to that of the No. 57 OGAs—with average $\varepsilon_{h,peak}$ values ranging from 5.2 to 10 percent (table 26).

Table 26. Peak shear stress parameters for No. 68 OGAs.

Parameter	Sample ID	L01	L02	L03	L04	L05	L06	$\bar{x}$	s	COV (percent)
$\tau_{peak,5psi}$ (psi)	No. 68-BA	7.6	6.8	9.1	7.5	39.5	26.8	16.2	13.7	84.6
	No. 68-DI	8.5	13.8	6.7	6.1	24.7	22.9	13.8	8.2	59.4
	No. 68-GG	7.7	11.8	6.4	6.2	16.8	14.9	10.6	4.6	43.4
	No. 68-LI	8.0	10.1	6.6	5.6	22.3	19.8	12.1	7.2	59.5
	No. 68-SI	7.3	14.4	7.4	5.8	27.9	23.4	14.4	9.3	64.6
$\tau_{peak,10psi}$ (psi)	No. 68-BA	13.8	14.1	14.2	10.6	51.2	33.6	22.9	16.1	70.3
	No. 68-DI	16.6	23.4	14.1	10.9	33.8	30.6	21.6	9.3	43.1
	No. 68-GG	13.2	18.7	13.7	9.5	34.8	19.3	18.2	8.9	48.9
	No. 68-LI	14.9	18.4	13.8	9.5	29.6	33.8	20.0	9.6	48.0
	No. 68-SI	13.4	21.5	14.5	12.4	44.7	32.6	23.2	13.0	56.0
$\tau_{peak,15psi}$ (psi)	No. 68-BA	21.3	24.3	21.6	18.5	64.2	46.7	32.8	18.5	56.4
	No. 68-DI	22.8	32.0	21.3	14.6	39.8	44.2	29.1	11.5	39.5
	No. 68-GG	18.3	23.6	19.5	15.3	40.0	25.0	23.6	8.8	37.3
	No. 68-LI	21.0	28.1	19.3	14.8	38.6	42.5	27.4	11.1	40.5
	No. 68-SI	20.6	35.5	20.2	15.2	53.3	44.3	31.5	15.3	48.6
$\tau_{peak,30psi}$ (psi)	No. 68-BA	36.8	52.8	37.6	34.2	101.3	68.9	55.3	26.1	47.2
	No. 68-DI	40.6	48.8	36.0	27.4	63.9	66.4	47.2	15.6	33.1
	No. 68-GG	35.7	44.4	35.4	27.3	60.1	37.4	40.1	11.2	27.9
	No. 68-LI	37.0	47.4	36.2	27.5	58.6	58.0	44.1	12.7	28.8
	No. 68-SI	35.5	56.8	36.5	29.6	89.0	71.4	53.1	23.6	44.4
$\varepsilon_{h,peak,5psi}$ (percent)	No. 68-BA	4.3	17.1	5.3	10.0	3.8	5.8	7.7	5.1	66.2
	No. 68-DI	2.9	11.0	5.8	2.5	5.5	7.8	5.9	3.2	54.2
	No. 68-GG	3.5	8.0	5.1	3.3	6.0	5.5	5.2	1.7	32.7
	No. 68-LI	3.0	16.4	5.9	2.1	7.1	7.1	6.9	5.1	73.9
	No. 68-SI	3.2	16.9	6.1	3.3	6.3	7.2	7.2	5.0	69.4
$\varepsilon_{h,peak,10psi}$ (percent)	No. 68-BA	4.5	9.8	6.7	2.1	5.9	7.3	6.1	2.6	42.6
	No. 68-DI	4.9	10.6	9.1	2.1	6.4	7.9	6.8	3.1	45.6
	No. 68-GG	4.5	18.4	6.7	1.3	5.3	6.3	7.1	5.9	83.1
	No. 68-LI	5.2	19.5	11.4	2.9	7.7	8.3	9.2	5.8	63.0
	No. 68-SI	4.4	20.0	4.9	3.8	6.8	19.8	10.0	7.8	78.0
$\varepsilon_{h,peak,15psi}$ (percent)	No. 68-BA	3.9	18.7	7.2	2.5	5.7	7.3	7.6	5.8	76.3
	No. 68-DI	4.2	13.5	8.0	2.5	10.6	7.3	7.7	4.0	51.9
	No. 68-GG	4.1	12.9	9.0	3.3	5.3	5.9	6.8	3.6	52.9
	No. 68-LI	5.5	14.0	9.3	3.8	7.7	7.9	8.0	3.5	43.8
	No. 68-SI	4.7	19.7	5.7	3.3	5.1	7.8	7.7	6.1	79.2
$\varepsilon_{h,peak,30psi}$ (percent)	No. 68-BA	4.8	19.8	6.7	3.8	8.5	7.8	8.6	5.8	67.4
	No. 68-DI	5.8	19.2	13.1	2.5	6.5	8.4	9.3	6.0	64.5
	No. 68-GG	4.3	15.4	8.2	3.8	6.1	8.1	7.7	4.2	54.5
	No. 68-LI	7.1	17.1	12.1	3.3	6.3	7.5	8.9	4.9	55.1
	No. 68-SI	4.1	15.9	7.8	3.8	8.5	8.8	8.2	4.4	53.7

Secant Friction Angle

The expected inverse correlation between ϕ_s and σ_n was generally found for No. 68 OGAs tested; however, the trend was not consistent among the laboratories (figure 25).

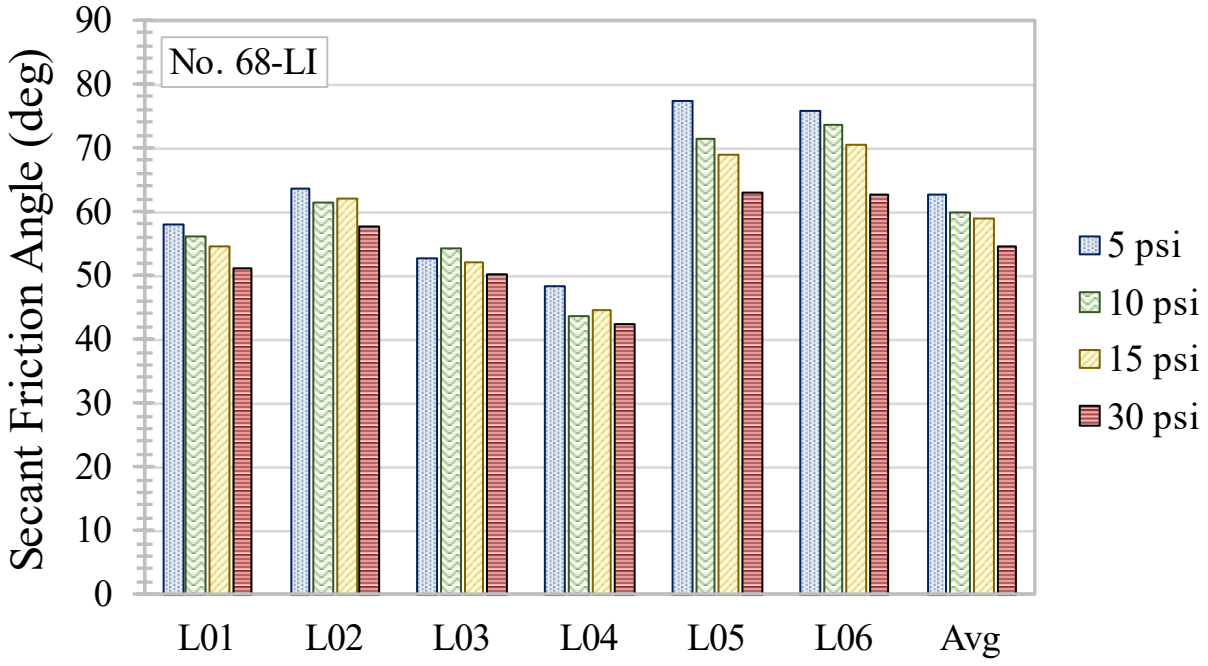

Source: FHWA.

Figure 25. Chart. Secant friction angles for No. 68-LI.

Average secant friction angles (ϕ_s) for the No. 68 OGAs ranged from 52.1 to 65.0 degrees, with COVs ranging from 13.6 to 21.0 percent (table 27); these COVs are slightly lower and slightly higher than those for the No. 57 OGAs, respectively (table 24).

Table 27. Shear strength parameters for No. 68 OGAs.

Parameter	Sample ID	L01	L02	L03	L04	L05	L06	$\bar{x}$	s	COV (percent)
$\phi_{s,5psi}$ (degree)	No. 68-BA	56.8	53.6	61.1	56.2	82.8	79.4	65.0	12.8	19.7
	No. 68-DI	59.6	70.0	53.1	50.6	78.6	77.7	64.9	12.2	18.8
	No. 68-GG	56.8	67.0	52.0	51.1	73.4	71.4	62.0	9.9	16.0
	No. 68-LI	58.0	63.6	52.8	48.2	77.4	75.8	62.6	12.0	19.2
	No. 68-SI	55.8	70.9	56.0	49.0	79.8	77.9	64.9	13.0	20.0
$\phi_{s,10psi}$ (degree)	No. 68-BA	54.0	54.6	54.8	46.6	78.9	73.4	60.4	12.7	21.0
	No. 68-DI	58.9	66.9	54.7	47.4	73.5	71.9	62.2	10.3	16.6
	No. 68-GG	53.0	61.8	53.8	43.6	74.0	62.6	58.1	10.4	17.9
	No. 68-LI	56.1	61.5	54.1	43.5	71.3	73.5	60.0	11.3	18.8
	No. 68-SI	53.2	65.1	55.5	51.2	77.4	72.9	62.6	11.0	17.6
$\phi_{s,15psi}$ (degree)	No. 68-BA	54.8	58.3	55.2	50.9	76.8	72.2	61.4	10.5	17.1
	No. 68-DI	56.7	64.9	54.8	44.2	69.3	71.2	60.2	10.2	16.9
	No. 68-GG	50.6	57.5	52.4	45.5	69.4	59.1	55.8	8.3	14.9
	No. 68-LI	54.5	61.9	52.2	44.5	68.8	70.6	58.8	10.2	17.3
	No. 68-SI	53.9	67.1	53.4	45.4	74.3	71.3	60.9	11.6	19.0
$\phi_{s,30psi}$ (degree)	No. 68-BA	50.8	60.4	51.4	48.7	73.5	66.5	58.6	10.0	17.1
	No. 68-DI	53.5	58.4	50.2	42.4	64.9	65.7	55.9	9.0	16.1
	No. 68-GG	50.0	56.0	49.7	42.3	63.5	51.3	52.1	7.1	13.6
	No. 68-LI	51.0	57.6	50.3	42.5	62.9	62.7	54.5	8.0	14.7
	No. 68-SI	49.8	62.2	50.6	44.6	71.4	67.2	57.6	10.8	18.8
c_a (psi)	No. 68-BA	2.4	-3.5	3.4	1.2	26.8	18.4	8.1	11.8	145.7
	No. 68-DI	3.2	9.1	2.2	2.1	17.3	14.7	8.1	6.7	82.7
	No. 68-GG	1.9	5.1	1.7	1.7	14.0	10.6	5.8	5.3	91.4
	No. 68-LI	3.1	3.8	1.5	1.1	15.5	17.0	7.0	7.2	102.9
	No. 68-SI	2.4	6.3	2.5	1.9	18.0	14.0	7.5	6.9	92.0
ϕ_t (degree)	No. 68-BA	49.3	61.8	48.9	47.7	68.1	59.6	55.9	8.5	15.2
	No. 68-DI	51.5	53.7	49.1	40.2	57.2	60.3	52.0	7.0	13.5
	No. 68-GG	48.3	52.5	48.7	40.6	57.9	42.1	48.4	6.4	13.2
	No. 68-LI	48.9	55.9	49.4	41.5	55.4	55.2	51.1	5.6	11.0
	No. 68-SI	48.3	59.7	48.9	42.8	67.2	62.6	54.9	9.6	17.5
ϕ_r (degree)	No. 68-BA	38.0	58.8	45.5	34.6	61.8	58.0	49.5	11.7	23.6
	No. 68-DI	43.0	58.9	45.7	28.1	53.7	59.6	48.2	11.9	24.7
	No. 68-GG	37.2	56.3	44.1	31.1	53.7	45.0	44.6	9.6	21.5
	No. 68-LI	42.3	58.1	45.9	31.8	56.7	59.0	49.0	10.9	22.2
	No. 68-SI	38.0	62.9	45.7	33.4	62.0	63.6	50.9	13.6	26.7
ϕ_{cv} (degree)	No. 68-BA	43.8	60.0	43.1	50.8	63.2	50.2	51.9	8.3	16.0
	No. 68-DI	44.2	—	48.8	38.9	51.1	51.8	47.0	5.4	11.5
	No. 68-GG	37.3	49.6	45.8	39.8	51.9	43.9	44.7	5.6	12.5
	No. 68-LI	42.4	45.9	50.2	38.7	50.8	54.1	47.0	5.8	12.3
	No. 68-SI	32.2	56.4	51.8	26.1	62.3	54.2	47.2	14.5	30.7

—Not measured/evaluated.

Tangent Friction Angle

Interlaboratory variability for ϕ_t results remained relatively low for the No. 68 OGAs, with ϕ_t ranging, on average, from 48.4 to 55.9 degrees (table 27); COVs ranged from 11.0 to 17.5 percent (table 27). Apparent cohesion (c_a) was still present in the linear Mohr-Coulomb failure envelopes (e.g., figure 26), with COVs up to 145.7 percent (table 27).

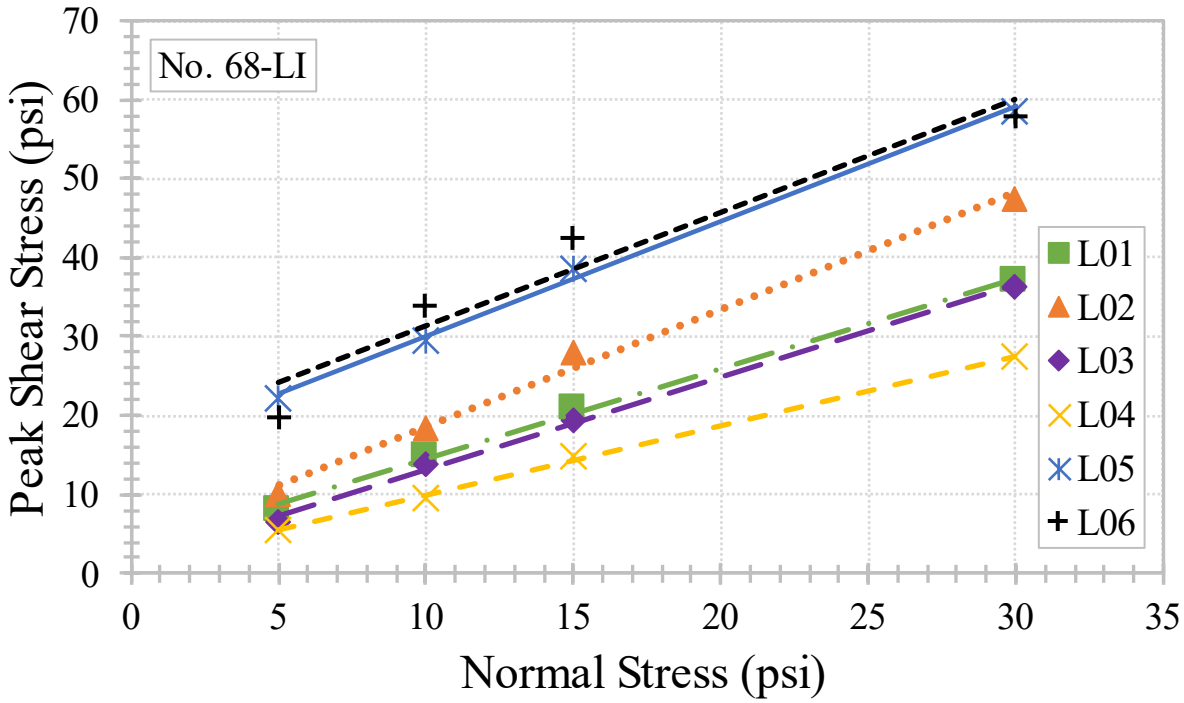

Source: FHWA.

Figure 26. Chart. Linear Mohr-Coulomb failure envelopes for No. 68-LI.

Residual Friction Angle

Compared to ϕ_t, $\phi_{t,r}$ had higher variability; COVs ranged from 21.5 to 26.7 percent (table 27). Average residual, tangent friction angles ($\phi_{t,r}$) ranged from 44.6 to 50.9 degrees—again, less than the No. 57 OGAs.

Constant Volume Friction Angle

Constant volume friction angles (ϕ_{cv}) ranged, on average, from 44.7 to 51.9 degrees (table 27). Variability in ϕ_{cv} for the No. 68 OGAs was in line with that of the No. 57 OGAs; the minimum COV was 11.5 percent, while the maximum was 30.7 percent (table 27).

Maximum Dilation Angle

Using the *n*-point centered moving average approach (table 21), ψ_{max} was computed for the No. 68 OGAs (table 28).

Table 28. Maximum dilation angles for No. 68 OGAs.

Parameter	Sample ID	L01	L02	L03	L04	L05	L06	$\bar{x}$	s	COV (percent)
$\psi_{max,5psi}$ (degree)	No. 68-BA	17.6	22.8	23.0	30.1	31.0	26.1	25.1	5.0	19.9
	No. 68-DI	24.3	—	22.1	26.6	22.4	24.3	23.9	1.8	7.5
	No. 68-GG	18.6	21.6	19.9	33.0	22.1	20.4	22.6	5.2	23.0
	No. 68-LI	19.8	10.7	25.5	35.0	23.3	20.8	22.5	7.9	35.1
	No. 68-SI	16.8	12.5	30.8	31.8	28.3	24.6	24.1	7.9	32.8
$\psi_{max,10psi}$ (degree)	No. 68-BA	15.1	9.5	23.6	33.0	26.5	23.6	21.9	8.4	38.4
	No. 68-DI	25.3	—	20.0	30.1	18.2	19.4	22.6	5.0	22.1
	No. 68-GG	16.1	14.1	23.1	23.7	21.2	14.5	18.8	4.4	23.4
	No. 68-LI	16.3	10.0	23.2	21.8	16.9	18.2	17.7	4.7	26.6
	No. 68-SI	16.0	13.0	33.9	33.4	23.4	18.2	23.0	8.9	38.7
$\psi_{max,15psi}$ (degree)	No. 68-BA	16.6	5.3	16.6	20.8	22.0	19.9	16.9	6.1	36.1
	No. 68-DI	21.9	—	32.3	15.6	15.0	17.9	20.5	7.1	34.6
	No. 68-GG	12.5	9.3	17.3	12.7	16.8	12.0	13.4	3.1	23.1
	No. 68-LI	18.5	11.8	10.4	26.6	15.3	14.8	16.2	5.8	35.8
	No. 68-SI	14.6	11.0	45.6	26.6	19.2	17.7	22.5	12.5	55.6
$\psi_{max,30psi}$ (degree)	No. 68-BA	9.8	4.2	15.4	22.8	16.4	15.1	14.0	6.3	45.0
	No. 68-DI	15.4	—	11.7	11.3	11.2	13.1	12.5	1.8	14.4
	No. 68-GG	12.5	8.6	19.6	10.2	11.8	5.1	11.3	4.8	42.5
	No. 68-LI	11.8	8.5	5.6	12.7	10.9	8.4	9.7	2.6	26.8
	No. 68-SI	13.2	11.7	26.6	24.7	14.5	13.7	17.4	6.5	37.4

—Not measured/evaluated.

The downward trend in ψ_{max} associated with increasing σ_n was more pronounced, and sporadic, among the No. 68 results (figure 27).

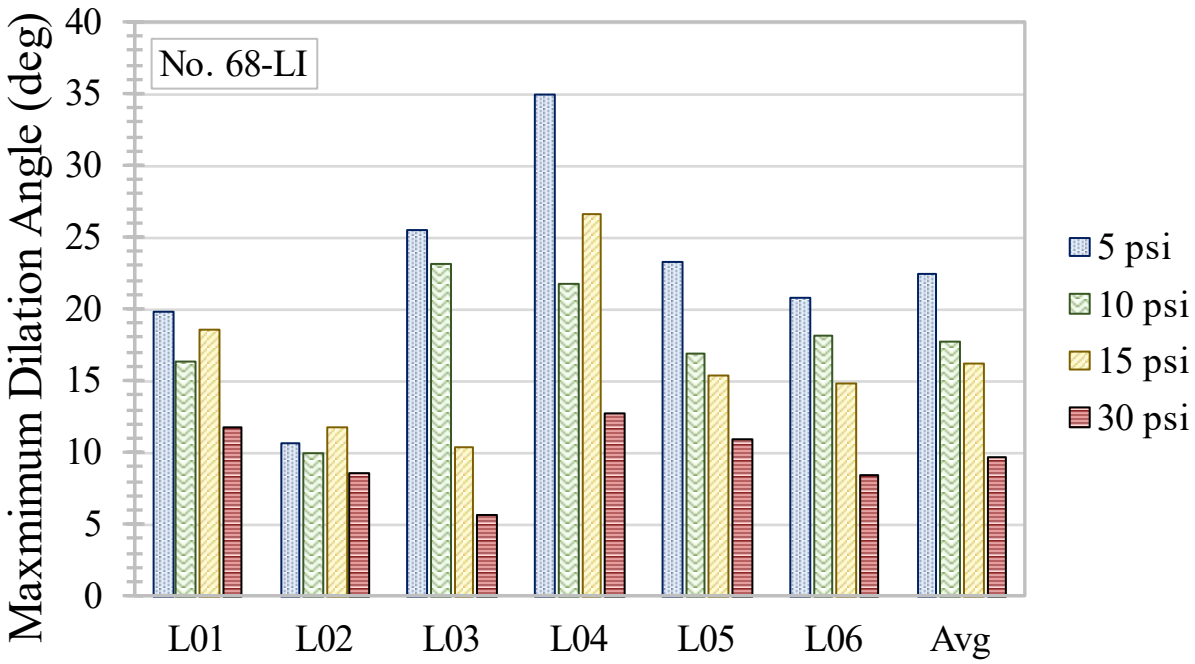

Source: FHWA.

Figure 27. Chart. Maximum dilation angle for No. 68-LI.

On average, ψ_{max} ranged from 9.7 to 25.1 degrees (table 28); COVs for ψ_{max} ranged from 7.5 to 55.6 percent.

No. 8 OGAs

The shear stress-horizontal strain curves and corresponding vertical-horizontal strain curves for the No. 8 OGAs are all presented in appendix D; No. 8-LI was selected as a representative sample (figure 28 and figure 29, respectively) to illustrate the main findings in this section. Recall that the vertical strain results presented represent an average of all LVDT measurements.

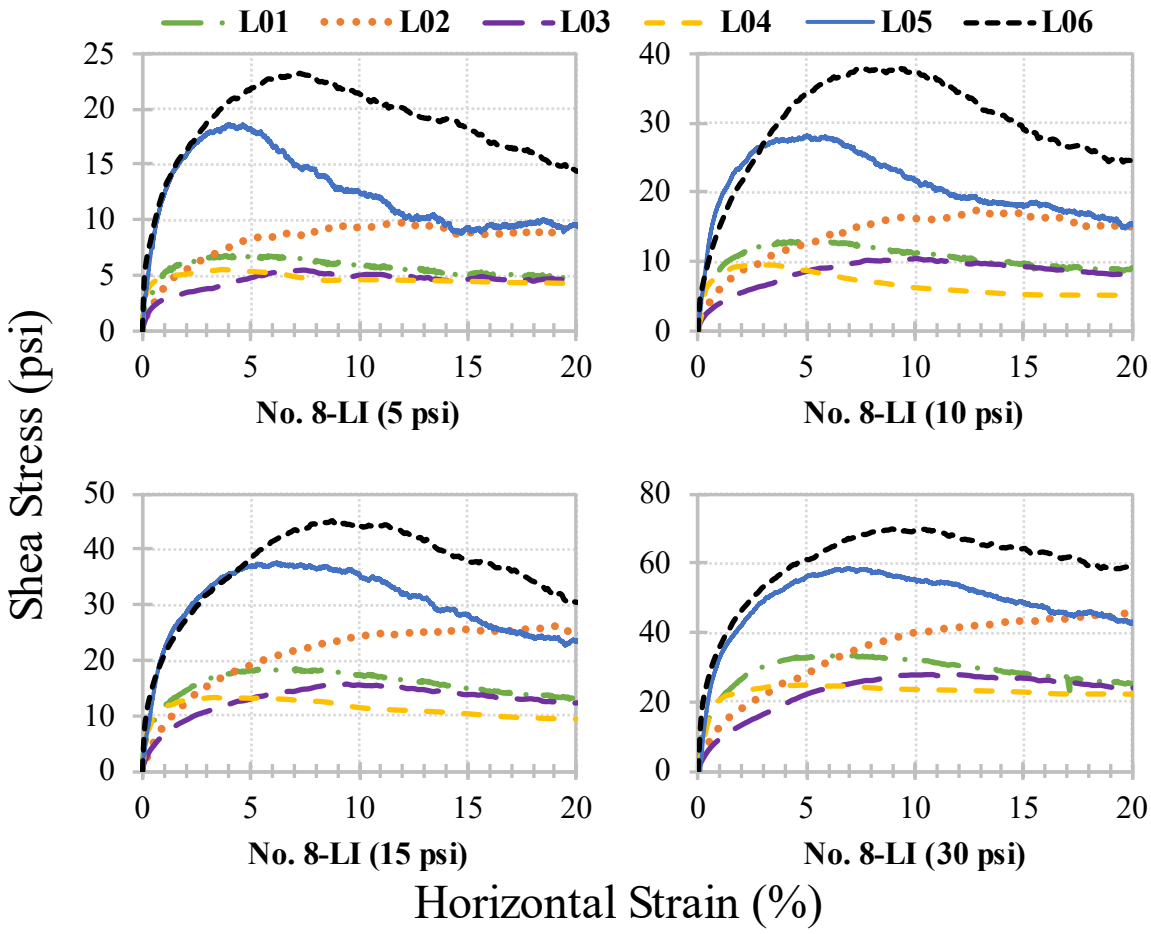

Source: FHWA.

Figure 28. Charts. Shear stress versus horizontal strain for No. 8-LI.

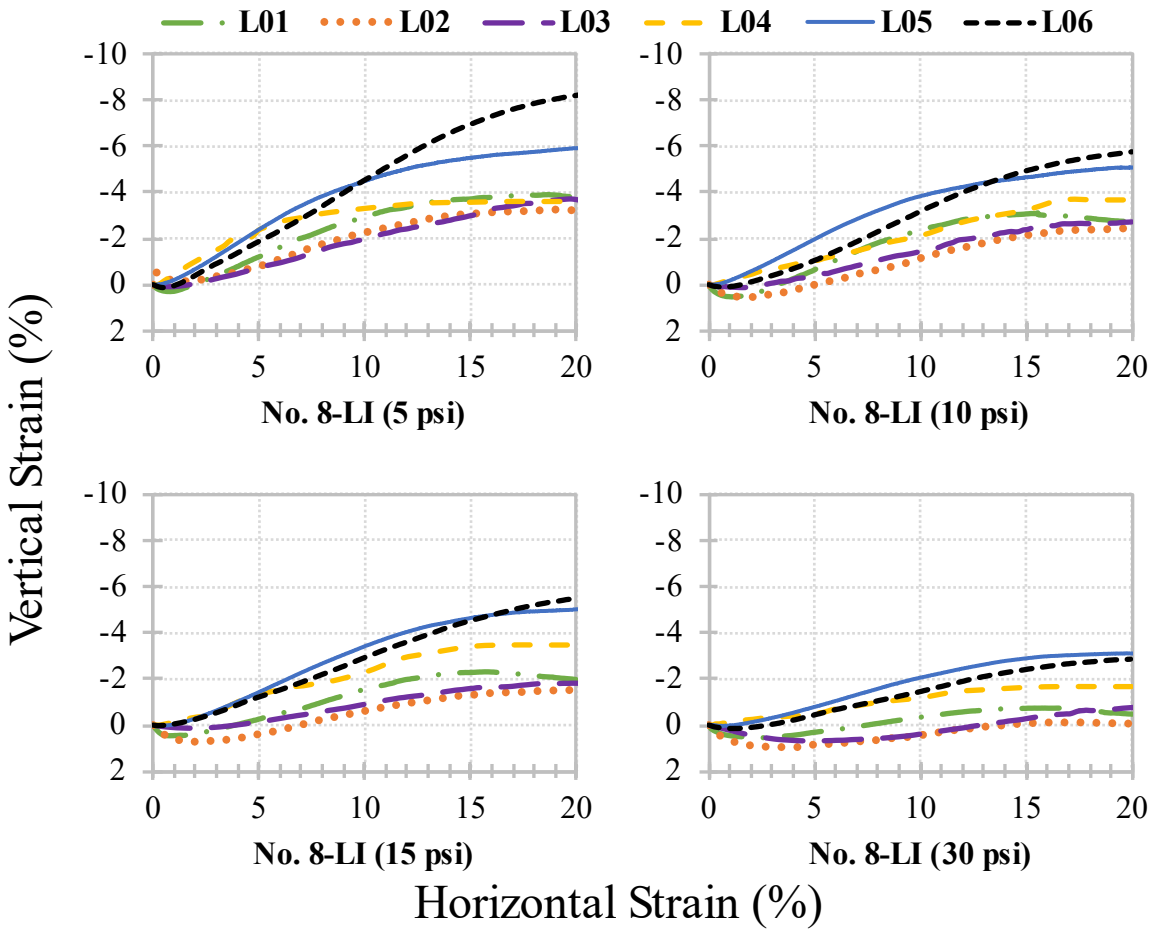

Source: FHWA.

Figure 29. Charts. Vertical strain versus horizontal strain for No. 8 OGAs.

Peak Shear Stress

The stress-strain curves for the No. 8 OGAs are the smoothest of the OGA samples, although the same general lack of distinct shear peaks and strain softening persists (appendix D). Each No. 8 OGA's τ_{peak} and corresponding $\varepsilon_{h,peak}$ are plotted in figure 30.

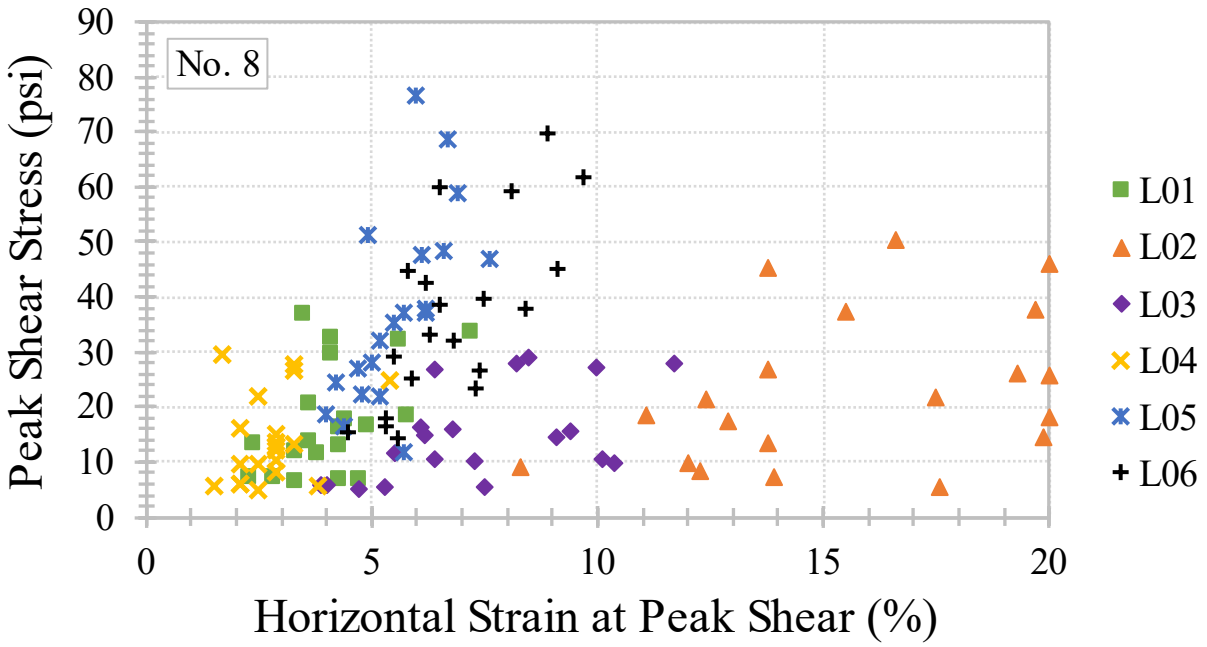

Source: FHWA.

Figure 30. Chart. Peak shear stress versus $\varepsilon_{h,peak}$ for No. 8 OGAs.

COVs for τ_{peak} are from 27.7 to 85.2 percent (table 29), consistent with that of the coarser OGAs tested (table 23 and table 26). Similarly, $\varepsilon_{h,peak}$ was, on average, between 4.9 and 10.0 percent, with COVs ranging from 40.8 to 98.3 percent (table 29).

Table 29. Peak shear stress parameters for No. 8 OGAs.

Parameter	Sample ID	L01	L02	L03	L04	L05	L06	$\bar{x}$	s	COV (percent)
$\tau_{peak,5psi}$ (psi)	No. 8-BA	7.4	5.3	5.1	5.8	24.4	29.0	12.8	10.9	85.2
	No. 8-DI	7.2	7.2	5.8	5.9	16.5	16.4	9.8	5.2	53.1
	No. 8-GG	6.4	9.1	5.5	5.0	11.8	15.5	8.9	4.1	46.1
	No. 8-LI	6.8	9.8	5.5	5.5	18.6	23.2	11.6	7.5	64.7
	No. 8-SI	6.8	8.3	5.8	6.0	21.9	14.2	10.5	6.4	61.0
$\tau_{peak,10psi}$ (psi)	No. 8-BA	13.5	14.4	9.7	12.0	37.3	33.1	20.0	12.0	60.0
	No. 8-DI	13.8	18.4	10.5	10.2	26.9	25.3	17.5	7.3	41.7
	No. 8-GG	11.7	13.5	10.0	8.3	22.4	17.9	14.0	5.3	37.9
	No. 8-LI	12.9	17.5	10.4	9.6	28.2	38.0	19.4	11.4	58.8
	No. 8-SI	11.9	18.2	11.7	9.7	32.2	26.5	18.4	9.2	50.0
$\tau_{peak,15psi}$ (psi)	No. 8-BA	20.6	21.8	14.5	16.1	51.4	44.6	28.2	15.7	55.7
	No. 8-DI	17.9	27.0	16.3	15.0	37.0	38.5	25.3	10.5	41.5
	No. 8-GG	16.2	21.5	15.0	12.7	35.3	32.2	22.2	9.5	42.8
	No. 8-LI	18.6	26.2	15.7	13.3	37.7	45.2	26.1	12.9	49.4
	No. 8-SI	16.7	25.7	16.1	13.7	47.6	39.8	26.6	14.1	53.0
$\tau_{peak,30psi}$ (psi)	No. 8-BA	36.9	37.6	26.7	29.6	76.6	60.1	44.6	19.6	43.9
	No. 8-DI	32.2	45.3	29.0	26.5	48.5	59.2	40.1	12.9	32.2
	No. 8-GG	29.6	37.3	27.3	22.1	46.8	42.7	34.3	9.5	27.7
	No. 8-LI	33.6	45.9	28.0	24.9	58.7	69.9	43.5	18.0	41.4
	No. 8-SI	32.5	50.4	28.0	27.9	68.6	61.6	44.8	17.9	40.0
$\varepsilon_{h,peak,5psi}$ (percent)	No. 8-BA	2.3	17.6	4.7	1.5	4.2	5.5	6.0	5.9	98.3
	No. 8-DI	2.8	13.9	3.9	2.1	4.4	5.3	5.4	4.3	79.6
	No. 8-GG	3.3	8.3	5.3	2.5	5.7	4.5	4.9	2.0	40.8
	No. 8-LI	4.7	12.0	7.5	3.8	4.0	7.3	6.6	3.1	47.0
	No. 8-SI	4.3	12.3	4.0	2.1	5.2	5.6	5.6	3.5	62.5
$\varepsilon_{h,peak,10psi}$ (percent)	No. 8-BA	2.4	19.9	10.4	2.9	5.7	6.3	7.9	6.5	82.3
	No. 8-DI	3.6	11.1	6.4	2.9	4.7	5.9	5.8	2.9	50.0
	No. 8-GG	3.8	13.8	7.3	2.9	4.8	5.3	6.3	4.0	63.5
	No. 8-LI	4.3	12.9	10.1	2.5	5.0	8.4	7.2	3.9	54.2
	No. 8-SI	3.3	20.0	5.5	2.1	5.2	7.4	7.3	6.5	89.0
$\varepsilon_{h,peak,15psi}$ (percent)	No. 8-BA	3.6	17.5	9.1	2.1	4.9	5.8	7.2	5.6	77.8
	No. 8-DI	4.4	13.8	6.1	2.9	6.2	6.5	6.7	3.8	56.7
	No. 8-GG	4.3	12.4	6.2	2.9	5.5	6.8	6.4	3.3	51.6
	No. 8-LI	5.8	19.3	9.4	3.3	6.2	9.1	8.9	5.6	62.9
	No. 8-SI	4.9	20.0	6.8	2.9	6.1	7.5	8.0	6.1	76.3
$\varepsilon_{h,peak,30psi}$ (percent)	No. 8-BA	3.5	19.7	6.4	1.7	6.0	6.5	7.3	6.4	87.7
	No. 8-DI	5.6	13.8	8.5	3.3	6.6	8.1	7.7	3.5	45.5
	No. 8-GG	4.1	15.5	10.0	2.5	7.6	6.2	7.7	4.7	61.0
	No. 8-LI	7.2	20.0	11.7	5.4	6.9	8.9	10.0	5.3	53.0
	No. 8-SI	4.1	16.6	8.2	3.3	6.7	9.7	8.1	4.8	59.3

Secant Friction Angle

The No. 8 OGAs continue to follow the classically expected trend of decreasing ϕ_s associated with increasing σ_n (e.g., figure 31). Average secant friction angles (ϕ_s) for the No. 8 OGAs ranged from 47.8 to 60.9 degrees, with COVs ranging from 16.7 to 26.8 percent (table 30). These ϕ_s values are generally lower than the No. 68 (table 27) and No. 57 (table 24) results; on the other hand, COVs for the No. 8 OGAs are generally higher than the COVs of the larger OGA stone sizes.

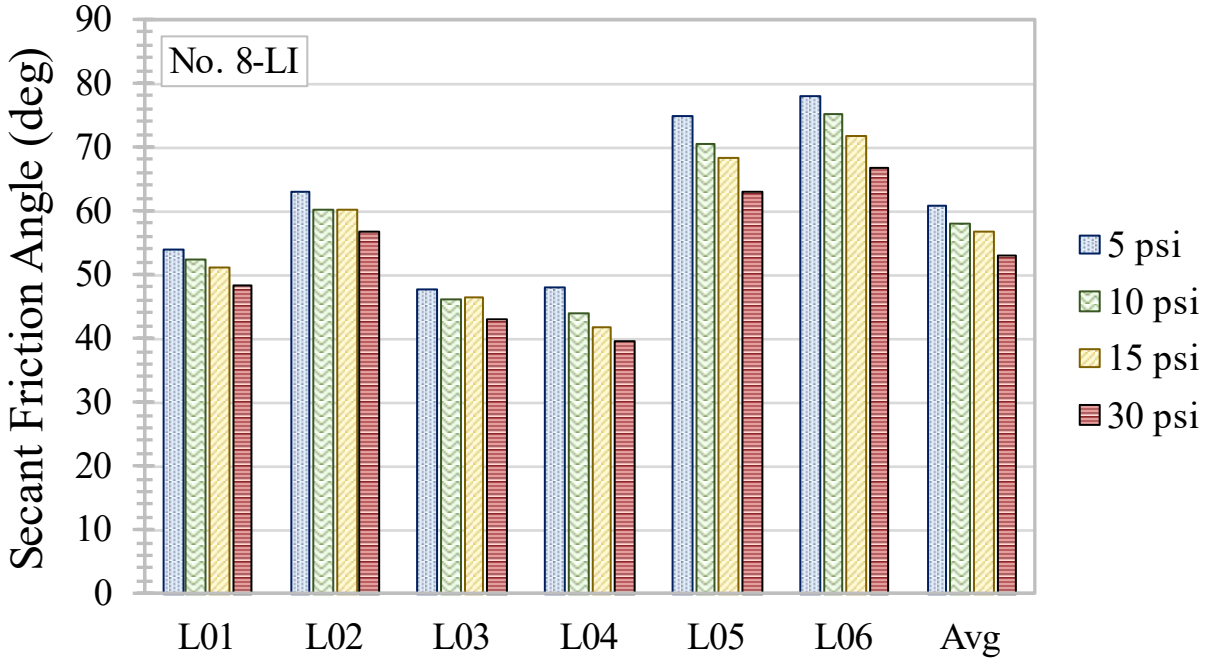

Source: FHWA.

Figure 31. Chart. Secant friction angles for No. 8-LI.

Tangent Friction Angle

Variability remained low for ϕ_t with COVs from 15.2 to 19.5 percent (table 30); average ϕ_t values range from 44.8 to 51.8 degrees, slightly less than those found for No. 57 (table 24) and No. 68 (table 27). As with the previous OGA stone sizes, c_a is still present in the linear Mohr-Coulomb failure envelopes (e.g., figure 32).

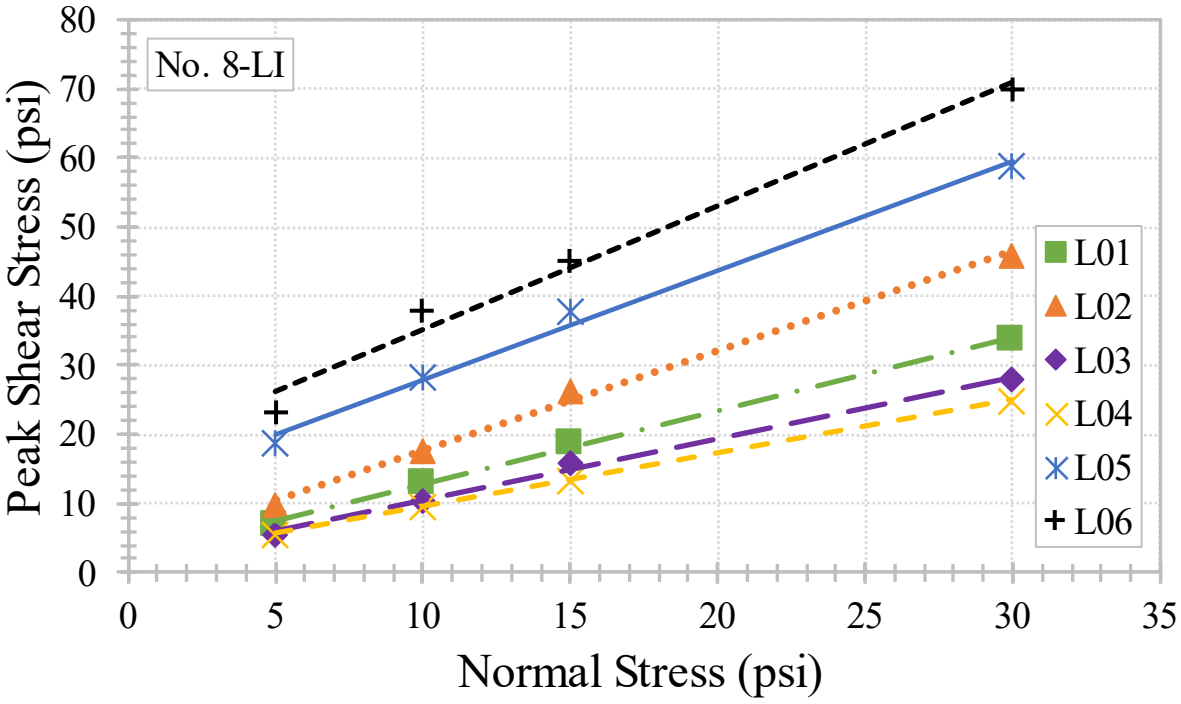

Source: FHWA.

Figure 32. Chart. Linear Mohr-Coulomb failure envelopes for No. 8-LI.

Residual Friction Angle

Like the other OGAs, variability in $\phi_{t,r}$ was greater than that of ϕ_t with COVs ranging from 19.5 to 25.8 percent (table 30). Average $\phi_{t,r}$ values ranged from 40.8 to 48.6 degrees, following the same general downward trend in friction angle with stone size.

Table 30. Shear strength parameters for No. 8 OGAs.

Parameter	Sample ID	L01	L02	L03	L04	L05	L06	$\bar{x}$	s	COV (percent)
$\phi_{s,5psi}$ (degree)	No. 8-BA	55.9	46.6	45.5	49.3	78.4	80.2	59.3	15.9	26.8
	No. 8-DI	55.3	55.4	49.4	49.7	73.1	73.0	59.3	10.9	18.4
	No. 8-GG	51.8	61.3	47.8	44.9	67.0	72.2	57.5	11.0	19.1
	No. 8-LI	53.8	62.9	47.6	47.9	75.0	77.9	60.9	13.3	21.8
	No. 8-SI	53.5	58.9	49.4	50.3	77.1	70.6	60.0	11.4	19.0
$\phi_{s,10psi}$ (degree)	No. 8-BA	53.4	55.2	44.3	50.2	75.0	73.2	58.6	12.6	21.5
	No. 8-DI	54.0	61.5	46.3	45.7	69.6	68.4	57.6	10.6	18.4
	No. 8-GG	49.4	53.5	44.9	39.8	65.9	60.8	52.4	9.8	18.7
	No. 8-LI	52.3	60.2	46.2	43.8	70.5	75.3	58.1	12.9	22.2
	No. 8-SI	50.1	61.2	49.4	44.0	72.8	69.3	57.8	11.7	20.2
$\phi_{s,15psi}$ (degree)	No. 8-BA	54.0	55.4	44.1	47.1	73.7	71.4	57.6	12.3	21.4
	No. 8-DI	50.0	61.0	47.5	45.0	68.0	68.7	56.7	10.6	18.7
	No. 8-GG	47.2	55.1	45.0	40.2	67.0	65.0	53.3	11.0	20.6
	No. 8-LI	51.2	60.2	46.4	41.6	68.3	71.7	56.6	12.1	21.4
	No. 8-SI	48.0	59.7	47.0	42.4	72.5	69.3	56.5	12.6	22.3
$\phi_{s,30psi}$ (degree)	No. 8-BA	50.9	51.4	41.7	44.6	68.6	63.5	53.5	10.6	19.8
	No. 8-DI	47.1	56.5	44.0	41.5	58.3	63.1	51.8	8.7	16.8
	No. 8-GG	44.6	51.2	42.3	36.4	57.3	54.9	47.8	8.0	16.7
	No. 8-LI	48.2	56.8	43.0	39.7	62.9	66.8	52.9	11.0	20.8
	No. 8-SI	47.3	59.2	43.0	42.9	66.4	64.0	53.8	10.7	19.9
c_a (psi)	No. 8-BA	1.9	0.9	1.1	1.9	16.6	22.7	7.5	9.6	128.0
	No. 8-DI	3.1	2.5	1.5	2.1	13.9	9.2	5.4	5.0	92.6
	No. 8-GG	2.2	3.2	1.4	1.7	8.8	10.1	4.6	3.9	84.8
	No. 8-LI	2.1	3.3	1.5	1.7	12.1	17.3	6.3	6.7	106.3
	No. 8-SI	1.5	0.7	2.4	1.0	14.8	7.6	4.7	5.6	119.1
ϕ_t (degree)	No. 8-BA	49.7	51.4	40.8	42.9	64.0	51.8	50.1	8.2	16.4
	No. 8-DI	44.4	55.8	42.8	39.4	50.7	59.6	48.8	7.9	16.2
	No. 8-GG	42.6	48.9	41.0	34.5	53.4	48.5	44.8	6.8	15.2
	No. 8-LI	46.7	55.2	41.8	37.7	57.7	60.8	50.0	9.3	18.6
	No. 8-SI	45.8	58.9	40.9	41.5	61.7	61.7	51.8	10.1	19.5
ϕ_r (degree)	No. 8-BA	37.1	52.0	38.5	33.4	52.3	51.1	44.1	8.6	19.5
	No. 8-DI	39.5	55.9	39.5	30.2	49.8	54.7	44.9	10.2	22.7
	No. 8-GG	36.3	49.8	38.8	27.8	47.2	44.6	40.8	8.1	19.9
	No. 8-LI	40.5	57.4	38.9	35.2	55.8	63.7	48.6	11.8	24.3
	No. 8-SI	37.0	59.2	40.0	31.2	52.5	59.1	46.5	12.0	25.8
ϕ_{cv} (degree)	No. 8-BA	37.0	59.1	39.8	34.3	58.2	35.3	44.0	11.5	26.1
	No. 8-DI	37.9	—	41.2	40.4	51.2	52.4	44.6	6.7	15.0
	No. 8-GG	38.1	45.3	44.3	35.4	50.1	49.4	43.8	5.9	13.5
	No. 8-LI	46.0	53.4	45.9	34.6	50.6	58.8	48.2	8.2	17.0
	No. 8-SI	42.5	66.6	43.5	31.9	53.9	56.8	49.2	12.3	25.0

—Not measured/evaluated.

Constant Volume Friction Angle

Constant volume friction angles (ϕ_{cv}) ranged, on average, from 43.8 to 49.2 degrees; COVs ranged from 13.5 to 26.1 percent, suggesting the variability of ϕ_{cv} for the No. 8 OGAs was in line with that of the other OGAs (table 30).

Maximum Dilation Angle

Using the *n*-point centered moving average approach (table 21), ψ_{max} was computed for the No. 8 OGAs (table 31).

Table 31. Maximum dilation angles for No. 8 OGAs.

Parameter	Sample ID	L01	L02	L03	L04	L05	L06	$\bar{x}$	*s*	COV (percent)
$\psi_{max,5psi}$ (degree)	No. 8-BA	19.2	35.7	15.4	25.6	26.9	26.7	24.9	7.0	28.1
	No. 8-DI	21.8	—	16.0	45.0	22.6	22.6	25.6	11.2	43.8
	No. 8-GG	15.9	12.5	17.1	31.0	18.3	22.3	19.5	6.5	33.3
	No. 8-LI	14.1	14.5	10.7	21.8	20.6	21.5	17.2	4.7	27.3
	No. 8-SI	12.3	14.4	17.4	30.6	23.8	21.1	19.9	6.7	33.7
$\psi_{max,10psi}$ (degree)	No. 8-BA	16.6	9.1	18.3	30.1	21.9	22.4	19.7	7.0	35.5
	No. 8-DI	19.8	—	17.5	24.5	15.3	18.1	19.0	3.5	18.4
	No. 8-GG	14.7	12.5	31.5	12.4	17.1	16.4	17.4	7.2	41.4
	No. 8-LI	13.8	11.6	12.4	11.3	16.9	16.4	13.7	2.4	17.5
	No. 8-SI	14.3	12.5	40.0	22.8	20.2	17.5	21.2	9.9	46.7
$\psi_{max,15psi}$ (degree)	No. 8-BA	18.3	23.6	18.8	26.6	19.4	20.8	21.3	3.2	15.0
	No. 8-DI	17.1	—	13.6	15.3	13.8	15.5	15.1	1.4	9.3
	No. 8-GG	9.8	10.8	8.7	11.6	13.9	10.5	10.9	1.8	16.5
	No. 8-LI	9.5	8.9	5.4	13.5	15.3	14.2	11.1	3.8	34.2
	No. 8-SI	9.8	12.7	23.5	19.8	17.7	16.4	16.7	4.9	29.3
$\psi_{max,30psi}$ (degree)	No. 8-BA	14.5	21.0	14.9	19.8	14.3	16.9	16.9	2.9	17.2
	No. 8-DI	11.1	—	8.7	11.3	9.4	13.0	10.7	1.7	15.9
	No. 8-GG	8.7	6.0	11.7	6.8	8.8	9.3	8.6	2.0	23.3
	No. 8-LI	4.7	6.0	10.0	11.3	10.4	9.2	8.6	2.6	30.2
	No. 8-SI	7.7	12.3	14.8	16.7	13.3	11.5	12.7	3.1	24.4

—Not measured/evaluated.

As expected, ψ_{max} generally decreased as σ_n increased (e.g., figure 33).

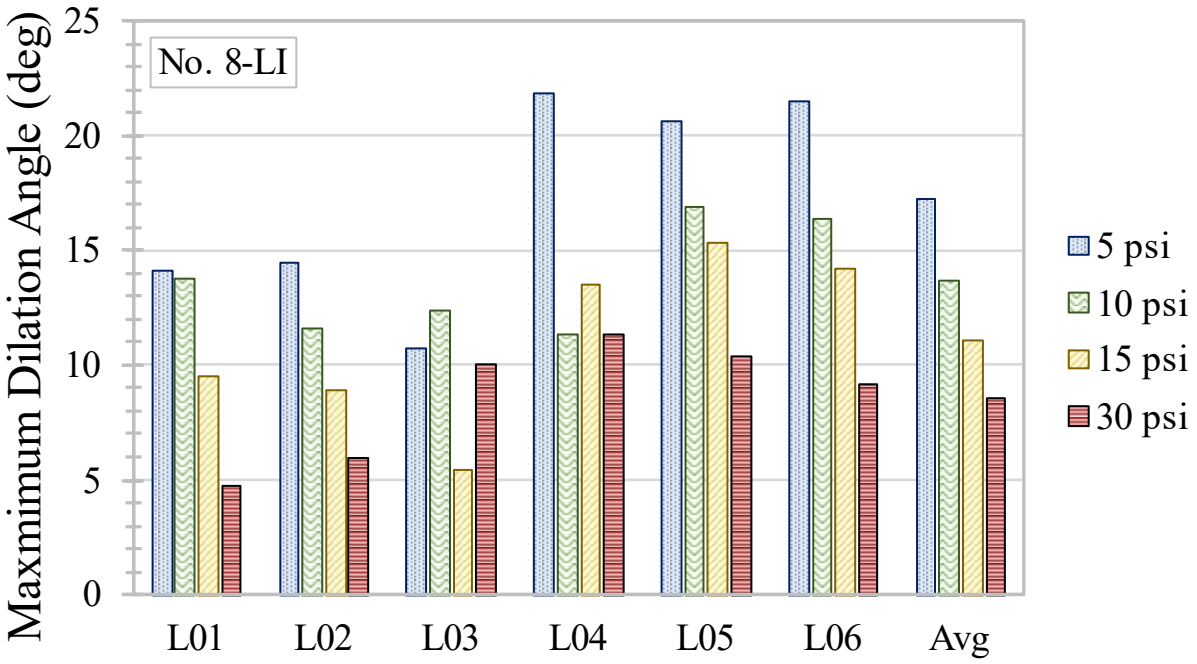

Source: FHWA.

Figure 33. Chart. Maximum dilation angle for No. 8-LI.

On average, ψ_{max} ranged from 8.6 to 25.6 degrees (table 31); COVs for ψ_{max} ranged from 9.3 to 46.7 percent.

SUMMARY

The round-robin interlaboratory testing program provided data on the physical properties and τ of select OGAs often used in road and bridge construction. From the dataset, the variability of key design parameters was found; a summary of the basic statistics (e.g., mean, standard deviation, and COV) for each OGA (and the entire dataset, as applicable) is provided in table 32. The findings indicated that OGA gradation (e.g., D_{85}) and unit weight (e.g., γ_{d95}) results between the laboratories were relatively consistent, suggesting that the gap size and target density specified for LSDS testing were not significant factors in the strength-deformation differences found between the laboratories. These differences were made clear in the larger variability found for the resulting friction angles, whether secant (ϕ_s), tangent (ϕ_t), residual, tangent ($\phi_{t,r}$), or constant volume (ϕ_{cv}), and the resulting maximum dilation angles (Ψ_{max}) (table 32). This variability in LSDS strength results was further highlighted when OS-20-30 was tested by each laboratory (table 20 and table 22), emphasizing the impact of LSDS box characteristics on the strength-deformation behavior and the derived results for soils and aggregates. Further analysis on the type of statistical distribution each parameter follows (e.g., normal, lognormal), the significance of LSDS devices and mineralogy of OGAs on the results, and the implications of these results found on geotechnical design, are presented in chapter 4.

Table 32. Summary of key, average OGA results and basic statistics.

Parameter	Sample ID	$\bar{x}$	s	COV (%)	Reference
D_{85} (inch)	No. 57-Avg.	0.80	0.07	8.8	table 8
	No. 68-Avg.	0.65	0.03	4.6	table 8
	No. 8-Avg.	0.36	0.02	5.6	table 8
γ_{d95} (lb/ft^3)	No. 57-Avg.	104.3	5.4	5.2	table 10
	No. 68-Avg.	107.6	6.1	5.7	table 11
	No. 8-Avg.	103.4	5.2	5.0	table 12
ϕ_s^+ (degree)	No. 57-Avg.	60.4	9.1	15.1	N/A
	No. 68-Avg.	59.9	10.4	17.4	N/A
	No. 8-Avg.	56.1	11.0	19.6	N/A
	All-Avg.	58.8	10.2	17.4	N/A
ϕ_t (degree)	No. 57-Avg.	53.6	6.0	11.2	table 24
	No. 68-Avg.	52.4	7.5	14.3	table 27
	No. 8-Avg.	49.1	8.3	16.9	table 30
	All-Avg.	51.7	7.3	14.1	N/A
$\phi_{t,r}$ (degree)	No. 57-Avg.	50.0	10.9	21.8	table 24
	No. 68-Avg.	48.4	11.0	22.7	table 27
	No. 8-Avg.	45.0	9.9	22.0	table 30
	All-Avg.	47.8	10.6	22.2	N/A
ϕ_{cv} (degree)	No. 57-Avg.	50.0	9.8	19.6	table 24
	No. 68-Avg.	47.6	8.4	17.6	table 27
	No. 8-Avg.	46.0	9.0	19.6	table 30
	All-Avg.	47.9	9.1	18.9	N/A
ψ_{max}^+ (degree)	No. 57-Avg.	19.2	7.7	39.9	N/A
	No. 68-Avg.	18.8	7.5	39.6	N/A
	No. 8-Avg.	16.5	6.9	42.1	N/A
	All-Avg.	18.2	7.4	40.5	N/A

$^+$Combined values over the range of σ_n values (i.e., 5 to 30 psi).
N/A = not applicable.

CHAPTER 4. ANALYSIS OF RESULTS

The results presented in the previous chapter suggest that the variability of physical properties and characteristics is relatively low; for example, COVs for γ_{d95} ranged from 1.1 to 3.1 percent for the OGAs (table 10 through table 12). The variability of shear strength (i.e., friction and dilation angles), however, was found to be higher; for example, COVs for ϕ_t ranged from 10.1 to 19.5 percent for the OGAs (table 24, table 27, and table 30). This chapter will evaluate potential reasons for the interlaboratory variability, primarily as these reasons relate to differences in the LSDS devices and test procedures at each of the laboratories. In addition, statistical methods such as standard normal variable plots and Anderson-Darling (AD) tests were employed to further analyze the distribution of the datasets for dry unit weight and shear strength within the context of probabilistic design. Finally, ANOVA was performed to evaluate the impact of the laboratory (i.e., LSDS device) and sample type (i.e., stone size and mineralogy) on the variability of results.

DISTRIBUTION TYPES

The basic statistics of all data in chapter 3 were reported in terms of mean, standard deviation, and COV. To further characterize the design parameters of interest (i.e., dry unit weight at *95RD* (selected as representative of field conditions), friction angles, and maximum dilation angle) statistically, an evaluation of the distribution type (e.g., normal, lognormal) was performed. This section presents varying approaches to determine the type of distribution that best fits the measured and/or derived data presented in chapter 3, including frequency histograms, normal probability plots, and AD tests to determine the goodness of fit for selected distribution types.

Histograms are the most common way to represent scattered data graphically (Baecher and Christian 2003). The *y*-axis in any histogram is the frequency, or number, of data points that fall into a certain, selected bin size (or bin width) on the *x*-axis. To maintain consistency in developing histograms for the relevant design parameters evaluated in this study (i.e., γ_{d95}, ϕ_s, ϕ_t, $\phi_{t,r}$, ϕ_{cv}, and ψ_{max}), Scott's normal reference rule was selected to calculate each histogram's optimal bin width (W) as a function of the associated standard deviation (s) and sample size (n) per equation 4 (Scott 1979).

$$W = 3.49 \times s \times n^{-1/3} \tag{4}$$

As the name implies, Scott's normal reference rule generates bin widths that approximate normal distributions in an unbiased manner (Scott 1979). While the exact distribution of the data was unknown before the histograms were developed, this method of selecting bin widths for each parameter evaluated only required inputs that were known in this study (i.e., s and n); see table 33. In all cases, the starting bin value in the histograms was set to the minimum value measured for each parameter (table 33). The histograms presented in this section are also overlayed with an idealized normal distribution curve as computed from the $\bar{x}$ and s of the plotted parameter. Note that each histogram combines the entire dataset for the parameter evaluated (i.e., no distinction is made between stone size, mineralogy, laboratory, or σ_n) and is not truncated for the purposes of illustrating the fit with the data.

Table 33. Histogram parameters.

Parameter	Units	Min.	Max.	Mode[++]	Median	$\bar{x}$	s	n	W	K_u	S_k
γ_{d95}	lb/ft^3	95.4	118.8	101.4 (111.6)	104.1	105.1	5.8	90	4.5	−0.5	0.5
ϕ_s[+]	deg	36.4	82.8	49.4	56.8	58.8	10.4	360	5.1	−1.0	0.2
ϕ_t	deg	34.5	68.1	48.9	51.0	51.7	7.5	90	5.8	−0.7	0.1
$\phi_{t,r}$	deg	27.8	65.2	47.2	47.2	47.8	10.7	90	8.3	−1.3	−0.1
ϕ_{cv}	deg	20.7	66.6	39.8 (44.2)	49.1	47.7	9.0	86	7.1	0.1	−0.2
ψ_{max}[+]	deg	3.5	45.6	12.5	17.2	18.3	7.3	346	3.6	0.9	0.8

[+]Combined values over the range of σ_n values (i.e., 5 to 30 psi).
[++]For bimodal distributions, first mode (second mode) identified.

Table 33 also includes additional parameters for a full characterization of a given (untruncated) histogram, including mode, median, kurtosis (K_u), and skewness (S_k). In a perfectly normal distribution, the mode, median, and mean ($\bar{x}$) are equal, and the K_u and S_k are zero. The values of K_u and S_k are properties of the distribution used to evaluate how peaked or flat and how skewed or symmetrical the tails of the distribution are, respectively (Selezneva et al. 2002). A positive and negative K_u value indicates a relatively peaked and flat distribution, respectively, whereas a positive and negative S_k value corresponds to a distribution with an asymmetric tail extending more toward the right (i.e., positive skew) and left (i.e., negative skew), respectively. Equation 5 and equation 6 were used to determine K_u and S_k of each parameter (Uzielli et al. 2006).

$$K_u = \left\{ \frac{n(n+1)}{(n-1)(n-2)(n-3)} \sum_{i=1}^{n} \left(\frac{x_i - \bar{x}}{s} \right)^4 \right\} - \frac{3(n-1)^2}{(n-2)(n-3)} \tag{5}$$

$$S_k = \frac{n}{(n-1)(n-2)} \sum_{i=1}^{n} \left(\frac{x_i - \bar{x}}{s} \right)^3 \tag{6}$$

Another graphical method to evaluate the distribution of the data for each parameter is to develop normal probability plots. This method of evaluation requires transforming the probability of the data into standard normal variables (Z) and then plotting those Z values versus the corresponding measured data and versus data predicted, assuming a given distribution type (e.g., normal, lognormal) (Allen et al. 2005). Each set of data was first arranged in ascending order, and a numeric rank (i), starting from 1, was assigned to each value. The Z was computed as the inverse of the standard normal cumulative distribution, or Z = NORMSINV (i/(n+1)), for each value and then plotted against the corresponding measured data. Theoretical normal and lognormal distributions for the datasets were then compared within the normal probability plot to evaluate the best-fit distribution. Note that the mean and standard deviation of each dataset were log-transformed and the inverse of the lognormal was computed to determine the predicted lognormal distribution for comparison.

Finally, the AD test was adopted to perform a goodness-of-fit test (Anderson and Darling 1954). AD tests are nonparametric tests where the null hypothesis states that the data follow a specified

distribution. Conversely, the alternative hypothesis would be that the data do not follow a specified distribution. Normal and lognormal were tested with an alpha (i.e., threshold *p*-value) of 0.05. A *p*-value less than or equal to the alpha of 0.05 corresponds to at least a 95-percent confidence level that random chance, based on the mean and standard deviation of the dataset, would generate results at least as extreme as those observed. If the *p*-value from the statistic test is greater than 0.05, the null hypothesis should be accepted. Summarized steps for the AD test are shown in appendix E.

Dry Unit Weight

The γ_{dmin} and γ_{dmax} for each OGA sample were measured by each laboratory; these measured unit weights were then used to compute the γ_{d95} for each sample (table 10 through table 12). Since γ_{d95} was used as the target density for LSDS testing and is most representative of compacted conditions in the field, only its histogram, based on the values in table 33, is presented in this subsection. Visual observation of the histogram indicates that the calculated γ_{d95} for all OGAs evaluated in this study are not normally distributed (figure 34). This finding is also evidenced by the nonequality of values among the mode, median, and mean (table 33). The K_u and S_k values (table 33) indicated a relatively flat distribution with positive skew, respectively.

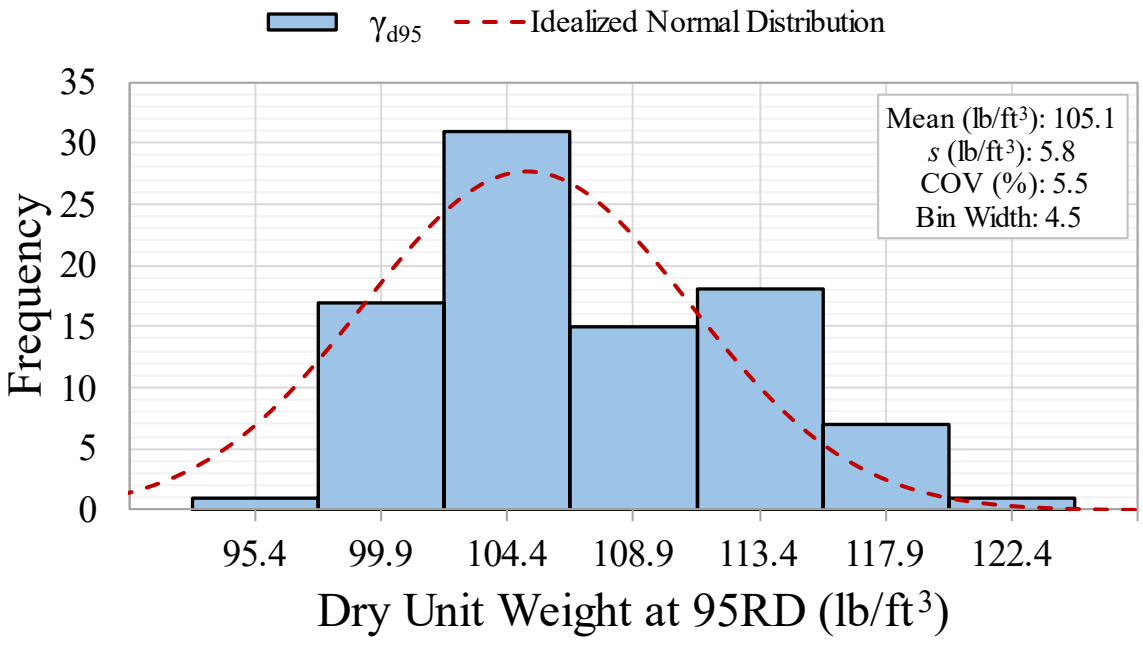

Source: FHWA.

Figure 34. Chart. Histogram of γ_{d95} with idealized normal distribution curve overlayed.

The normal probability plot for γ_{d95} is shown in figure 35, along with the predicted normal and lognormal distributions of the dataset for comparison. The measured γ_{d95} data were not in good agreement with either the predicted normal or lognormal distribution curves. This fact is unsurprising given the diversity of source quarries and AASHTO stone sizes tested. There is a distinct break in the normal probability plot between 106 and 108 lb/ft^3 that corresponds to a change in mineralogy.

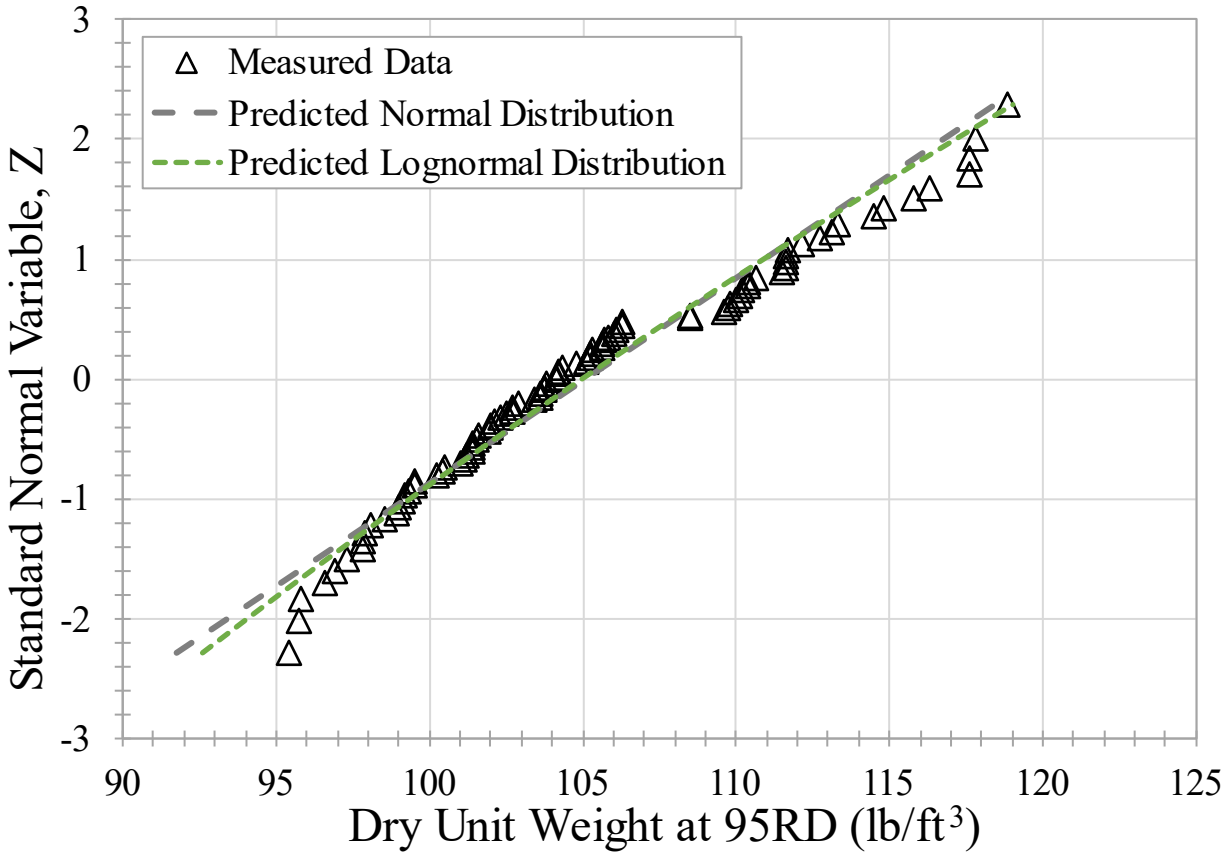

Source: FHWA.

Figure 35. Chart. Normal probability plot for γ_{d95}.

All γ_{d95} values in excess of 108 lb/ft^3 are composed of mafic mineralogy (i.e., DI and BA), with *Gsb* values above 2.9 versus the lighter sedimentary or felsic mineralogy (i.e., GG, LI, and SI), which had *Gsb* values around 2.7 (figure 36).

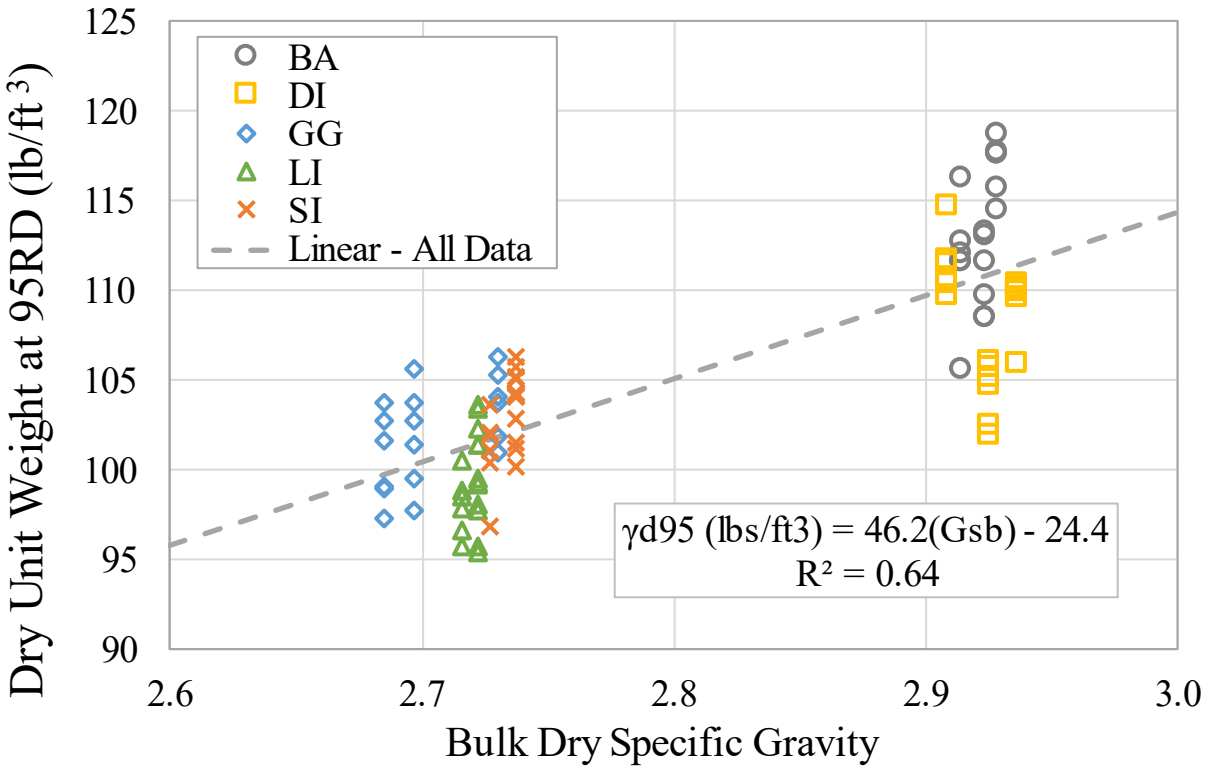

Source: FHWA.

Figure 36. Chart. Relationship between γ_{d95} and *Gsb*.

The AD test for γ_{d95} was initially performed for the entire 90-point dataset. The test found that the entirety of γ_{d95} does not follow a normal distribution (i.e., p-value = 0.00) or a lognormal distribution (p-value = 0.01) (appendix E). However, separating the 90-point dataset into lighter (i.e., GG, LI, and SI) and heavier weight (i.e., BA and DI) OGAs in the AD test resulted in two normal distribution curves with p-values of 0.30 and 0.40, respectively (appendix E). As such, the bimodal nature of γ_{d95} would be best represented by two separate normal distributions with $\bar{x}$ = 101.4 lb/ft^3 and s = 2.9 lb/ft^3 for the lighter sedimentary or felsic mineralogy evaluated, in contrast to $\bar{x}$ = 110.8 lb/ft^3 and s = 4.3 lb/ft^3 for the heavier mafic mineralogy. The mean of 105.1 (table 33) is an appropriate approximation of γ_{d95} for preliminary design in the absence of mineralogy information. A selection of OGAs covering a more continuous spectrum of bulk dry specific gravities may reveal a singular normal distribution curve.

Friction Angles

The secant (ϕ_s), tangent (ϕ_t), residual tangent ($\phi_{t,r}$), and constant volume (ϕ_{cv}) friction angles were all determined for each sample; a summary of these strength parameters for all OGAs are shown in table 24, table 27, and table 30 in chapter 3.

Secant Friction Angle

To evaluate the distribution of ϕ_s, all of the values (table 24, table 27, and table 30) were combined over the range of σ_n values (i.e., 5 to 30 psi) into a single, 360-point dataset to

determine the overall statistics of the parameter (table 33). Visual observation of the histogram for the combined ϕ_s dataset (figure 37) suggests that ϕ_s for all OGAs evaluated in this study are not normally distributed. Similarly, evaluation of the mode, median, and mean, along with the K_u and S_k values (table 33), indicate nonnormality of the ϕ_s parameter.

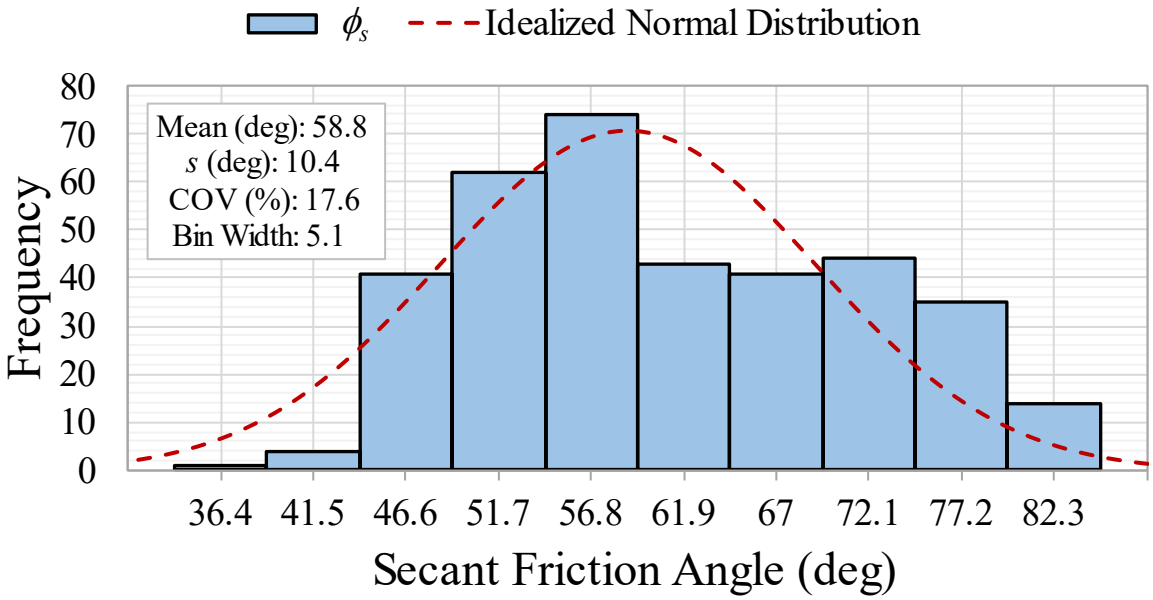

Source: FHWA.

Figure 37. Chart. Histogram of ϕ_s with idealized normal distribution curve overlayed.

The normal probability plot for ϕ_s is shown in figure 38-A, along with the predicted normal and lognormal distributions of the dataset for comparison. The measured ϕ_s data were not in good agreement with either predicted distribution curve. In addition, there appears to be two distinct groupings present in the data (figure 38-A)—as was the case with γ_{d95}. Further investigation revealed that L01, L03, and L04 are overwhelmingly located to the left of the inflection point at approximately 58 degrees (figure 38-B); likewise, most points to the right of 58 degrees were from L02, L05, and L06. These left and right groupings coincide with mobile and fixed upper shear boxes, respectively (table 6).

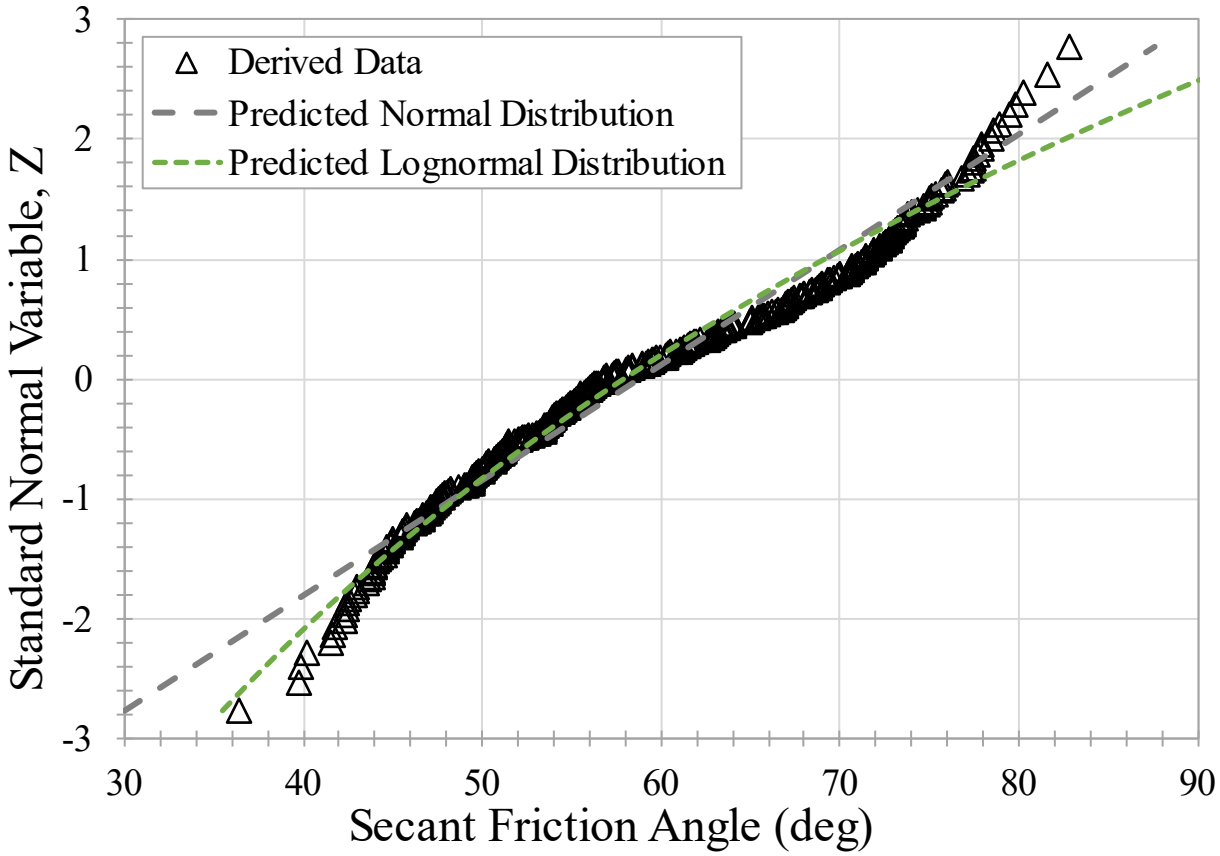

Source: FHWA.

A. All data with predicted distributions.

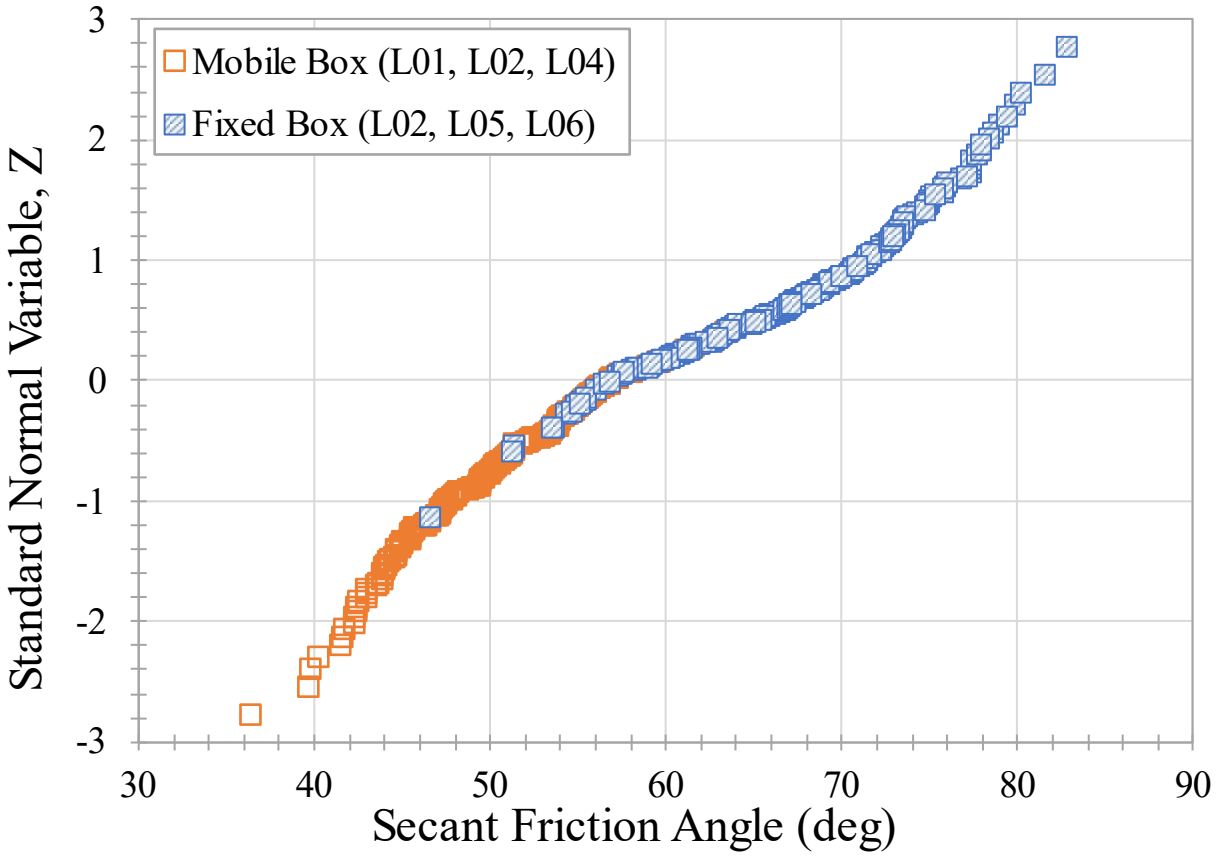

Source: FHWA.

B. All data by box mobility.

Figure 38. Charts. Normal probability plots for ϕ_s.

The AD test for ϕ_s performed for the combined 360-point dataset indicated that neither distribution type fit the ϕ_s data. Additional AD testing according to the upper box fixity groupings showed that ϕ_s followed normal behavior (p-value = 0.16) within the fixed upper box group (i.e., L02, L05, and L06). The ϕ_s remained neither normally nor lognormally distributed for the mobile upper box group (i.e., L01, L03, and L04) (appendix E). This analysis lends credence to devices with fixed upper boxes, yet further research is still needed, particularly considering that the laboratories with fixed upper boxes in this study were research-based laboratories, whereas the mobile upper box results were from commercial laboratories (table 6). Therefore, ϕ_s is best approximated by a normal distribution where $\bar{x}$ = 67.1 degrees and s = 7.1 degrees for data collected from fixed upper boxes. Additional distribution types (e.g., Weibull, beta, etc.) would need to be checked for data collected from mobile upper boxes based on $\bar{x}$ = 50.5 degrees and s = 5.1 degrees.

Tangent Friction Angle

The ϕ_t for each OGA sample was determined assuming a linear Mohr-Coulomb failure envelope (table 24, table 27, and table 30); a total number of 90 data points were used to establish the histogram for ϕ_t (figure 39). The calculated values of K_u (i.e., 0.7) and S_k (i.e., 0.1) shown in

table 33 indicate a relatively flat, but fairly symmetrical, distribution. The mode, median, and mean are not equal; however, their differences are relatively small, particularly with respect to the standard deviation of the parameter (table 33). These observations suggest that ϕ_t could reasonably be assumed to be a normal distribution; however, further evaluations were performed, as discussed next.

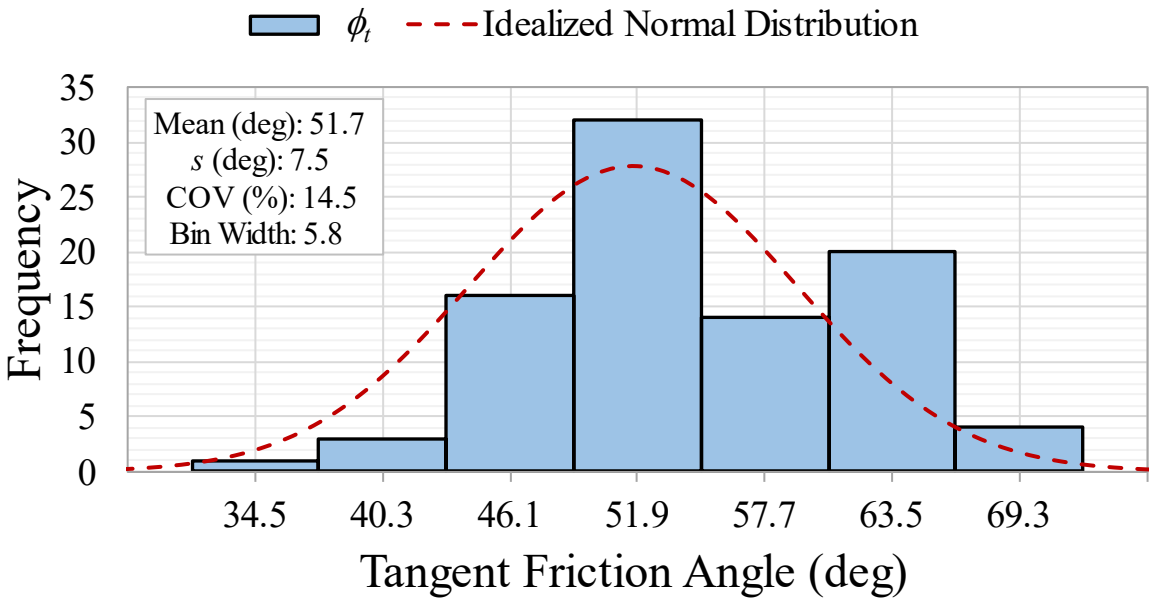

Source: FHWA.

Figure 39. Chart. Histogram for ϕ_t with idealized normal curve overlayed.

The normal probability plot for ϕ_t, along with the predicted normal and lognormal distribution curves, are shown in figure 40. Both distribution types visually fit the data fairly well. However, the predicted normal distribution better represents the full spectrum of values, while the predicted lognormal distribution better fits the lower tail of values. To determine if normality (or lognormality) can be reasonably assumed for ϕ_t, a goodness-of-fit test was performed.

The AD test for ϕ_t was based on the 90-point dataset. Similar to the observations from the normal probability plot (figure 40), both normal and lognormal distributions reasonably fit the frequency distribution of ϕ_t (appendix E). Since normality was found (i.e., p-value > 0.05), ϕ_t can statistically be approximated, assuming a normal distribution with $\bar{x}$ = 67.1 degrees and s = 7.1 degrees for the OGAs evaluated in this study. This finding also suggests that incorporating the spectrum of ϕ_s values in determining ϕ_t offsets nonnormality in the broader ϕ_s dataset. This finding is corroborated by the lower COV of ϕ_t compared to ϕ_s (table 32).

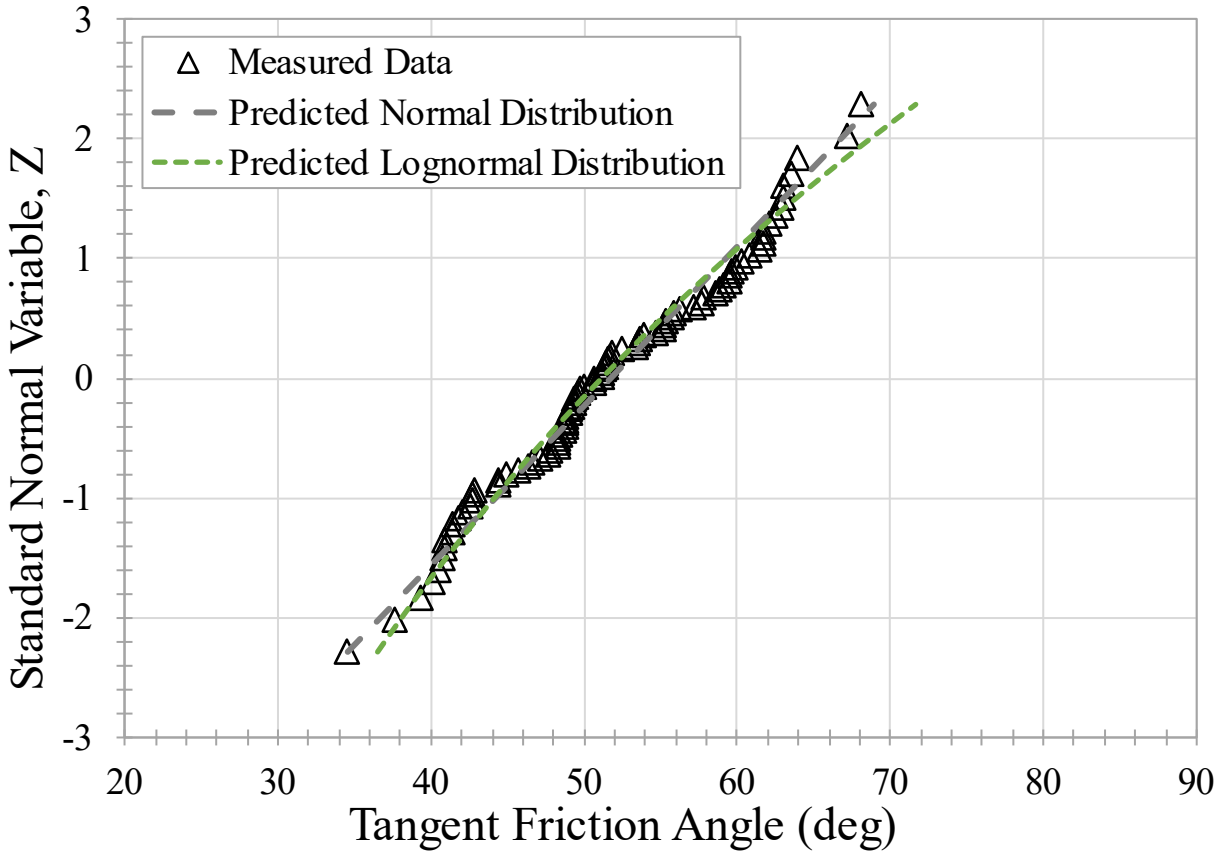

Source: FHWA.

Figure 40. Chart. Normal probability plot for ϕ_t.

Residual Friction Angle

The histogram for $\phi_{t,r}$ is shown in figure 41; 90 data points (table 24, table 27, and table 30) were used to establish the $\phi_{t,r}$ histogram. Visual and numerical observation of the histogram indicates $\phi_{t,r}$ follows a relatively flat distribution (i.e., $K_u = -1.3$) with minimal negative S_k (i.e., $S_k = -0.1$). In addition, the mode, median, and mean for $\phi_{t,r}$ were practically equal (table 33); the S_k and K_u values also suggests that $\phi_{t,r}$ generally follows a uniform distribution (i.e., nonnormal).

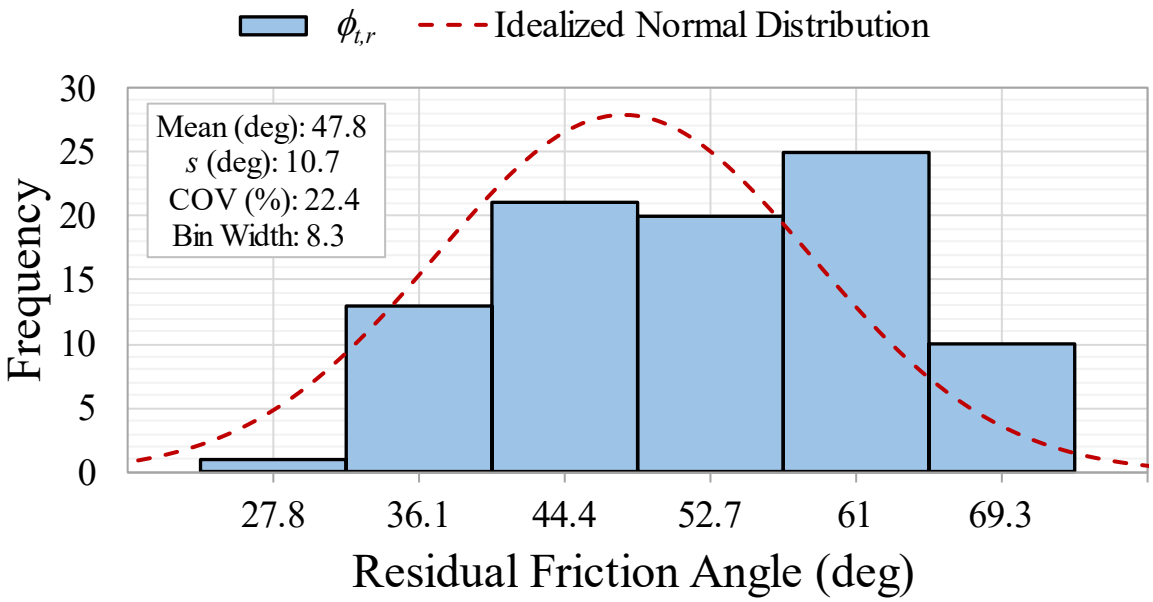

Source: FHWA.

Figure 41. Chart. Histogram for $\phi_{t,r}$ with idealized normal distribution curve overlayed.

The normal probability plot, along with the predicted normal and lognormal distribution curves for $\phi_{t,r,}$ is shown in figure 42. Neither predicted distribution type visually matches the data well across the entire dataset. Therefore, in the absence of testing higher order distribution types, $\phi_{t,r}$ can reasonably be approximated assuming a uniform distribution over the range of values (i.e., 27.8–65.2 degrees) found within this study. The AD test for $\phi_{t,r}$ was based on 90-point dataset. The findings strongly suggested that neither normal nor lognormal distributions fit the data. However, $\phi_{t,r}$ can be approximated with a uniform distribution with $\bar{x}$ = 46.5 degrees and s = 10.8 degrees given the descriptive statistics for $\phi_{t,r}$ (table 33).

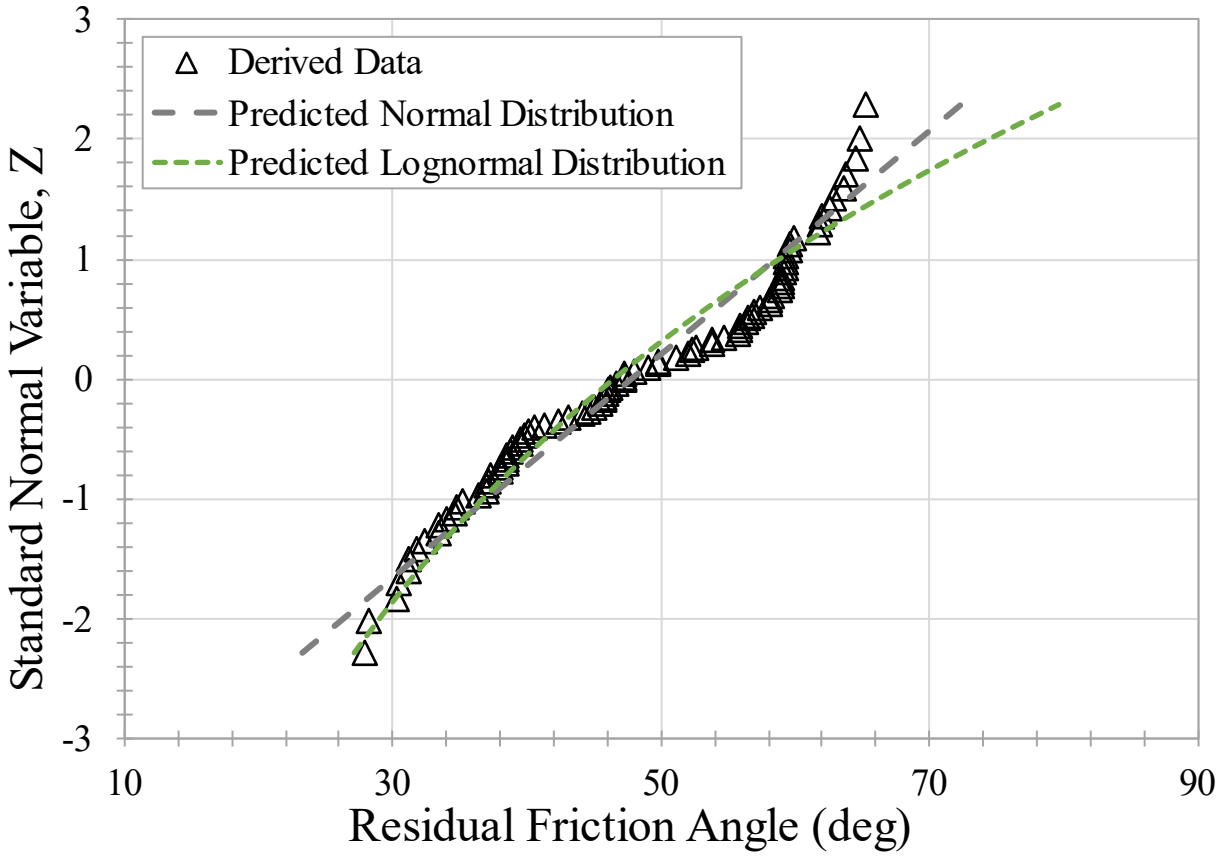

Source: FHWA.

Figure 42. Chart. Normal probability plot for $\phi_{t,r}$.

Constant Volume Friction Angle

The histogram for ϕ_{cv}, along with the overlayed normal distribution curve, is shown in figure 43 based on 86 data points (table 24, table 27, and table 30). Visual observation of the histogram shows the data are skewed to the left (figure 43). The frequency distribution was found to be bimodal (table 33); however, unlike γ_{d95}, this frequency distribution was likely just a factor of the sample size because, within the entire dataset, there were only two values at each mode. Regardless, the modes, median, and mean are unequal (table 33). However, K_u and S_k indicate similarities with a normal distribution.

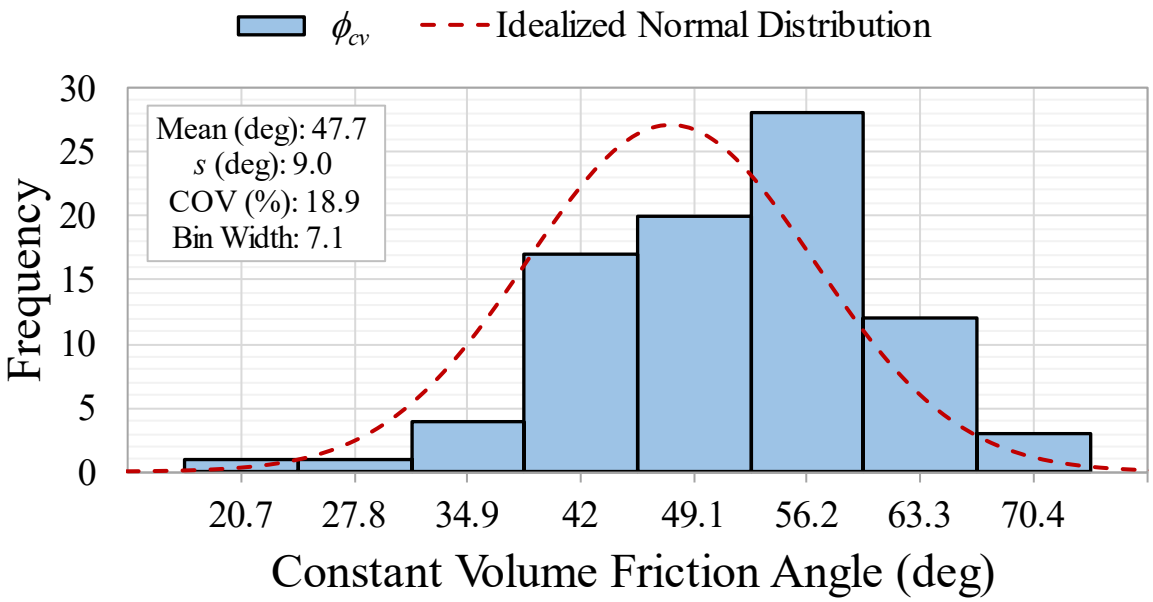

Source: FHWA.

Figure 43. Chart. Histogram for ϕ_{cv} with idealized normal distribution curve overlayed.

The normal probability plot for ϕ_{cv}, along with the predicted normal and lognormal distribution curves, are illustrated in figure 44. The data generally fit well with a normal distribution, except for two data points at the extreme lower tail; therefore, ϕ_{cv} can reasonably be captured by assuming a normal distribution. The AD normality test for ϕ_{cv} was based on the 86-point dataset and found a p-value of 0.70 (appendix E); this finding agrees with the observations found in the normal probability plot (figure 44). Therefore, ϕ_{cv} is normally distributed with $\bar{x} = 47.7$ degrees and $s = 9.0$ degrees.

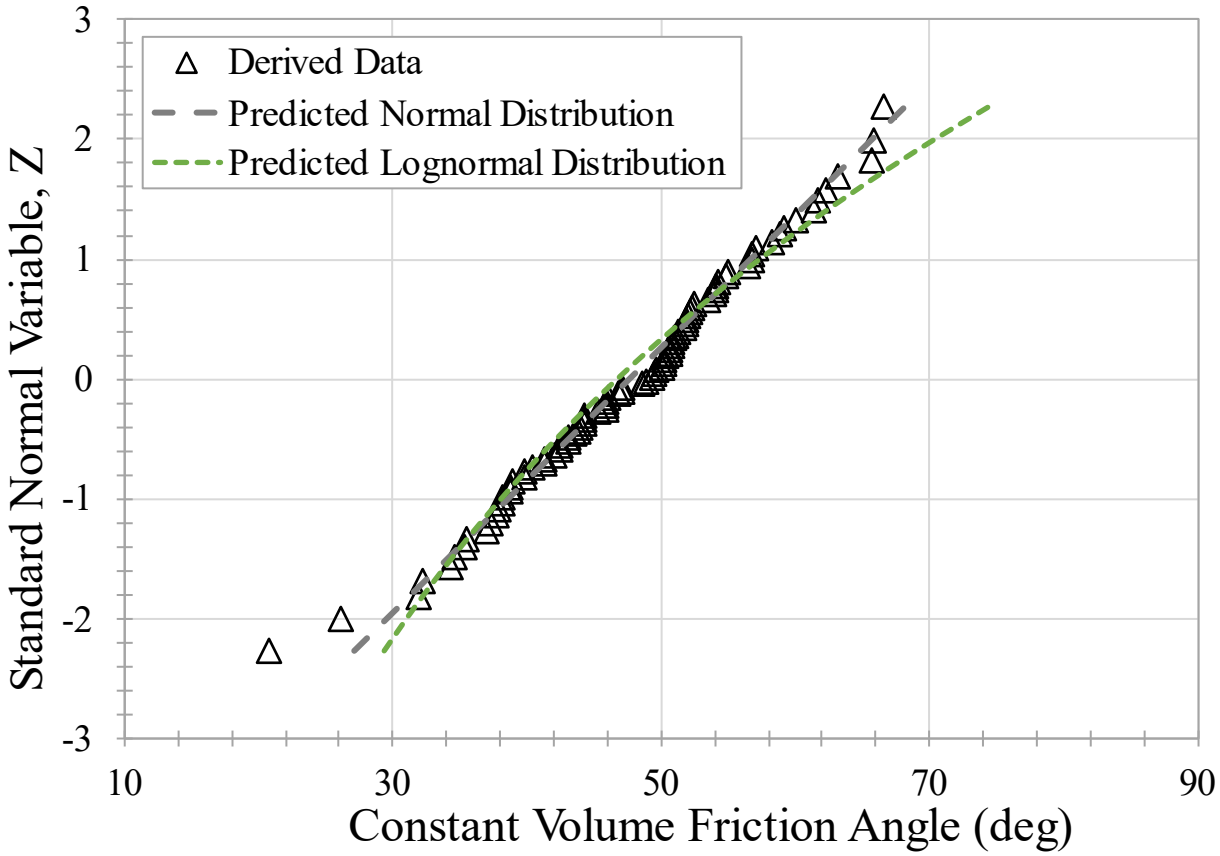

Source: FHWA.

Figure 44. Chart. Normal probability plot for ϕ_{cv}.

Maximum Dilation Angle

To evaluate the distribution of ψ_{max}, all of the values (table 25, table 28, and table 31) were combined over the range of σ_n values (i.e., 5 to 30 psi) into a single, 346-point dataset to determine the overall statistics of the parameter (table 33). Visual observation of the histogram for the combined ψ_{max} dataset (figure 45) suggests that ψ_{max} for all OGAs evaluated in this study are not normally distributed, with the data more skewed to the right. The descriptive statistics (table 33) indicate unequal mode, median, and mean with K_u and S_k indicating a relatively peaked distribution and positive skew, respectively.

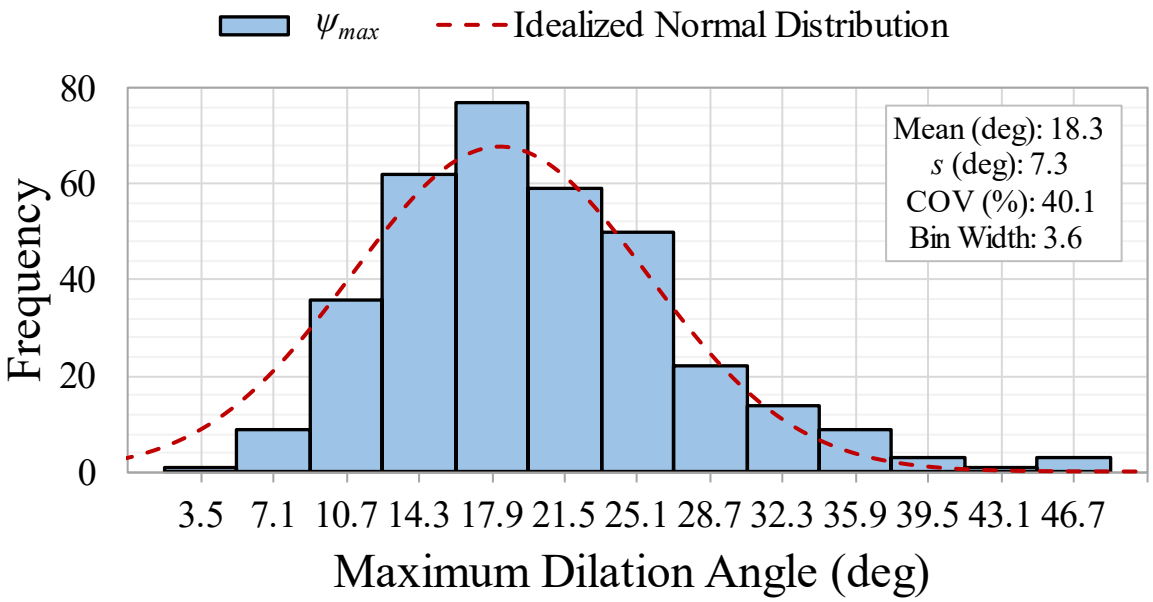

Source: FHWA.

Figure 45. Chart. Histograms for ψ_{max} with idealized normal distribution curve overlayed.

The normal probability plot for the combined 346-point ψ_{max} dataset, along with the predicted normal and lognormal distribution curves, are illustrated in figure 46. The results show that the idealized lognormal distribution fits better than the normal distribution, particularly at the lower tail of the data. The AD test results for ψ_{max}, however, demonstrate that ψ_{max} is not normally (or lognormally) distributed when all laboratories are considered (appendix E).

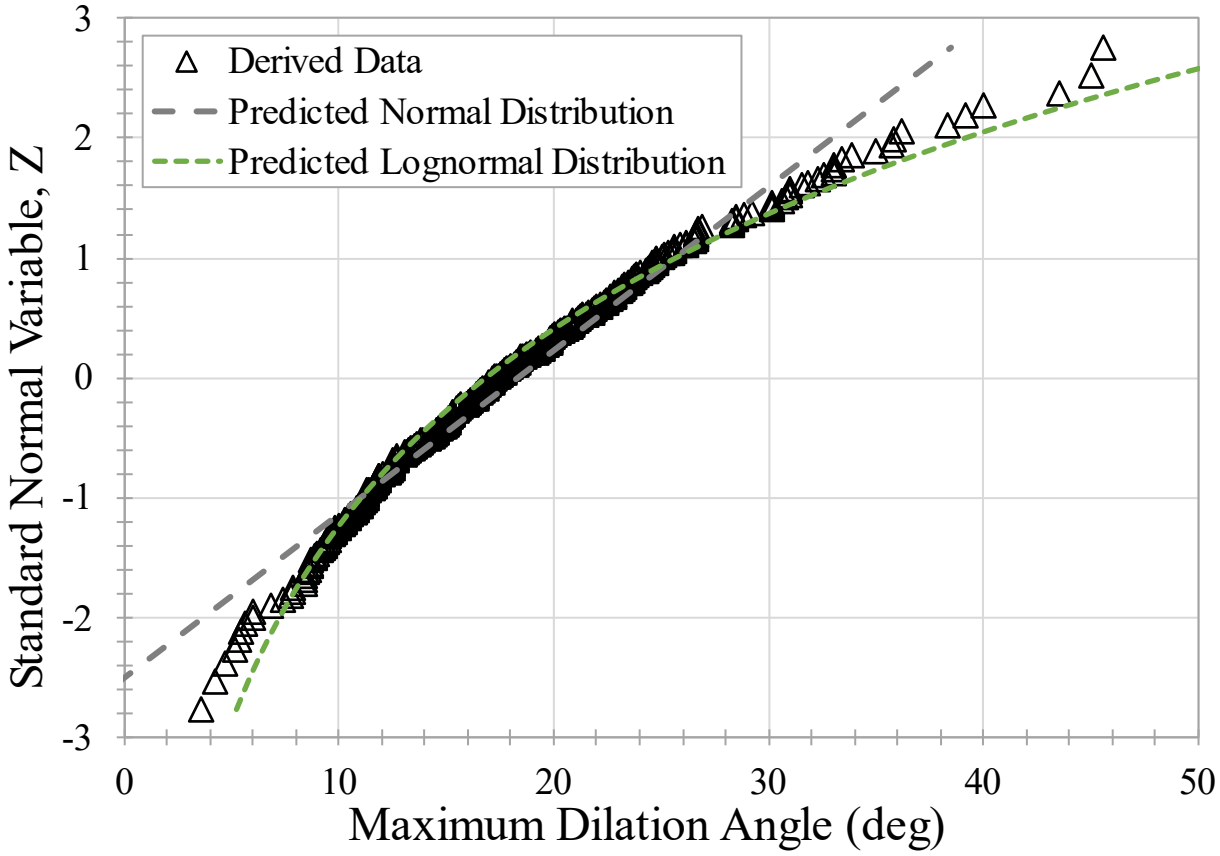

Source: FHWA.

Figure 46. Chart. Standard normal variable plots for ψ_{max}.

Further investigation of the data showed that ψ_{max} is highly sensitive to the *n*-point centered moving average selected (table 21), as evidenced by the elevated ψ_{max} values found by L03 and L04 (table 25, table 28, and table 31), which required no manipulation of the data (i.e., *n* point = 1) because of their low frequency of data collection. Separating the broader ψ_{max} dataset into laboratories where ψ_{max} was calculated using multipoint moving averages (i.e., L01, L02, L05, and L06) and laboratories where no data smoothing was performed (i.e., L03 and L04) resulted in normal behavior among both groups, with p-values of 0.621 and 0.076, respectively (appendix E). As such, ψ_{max} is best approximated by a normal distribution with $\bar{x}$ = 16.2 degrees and s = 5.4 based on the smoothed dilation data from L01, L02, L05, and L06. Notably, much like ϕ_s and ϕ_t, the nonnormality of the broader ψ_{max} and ϕ_s datasets is mitigated in the calculation of ϕ_{cv}.

Summary

The researchers made use of descriptive statistics and graphical approaches such as histograms and normal probability plots, along with more formal goodness-of-fit tests (e.g., AD) to evaluate the underlying distribution of the key physical properties and characteristics and shear strengths evaluated in the round-robin study. Based on that analysis, table 34 provides suggested

distribution types that reasonably fit the data best. Depending on the accuracy needed, higher order distribution types, such as Weibull and beta distributions, could be tested to evaluate their suitability.

Table 34. Summary of suggested statistics for key OGA design parameters.

Parameter	*n*	Distribution Type	$\bar{x}$	*s*
γ_{d95}+ (lb/ft^3)	54	Bimodal normal	101.4	2.9
	36		110.8	4.3
ϕ_s^ (degree)	180	Normal	67.1	7.1
ϕ_t (degree)	90	Normal	51.7	7.5
$\phi_{t,r}$ (degree)	90	Uniform	46.5	10.8
ϕ_{cv} (degree)	86	Normal	47.7	9.0
ψ_{max}* (degree)	226	Normal	16.2	5.4

+Statistics based on sedimentary/felsic mineralogy (top) and mafic mineralogy (bottom).
^Statistics based on the fixed upper shear box group.
*Statistics based on calculations with multipoint moving averages.

IMPACT OF STONE SIZE, MINERALOGY, AND LABORATORY

Within this round-robin study, the primary variables included stone size (i.e., No. 57, No. 68, and No. 8), mineralogy (i.e., BA, DI, GG, LI, and SI) and laboratory (i.e., L01–L06). Stone size and mineralogy relate to the inherent variability of the OGAs, while laboratory relates to the measurement variability. Each of these variables, whether alone or in combination with one another, can impact the resulting dry unit weights, friction angles, and maximum dilation angles.

The results suggested that stone size does play a minor role in the measured and computed parameters, as evidenced by the means and COVs for the key OGA parameters evaluated, such as γ_{d95}, ϕ_s, ϕ_t, $\phi_{t,r}$, and ϕ_{cv} (table 32). On average, the No. 8 OGAs resulted in lower values with slightly more variability compared to the larger No. 57 OGAs; for example, figure 47 shows the normal distribution curves for ϕ_t based on stone size. This general trend supports the previous findings by Nicks et al. (2015). Whether this fact is solely a result of stone size, the larger percentage of F&E particles for the No. 8 OGAs (table 16), or a factor of the ratio between stone size and LSDS box/cylinder size would need further evaluation.

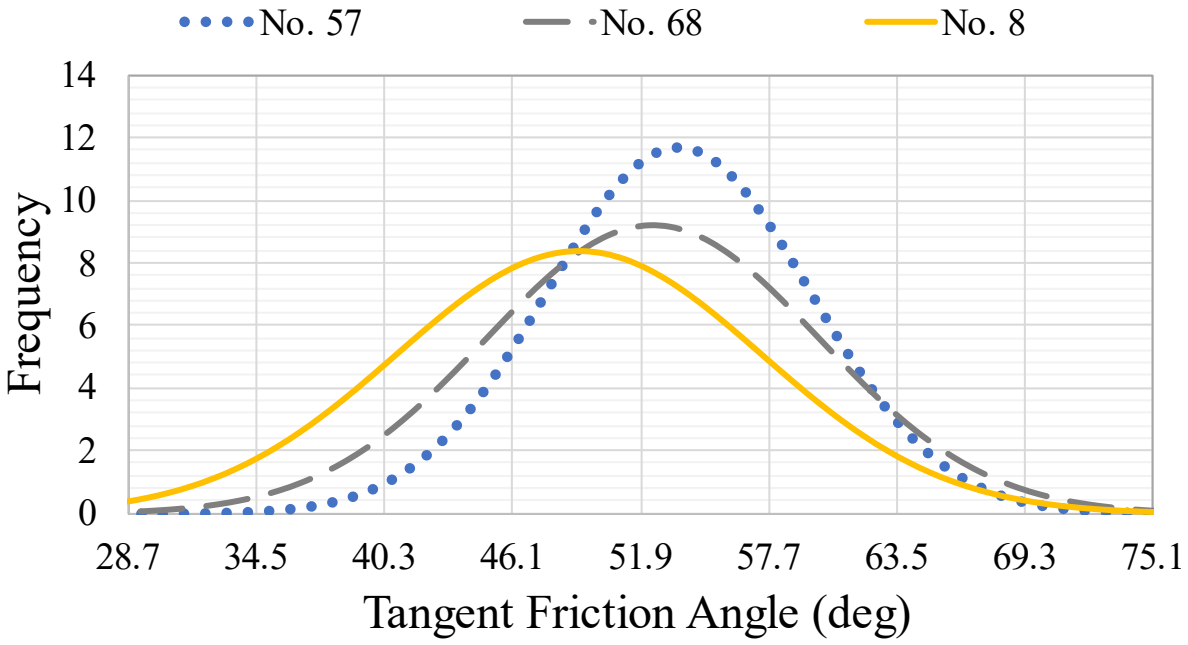

Source: FHWA.

Figure 47. Chart. Normal distribution curves for ϕ_t per stone size.

Similar to stone size, observations of the LSDS results (e.g., figure 48 and figure 49) suggest that mineralogy is not a significant factor in the strength variability found in the study. This finding is particularly notable given the previously discussed presence of two distinct clusters of bulk dry specific gravity and corresponding γ_{d95} values.

When the differences are compared in shear stress—horizontal strain behavior due to mineralogy, the variability of responses seems to be more pronounced for L05 and L06 (figure 48); however, the vertical—horizontal strain data show variability across the board (figure 49). Generally, the vertical—horizontal strain response appears to correlate with the peak shear stress. The samples with higher peak shear stress exhibited steeper dilation behavior, particularly for BA and SI mineralogy. The largest impact, therefore, appears to come from measurement variability, namely the differences in LSDS devices between the laboratories. The researchers performed an ANOVA on the LSDS results to statistically investigate the significance of the inherent variability (e.g., stone size and mineralogy) and measurement variability (e.g., different LSDS devices).

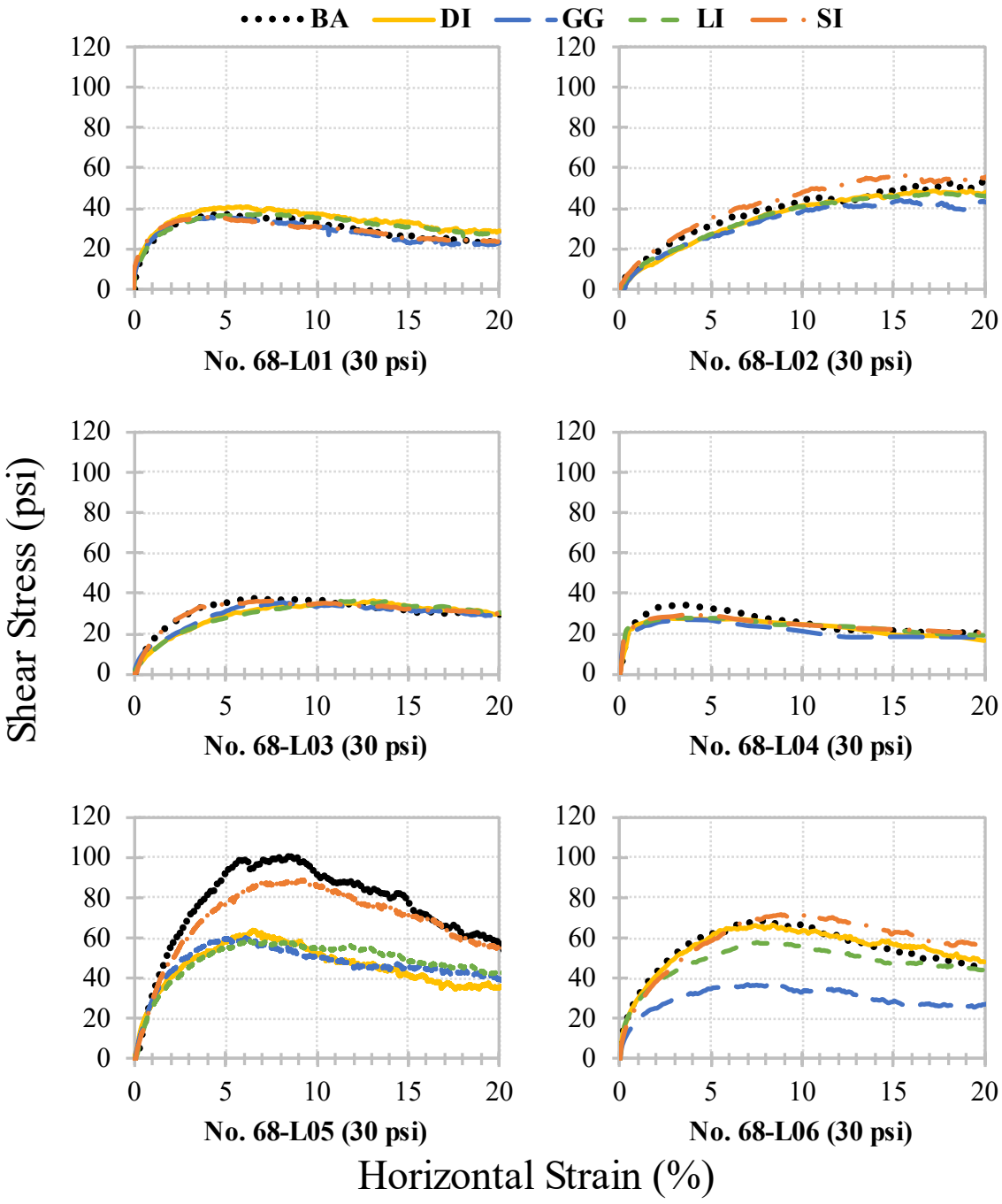

Source: FHWA.

Figure 48. Charts. No. 68 stress-strain curves by mineralogy for all laboratories.

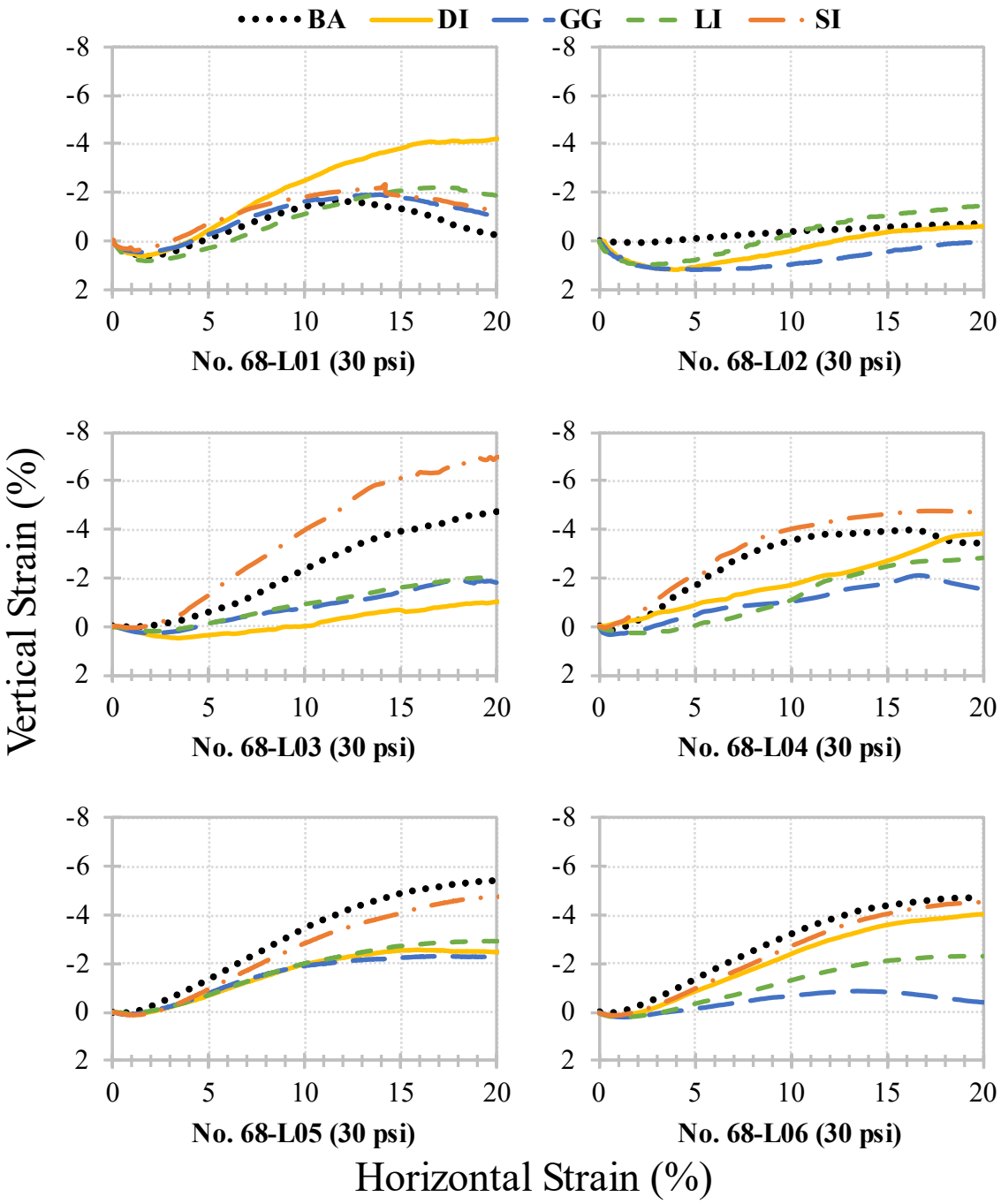

Source: FHWA.

Figure 49. Charts. No. 68 vertical-horizontal strain curves by mineralogy for all laboratories.

ANOVA is a common statistical analysis method used to compare the differences between the means of measurement data (Casella and Berger 2002). The following two factors were considered in the ANOVA analysis: Factor A—sample type (e.g., stone size and mineralogy); and Factor B—testing laboratory (e.g., LSDS device, operator). The two-factor without

replication ANOVA approach was employed to analyze the data (Zaiontz 2020). A three-factor ANOVA approach could have been employed instead, splitting the sample type factor into separate stone size and mineralogy factors; however, with the relatively limited dataset for those factors, combining them into one factor was considered reasonable by the research team.

As with the AD approach, an alpha of 0.05 was selected to determine *F*-critical thresholds. If the *F*-statistic of the target factor is less than the corresponding *F*-critical then the null hypothesis (H_0) is validated. In this case, H_0 states that no statistically significant influence on the physical properties and shear strength due to the considered factor (e.g., sample type or laboratory) exist. The alternative hypothesis (H_1) is that the examined factor is significant enough to impact the physical or strength parameter results of the OGAs. If the *F*-statistic exceeds the *F*-critical, then H_0 is rejected and H_1 is accepted. Summarized steps for computing the *F*-statistic and *F*-critical for each parameter evaluated, the full ANOVA results, and the procedures needed to ensure that the major assumptions for the two-factor ANOVA test were satisfied are provided in appendix E.

The ANOVA analysis indicates that H_0 was rejected for γ_{d95} whereby γ_{d95} was found to be statistically sensitive to both sources of variability (i.e., the sample type and the laboratory). However, the results suggest that sample type significantly outweighs the variability due to the laboratory performing the density test (appendix E). Similarly, the sample type and laboratory are also statistically significant sources of variability for every strength and dilatancy parameter except ϕ_{cv}, which was statistically impacted only by the laboratory performing the LSDS test (appendix E). Unlike the γ_{d95} ANOVA results, however, the laboratory performing the test plays a more profound role than the sample type for all strength and dilatancy parameters. Given the wide range of device characteristics within this round-robin study (table 6), it is not surprising that the laboratory performing the test plays a significant role in the variability found.

DS TESTING DEVICES AND PROCEDURES

The LSDS devices used by each laboratory in this round-robin study were all configured differently (table 6 and figure 6), yet most devices met the ASTM D3080 requirements dictating the size of the device relative to the size of the sample (ASTM 2011a). The exception was L05 and L06 where the diameter/width-to-thickness ratios deviated slightly from the minimum of 2:1 per ASTM D3080; both laboratories utilized a ratio of 1.6:1 instead. The impact of this diameter/width to thickness ratio, as well as other device characteristics and/or the associated test procedures, on the variability in the resulting strength-deformation characteristics reported in chapter 3 needs further investigation.

Box Shape

Four of the six laboratories had square-shaped LSDS boxes, one laboratory (i.e., L03) had a rectangular-shaped LSDS box, and one laboratory (i.e., L05) used a circular device; however, the nominal width/diameter of all specimens within the LSDS device were the same (i.e., 12 inches). There was no apparent difference in the measured shear responses of L03 and L05 that would indicate the nonsquare shape played a role. In fact, the results of L05 with a cylindrical device tended to most closely match the results of L06 which had a square device (e.g., figure 16, figure 17, figure 22, figure 23, figure 28, and figure 29). In terms of this study, particularly when

area corrections were not applied to the results, box shape alone likely did not play a role in the variability of the results.

Box Mobility

One of the most notable differences between the LSDS devices was the mobility of the upper shear box (i.e., restrained or unrestrained). The test devices from L01, L03, and L04 had mobile upper boxes that could theoretically move vertically during shear, while L02, L05, and L06 had fixed upper boxes (figure 6). The mobility of the upper box can also influence the gap size between the two shear boxes; a mobile box could allow the gap to fluctuate during shear, whereas a fixed box would result in a constant gap size during shear. In addition, larger frictional forces could develop between the specimen and the walls of the box due to the specimen's volume change during shear when the upper box is fixed versus mobile due to the restraint (Shibuya et al. 1997; Lings and Dietz 2004; Liu et al. 2005). These frictional forces could then result in a larger imposed vertical stress at the shear interface not captured by the load cell at the top of the specimen measuring the applied normal load; therefore, the reported friction angles from devices with a fixed upper box would be higher than those from devices with a mobile upper box. This hypothesis could potentially explain the higher reported values of shear strength parameters for the laboratories with a fixed upper box in this study (i.e., L02, L05, and L06) as shown in table 24, table 27, and table 30 from chapter 3.

In addition, ϕ_s does not follow normal or lognormal distribution curves when all laboratories are combined (figure 38); however, by grouping the datasets according to box mobility, normal behavior was clearly found (appendix E). The differences between the laboratories with fixed versus mobile upper boxes is also clearly reflected in the strength-dilatancy relationships for all the OGAs evaluated in this round-robin study (figure 50). Devices with a fixed upper box exhibited relatively low scatter when grouped together (i.e., $R^2 \approx 0.4$), resulting in a ϕ_{cv} of 55.3 degrees. In contrast, the strength-dilatancy relationship for laboratories with mobile upper boxes has excessive scatter (i.e., $R^2 \approx 0.08$) and resulted in a lower ϕ_{cv} of 47.0 degrees.

The coefficients (i.e., slopes) relating secant friction angle to maximum dilation angle were also different between fixed (i.e., 0.75) and mobile (i.e., 0.18) upper boxes (figure 50). Based on the strength-dilatancy relationships found for different dense sands in axisymmetric and plane strain conditions, Bolton (1986) suggested a coefficient of 0.8 between secant friction angle and maximum dilation angle (i.e., $\phi_s = \phi_{cv} + 0.8\psi_{max}$). This coefficient also roughly estimated the LSDS strength-dilatancy of OGAs from an earlier FHWA study (Nicks et al. 2018). The OGA results from fixed upper boxes in this round-robin study fit well with this past work, lending further credence to that device characteristic; however, further research is needed to fully investigate the impact of box mobility and its influence on aggregate behavior during LSDS testing.

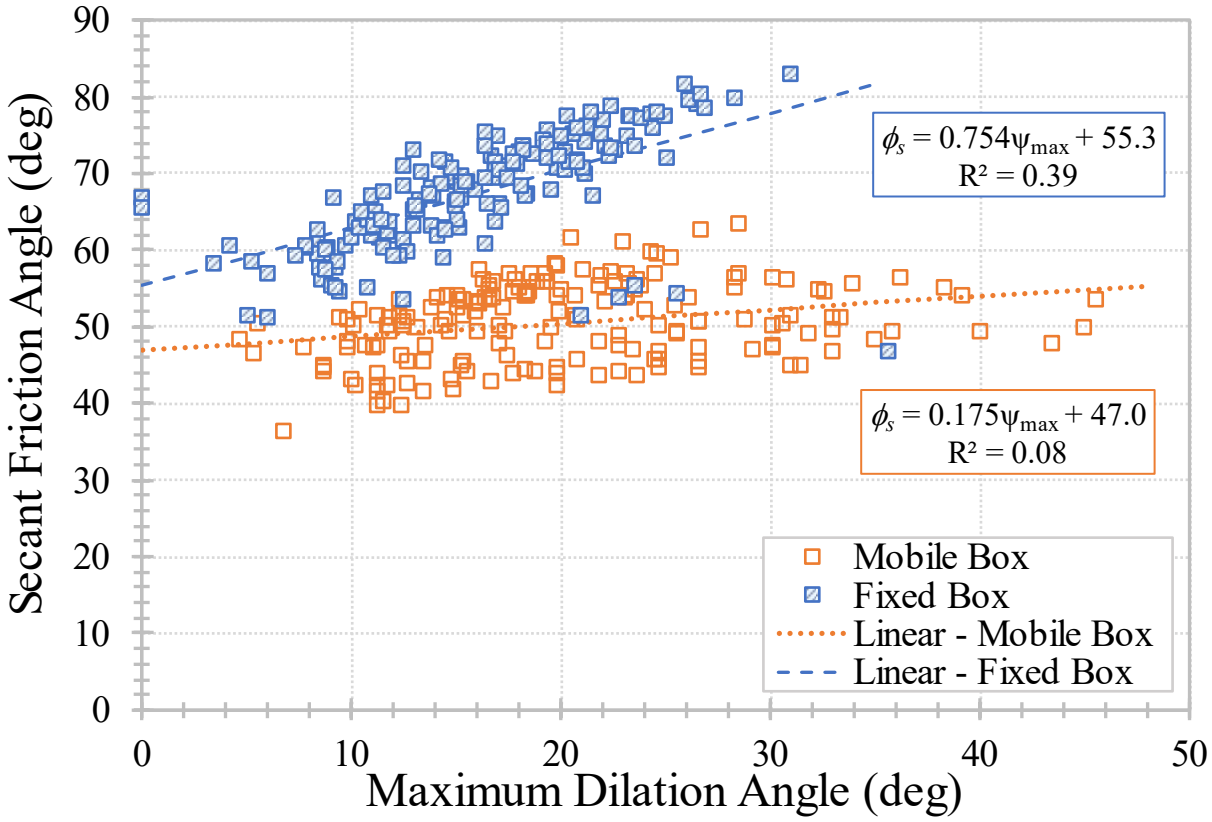

Source: FHWA.

Figure 50. Chart. Impact of box mobility on the strength-dilatancy relationship.

Base of the Loading Platen

The base of the loading platen is in direct contact with the sample and can be smooth, grooved, or textured (figure 51). The base boundaries for L01, L05, and L06 are smooth, L02 and L03 are grooved, and L04 is textured; the exact details of the grooved and TX platens used are unknown. The impact of the base boundaries has not been investigated for LSDS devices; however, Kittu and Bernhardt (2017) investigated this factor in standard DS testing and found that the boundary of the platen base seemed to have minimal impact on the soil behavior during shear and the resulting friction angle. It is, therefore, difficult to specifically state the effect of boundary textures on the testing devices considered in this study. Two of the three laboratories with smooth boundaries produced results having the highest shear strength. However, other factors involved (e.g., box mobility) might explain those results. Further investigation isolating the boundary's impact would need to be performed for LSDS testing to determine the influence on the overall response of OGAs during shear.

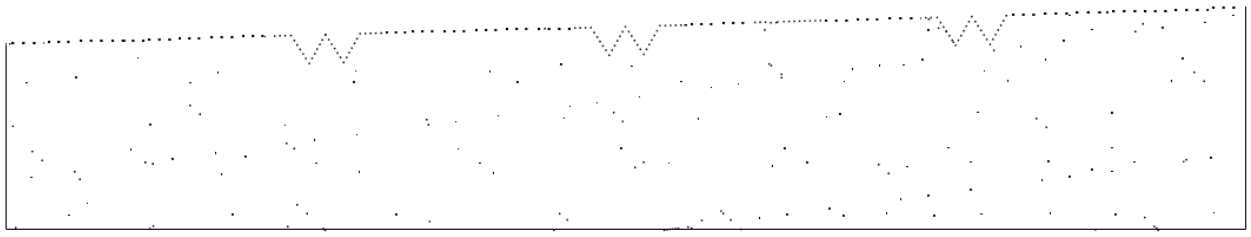

Source: FHWA.

A. Smooth base.

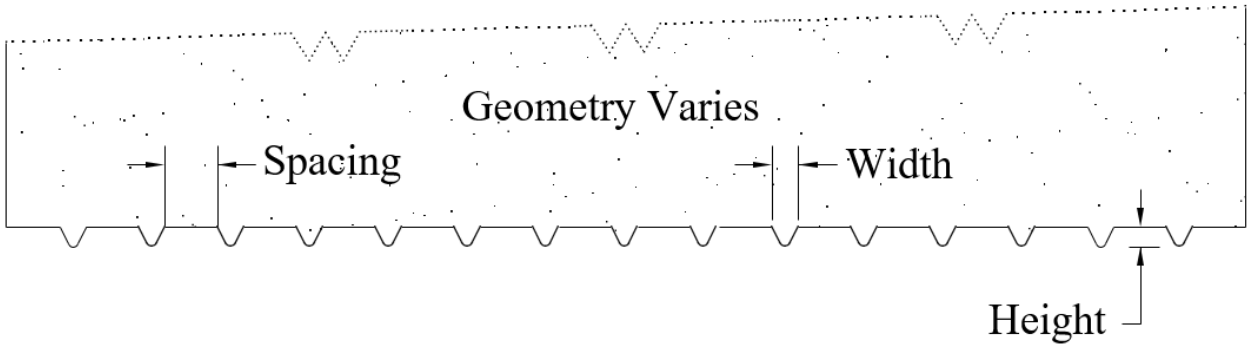

Source: FHWA.

B. Grooved base.

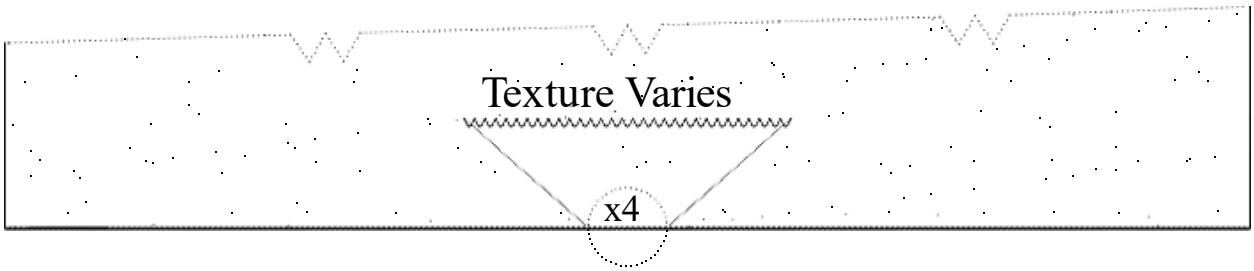

Source: FHWA.

C. Textured base.

Figure 51. Illustrations. Types of loading platen bases.

Connection Between the Load Platen and Normal Load

The nature of the connection between the load platen and the normal load application (e.g., fixed or hinged) is another potential source of variability. Fixing the platen to the normal load, as done by L01, L04, and L05, should eliminate any tilting of the platen that may occur during shear. The use of ball bearings instead, as done by L02 and L06, could allow for rotation of the platen as the sample shears. Note that L03 is unique because the normal load was applied by either dead weight or an airbag dead weight would theoretically limit any tilting, whereas an airbag might allow tilting. The impact of this connection could not readily be discerned with the dataset, but the impact of platen tilting, and the resulting change in normal pressure distribution across the sample, needs further research.

Specimen Versus Box Dimensions

For all laboratories, the specimen dimensions were different from the box dimensions (table 6). Spacers were used by L01, L02, and L04 to limit the sample height within the box to 6 inches. No spacers were needed for the L03 device. The use of spacers served to reduce the amount of aggregate required for testing while meeting the ASTM D3080 requirements (i.e., the minimum specimen diameter/width -to- thickness ratio of 2:1). On the other hand, L05 and L06 both had the tallest specimens at 7.5 inches, leaving a 0.5-inch inset for the load platen within the upper box (or cylinder in the case of L05). The 2:1 ratio for specimen width to thickness per ASTM D3080 was, therefore, not met by L05 and L06; however, considering that the height of aggregates above and below the shear zone is nearly equal for all laboratories, the effect of this height difference could be minimal.

Another difference in specimen versus box dimensions was found for L03. Unlike those for the other laboratories, the lower box of L03 was larger than the upper box by 3 inches (table 6). The rationale for this device configuration is to ensure a constant contact area throughout shear, eliminating any need for area corrections. The impact of this factor on the results is not readily apparent; therefore, additional testing isolating this device characteristic is needed.

Vertical Displacement Measurements

ASTM D3080 requires measurement of both horizontal and vertical displacements throughout the test; however, not all participant laboratories routinely measured vertical displacement as part of their standard practice (i.e., L02 and L04). For example, L02, which had routinely used an airbag to distribute the vertical load to the specimen, retrofitted its device between rounds one (i.e., DI) and two (i.e., LI) to switch from the airbag to hydraulic pressure. The retrofitting then allowed for vertical displacement measurements. This change created some issues; L02's retrofitted LVDTs often bottomed out, leading to plateauing of its vertical displacement results (e.g., figure 17). Anomalous compression of the sample was also reported for No. 57-LI-L02 at 15 and 30 psi (figure 17); this result may be an error in the sign convention of the LVDT measurements, but without confirmation, the data were reported as is. Ultimately, this anomaly highlights the potential errors that can occur in measuring and reporting vertical displacement data.

The number and locations of vertical displacement measurements using LVDTs were also different. L01 and L06 used four LVDTs located close to the four corners of the square shaped load platen, with the average reported. The remaining laboratories had fewer LVDTs (table 6) and located them around the platen's center; the average vertical displacement was reported if there was more than one LVDT.

Application of Normal Load

The method of applying and measuring the normal loads/pressures is another source of differences between the laboratories. The different methods primarily influence the distribution of the load/pressure to the shear plane and the consistency in load/pressure throughout the duration of the test. The methods of applying the load/pressure in the study included dead weight, an airbag, hydraulic load, and a microstepper motor (table 6). Dead weight, used by L03

for the lower normal stresses (i.e., 5 and 10 psi), is considered the most accurate but is generally applicable only at lower target normal stresses due to the difficulty and danger of stacking large weights. Airbags, used by L02 in round one (i.e., DI) and L03 for higher normal stresses (i.e., 15 and 30 psi), are considered next best in the sense that the pressure is more evenly distributed across the surface of the sample; however, there were no noticeable differences in shear response between the tests with an airbag and the other methods of normal load application for L02 and L03. Hydraulic and microstepper motors are also capable of applying loads with accuracy; however, depending on the rotation of the load platen (i.e., fixed or hinged), stresses may redistribute across the surface of the sample during testing. In addition, the fixity of the upper box may result in more load reaching the horizontal shear plane due to the frictional forces along the sidewalls, as discussed in the Box Mobility section. These aspects were not explicitly evaluated in the round-robin study but may be sources of potential variability in the results.

Regardless of the method of normal load application, the consistency in load/pressure throughout the duration of the test is another factor. For example, L04 set the target normal pressure at the start of their tests and manually adjusted, as needed, based on the digital readout. Unfortunately, the pressure measurements throughout the duration of the test were not supplied by L04, limiting evaluation of any changes. Similarly, real-time normal pressure data were absent for L02, leading to uncertainty about its consistency throughout shear testing. The unique shear stress—horizontal strain results from L02 whereby the curve never reaches a distinct peak could potentially be a result of such inconsistent normal stresses during testing; however, there is no way to verify one way or the other for the purposes of this study. The other laboratories, save L03 when using dead weight, had automated normal loading systems. Based on the results from this study, no obvious trend that shows an increase or decrease in stress-strain and/or dilation response in relation to one of these identified factors exists.

Data Collection Frequency

All laboratories satisfied the minimum data readings in accordance with ASTM D3080; however, there was a big difference in the amount of data collected per test. The amount of data collected ranged from close to 10,000 data points for L05 to 33 data points for L04. The typical time step, or frequency, for data collection for each lab is shown in table 6. The frequency of data collection has an impact on the degree of smoothness of the stress-strain curve and the vertical-horizontal strain curves. As indicated in table 21, different *n*-point centered moving averages were used to achieve a similar degree of data collection frequency among the vertical and horizontal deformation measurements. Without this approach, the computed dilation angles varied significantly simply due to the distance/time between data points. The approach also had an impact on the distribution of the ψ_{max} dataset, which did not fit predicted normal nor lognormal distributions according to the AD tests (appendix E). Normality was found by separating the broader ψ_{max} dataset into laboratories where ψ_{max} was calculated using multipoint moving averages (i.e., L01, L02, L05, and L06) and laboratories without any data smoothing (i.e., L03 and L04) (appendix E).

Setting the Shear Gap

Per ASTM D3080, after consolidation of the specimen, the shear box halves should be separated to create a gap (i.e., D_{85} in this study) before shear is initiated; however, there was inconsistency

in this practice among the laboratories (ASTM 2011a). L01, L05, and L06 applied the shear gap after consolidation, L02 and L03 before consolidation, and L04 before sample placement. The primary reason for L02, L03, and L04 setting the gap earlier was the configuration of their LSDS devices; the devices did not allow for setting the gap during the test. Setting the shear gap before the consolidation phase may have an impact on the aggregate behavior during shear and thus the results.

When establishing the gap before sample placement, as in the case of L04, side flow of the aggregates within the gap and/or weakening in the shear plane may occur during compaction. This gap setting procedure could potentially be a reason for their unique and consistent results for exhibiting early failure, although this idea needs further investigation (e.g., figure 18, figure 24, and figure 30). There was no clear trend in shear response associated with whether the shear gap was applied before or after consolidation in this study. Of note, however, is that relatively large tensile loads were registered for L06 as a result of setting the gap post-consolidation (see appendix D). While these initial loads were "zeroed out" in the data reduction approach employed in this study, the influence of those tensile loads needs further investigation. Initial shear stress values before the shear phase ($\tau_{initial}$) for all performed LSDS tests are reported in appendix D.

Specimen Compaction

To maintain consistency between the laboratories, test instructions were prepared outlining the sampling procedures and compaction requirements before testing (appendix A). The target density for compaction was specified as γ_{d95}, which, based on the results from the round-robin study, had low variability across the laboratories (see table 10 through table 12). The compaction of the aggregates was performed in three lifts by all laboratories, except for L05 and L06, which compacted the stones in five lifts. All laboratories besides L02 hand tamped the OGAs (and OS-20-30) to the target density during sample compaction. L02 vibrated its samples to the target density, and it is not clear how this process may factor into the overall response of the aggregates during shear, provided the target density was still achieved. A distinct difference in the stress-strain behavior and the volumetric response of the samples, however, was found in the results produced by L02, despite sharing similar features with L05 and L06. Specifically, the stress-strain curves from L02 exhibited ductile behavior compared to the more brittle responses found by L05 and L06. Further evaluation on the impact of the compaction procedure, particularly the uniformity of density throughout the specimen, is therefore warranted.

Test Reports Versus Analyzed Data

The test reports submitted by the laboratories for both the physical and mechanical tests were carefully examined to verify the accuracy and reliability of the data. A few irregularities were identified on some reports and subsequently corrected before analysis. This finding of irregularities highlights the fact that users requesting LSDS tests should independently verify (i.e., spot check) the results in the test report. It is also important to note that test reports typically provide the results as is without any corrections or manipulations (e.g., zeroing out of the initial shear stress, zeroing out of the initial vertical displacement measurement, area corrections, etc.) included. These corrections and manipulations can all impact the resulting friction angle(s) measured versus reported.

Sometimes what is not included in the test report is also important. Data from the consolidation phase, normal load/pressure versus time, and data from each LVDT (if more than one) are not commonly included, yet this information can prove valuable in the context of interpreting LSDS results. In addition, details about the LSDS device (e.g., upper box mobility, smoothness of the platen base, connection between the normal load and the platen, specimen versus box dimensions, etc.) are often absent in the test reports; however, given the broad range of LSDS devices available around the country, and their significant impact on the results, these details may be essential to note or verify with the laboratory.

DESIGN IMPLICATIONS

In the *AASHTO LRFD Bridge Design Specifications*, which govern most highway geotechnical structures, the resistance factors for each design model (e.g., bearing resistance, sliding, etc.) have been either empirically or statistically calibrated (AASHTO 2020). The variability of the design parameters within each model (e.g., unit weight, friction angle, etc.), however, are not individually accounted for in those calibration efforts. By including the variability of geotechnical design parameters, the reliability of each design equation can be better defined. When OGAs are used as a structural backfill, the basic statistics (table 33) and suggested distribution type (table 34) defined for each parameter found through this round-robin study could then be used as inputs in future resistance factor calibration efforts for geotechnical design models. Similarly, AASHTO (2020) provides permanent load factors for the vertical pressure from the dead load of earth fill (i.e., EV) and the horizontal earth pressure load (i.e., EH); however, those factors were developed for traditional soils. Similar efforts could be employed to calibrate OGA-specific load factors if needed.

To highlight the impact of parameter variability on geotechnical design, consider a simple example of calculating the σ_h due to a dry OGA backfill behind a vertical retaining wall with a level backslope (equation 7).

$$\sigma_h = \gamma z K_a = \gamma z \left(\frac{1 - \sin \phi}{1 + \sin \phi}\right) \tag{7}$$

Where:

γ = the unit weight of the aggregate, assumed to equal γ_{d95} for this example.
z = the depth below the top of the retaining wall.
K_a = the active earth pressure coefficient based on the friction angle (ϕ) of the aggregate, assumed to equal ϕ_t for this example.

The depth (z) can reasonably be assumed as a deterministic value; therefore, equation 7 includes two variable parameters (i.e., γ and ϕ). To approximate the COV of the lateral pressure using the known statistical results (table 33) of the design parameters (i.e., γ_{d95} and ϕ_t) based on the overall datasets, the delta method was adopted (Casella and Berger 2002). The results of this analysis indicated that the COV of the design model (equation 7) is around 42 percent compared to COVs of 5.5 and 14.5 percent for γ_{d95} and ϕ_t, respectively. This model variability would change if the parameter statistics changed. For example, if the specified OGA was known to be a LI, then the statistics of γ_{d95} could be based on the bimodal normal distribution for lighter sedimentary

mineralogy instead (table 34). This change would result in a lower COV for the design model. This propagation of errors is important to consider when calibrating design models.

In that example, ϕ_t was used; however, another friction angle (e.g., secant, residual tangent, or constant volume) could be substituted, depending on the design situation. Note that by substituting a different friction angle, the statistics of that parameter would thus change the variability of equation 7. The decision on which friction angle to use in design remains. As mentioned in chapter 3, the design requirements for a project, plus engineering judgment, will often determine which friction angle to use to evaluate τ. For instance, if the applied loads are well defined and not expected to change throughout the design life of the structure, then use of a secant friction angle determined from a single LSDS test under that applied normal load may be appropriate. When the loads are more uncertain or may change across the design life of the structure, then use of a tangent friction angle determined through a three- or four-point LSDS test under a reasonable range of applied normal loads may be appropriate. This method mitigates the influence of LSDS device design on ϕ_s. Note that the findings from this round-robin study suggest that the secant friction angle determined at the highest σ_n in the range specified to determine the tangent friction angle gives similar values between the two, regardless of the LSDS device used (figure 52). In other words, the tangent friction angle could perhaps be defined solely by conducting a single LSDS test at the highest normal stress that would have been specified and then simply determining the corresponding secant friction angle; however, further research is needed to validate this potential finding.

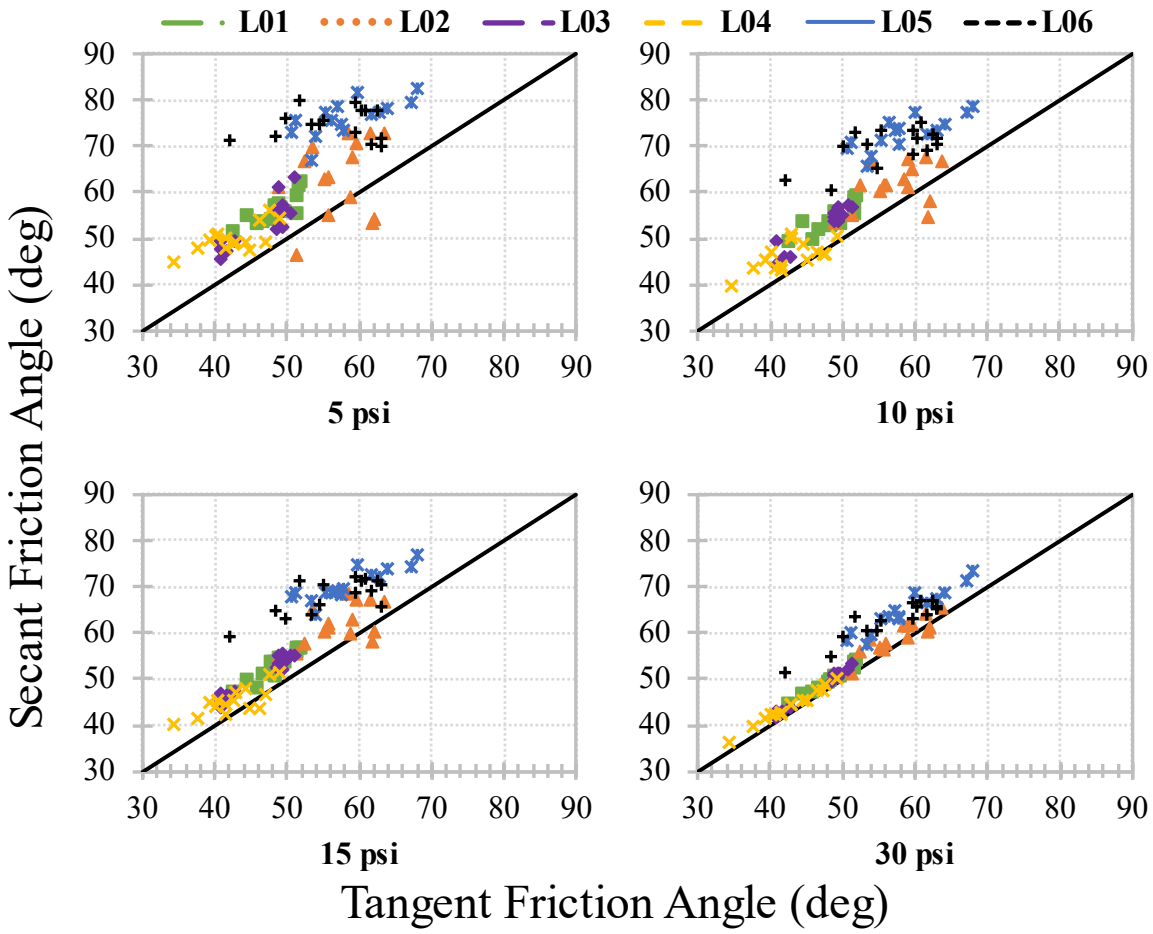

Source: FHWA.

Figure 52. Charts. Comparison of ϕt and ϕs.

The residual friction angle is often used when large deformations are expected in the design, such as in areas with slope stability concerns or in areas of seismic activity. Constant volume friction angles represent the critical state, or the lower bound of shear resistance; their use may be appropriate when the structure behaves with Poisson's ratio near 0.5 (e.g., geosynthetic reinforced soil) and/or when lateral deformations need to be similarly controlled. Generally, ϕ_{cv} should be close, if not slightly greater than, $\phi_{t,r}$; the results of this study showed this general relationship (figure 53), albeit with some variability.

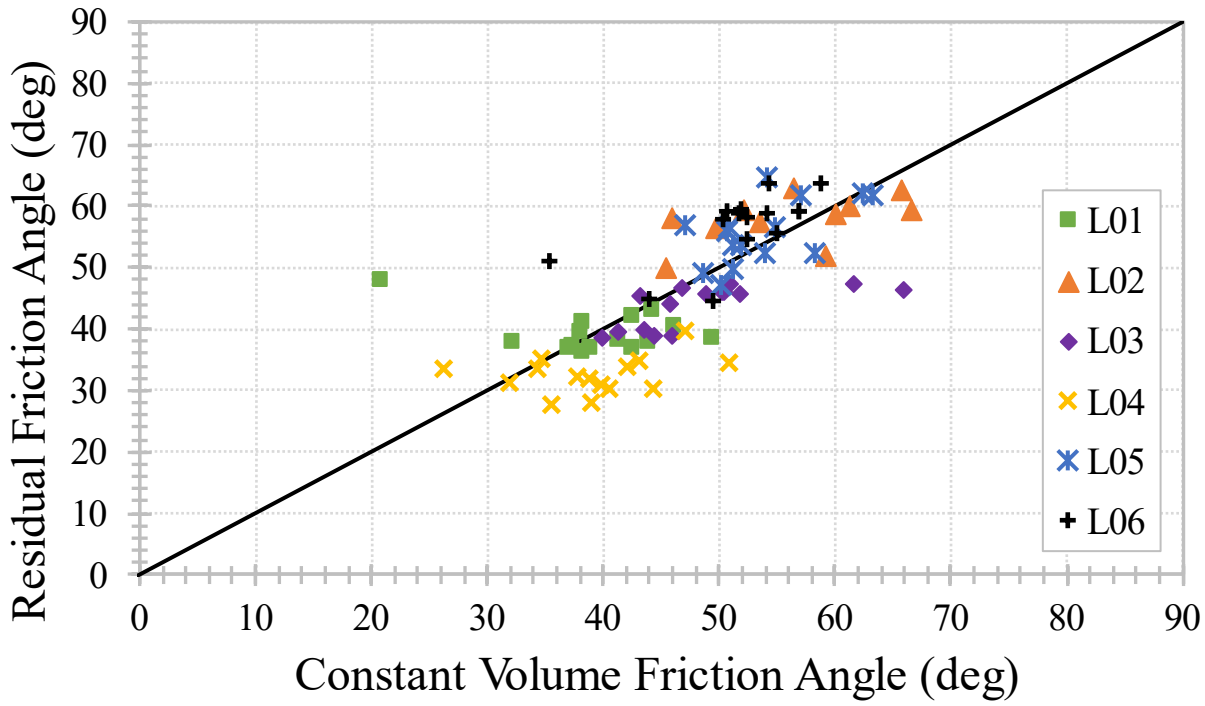

Source: FHWA.

Figure 53. Chart. Residual versus constant volume friction angle.

To extrapolate the cumulative distributions of the design parameters evaluated (based on the 90-point dataset collected in this study), Monte Carlo simulations can be performed based on the mean, standard deviation, and distribution type (table 33 and table 34). For example, 10,000 data points were generated using the Monte Carlo method for γ_{d95} and ϕ_t to evaluate their extrapolated (normal) cumulative distributions (figure 54 and figure 55). Note that the combined γ_{d95} dataset was simulated using a normal distribution for illustrative purposes only. Additional simulations are plotted to illustrate the influence of OGA specific gravity and box fixity on γ_{d95} and ϕ_t, respectively. Note that OGAs with G_{sb} less than 2.8 are considered "lightweight," while OGAs with G_{sb} greater than 2.8 are considered "heavyweight" (within figure 54). These extrapolated cumulative distributions could then be used to evaluate the probability of exceedance for any proposed OGA design value. In the examples for γ_{d95} and ϕ_t, 95.6 lb/ft^3 and 39.1 degrees, respectively, represent values that have a 95 percent probability of exceedance (i.e., only a 5 percent chance that values smaller than those would be found).

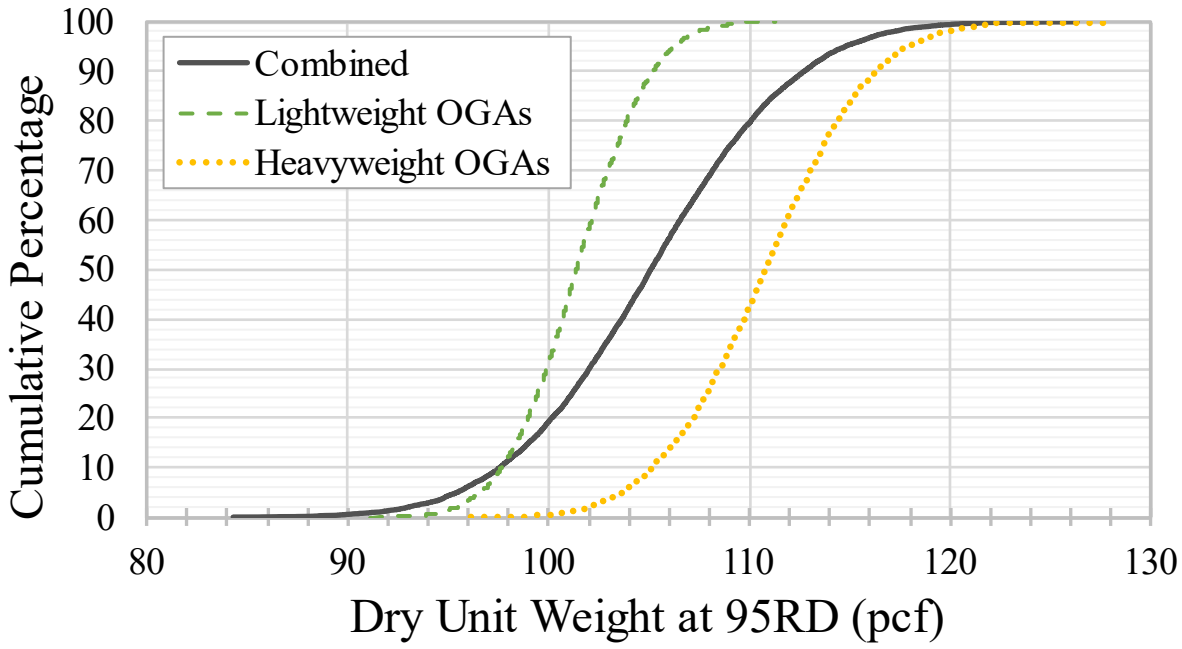

Source: FHWA.

Figure 54. Chart. Extrapolated cumulative distributions for dry unit weight at 95RD.

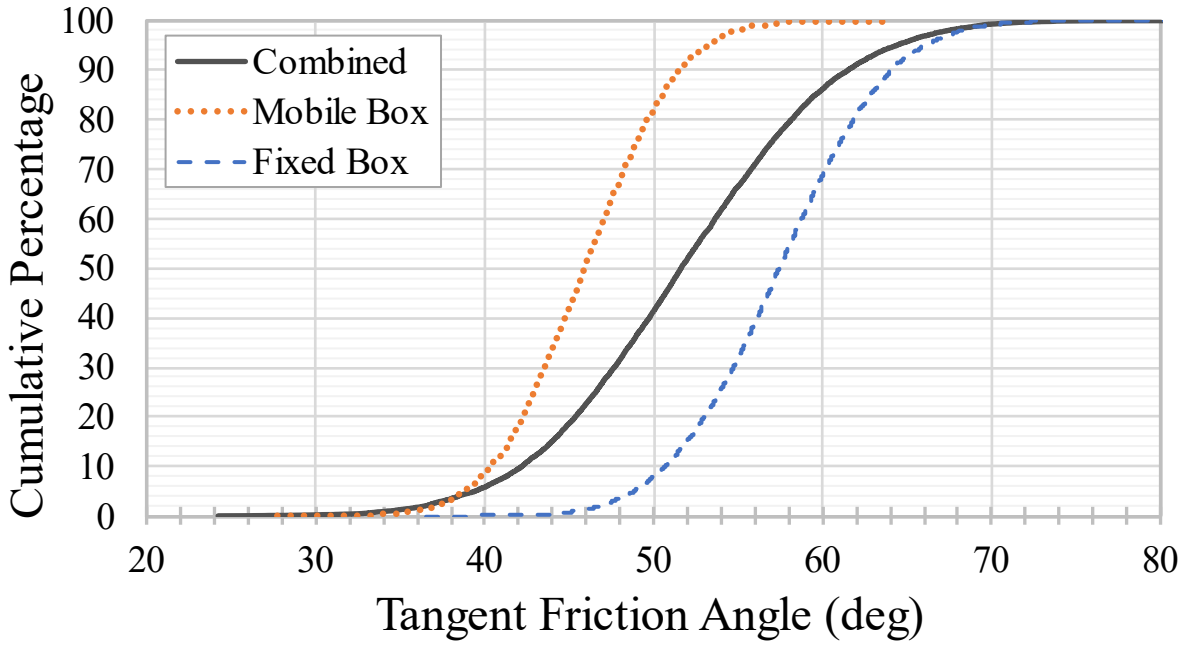

Source: FHWA.

Figure 55. Chart. Extrapolated cumulative distributions for tangent friction angle.

CHAPTER 5. CONCLUSIONS

FHWA initiated a six-laboratory round-robin study to evaluate the variability of physical properties and characteristics and shear strength for three common OGA gradations (i.e., No. 57, No. 68, and No. 8) from five different rock sources (i.e., BA, DI, GG, LI, and SI). In total, 90 OGAs were evaluated as part of this study. OS-20-30 was also included as a standard soil for further comparison. Testing for physical properties and characteristics by each laboratory included sieve analysis (both on the as-received samples and the post-shear tested samples) and minimum and maximum dry density testing (chapter 2). In addition, FHWA performed AIMS2 and Micro-Deval testing (chapter 2), with bulk dry specific gravity, L.A. Abrasion, and magnesium sulfate soundness results provided directly by the source quarries (chapter 3). LSDS testing was then performed by each laboratory (chapter 2) to determine the τ of the OGAs (and OS-20-30), namely the strength-deformation characteristics. Test instructions were provided to each laboratory to ensure consistency during sample preparation and testing (appendix A).

The key results from all tests (chapter 3), alongside further quantitative statistical analyses (chapter 4), provided insights into the degree of interlaboratory variability of the physical and strength parameters of OGAs and the factors impacting these parameters (e.g., stone size, mineralogy, and laboratory). A summary of the basic statistics (e.g., mean, standard deviation, and COV) for each OGA (and the entire dataset, as applicable) are provided in table 32. Understanding this variability is important for designers to assess more reasonable values for geotechnical designs, agencies in the development of material specifications, contractors in their selection of structural backfills, and researchers to evaluate the reliability of various design methods and to calibrate load and resistance factors in the framework of LRFD. Additionally, the results of this study suggest that modifications to ASTM D3080 are needed when aggregates are tested. A summary of the key results and findings from this study is provided in the following subsection below.

GRADATION

Key findings related to gradation include the following:

- The sieve analysis (appendix B) indicated many of the delivered OGAs were not compliant with the AASHTO M 43 size specifications (table 7); however, this finding was based on only one sieve test per laboratory.

- The interlaboratory variability of D_{85} was relatively low, with COVs ranging, on average, between 2.7 percent for the No. 8 OGAs and 7.5 percent for the No. 57 OGAs (table 8). The low variability in D_{85} suggests that similar gap sizes were set in LSDS testing by each laboratory.

- The breakage index (B_I) was computed by comparing the post-shear with the initial gradations (table 9); the largest variability in breakage occurred for the No. 57 OGAs, with an average COV of 65.7 percent.

- The B_I potentially provides insights on the LSDS devices used and the impact that crushing may have had on strength-deformation characteristics. For example, L03 and L04 generally demonstrated the highest B_I values and had lower friction angles than L05 and L06, which had the lowest B_I values (table 9).

DRY UNIT WEIGHT AND BULK DRY SPECIFIC GRAVITY

Key findings related to the dry unit weight and bulk dry specific gravity include the following:

- Researchers used three different methods to measure unit weight (chapter 2); however, the low variability of γ_{d95} within individual sample types (maximum COV of 3.1 percent) suggests that compacted OGA density was not sensitive to the device or test procedure.

- Researchers found the variability in γ_{dmin} and γ_{dmax} for OGAs to be similar to the variability other researchers found for poorly graded sands (table 1).

- Variability of γ_{d95} between sample types was significant, despite low variability within each stone size-mineralogy combination. Compacted unit weight is heavily influenced by the bulk dry specific gravity (table 13) and thus the mineralogy of the stones; BA and DI OGAs are significantly denser than LI and GG.

- The distribution of the entire γ_{d95} dataset was not normal. However, two overlapping normal distributions were revealed when the lighter, felsic metamorphic (i.e., GG) and sedimentary mineralogy (i.e., LI and SI) were normality tested separately from the denser, mafic igneous mineralogy (i.e., BA and DI).

- The two-factor ANOVA analysis found that γ_{d95} was significantly dependent on the sample type and, to a lesser degree, the laboratory performing the test (appendix E). The laboratory variability found by ANOVA is a product of ranking within the data. L02 and L06 routinely found the highest γ_{d95} values; meanwhile, L04 and L01 consistently found the lowest. This aspect of variability is not captured in the COVs of γ_{d95}.

PARTICLE SHAPE CHARACTERISTICS

Key findings related to the particle shape characteristics include the following:

- AIMS2 tests were performed by FHWA to evaluate the particle characteristics such as angularity, SP, F&E particles, and TX (appendix C).

- The angularity index was classified as low for all OGAs evaluated (and the OS-20-30) (table 14). This low classification is contrary to the expectation that a crushed, manufactured rock is angular. Since AIMS2 classifications were developed for pavement materials, there may be a need to update those classifications for structural backfills.

- The SP index was designated as medium for all OGAs (table 15); however, when the F&E values were evaluated (table 16), it was found that the No. 8 had the largest percentage of F&E particles, while No. 57 had the lowest percentage.

- Texture was noticeably dependent on mineralogy, unlike the other shape factors (table 17): SI OGAs consistently had the lowest TX index (classified as medium), while GG OGAs exhibited the roughest TX index (classified as high).

PARTICLE DURABILITY

Key findings related to particle durability include the following:

- Particle durability was evaluated through Micro-Deval, L.A. abrasion, and magnesium sulfate soundness tests (table 18); tests were performed by FHWA and the source quarries.

- The data showed that the OGAs with SI and GG exhibited the most and least durability, respectively, regardless of the type of test (table 18).

SHEAR STRENGTH

Key findings related to shear strength include the following:

- LSDS tests were generally conducted per ASTM D3080 under the following test conditions: dry moisture state, shear gap set at D_{85}, target compaction at *95RD*, fixed strain rate at 0.015 inches per min, four imposed σ_n levels (i.e., 5, 10, 15, and 30 psi), and termination of the tests at 20 percent horizontal strain. All LSDS results are presented in appendix D.

- The LSDS results showed markedly pronounced differences in the shear stress—horizontal strain and vertical-horizontal strain responses between the laboratories for all stone sizes (e.g., figure 16, figure 17, figure 22, figure 23, figure 28, and figure 29) and the OS-20-30 (figure 11 and figure 12). These results are a strong indication that the variability is highly laboratory dependent.

- The horizontal strain corresponding to the peak shear stress ($\varepsilon_{h,peak}$) for OGAs was considerably higher (about 5 to 11 percent, on average) than that for the OS-20-30 (about 1 to 3 percent); see table 19, table 23, table 26, and table 29.

- Secant friction angles (ϕ_s) over the range of 5 to 30 psi ranged from 36.4 to 82.8 degrees, and tangent friction angles (ϕ_t) ranged from 34.5 to 68.1 degrees (table 33); those LSDS devices that had a fixed upper box were on the upper end of the range. Meanwhile, devices with a mobile upper box were on the lower end of the range (figure 38).

- The variability of $\phi_{t,r}$ was the highest of all OGA friction angles evaluated (i.e., average COV of 22 percent), followed by ϕ_{cv} (average COV of 19 percent), ϕ_s, (average COV of 17 percent) and ϕ_t (average COV of 14 percent); see table 32. Less variability was found for OS-20-30 (table 20) compared to OGAs.

- The variability in τ found for OGAs was similar to the variability found by other researchers for sands and other granular materials (see chapter 1).

- Dilation angles for each stone size ranged from about 16 to 19 degrees (table 32); however, COVs up to 42 percent were found. This relatively high variability may be a function of the *n*-point centered moving average approach that was employed to achieve consistency in comparing LSDS results (table 21); *n*-points specific to the laboratory device would have resulted in different dilation angles for each laboratory.

- An evaluation of the strength-dilatancy relationships showed that results produced by fixed upper boxes matches well with past work (i.e., $\phi_s = \phi_{cv} + 0.8\psi_{max}$), resulting in an overall ϕ_{cv} of 55.3 degrees (figure 50).

- Based on AD tests (appendix E), ϕ_t and ϕ_{cv} were normally distributed; $\phi_{t,r}$ exhibited a uniform distribution (table 34). In contrast, ψ_{max} and ϕ_s were not normally distributed when all laboratories were evaluated together.

- Additional ϕ_s AD tests where laboratories were grouped by upper shear box fixity found that ϕ_s was normally distributed for the three laboratories (i.e., L02, L05, and L06) with fixed upper shear boxes.

- ψ_{max} was reevaluated by grouping laboratories with similar data collection frequencies. AD testing showed ψ_{max} followed a normal distribution for data with both high (L01, L02, L05, and L06) and low (L03 and L04) data collection frequency groups. Collection frequency and data smoothing (table 21) clearly influence ψ_{max}.

- The two-factor ANOVA showed that all friction and dilation angles were significantly impacted by sample type (i.e., stone size and mineralogy) and laboratory, although the laboratory far outweighed the sample type in terms of significance (appendix E).

LSDS DEVICES AND PROCEDURES

Conclusions regarding LSDS devices and procedures include the following:

- There were six unique LSDS devices with varying configurations included in the study (figure 6); however, other configurations likely exist nationally and internationally. The key differences in this study, summarized in table 6, were box shape, upper shear box mobility, base smoothness of the loading platen, connection between the loading platen and normal load, box and specimen dimensions, number of LVDTs to measure vertical displacement, and application of normal load.

- Procedural differences in conducting LSDS tests included the frequency of data collection (i.e., sampling rate), timing of setting the shear gap, and method of specimen compaction (chapter 4).

- Whether the upper shear box was fixed was the most influential LSDS device configuration variable on OGA strength results. The strength-dilatancy relationships showed that the devices with a fixed upper box had less scatter and were closer to conventional expectations (figure 50). Further AD tests performed on ϕ_s found that the

data from laboratories with fixed upper boxes followed a normal distribution. In contrast, laboratories with mobile upper boxes remained neither normal nor lognormal behavior.

- The main conclusion is that LSDS testing needs to be standardized to reduce variability; particularly, standard device configurations should be developed and used. This standardization would require either modifications to ASTM D3080 to account for differences in larger devices or the development of a new standard for LSDS testing.

LESSONS LEARNED

Setting up a round-robin study seems straightforward: Select a certain number of laboratories, the test method(s) to follow, and the sample(s) to test. Unfortunately, a complete picture is typically only clear in hindsight, after the results are in. Particular to this study, as data analysis proceeded and knowledge of LSDS testing improved, researchers found that there was more to the LSDS test than just a box of rocks. Setting up this interlaboratory study and evaluating the resulting data imparted some general wisdom about best practices. Going forward, researchers would benefit from doing the following in setting up similar round-robin studies:

- Conduct an extensive literature review and/or an industry survey in advance. This practice would have helped better identify the laboratories (and thus LSDS devices) to select for the round-robin. Before the study, the seemingly subtle differences in LSDS device configurations were not well understood but may have led to different laboratories/devices being selected to ensure those differences could be quantified through the results.

- Set up site visits and/or phone calls with the laboratories before the start of the study. This practice would have allowed for more extensive discussions to better understand their devices and test practices and to explain the requirements for consistency in testing. Clearly communicating the test instructions (appendix A) verbally could have clarified the procedures, avoided delays, and reduced unexpected sources of variability.

- Be specific in the data outputs expected from the laboratories. While the test instructions (appendix A) provided a list of data to be submitted by each lab, there was not enough specificity to clearly identify the level of detail expected. For example, it was assumed that consolidation data would be provided since that is part of the LSDS tests; however, most laboratories do not record or store this information. Similarly, photos were requested to document the laboratory procedures; however, photos do not fully express everything, so having written procedures or descriptions would have been helpful.

- Start with a standard soil (e.g., OS-20-30) to identify any potential issues and iron out the kinks before testing the samples of interest. In this study, OS-20-30 was included at the end of the round-robin to help decipher the OGA results, but some of the pitfalls could have been avoided from the beginning.

- Develop troubleshooting protocols for what to do if things do not go as planned. In this study, for example, many of the sieve tests suggested the OGAs delivered to the laboratories did not meet the AASHTO M 43 specifications; while the test instructions

(appendix A) briefly told the laboratories to stop and await further instructions, there were not internal procedures on how to handle noncompliance, resulting in a case-by-case determination to move forward.

- Verify results from the laboratories providing them. During lab report evaluation, some inconsistencies were found that could have been overlooked in a typical review.

- Request any clarifications from the laboratories in a straightforward, concise manner to avoid back-and-forth correspondence and reduce delays. Once questions were raised, the laboratories were immediately contacted for an answer resulting in multiple requests for information. This back-and-forth could have best been conducted by planning and consolidating all inquiries for more efficient responses.

- Begin data reduction and analysis procedures before all the data is collected. Clearly analyze the data early so trends or anomalies for intra- and interlaboratory reliability can be identified early on. Some discrepancies in internal data analyses were found after the fact. These discrepancies could have been corrected before additional testing began.

- Independently check the data, both from the laboratories providing the results and from in-house data reduction and analysis efforts; everyone makes mistakes. This data validation will ensure data quality from the beginning. Including this type of procedure early on would have avoided going back and forth with this large amount of data and thus limiting delays.

- Develop clear data management protocols (e.g., file names, file structure, formats, file organization, version control, etc.) before starting any study. The quantity of data collected was by no means considered "big data"; however, the datasets were large enough that the files required time-consuming restructuring that could have been avoided with advanced and thoughtful planning.

GEOTECHNICAL DESIGN APPLICATION

Ultimately, the variability of measured design parameters has an impact on the resulting design. Key findings from this study through a design implication lens are as follows:

- The comparison of ϕ_s and ϕ_t from all LSDS tests indicated that, at the highest normal stress level (i.e., 30 psi), the two parameters were similar regardless of the laboratory performing the LSDS test (figure 52). The practical application of this finding is that a secant friction angle from a single test at the highest normal stress of a test series may sufficiently represent the tangent friction angle. Additional research is needed to verify this result for all potential ranges of σ_n.

- Both $\phi_{t,r}$ and ϕ_{cv} are generally conservative measures of strength; as expected, these parameters were found to be nearly equal in magnitude (figure 53).

- The variability of a design parameter is different from the variability of a design model that uses that parameter; this propagation of errors should be considered when any design model is calibrated.

- Suggested values for γ_{d95} and ϕ_t are proposed (table 35) based on extrapolated cumulative distribution functions established from 10,000 data points generated using a Monte-Carlo approach (chapter 4). A range for γ_{d95} that encompasses the middle 90 percent of the combined dataset is provided in the absence of mineralogy information for the specified OGA on a project (figure 54). The suggested default value of 40 degrees for ϕ_t closely represents a 95-percent probability of being exceeded based on the combined dataset in this round-robin study (figure 55). This default value agrees with past FHWA research recommendations for OGAs by Nicks et al. (2018), despite the variability in LSDS testing this round-robin study found.

Table 35. Proposed default values for key geotechnical design parameters.

Parameter	Suggested Values
γ_{d95}	96–115 lb/ft^3
ϕ_t	40 degrees

NEXT STEPS AND FUTURE RESEARCH

With all the results collected in this round-robin study, the next immediate step is to archive the data for public use. The FHWA InfoMaterials™ web portal is one centralized gateway to infrastructure research and materials testing data that could be used for this purpose (FHWA 2022). In addition, the data will be further mined to identify the influence of intrinsic factors (e.g., particle shape characteristics, unit weight, stone size, durability, etc.) on τ of OGAs. A nonlinear multivariate regression analysis could also be performed on the data to develop correlations between parameters. Regardless, the impact of LSDS devices and test procedures for structural backfills was profound, suggesting standardization for testing the strength of larger materials is needed. This avenue of research will be further investigated through experimental and numerical studies to home in on the most appropriate device configurations for producing repeatable and reliable results, with the aim of taming the wild west of LSDS testing.

APPENDIX A. SAMPLE PREPARATION PROTOCOL AND INSTRUCTIONS

It is understood that many testing laboratories have their own internal procedures for DS testing; however, to maintain consistency in both sample preparation and key test procedures, the following test instructions were sent to each laboratory at the beginning of the round-robin study.

TEST SAMPLES (AASHTO NO. 8, NO. 68, AND NO. 57)

Each lab will receive a pallet containing four 5-gal buckets for each aggregate type; a total of 12 buckets. Sample identification labels are attached on the outside of the bucket and inside the bucket. Use this label code in the indentation of the aggregate types and related test results.

Please complete the testing of each aggregate one at a time, before proceeding to the next aggregate sample.

Please take photographs of the aggregates, test devices, sample preparation, and test procedures used in this project for reporting and publications requirements. A permission release form will be provided.

SAMPLE PREPARATION

For each aggregate type, all buckets should be emptied and placed in an oven at 110 ℃ to evaporate any moisture in the aggregates and to determine the dry mass needed for each planned test.

SAMPLE REDUCTION

The oven-dried aggregates for each aggregate type should be poured onto a tarp to produce a mini, uncontaminated stockpile, then mixed thoroughly, with samples collected for sieve analysis and density tests using a quartering sample reduction method, as per AASHTO T 248—Method B Quartering (AASHTO 2014) (figure 56). The samples used for sieve analysis and density testing must be mixed thoroughly and blended back with the original source.

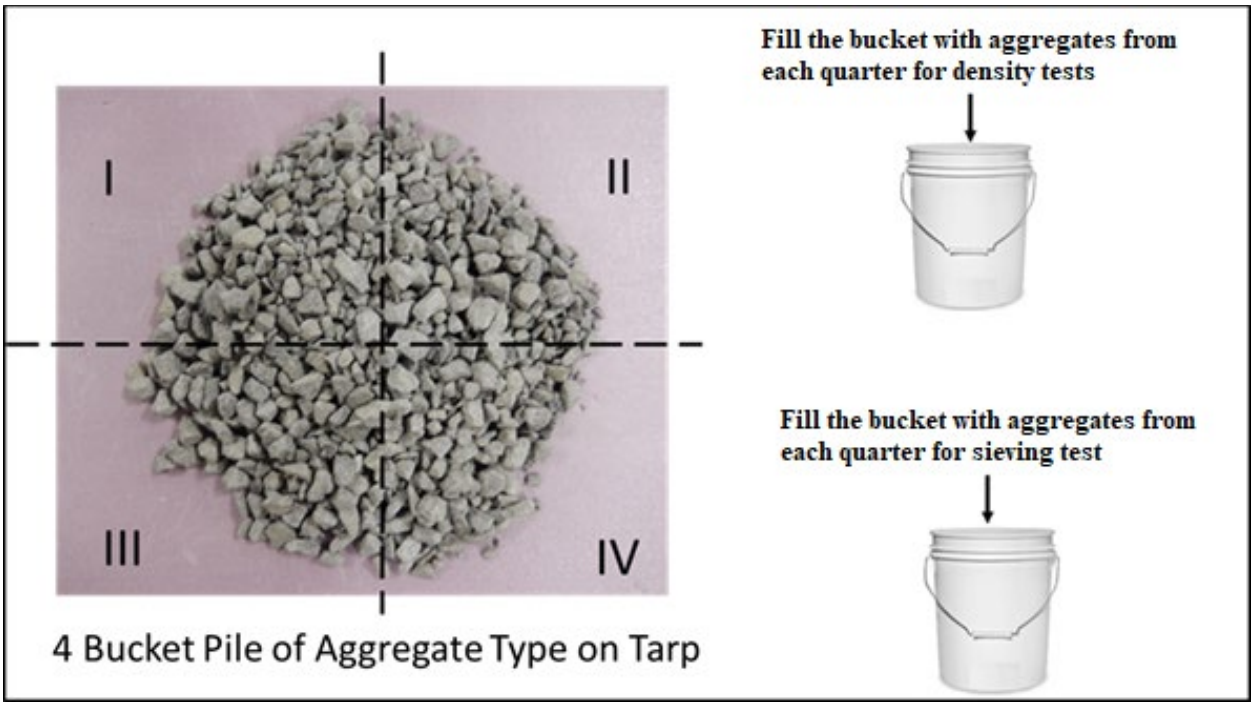

Source: FHWA.

Figure 56. Illustration. Sampling procedure using a quartering method.

SIEVE ANALYSIS (ASTM C136) AND MAXIMUM/MINIMUM INDEX (RELATIVE) DENSITY (ASTM D4253 AND D4254)

Grain size analysis must be conducted by each lab first for each aggregate to ensure the laboratory has the correct samples (i.e., meets AASHTO specifications) before density and LSDS testing is conducted. To have a compatible comparison with the AASHTO M 43-05 aggregate designation, use the sieves that match with the sieve numbers indicated in table 36 for each aggregate type (AASHTO 2018a). If the sieve results of the aggregates do not fall within the limits of the specifications, immediately contact FHWA, and do not conduct any additional tests.

Table 36. Selected AASHTO M 43 aggregate designations (AASHTO 2005).

Sieve No.	Particle Size (inches)	Percent Passing Through Sieve		
		No. 57	No. 68	No. 8
1.5 inch	1.5	100	—	—
1 inch	1.0	95–100	100	—
3/4 inch	0.75	—	90–100	—
1/2 inch	0.50	25–60	—	100
3/8 inch	0.375	—	30–65	85–100
No. 4	0.187	0–10	5–25	10–30
No. 8	0.093	0–5	0–10	0–10
No. 16	0.046	—	0–5	0–5

—Not specified.

Note: Please submit all initial sieve analysis results before commencing the LSDS tests, regardless of whether the aggregates meet the specifications or not.

Following the concurrence of the aggregates' gradation with the AASHTO designation, the minimum density test should be performed first, followed by the maximum density test.

LSDS TESTING (ASTM D3080)

Test instructions related to sample preparation, compaction procedures, and LSDS test setup protocols are listed in the following subsections.

Sample Preparation

After testing the aggregate for the density and sieve analysis, blend them back in the original four-bucket pile. The quartering method should be used again to thoroughly mix the aggregates again before LSDS testing.

Fill a bucket by taking aggregate from each quarter until the required target dry mass is reached to achieve the dry maximum index density of 95 percent. Repeat this step to fill the three remaining buckets. Each bucket will be used to perform a single point of the LSDS shear test. If there is not enough material to conduct virgin samples for each point of the LSDS shear test, then blend the samples back together to complete the final test.

LSDS Test Setup

The testing procedures related to the sample compaction and DS tests are as follows:

1. Avoid unreasonable breakdown of the aggregate during the compaction process (such as with a mechanical or vibratory device). For instance, instead of using vibratory hammers, the aggregates can be compacted in four to five layers using a wooden hammer.

2. Adhere to the following parameters and procedures for each of the LSDS shear tests:

    a. Shear rate: 0.015 inch/min.

    b. Density: 95 percent relative density (based on minimum and maximum index densities).

    c. Shear gap: D85 determined from the sieve analysis for each aggregate type.

    d. Normal stress increments: 5, 10, 15, and 30 psi.

    e. Determination of failure: Terminate the test at 20 percent horizontal strain, or 2.4 inches, regardless of whether the peak shear stress occurs before this termination point.

Post-LSDS Sieve Analysis

At the end of the four-point test series for each aggregate type, reblend the aggregates back into a single source, four-bucket pile, and resample to perform the posttest sieve analysis.

TEST DATA

Submit a separate summary report for each aggregate type that include the following data:

1. Initial sieve analysis data and results.

2. Minimum and maximum density data and results.

3. LSDS test results:

    a. Summary information of the results.

    b. Disclosure of any anomalies.

    c. Both the raw and reduced data files for each aggregate type. The raw data must include the horizontal strain, the vertical strain, the horizontal load/stress, the vertical load/stress, and the elapsed time.

4. Post-sieve analysis data and results.

5. Photos to document the procedure.

APPENDIX B. PRE- AND POST-SHEAR SIEVE ANALYSIS

This following appendix contains the pre- (i.e., as-received) and post-shear sieve analysis for all tested aggregates. Sieving results are presented as percent passing values. The AASHTO M 43 specifications per sieve size are also included in each table for each aggregates' respective stone size (AASHTO 2005). Aggregates are presented in descending gradation coarseness followed by mineralogy in alphabetic order**.**

NO. 57

The pre- and post-shear sieving data for the No. 57 OGAs are presented in table 37 through table 41.

Table 37. Pre- and post-shear sieving data for No. 57-BA.

Sieve No.	Sieve Size (inches)	No. 57 Gradation Specification	Percent Passing for Each Participant Laboratory											
			L01		L02		L03		L04		L05		L06	
			Pre-Shear	Post-Shear	Pre-Shear	Post-Shear	Pre-Shear	Post-Shear	Pre-Shear	Post-Shear	Pre-Shear	Post-Shear	Pre-Shear	Post-Shear
3 inch	3	—	100	100	100	100	100	100	100	100	100	100	100	100
2 inch	2	—	100	100	100	100	100	100	100	100	100	100	100	100
1.5 inch	1.5	100	100	100	100	100	100	100	100	100	100	100	100	100
1 inch	1.0	95-100	100	100	100	100	100	100	100	100	99.6	99.1	100	99.9
3/4 inch	0.75	—	88.0	84.0	83.8	75.5	88.0	91.3	85.0	83.0	79.7	79.4	—	—
1/2 inch	0.5	25–60	37.0	37.0	30.1	26.9	49.3	50.9	34.0	27.0	29.0	29.9	34.8	33.2
3/8 inch	0.375	—	17.0	12.0	6.1	4.5	24.2	26.7	12.0	8.0	9.4	10.4	—	—
No. 4	0.187	0–10	4.0	5.0	0.5	1.5	3.8	5.0	2.0	1.0	1.1	2.0	3.1	2.3
No. 8	0.0937	0–5	2.0	2.0	0.5	1.5	1.5	1.7	1.0	1.0	0.5	1.3	1.7	1.3
No. 16	0.0469	—	1.0	1.0	0.5	1.4	1.1	1.2	1.0	1.0	0.5	1.0	—	—
No. 30	0.0234	—	1.0	1.0	0.5	1.4	1.0	1.1	1.0	1.0	—	—	—	—
No. 50	0.0117	—	1.0	1.0	0.5	1.4	0.9	1.0	1.0	1.0	—	—	—	—
No. 100	0.0059	—	1.0	1.0	0.5	1.3	0.8	0.9	1.0	1.0	—	—	—	—
No. 200	0.0029	—	0.7	0.7	0.5	1.3	0.7	0.9	0.4	0.3	0.4	0.7	0.8	0.7

—No data.

Table 38. Pre- and post-shear sieving data for No. 57-DI.

Sieve No.	Sieve Size (inches)	No. 57 Gradation Specification	Percent Passing for Each Participant Laboratory											
			L01		L02		L03		L04		L05		L06	
			Pre-Shear	Post-Shear	Pre-Shear	Post-Shear	Pre-Shear	Post-Shear	Pre-Shear	Post-Shear	Pre-Shear	Post-Shear	Pre-Shear	Post-Shear
3 inch	3	—	100	100	100	—	100	100	100	100	100	100	100	100
2 inch	2	—	100	100	100	—	100	100	100	100	100	100	100	100
1.5 inch	1.5	100	100	100	100	—	100	100	100	100	100	100	100	100
1 inch	1.0	95-100	100	100	100	—	100	99.5	99.0	100	99.6	99.5	100	100
3/4 inch	0.75	—	88.0	88.0	89.4	—	92.8	90.4	91.0	95.0	88.8	90.1	—	—
1/2 inch	0.5	25–60	36.0	35.0	42.3	—	41.5	46.0	40.0	54.0	40.9	43.4	47.6	51.7
3/8 inch	0.375	—	13.0	11.0	13.5	—	16.4	19.9	17.0	28.0	13.0	15.3	—	—
No. 4	0.187	0–10	2.0	1.0	1.5	—	3.1	3.4	3.0	8.0	1.4	2.4	2.7	4.9
No. 8	0.0937	0–5	1.0	1.0	1.3	—	1.9	1.2	2.0	3.0	0.6	0.7	1.4	2.5
No. 16	0.0469	—	1.0	0.0	1.2	—	1.7	0.9	1.0	2.0	0.6	0.5	—	—
No. 30	0.0234	—	0.0	0.0	1.2	—	1.6	0.8	1.0	2.0	—	—	—	—
No. 50	0.0117	—	0.0	0.0	1.2	—	1.4	0.8	1.0	2.0	—	—	—	—
No. 100	0.0059	—	0.0	0.0	1.1	—	1.0	0.7	1.0	1.0	—	—	—	—
No. 200	0.0029	—	0.0	0.0	1.0	—	0.6	0.5	0.6	1.0	0.0	0.0	0.0	1.2

—No data.

Table 39. Pre- and post-shear sieving data for No. 57-GG.

Sieve No.	Sieve Size (inches)	No. 57 Gradation Specification	Percent Passing for Each Participant Laboratory											
			L01		L02		L03		L04		L05		L06	
			Pre-Shear	Post-Shear	Pre-Shear	Post-Shear	Pre-Shear	Post-Shear	Pre-Shear	Post-Shear	Pre-Shear	Post-Shear	Pre-Shear	Post-Shear
3 inch	3	—	100	100	100	100	100	100	100	100	100	100	100	100
2 inch	2	—	100	100	100	100	100	100	100	100	100	100	100	100
1.5 inch	1.5	100	100	100	100	100	100	100	100	100	100	100	100	100
1 inch	1.0	95-100	100	100	100	100	99.5	98.7	100	100	99.7	99.0	99.4	99.5
3/4 inch	0.75	—	86.0	85.0	86.6	71.9	72.3	76.5	80.0	84.0	80.1	72.1	—	—
1/2 inch	0.5	25–60	35.0	31.0	20.7	13.3	19.2	20.1	23.0	26.0	29.3	20.8	27.4	34.2
3/8 inch	0.375	—	18.0	12.0	4.6	3.0	6.8	5.9	6.0	6.0	8.0	4.0	—	—
No. 4	0.187	0–10	7.0	8.0	0.7	0.4	4.1	4.8	3.0	1.0	4.1	0.9	1.2	5.2
No. 8	0.0937	0–5	5.0	7.0	0.4	0.4	3.6	4.0	2.0	1.0	3.3	0.4	1.0	3.9
No. 16	0.0469	—	5.0	6.0	0.4	0.3	3.2	3.4	2.0	1.0	2.9	0.4	—	—
No. 30	0.0234	—	4.0	5.0	0.4	0.3	3.0	3.3	2.0	1.0	—	—	—	—
No. 50	0.0117	—	3.0	4.0	0.4	0.3	2.5	2.9	2.0	1.0	—	—	—	—
No. 100	0.0059	—	2.0	3.0	0.3	0.3	1.7	2.3	1.0	1.0	—	—	—	—
No. 200	0.0029	—	0.5	1.6	0.3	0.2	0.7	0.6	0.9	0.3	0.9	0.2	0.4	0.9

—No data.

Table 40. Pre- and post-shear sieving data for No. 57-LI.

Sieve No.	Sieve Size (inches)	No. 57 Gradation Specification	Percent Passing for Each Participant Laboratory											
			L01		L02		L03		L04		L05		L06	
			Pre-Shear	Post-Shear	Pre-Shear	Post-Shear	Pre-Shear	Post-Shear	Pre-Shear	Post-Shear	Pre-Shear	Post-Shear	Pre-Shear	Post-Shear
3 inch	3	—	100	100	100	100	100	100	100	100	100	100	100	100
2 inch	2	—	100	100	100	100	100	100	100	100	100	100	100	100
1.5 inch	1.5	100	100	100	100	100	100	100	100	100	100	100	100	100
1 inch	1.0	95-100	99.0	99.0	100	100	99.3	99.0	100	100	99.2	99.8	98.8	99.0
3/4 inch	0.75	—	83.0	77.0	84.9	95.1	83.9	88.7	84.0	87.0	78.8	78.8	—	—
1/2 inch	0.5	25–60	29.0	28.0	33.7	42.1	31.0	45.3	34.0	36.0	30.4	31.5	25.3	33.2
3/8 inch	0.375	—	8.0	8.0	9.4	12.9	11.1	24.4	12.0	13.0	7.1	7.6	—	—
No. 4	0.187	0–10	1.0	1.0	1.1	0.9	2.8	9.6	3.0	2.0	0.6	0.4	1.5	5.5
No. 8	0.0937	0–5	1.0	1.0	0.9	0.5	2.1	6.4	2.0	1.0	0.5	0.2	1.2	4.1
No. 16	0.0469	—	0.3	0.3	0.9	0.5	1.7	4.7	1.0	1.0	0.5	0.2	—	—
No. 30	0.0234	—	0.3	0.3	0.9	0.5	1.5	3.6	1.0	1.0	—	—	—	—
No. 50	0.0117	—	0.3	0.3	0.9	0.5	1.2	2.6	1.0	1.0	—	—	—	—
No. 100	0.0059	—	0.3	0.3	0.8	0.5	0.7	1.4	1.0	1.0	—	—	—	—
No. 200	0.0029	—	0.3	0.3	0.8	0.4	0.3	0.7	0.7	0.3	0.1	0.1	0.0	1.4

—No data.

Table 41. Pre- and post-shear sieving data for No. 57-SI.

Sieve No.	Sieve Size (inches)	No. 57 Gradation Specification	Percent Passing for Each Participant Laboratory											
			L01		L02		L03		L04		L05		L06	
			Pre-Shear	Post-Shear	Pre-Shear	Post-Shear	Pre-Shear	Post-Shear	Pre-Shear	Post-Shear	Pre-Shear	Post-Shear	Pre-Shear	Post-Shear
3 inch	3	—	100	100	100	100	100	100	100	100	100	100	100	100
2 inch	2	—	100	100	100	100	100	100	100	100	100	100	100	100
1.5 inch	1.5	100	100	100	100	100	100	100	100	100	100	100	100	100
1 inch	1.0	95-100	98.0	98.0	93.1	100	100	98.2	98.0	100	95.9	98.4	97.0	98.4
3/4 inch	0.75	—	85.0	85.0	76.9	73.6	91.2	87.6	80.0	85.0	75.3	84.6	—	—
1/2 inch	0.5	25–60	56.0	61.0	40.4	48.4	70.6	61.6	49.0	58.0	50.6	57.9	60.4	60.6
3/8 inch	0.375	—	40.0	44.0	24.5	35.8	52.8	45.0	34.0	40.0	34.3	37.5	—	—
No. 4	0.187	0–10	5.0	7.0	2.1	5.0	6.6	6.1	4.0	5.0	4.6	4.4	6.9	7.1
No. 8	0.0937	0–5	1.0	1.0	0.6	1.3	0.7	1.7	1.0	1.0	0.5	0.4	1.1	1.4
No. 16	0.0469	—	1.0	1.0	0.6	1.1	0.5	1.1	1.0	1.0	0.3	0.3	—	—
No. 30	0.0234	—	0.1	1.0	0.6	1.1	0.5	0.7	1.0	1.0	—	—	—	—
No. 50	0.0117	—	0.1	1.0	0.6	1.0	0.4	0.6	1.0	1.0	—	—	—	—
No. 100	0.0059	—	0.1	0.1	0.6	1.0	0.2	0.4	1.0	1.0	—	—	—	—
No. 200	0.0029	—	0.1	0.1	0.6	1.0	0.0	0.4	0.2	0.3	0.2	0.2	0.4	0.6

—No data.

NO. 68

The pre- and post-shear sieving data for the No. 68 OGAs are presented in table 42 through table 46.

Table 42. Pre- and post-shear sieving data for No. 68-BA.

Sieve No.	Sieve Size (inches)	No. 68 Gradation Specification	Percent Passing for Each Participant Laboratory											
			L01		L02		L03		L04		L05		L06	
			Pre-Shear	Post-Shear	Pre-Shear	Post-Shear	Pre-Shear	Post-Shear	Pre-Shear	Post-Shear	Pre-Shear	Post-Shear	Pre-Shear	Post-Shear
3 inch	3	—	100	100	100	100	100	100	100	100	100	100	100	100
2 inch	2	—	100	100	100	100	100	100	100	100	100	100	100	100
1.5 inch	1.5	—	100	100	100	100	100	100	100	100	100	100	—	—
1 inch	1.0	100	100	100	100	100	100	100	100	100	100	100	100	100
3/4 inch	0.75	90-100	95.0	95.0	94.6	96.8	93.8	96.9	95.0	95.0	93.3	94.3	92.0	95.6
1/2 inch	0.5	—	65.0	70.0	77.2	78.4	71.7	81.1	70.0	71.0	67.8	72.6	—	—
3/8 inch	0.375	30–65	44.0	51.0	60.7	66.1	54.9	65.4	53.0	53.0	46.6	52.4	53.0	54.0
No. 4	0.187	5–25	10.0	14.0	15.7	18.6	13.5	20.3	13.0	14.0	9.8	17.5	14.5	15.6
No. 8	0.0937	0–10	2.0	3.0	2.3	3.4	2.7	4.6	2.0	2.0	0.8	2.0	2.4	2.8
No. 16	0.0469	0–5	1.0	2.0	1.1	2.2	1.5	2.6	1.0	1.0	0.4	0.8	1.2	1.3
No. 30	0.0234	—	1.0	1.0	1.0	1.9	1.3	2.1	1.0	1.0	—	—	—	—
No. 50	0.0117	—	1.0	1.0	1.0	1.8	1.2	1.8	1.0	1.0	—	—	—	—
No. 100	0.0059	—	1.0	1.0	1.0	1.7	1.1	1.7	1.0	1.0	—	—	—	—
No. 200	0.0029	—	0.7	1.0	0.9	1.6	1.0	1.5	0.8	0.5	0.3	0.6	0.8	0.7

—No data.

Table 43. Pre- and post-shear sieving data for No. 68-DI.

Sieve No.	Sieve Size (inches)	No. 68 Gradation Specification	Percent Passing for Each Participant Laboratory											
			L01		L02		L03		L04		L05		L06	
			Pre-Shear	Post-Shear	Pre-Shear	Post-Shear	Pre-Shear	Post-Shear	Pre-Shear	Post-Shear	Pre-Shear	Post-Shear	Pre-Shear	Post-Shear
3 inch	3	—	100	100	100	—	100	100	100	100	100	100	100	100
2 inch	2	—	100	100	100	—	100	100	100	100	100	100	100	100
1.5 inch	1.5	—	100	100	100	—	100	100	100	100	100	100	—	—
1 inch	1.0	100	100	100	100	—	100	100	100	100	100	100	100	100
3/4 inch	0.75	90-100	92.0	92.0	95.7	—	94.8	93.9	92.0	94.0	93.8	92.9	94.7	94.1
1/2 inch	0.5	—	48.0	47.0	71.5	—	55.3	45.2	52.0	62.0	49.7	49.0	—	—
3/8 inch	0.375	30–65	31.0	28.0	58.1	—	33.3	24.3	32.0	44.0	30.2	26.7	41.1	35.1
No. 4	0.187	5–25	5.0	4.0	18.6	—	5.0	4.1	4.0	10.0	4.9	3.2	6.6	7.5
No. 8	0.0937	0–10	1.0	1.0	8.2	—	2.3	1.6	1.0	3.0	0.9	0.5	1.6	3.1
No. 16	0.0469	0–5	0.0	1.0	0.8	—	2.0	1.2	1.0	2.0	0.9	0.4	1.3	2.4
No. 30	0.0234	—	0.0	0.0	0.7	—	1.9	1.0	1.0	2.0	—	—	—	—
No. 50	0.0117	—	0.0	0.0	0.6	—	1.7	0.9	1.0	1.0	—	—	—	—
No. 100	0.0059	—	0.0	0.0	0.6	—	1.2	0.8	1.0	1.0	—	—	—	—
No. 200	0.0029	—	0.0	0.0	0.5	—	0.5	0.6	0.5	1.0	0.0	0.0	0.0	1.3

—No data.

Table 44. Pre- and post-shear sieving data for No. 68-GG.

Sieve No.	Sieve Size (inches)	No. 68 Gradation Specification	Percent Passing for Each Participant Laboratory											
			L01		L02		L03		L04		L05		L06	
			Pre-Shear	Post-Shear	Pre-Shear	Post-Shear	Pre-Shear	Post-Shear	Pre-Shear	Post-Shear	Pre-Shear	Post-Shear	Pre-Shear	Post-Shear
3 inch	3	—	100	100	100	100	100	100	100	100	100	100	100	100
2 inch	2	—	100	100	100	100	100	100	100	100	100	100	100	100
1.5 inch	1.5	—	100	100	100	100	100	100	100	100	100	100	—	—
1 inch	1.0	100	100	100	100	100	100	100	100	100	100	100	100	100
3/4 inch	0.75	90-100	100	100	99.4	98.8	99.6	99.2	100	100	99.7	94.9	99.4	99.6
1/2 inch	0.5	—	67.0	66.0	58.0	58.5	53.0	58.0	65.0	74.0	60.9	68.7	—	—
3/8 inch	0.375	30–65	48.0	47.0	39.7	37.4	31.1	25.8	42.0	55.0	36.8	45.7	37.1	41.5
No. 4	0.187	5–25	8.0	11.0	3.8	2.4	6.9	8.9	5.0	14.0	2.7	13.2	5.2	8.1
No. 8	0.0937	0–10	5.0	6.0	0.8	0.4	4.8	5.1	2.0	7.0	0.2	7.1	2.3	3.8
No. 16	0.0469	0–5	5.0	5.0	0.7	0.4	4.2	4.7	2.0	5.0	0.2	5.9	1.8	2.9
No. 30	0.0234	—	4.0	4.0	0.7	0.4	3.8	3.7	1.0	4.0	—	—	—	—
No. 50	0.0117	—	3.0	3.0	0.7	0.4	3.2	3.0	1.0	3.0	—	—	—	—
No. 100	0.0059	—	2.0	2.0	0.6	0.3	2.2	2.8	1.0	2.0	—	—	—	—
No. 200	0.0029	—	1.0	1.2	0.5	0.2	0.9	1.2	0.3	1.2	0.1	1.4	0.6	0.7

—No data.

Table 45. Pre- and post-shear sieving data for No. 68-LI.

Sieve No.	Sieve Size (inches)	No. 68 Gradation Specification	Percent Passing for Each Participant Laboratory											
			L01		L02		L03		L04		L05		L06	
			Pre-Shear	Post-Shear	Pre-Shear	Post-Shear	Pre-Shear	Post-Shear	Pre-Shear	Post-Shear	Pre-Shear	Post-Shear	Pre-Shear	Post-Shear
3 inch	3	—	100	100	100	100	100	100	100	100	100	100	100	100
2 inch	2	—	100	100	100	100	100	100	100	100	100	100	100	100
1.5 inch	1.5	—	100	100	100	100	100	100	100	100	100	100	—	—
1 inch	1.0	100	100	100	100	100	100	100	100	100	100	100	100	100
3/4 inch	0.75	90-100	100	98.0	100	98.2	99.4	97.2	100	99.0	99.0	98.6	99.5	99.8
1/2 inch	0.5	—	67.0	64.0	83.5	81.7	72.8	70.6	71.0	74.0	64.7	66.5	—	—
3/8 inch	0.375	30–65	46.0	42.0	66.0	65.4	53.9	52.0	48.0	54.0	39.1	41.1	45.9	47.9
No. 4	0.187	5–25	9.0	5.0	16.4	17.0	13.6	8.2	10.0	14.0	6.6	7.1	8.6	11.1
No. 8	0.0937	0–10	2.0	0.0	4.2	3.5	5.4	1.1	3.0	4.0	1.0	1.1	2.2	3.4
No. 16	0.0469	0–5	1.0	0.0	2.4	1.8	3.5	0.9	2.0	2.0	0.8	0.6	1.4	2.0
No. 30	0.0234	—	1.0	0.0	1.9	1.5	2.4	0.9	1.0	1.0	—	—	—	—
No. 50	0.0117	—	1.0	0.0	1.7	1.4	1.7	0.8	1.0	1.0	—	—	—	—
No. 100	0.0059	—	0.3	0.0	1.5	1.3	0.8	0.5	1.0	1.0	—	—	—	—
No. 200	0.0029	—	0.3	0.0	1.5	1.2	0.3	0.3	0.5	0.4	0.5	0.2	0.0	0.7

—No data.

Table 46. Pre- and post-shear sieving data for No. 68-SI.

Sieve No.	Sieve Size (inches)	No. 68 Gradation Specification	Percent Passing for Each Participant Laboratory											
			L01		L02		L03		L04		L05		L06	
			Pre-Shear	Post-Shear	Pre-Shear	Post-Shear	Pre-Shear	Post-Shear	Pre-Shear	Post-Shear	Pre-Shear	Post-Shear	Pre-Shear	Post-Shear
3 inch	3	—	100	100	100	100	100	100	100	100	100	100	100	100
2 inch	2	—	100	100	100	100	100	100	100	100	100	100	100	100
1.5 inch	1.5	—	100	100	100	100	100	100	100	100	100	100	—	—
1 inch	1.0	100	100	100	100	100	100	100	100	100	100	100	100	100
3/4 inch	0.75	90-100	96.0	95.0	94.1	95.5	98.1	94.4	95.0	93.0	93.9	95.5	95.0	94.5
1/2 inch	0.5	—	59.0	57.0	56.1	64.7	72.2	67.2	55.0	60.0	63.1	62.0	—	—
3/8 inch	0.375	30–65	41.0	37.0	35.9	51.2	54.8	51.9	36.0	41.0	44.9	42.3	44.4	45.2
No. 4	0.187	5–25	9.0	6.0	6.1	11.3	11.4	12.7	6.0	9.0	10.0	8.3	8.8	9.9
No. 8	0.0937	0–10	2.0	1.0	1.1	2.3	1.8	3.2	1.0	1.0	1.6	1.0	1.2	1.7
No. 16	0.0469	0–5	1.0	1.0	1.0	1.4	1.2	2.1	1.0	1.0	1.0	0.7	0.9	1.7
No. 30	0.0234	—	1.0	1.0	1.0	1.0	1.0	1.5	1.0	1.0	—	—	—	—
No. 50	0.0117	—	1.0	1.0	1.0	0.9	0.8	0.8	1.0	1.0	—	—	—	—
No. 100	0.0059	—	1.0	1.0	0.9	0.7	0.4	0.2	1.0	1.0	—	—	—	—
No. 200	0.0029	—	0.3	0.1	0.9	0.7	0.1	0.0	0.5	0.2	0.4	0.4	0.7	0.9

—No data.

NO. 8

The pre- and post-shear sieving data for the No. 8 OGAs are presented in table 47 through table 51.

Table 47. Pre- and post-shear sieving data for No. 8-BA.

Sieve No.	Sieve Size (inches)	No. 8 Gradation Specification	Percent Passing for Each Participant Laboratory											
			L01		L02		L03		L04		L05		L06	
			Pre-Shear	Post-Shear	Pre-Shear	Post-Shear	Pre-Shear	Post-Shear	Pre-Shear	Post-Shear	Pre-Shear	Post-Shear	Pre-Shear	Post-Shear
3 inch	3	—	100	100	100	100	100	100	100	100	100	100	100	100
2 inch	2	—	100	100	100	100	100	100	100	100	100	100	100	100
1.5 inch	1.5	—	100	100	100	100	100	100	100	100	100	100	—	—
1 inch	1.0	—	100	100	100	100	100	100	100	100	100	100	—	—
3/4 inch	0.75	—	100	100	100	100	100	100	100	100	100	100	—	—
1/2 inch	0.5	100	100	100	100	100	100	100	100	100	100	100	99.9	99.9
3/8 inch	0.375	85-100	86.0	84.0	91.2	88.3	72.4	89.7	89.0	93.0	89.9	89.1	88.4	89.3
No. 4	0.187	10–30	20.0	10.0	23.4	19.2	15.6	17.3	19.0	31.0	21.7	22.6	19.8	23.3
No. 8	0.0937	0–10	4.0	1.0	2.2	2.6	3.4	2.3	2.0	7.0	1.4	3.0	1.8	2.9
No. 16	0.0469	0–5	2.0	0.1	0.8	0.8	2.0	1.1	2.0	3.0	0.4	1.3	0.6	2.9
No. 30	0.0234	—	1.0	0.1	0.8	0.6	1.6	0.9	2.0	2.0	—	—	—	—
No. 50	0.0117	—	1.0	0.1	0.8	0.6	1.5	0.8	2.0	1.0	—	—	—	—
No. 100	0.0059	—	1.0	0.1	0.8	0.6	1.4	0.7	2.0	1.0	—	—	—	—
No. 200	0.0029	—	0.8	0.1	0.8	0.5	1.3	0.7	0.3	1.0	0.3	0.8	0.5	0.5

—No data.

Table 48. Pre- and post-shear sieving data for No. 8-DI.

Sieve No.	Sieve Size (inches)	No. 8 Gradation Specification	Percent Passing for Each Participant Laboratory											
			L01		L02		L03		L04		L05		L06	
			Pre-Shear	Post-Shear	Pre-Shear	Post-Shear	Pre-Shear	Post-Shear	Pre-Shear	Post-Shear	Pre-Shear	Post-Shear	Pre-Shear	Post-Shear
3 inch	3	—	100	100	100	—	100	100	100	100	100	100	100	100
2 inch	2	—	100	100	100	—	100	100	100	100	100	100	100	100
1.5 inch	1.5	—	100	100	100	—	100	100	100	100	100	100	—	—
1 inch	1.0	—	100	100	100	—	100	100	100	100	100	100	—	—
3/4 inch	0.75	—	100	100	100	—	100	100	100	100	100	100	—	—
1/2 inch	0.5	100	100	100	100	—	100	100	100	100	100	100	100	100
3/8 inch	0.375	85-100	90.0	89.0	93.1	—	94.4	90.8	93.0	94.0	91.7	93.1	92.3	92.9
No. 4	0.187	10–30	14.0	14.0	15.2	—	21.0	13.6	16.0	20.0	12.0	16.9	18.3	18.2
No. 8	0.0937	0–10	1.0	2.0	1.0	—	5.4	2.5	2.0	1.0	0.7	0.6	2.5	1.8
No. 16	0.0469	0–5	1.0	1.0	0.8	—	4.6	2.1	1.0	1.0	0.6	0.3	1.8	1.2
No. 30	0.0234	—	0.0	0.0	0.7	—	4.1	2.1	1.0	1.0	—	—	—	—
No. 50	0.0117	—	0.0	0.0	0.7	—	3.6	2.0	1.0	1.0	—	—	—	—
No. 100	0.0059	—	0.0	0.0	0.6	—	2.5	2.0	1.0	1.0	—	—	—	—
No. 200	0.0029	—	0.0	0.0	0.5	—	0.8	1.8	0.7	0.6	0.0	0.0	0.0	0.8

—No data.

Table 49. Pre- and post-shear sieving data for No. 8-GG.

Sieve No.	Sieve Size (inches)	No. 8 Gradation Specification	Percent Passing for Each Participant Laboratory											
			L01		L02		L03		L04		L05		L06	
			Pre-Shear	Post-Shear	Pre-Shear	Post-Shear	Pre-Shear	Post-Shear	Pre-Shear	Post-Shear	Pre-Shear	Post-Shear	Pre-Shear	Post-Shear
3 inch	3	—	100	100	100	100	100	100	100	100	100	100	100	100
2 inch	2	—	100	100	100	100	100	100	100	100	100	100	100	100
1.5 inch	1.5	—	100	100	100	100	100	100	100	100	100	100	—	—
1 inch	1.0	—	100	100	100	100	100	100	100	100	100	100	—	—
3/4 inch	0.75	—	100	100	100	100	100	100	100	100	100	100	—	—
1/2 inch	0.5	100	100	100	99.6	100	100	100	100	100	100	100	100	100
3/8 inch	0.375	85-100	86.0	83.0	87.4	84.9	80.8	83.7	79.0	90.0	86.0	88.6	85.0	89.0
No. 4	0.187	10–30	12.0	9.0	6.4	5.3	4.0	6.8	6.0	16.0	11.5	5.9	9.9	3.1
No. 8	0.0937	0–10	7.0	5.0	1.4	0.7	1.4	2.5	3.0	8.0	4.2	0.4	4.3	2.6
No. 16	0.0469	0–5	5.0	4.0	1.2	0.6	1.2	1.5	2.0	5.0	2.9	0.2	3.5	1.0
No. 30	0.0234	—	4.0	3.0	1.2	0.6	1.1	1.3	2.0	3.0	—	—	—	—
No. 50	0.0117	—	3.0	2.0	1.1	0.5	1.1	1.2	1.0	2.0	—	—	—	—
No. 100	0.0059	—	2.0	1.0	1.0	0.5	0.9	1.1	1.0	1.0	—	—	—	—
No. 200	0.0029	—	0.5	0.7	0.9	0.4	0.5	0.7	0.5	0.7	0.7	0.1	0.8	0.9

—No data.

Table 50. Pre- and post-shear sieving data for No. 8-LI.

Sieve No.	Sieve Size (inches)	No. 8 Gradation Specification	Percent Passing for Each Participant Laboratory											
			L01		L02		L03		L04		L05		L06	
			Pre-Shear	Post-Shear	Pre-Shear	Post-Shear	Pre-Shear	Post-Shear	Pre-Shear	Post-Shear	Pre-Shear	Post-Shear	Pre-Shear	Post-Shear
3 inch	3	—	100	100	100	100	100	100	100	100	100	100	100	100
2 inch	2	—	100	100	100	100	100	100	100	100	100	100	100	100
1.5 inch	1.5	—	100	100	100	100	100	100	100	100	100	100	—	—
1 inch	1.0	—	100	100	100	100	100	100	100	100	100	100	—	—
3/4 inch	0.75	—	100	100	100	100	100	100	100	100	100	100	—	—
1/2 inch	0.5	100	100	100	100	99.7	100	100	100	100	100	100	100	100
3/8 inch	0.375	85–100	95.0	97.0	95.8	94.1	92.0	95.1	95.0	97.0	93.2	95.1	91.8	91.7
No. 4	0.187	10–30	29.0	35.0	32.0	31.4	18.8	27.9	29.0	39.0	25.3	28.1	22.3	27.0
No. 8	0.0937	0–10	4.0	6.0	6.2	4.0	2.0	3.8	3.0	6.0	2.3	3.3	3.3	5.5
No. 16	0.0469	0–5	2.0	2.0	2.9	1.2	1.1	1.6	1.0	1.0	0.7	1.2	1.6	2.4
No. 30	0.0234	—	1.0	2.0	2.1	1.1	0.9	1.1	1.0	1.0	—	—	—	—
No. 50	0.0117	—	1.0	1.0	1.8	1.0	0.8	1.0	1.0	1.0	—	—	—	—
No. 100	0.0059	—	1.0	1.0	1.6	1.0	0.5	0.6	1.0	1.0	—	—	—	—
No. 200	0.0029	—	0.4	0.6	1.5	1.0	0.2	0.4	0.8	0.3	0.3	0.5	0.0	0.7

—No data.

Table 51. Pre- and post-shear sieving data for No. 8-SI.

Sieve No.	Sieve Size (inches)	No. 8 Gradation Specification	Percent Passing for Each Participant Laboratory											
			L01		L02		L03		L04		L05		L06	
			Pre-Shear	Post-Shear	Pre-Shear	Post-Shear	Pre-Shear	Post-Shear	Pre-Shear	Post-Shear	Pre-Shear	Post-Shear	Pre-Shear	Post-Shear
3 inch	3	—	100	100	100	100	100	100	100	100	100	100	100	100
2 inch	2	—	100	100	100	100	100	100	100	100	100	100	100	100
1.5 inch	1.5	—	100	100	100	100	100	100	100	100	100	100	—	—
1 inch	1.0	—	100	100	100	100	100	100	100	100	100	100	—	—
3/4 inch	0.75	—	100	100	100	100	99.8	100	100	100	100	99.6	—	—
1/2 inch	0.5	100	99.0	100	98.9	99.5	97.1	97.7	99.0	99.0	98.9	98.3	99.2	98.1
3/8 inch	0.375	85-100	86.0	86.0	93.7	93.0	88.0	88.8	90.0	91.0	88.9	87.6	87.9	84.3
No. 4	0.187	10–30	20.0	20.0	26.1	30.6	23.5	24.0	25.0	32.0	25.8	23.4	24.0	23.7
No. 8	0.0937	0–10	4.0	2.0	5.6	2.7	2.5	5.8	2.0	7.0	1.9	1.7	2.3	3.2
No. 16	0.0469	0–5	2.0	2.0	1.9	1.2	1.5	3.5	1.0	6.0	1.2	1.0	1.4	1.8
No. 30	0.0234	—	1.0	1.0	1.3	1.0	1.3	2.2	1.0	6.0	—	—	—	—
No. 50	0.0117	—	1.0	1.0	1.1	0.8	1.1	1.0	1.0	5.0	—	—	—	—
No. 100	0.0059	—	1.0	1.0	1.0	0.7	0.6	0.2	1.0	5.0	—	—	—	—
No. 200	0.0029	—	0.8	0.2	1.0	0.6	0.1	0.1	0.5	5.0	0.7	0.7	0.9	0.9

—No data.

APPENDIX C. AIMS2 PARTICLE CHARACTERISTIC RESULTS

This appendix contains the main results of AIMS2 digital image analyses conducted by FHWA, including angularity (GA) index, TX index, SP index, and flat and elongated (F&E) values. The plots shown in this appendix have the same x-axis scale for ease of visual comparison and are followed by summary tables containing the weighted average values for GA, TX, SP, and F&E results. Weighted averages were calculated for each parameter by summing the per-sieve results multiplied by the percentage of material retained on that sieve. Classifications per AASHTO R 91-18 are included for the weighted average angularity, TX, and SP indexes (AASHTO 2018b).

OS-20-30

Figure 57 shows the cumulative angularity results for OS-20-30; the weighted GA index is 674, which classifies OS-20-30 as having low angularity.

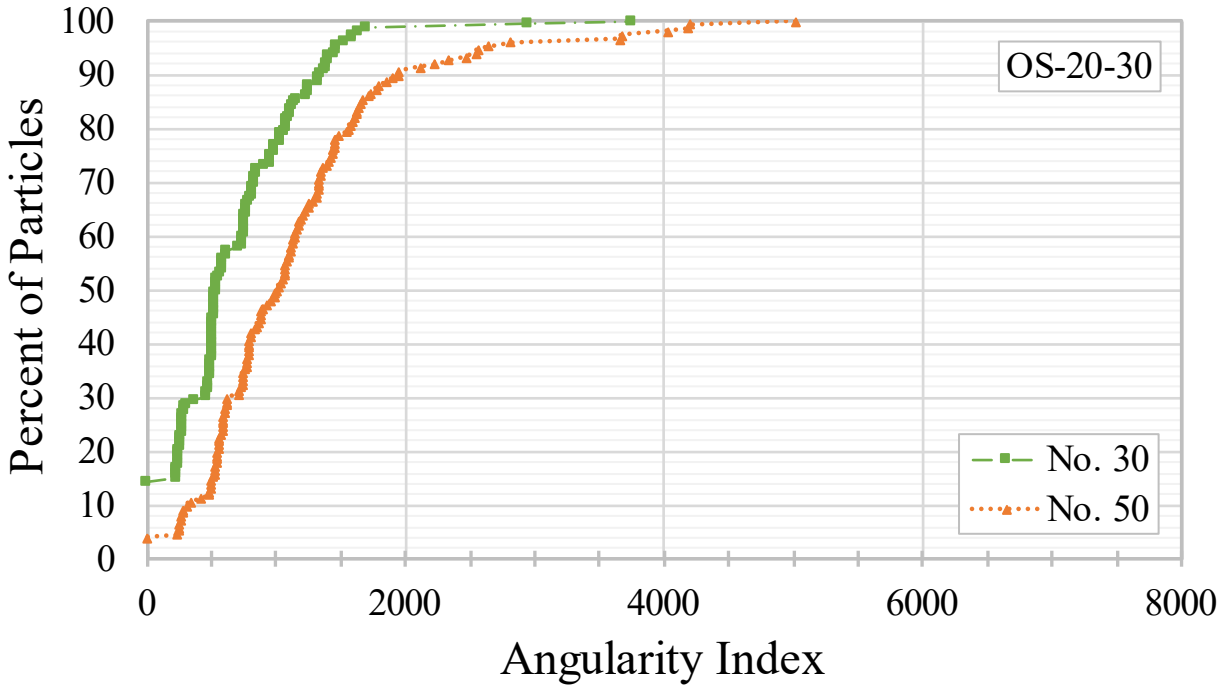

Source: FHWA.

Figure 57. Chart. AIMS2 cumulative angularity distributions for OS-20-30.

NO. 57 OGAs

The cumulative angularity, TX, and SP results are presented for No. 57-BA (figure 58), No. 57-DI (figure 59), No. 57-GG (figure 60), No. 57-LI (figure 61), and No. 57-SI (figure 62).

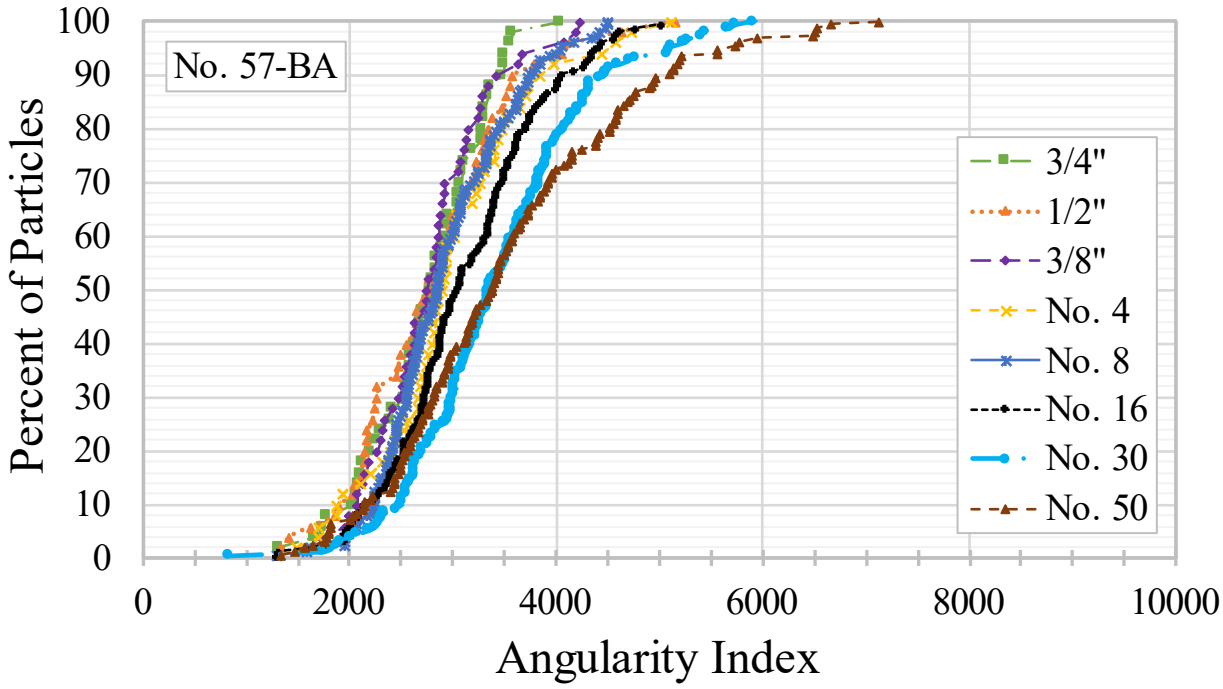

Source: FHWA.

A. Angularity.

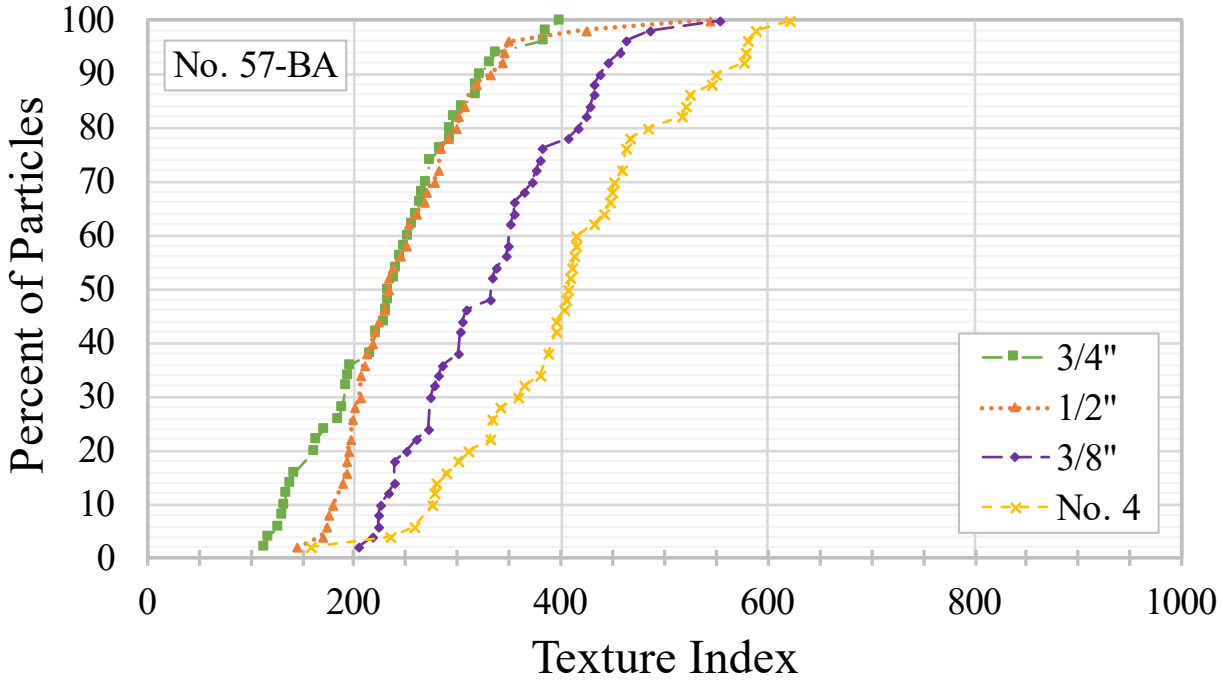

Source: FHWA.

B. TX.

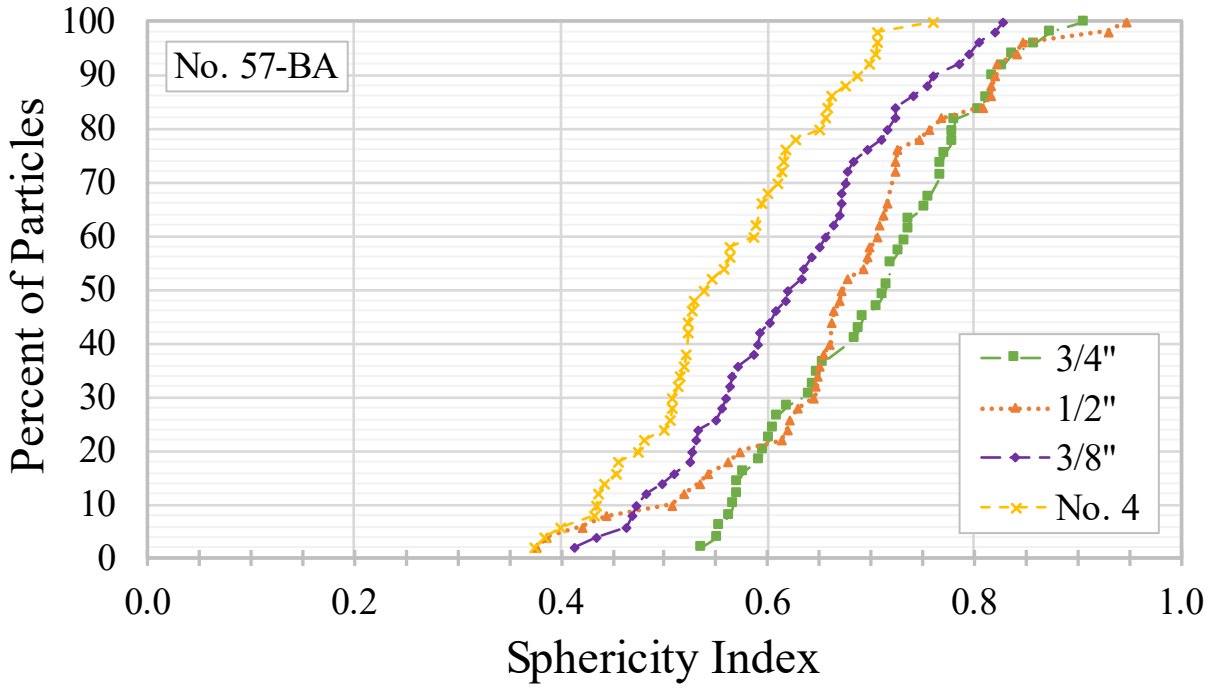

Source: FHWA.

C. SP.

Figure 58. Charts. AIMS2 cumulative distributions for No. 57-BA.

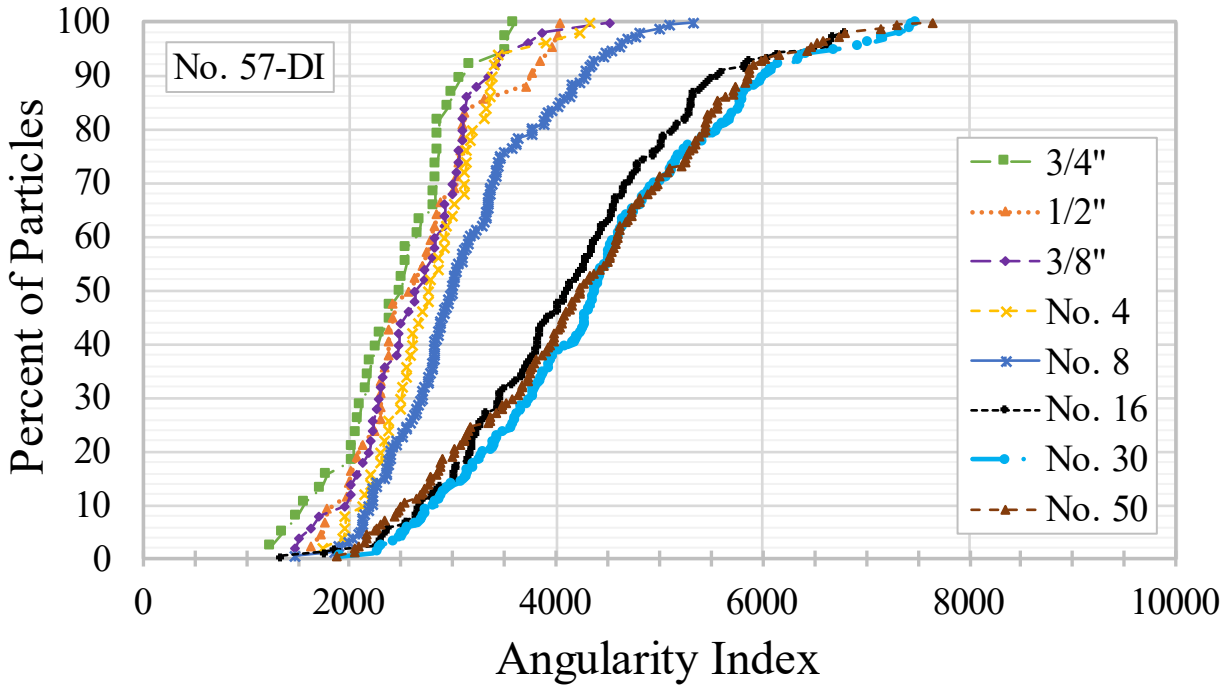

Source: FHWA.

A. Angularity.

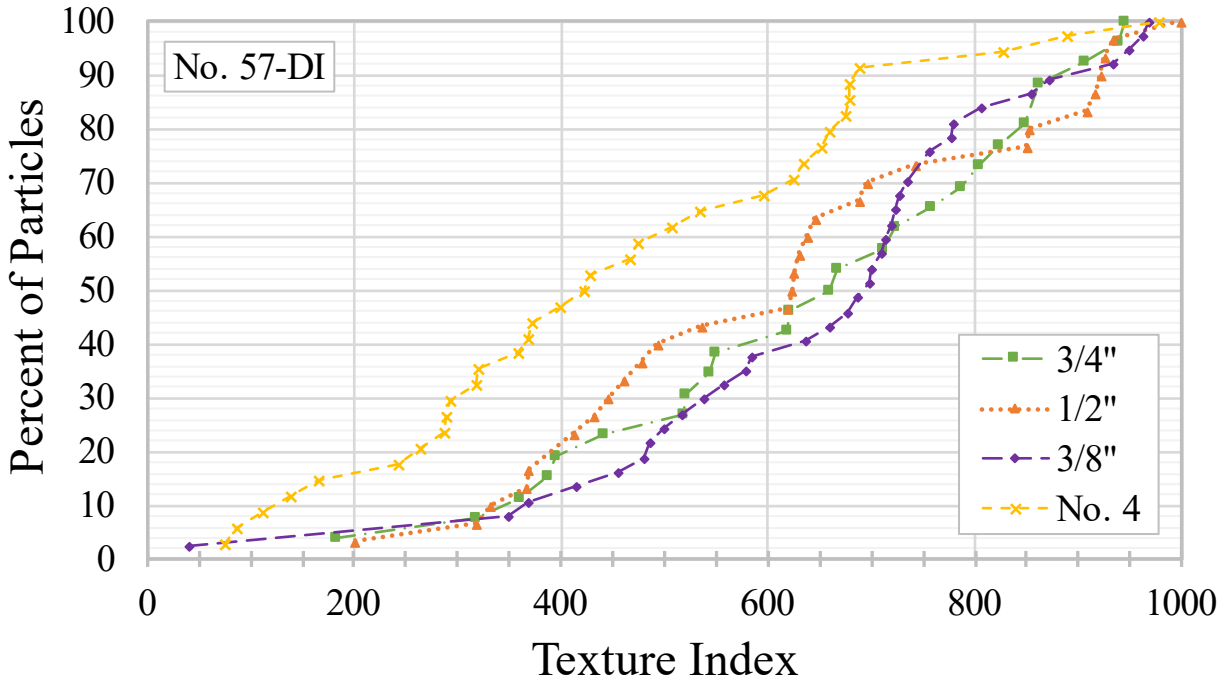

Source: FHWA.

B. TX.

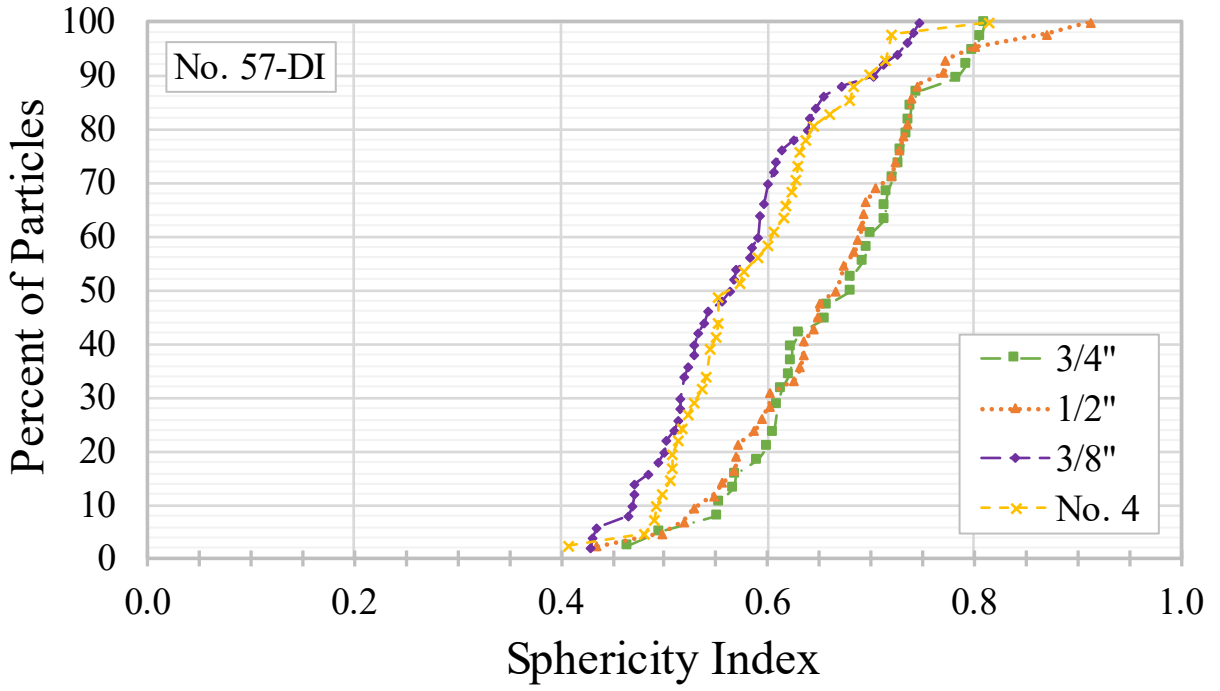

Source: FHWA.

C. SP.

Figure 59. Charts. AIMS2 cumulative distributions for No. 57-DI.

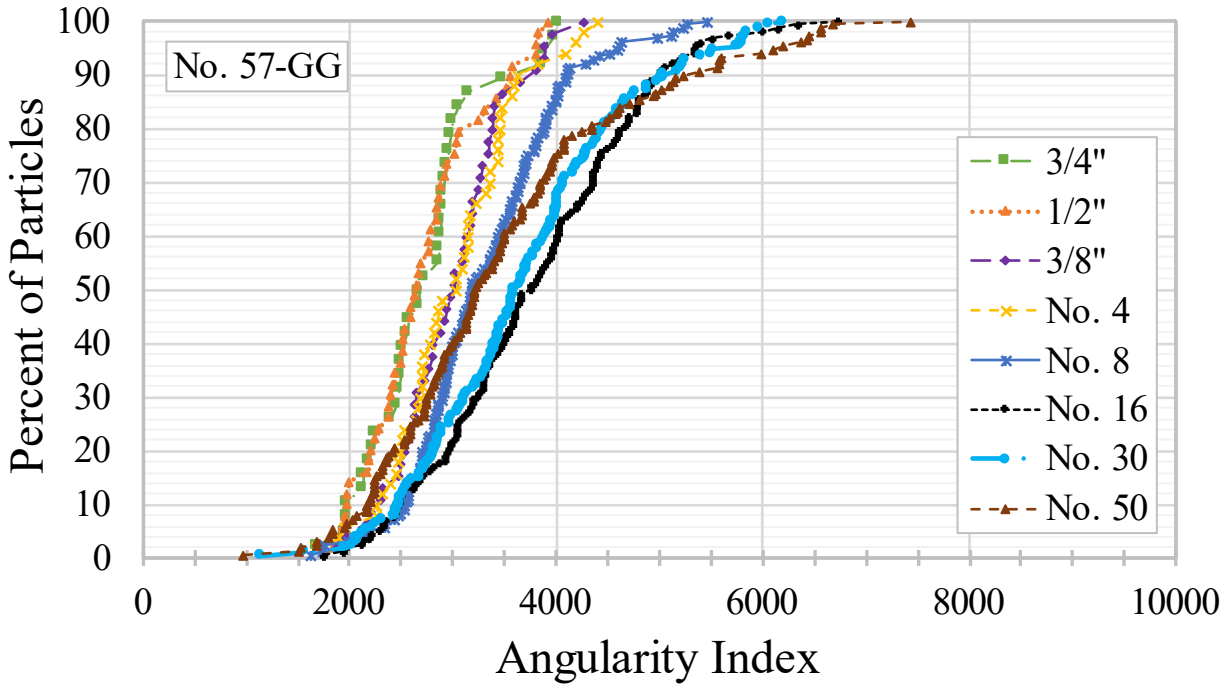

Source: FHWA.

A. Angularity.

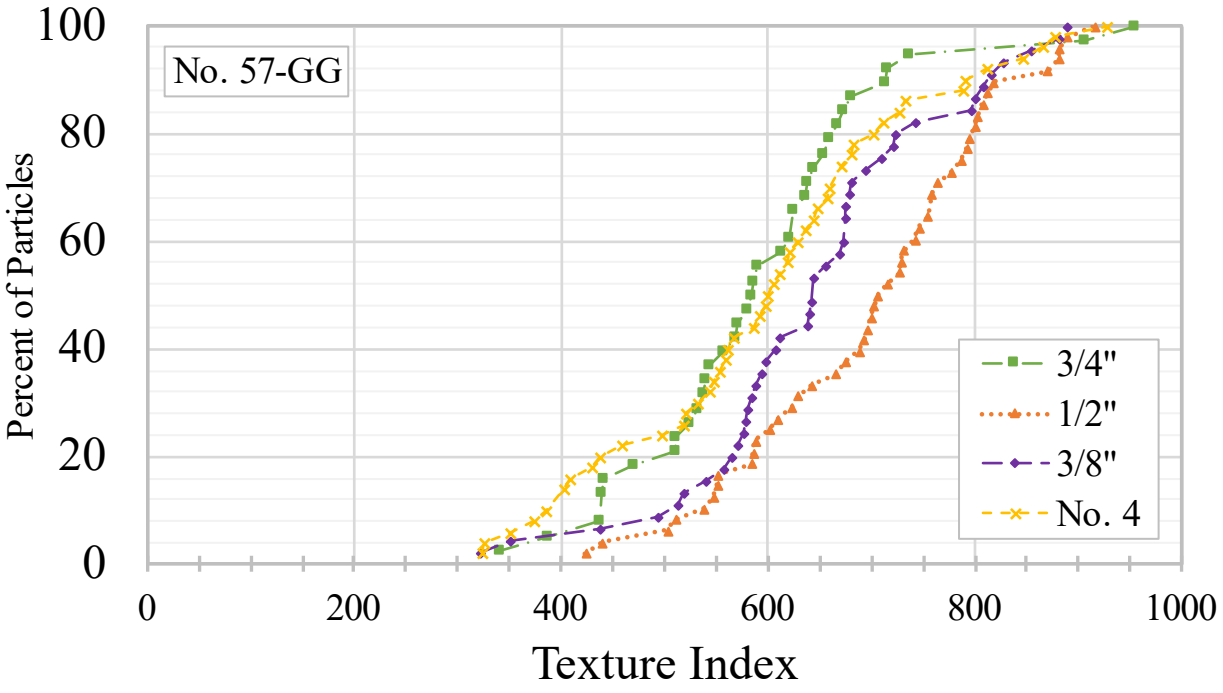

Source: FHWA.

B. TX.

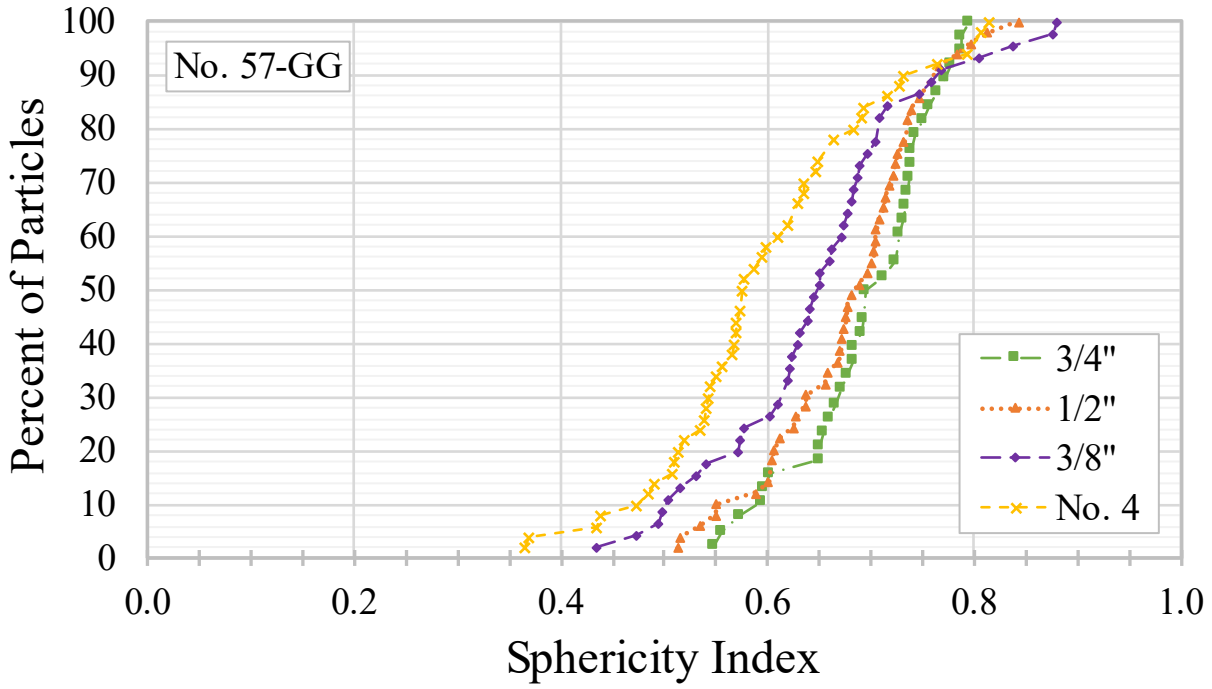

Source: FHWA.

C. SP.

Figure 60. Charts. AIMS2 cumulative distributions for No. 57-GG.

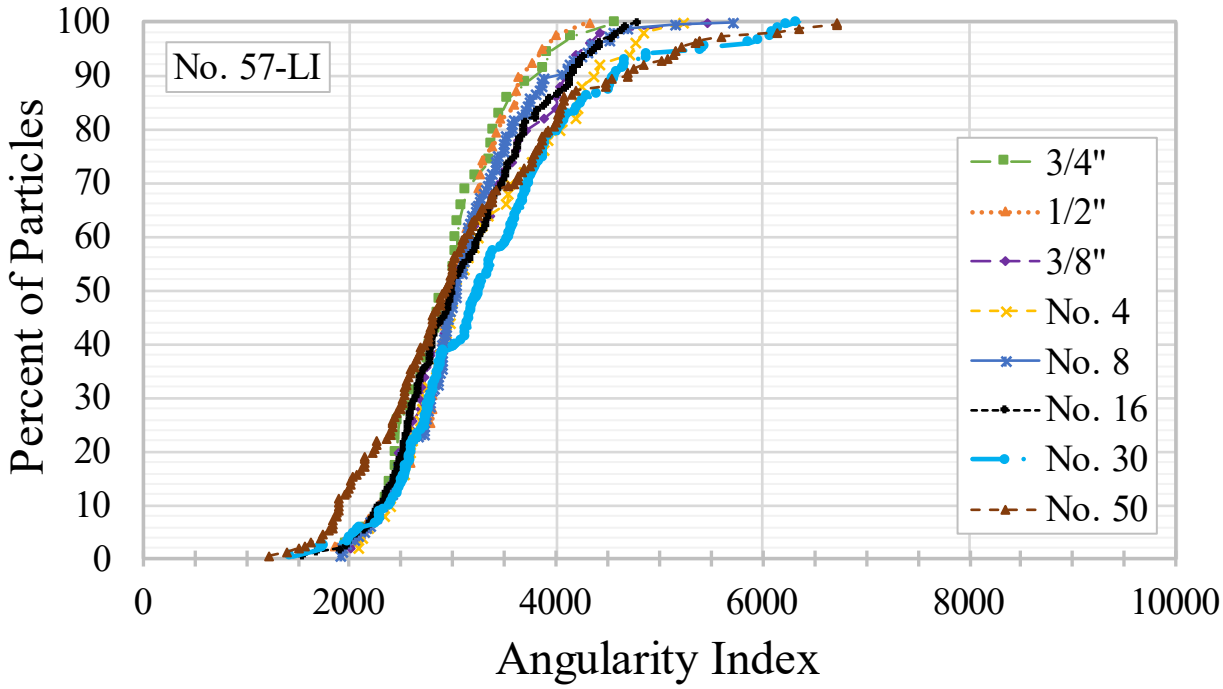

Source: FHWA.

A. Angularity.

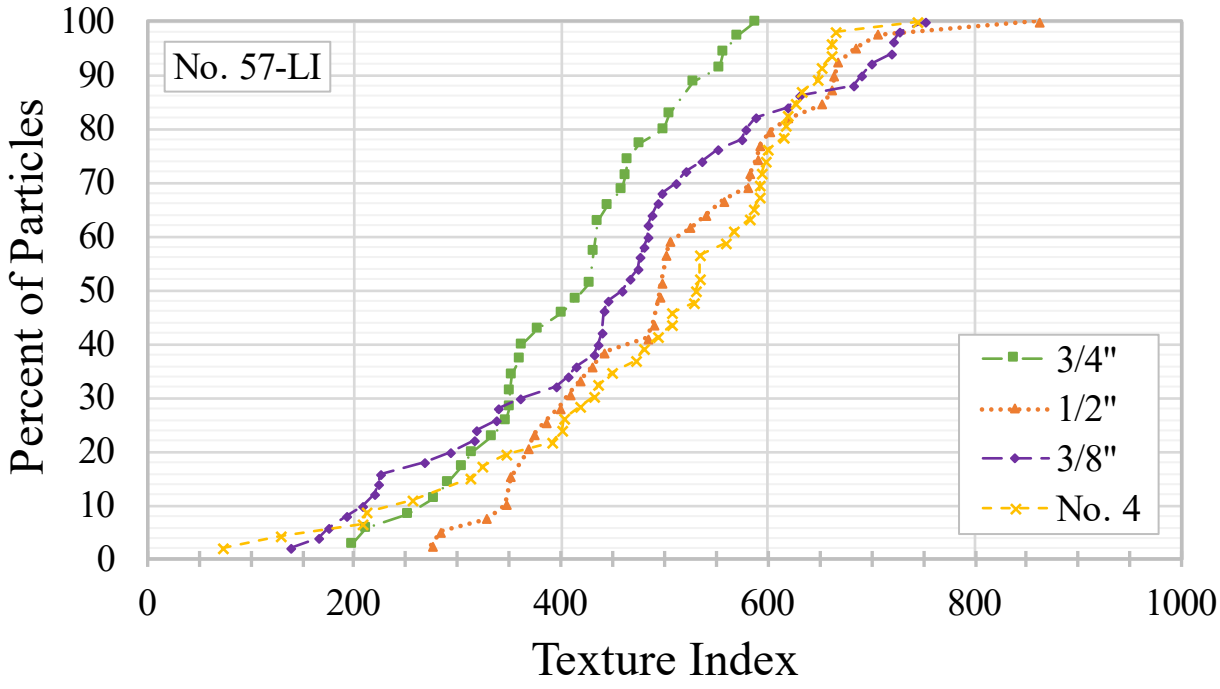

Source: FHWA.

B. TX.

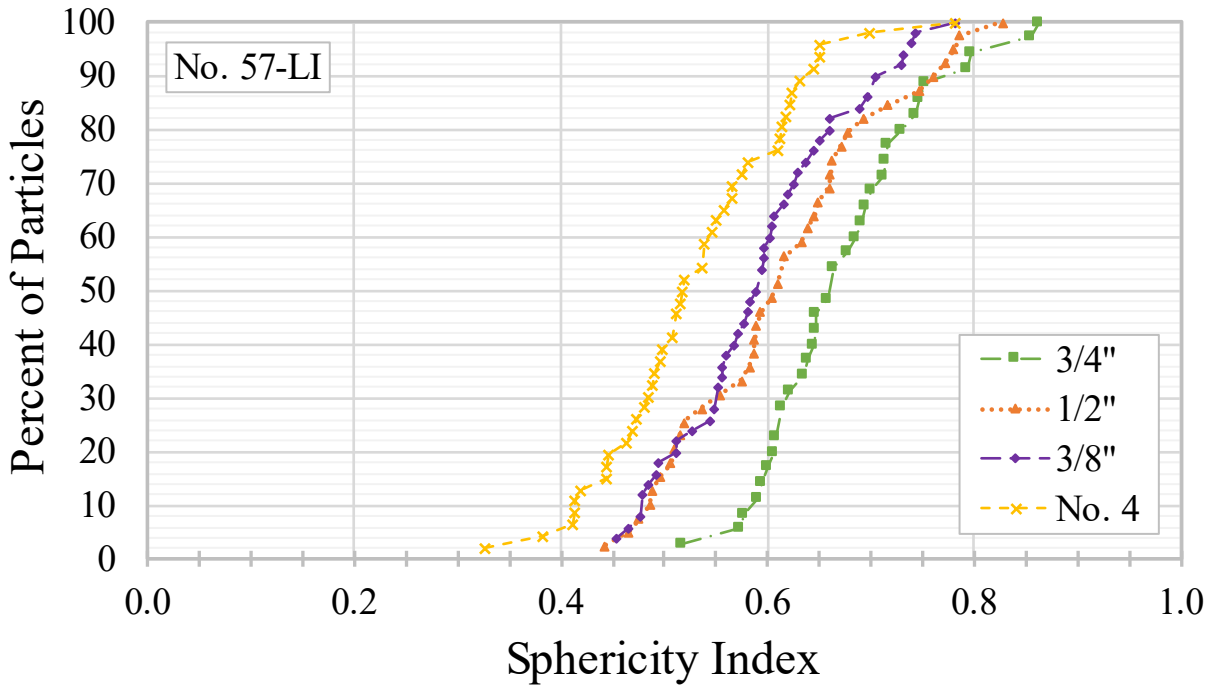

Source: FHWA.

C. SP.

Figure 61. Charts. AIMS2 cumulative distributions for No. 57-LI.

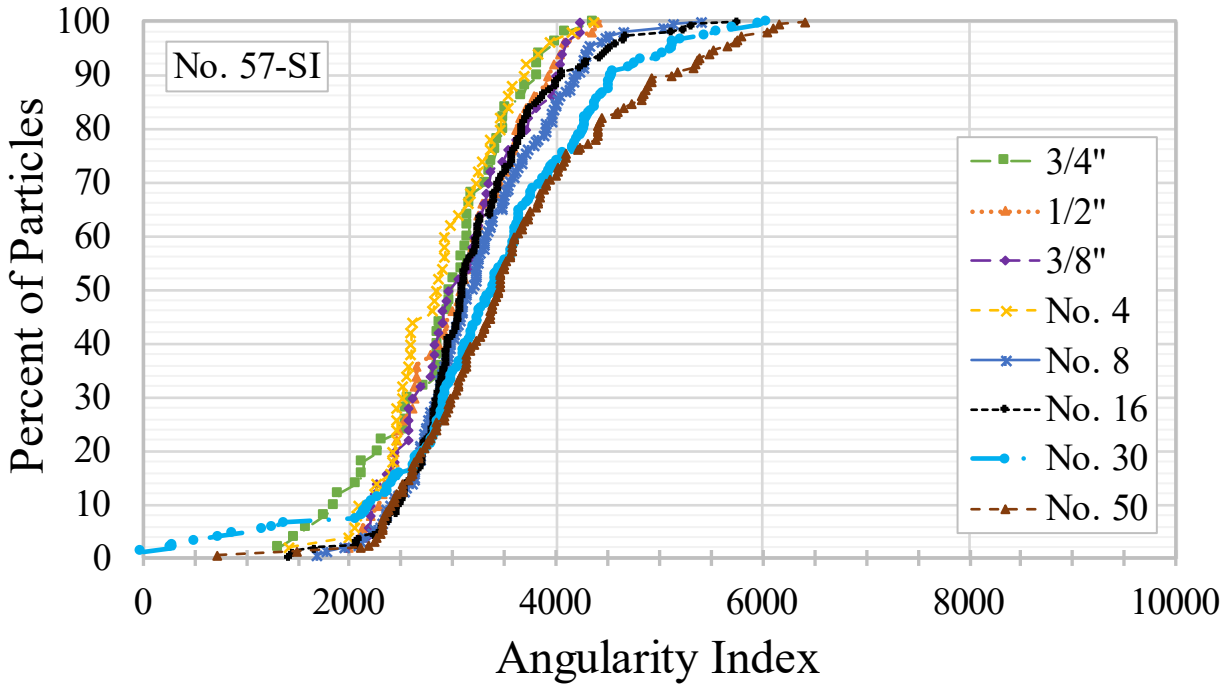

Source: FHWA.

A. Angularity.

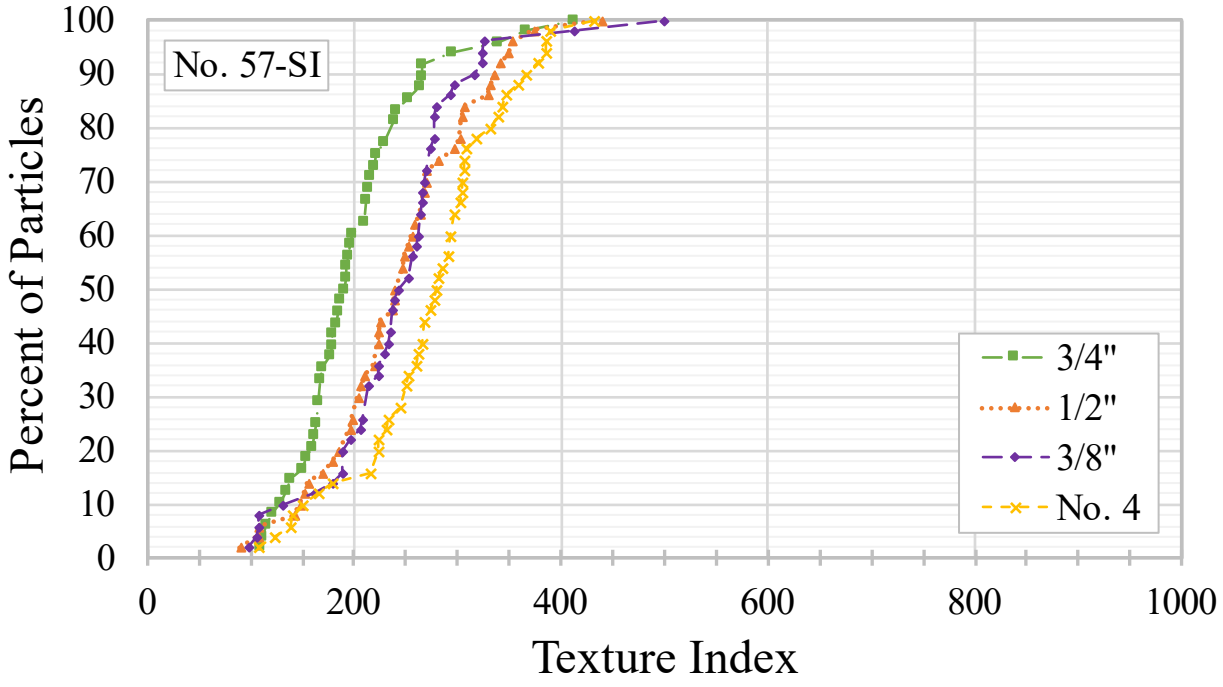

Source: FHWA.

B. TX.

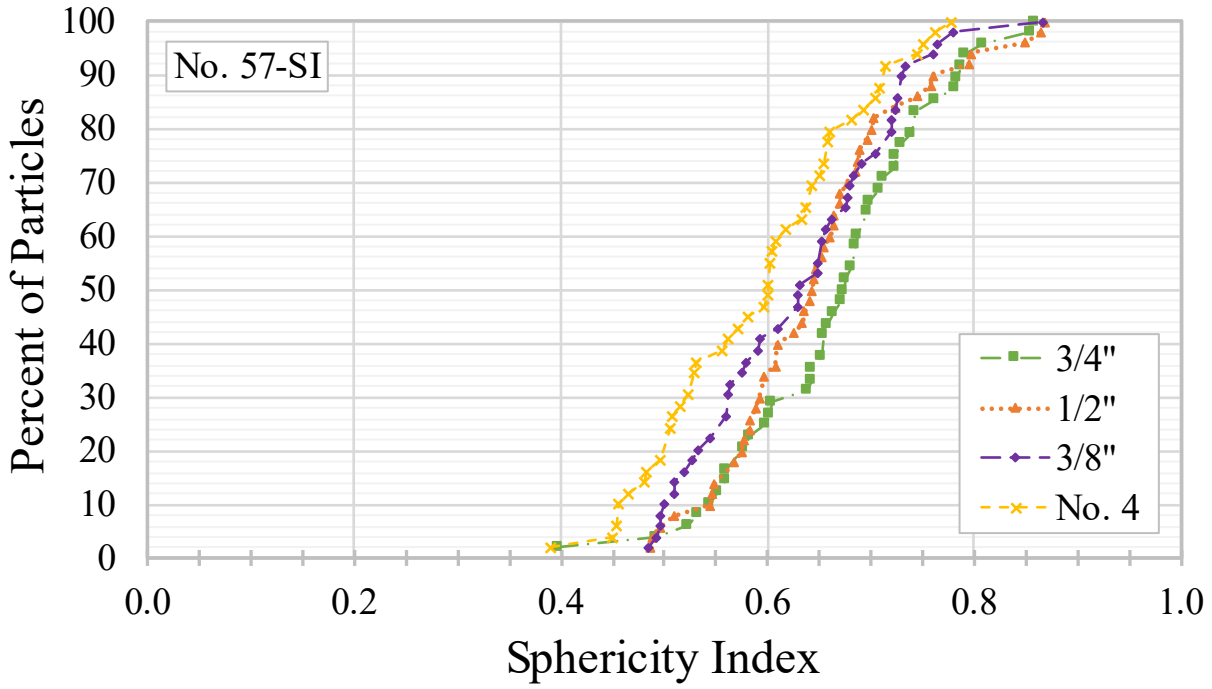

Source: FHWA.

C. SP.

Figure 62. Charts. AIMS2 cumulative distributions for No. 57-SI.

Summary tables with the weighted averages and F&E values are provided in table 52 and table 53, respectively.

Table 52. Summary of AIMS2 weighted averages for No. 57 OGAs.

Sample ID	Avg. GA Index	GA Classification	Avg. TX Index	TX Classification	Avg. SP Index	SP Classification
No. 57-BA	2948	Low	335	Medium	0.568	Medium
No. 57-DI	2957	Low	523	Medium	0.588	Medium
No. 57-GG	2934	Low	633	High	0.607	Medium
No. 57-LI	3177	Low	479	Medium	0.541	Medium
No. 57-SI	3031	Low	261	Medium	0.595	Medium
No. 57-Avg.	3009	Low	446	Medium	0.580	Medium

Table 53. Summary of AIMS2 weighted average F&E values for No. 57 OGAs.

Sample ID	F&E Distribution (Percent)				
	L/S ≥ 1:1	L/S > 2:1	L/S > 3:1	L/S > 4:1	L/S > 5:1
No. 57-BA	98.0	73.3	33.6	13.8	7.7
No. 57-DI	96.8	79.6	42.3	16.9	3.6
No. 57-GG	99.4	68.5	23.8	10.8	2.0
No. 57-LI	96.9	80.9	38.6	16.6	7.2
No. 57-SI	93.8	81.6	43.1	20.4	8.8
No. 57-Avg.	97.0	76.8	36.3	15.7	5.9

NO. 68 OGAs

The cumulative angularity, TX, and SP results are presented for No. 68-BA (figure 63), No. 68-DI (figure 64), No. 68-GG (figure 65), No. 68-LI (figure 66), and No. 68-SI (figure 67).

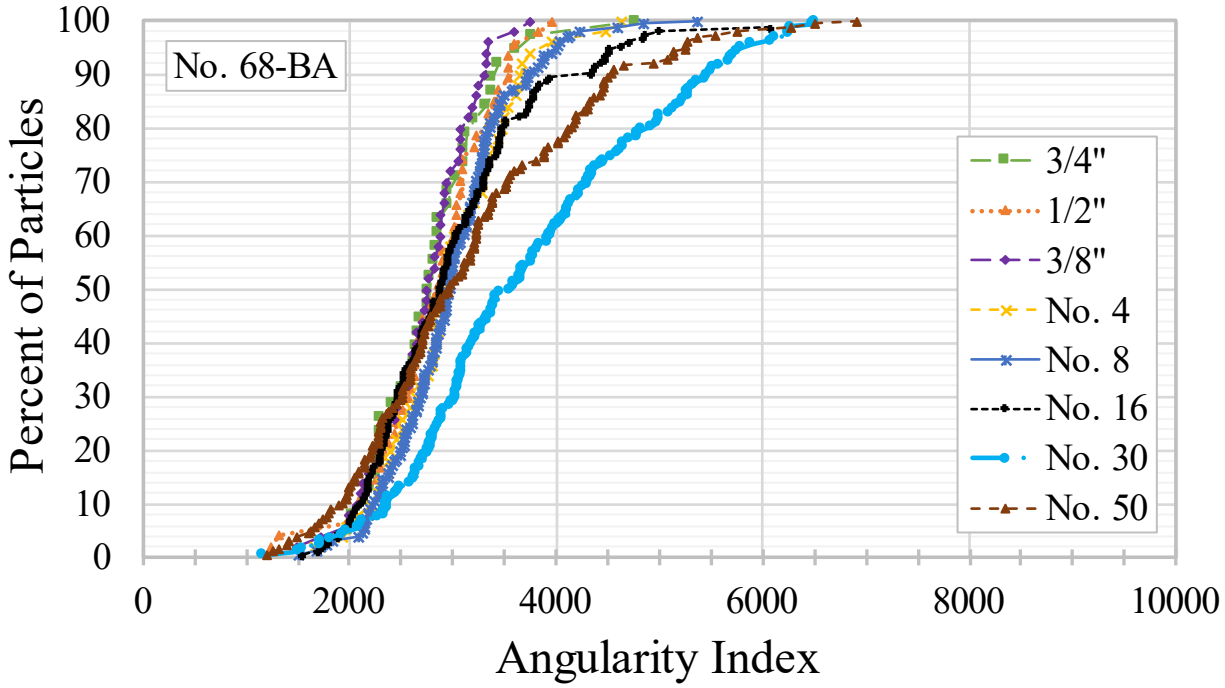

Source: FHWA.

A. Angularity.

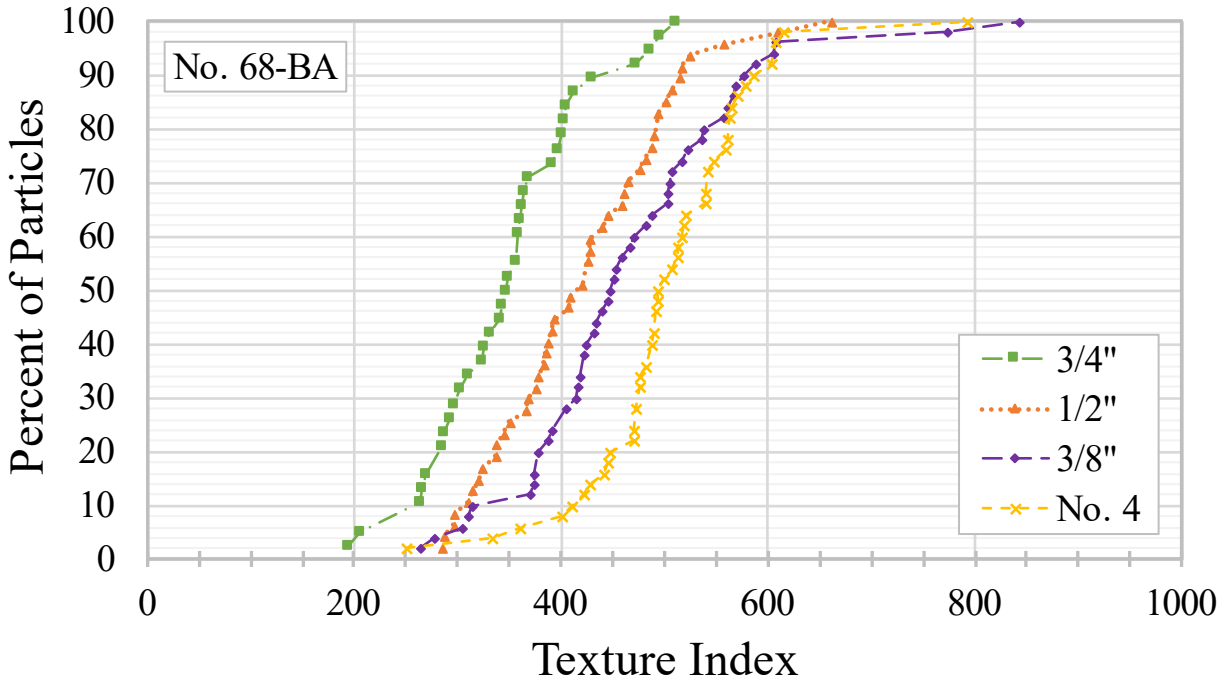

Source: FHWA.

B. TX.

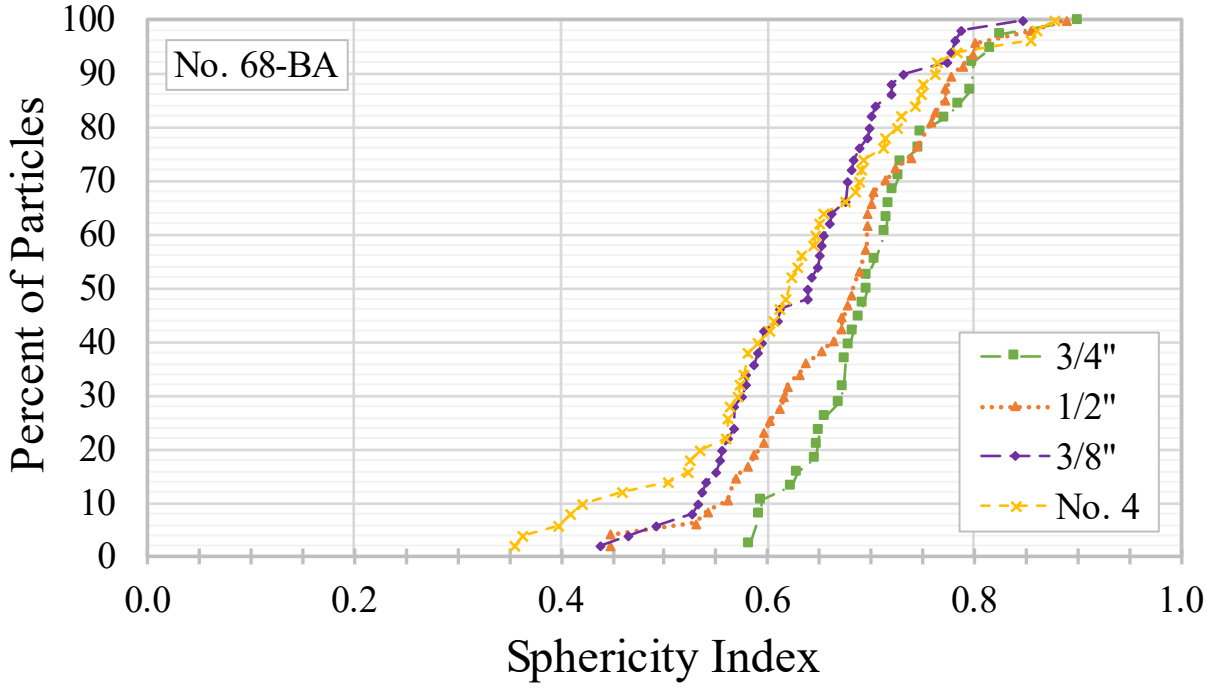

Source: FHWA.

C. SP.

Figure 63. Charts. AIMS2 cumulative distributions for No. 68-BA.

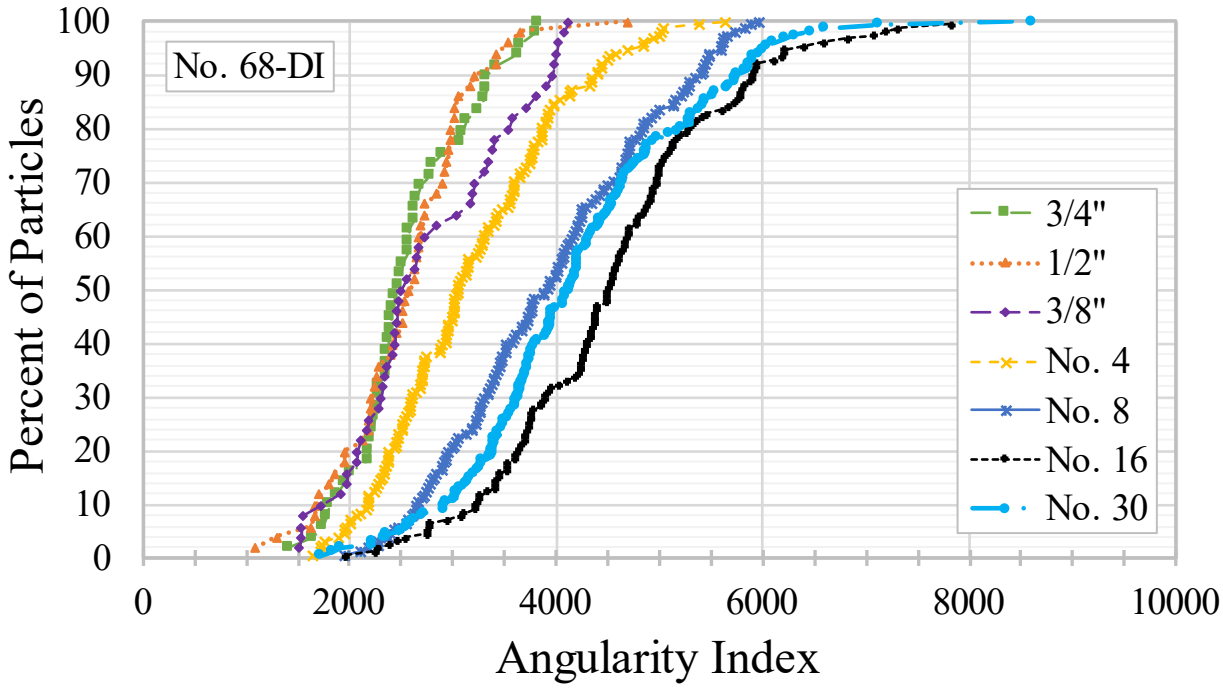

Source: FHWA.

A. Angularity.

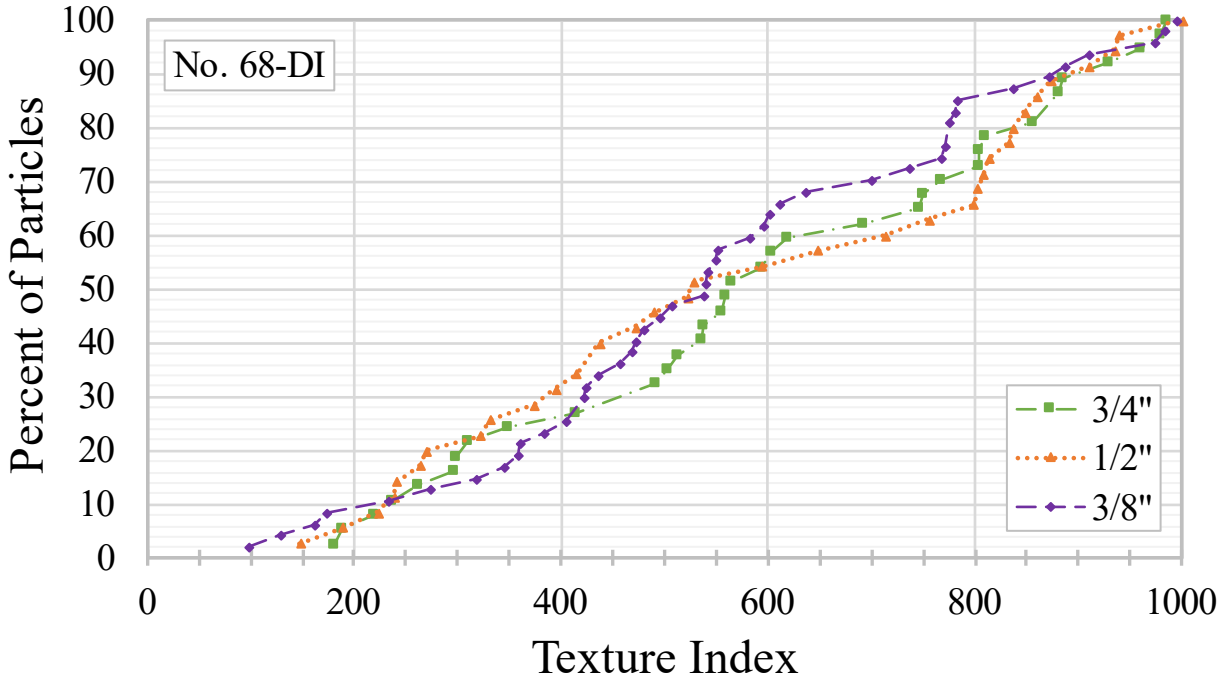

Source: FHWA.

B. TX.

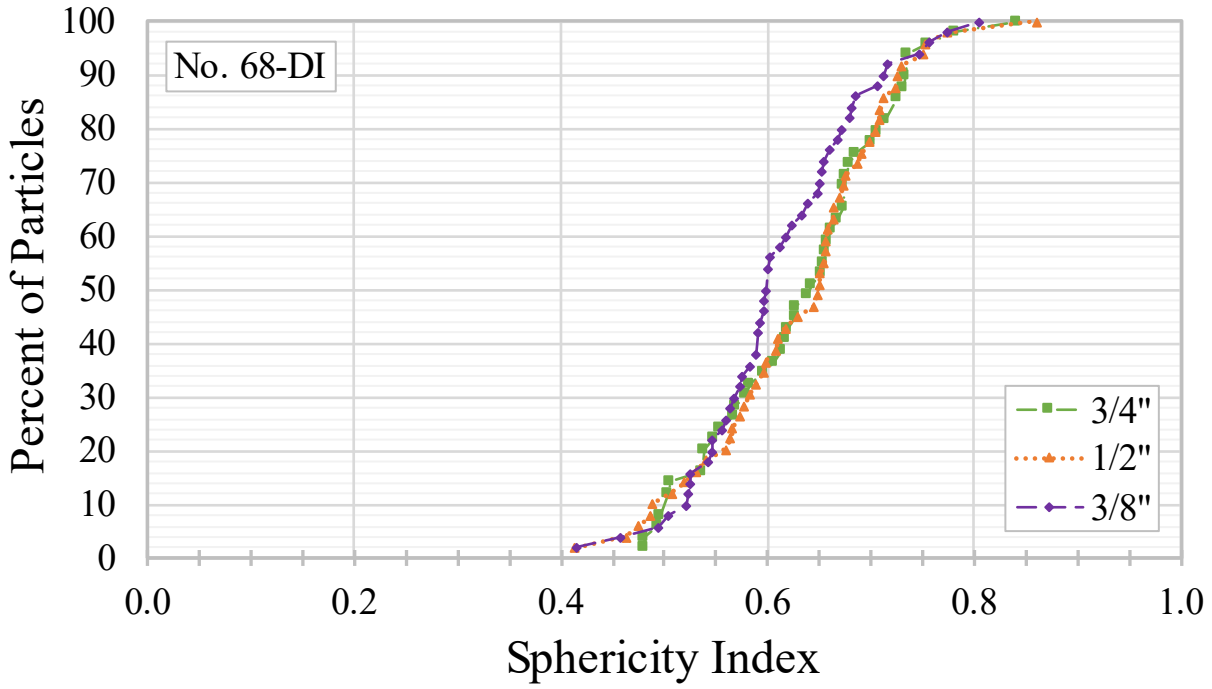

Source: FHWA.

C. SP.

Figure 64. Charts. AIMS2 cumulative distributions for No. 68-DI.

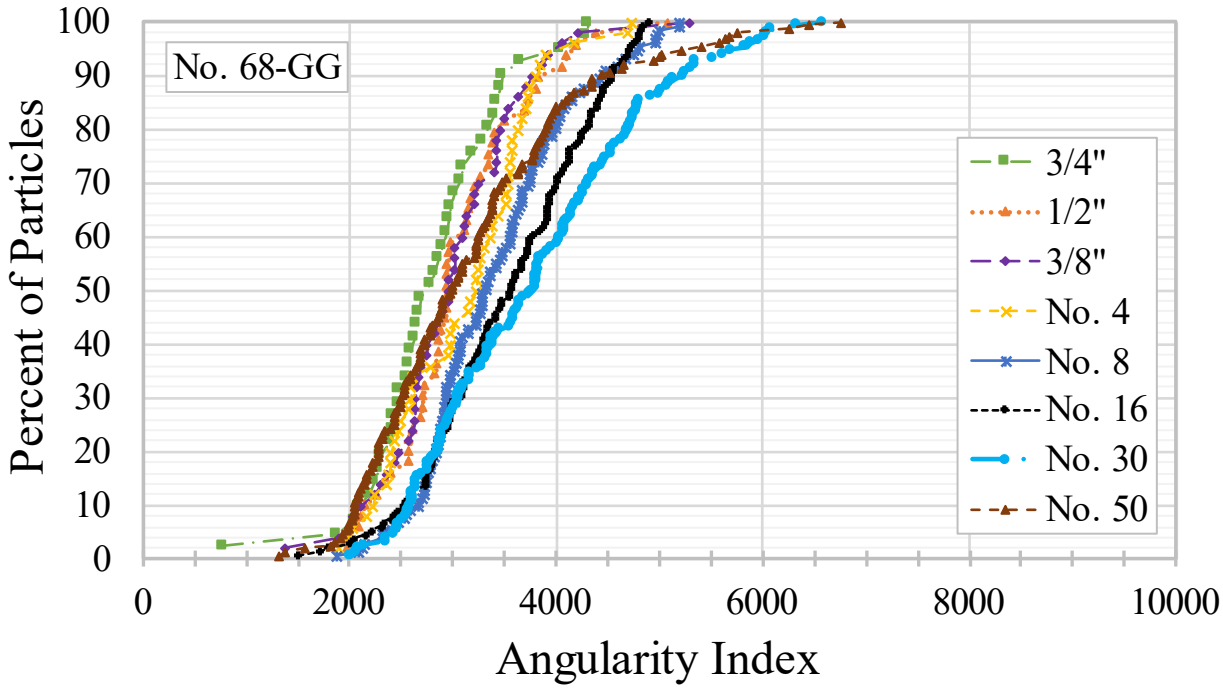

Source: FHWA.

A. Angularity.

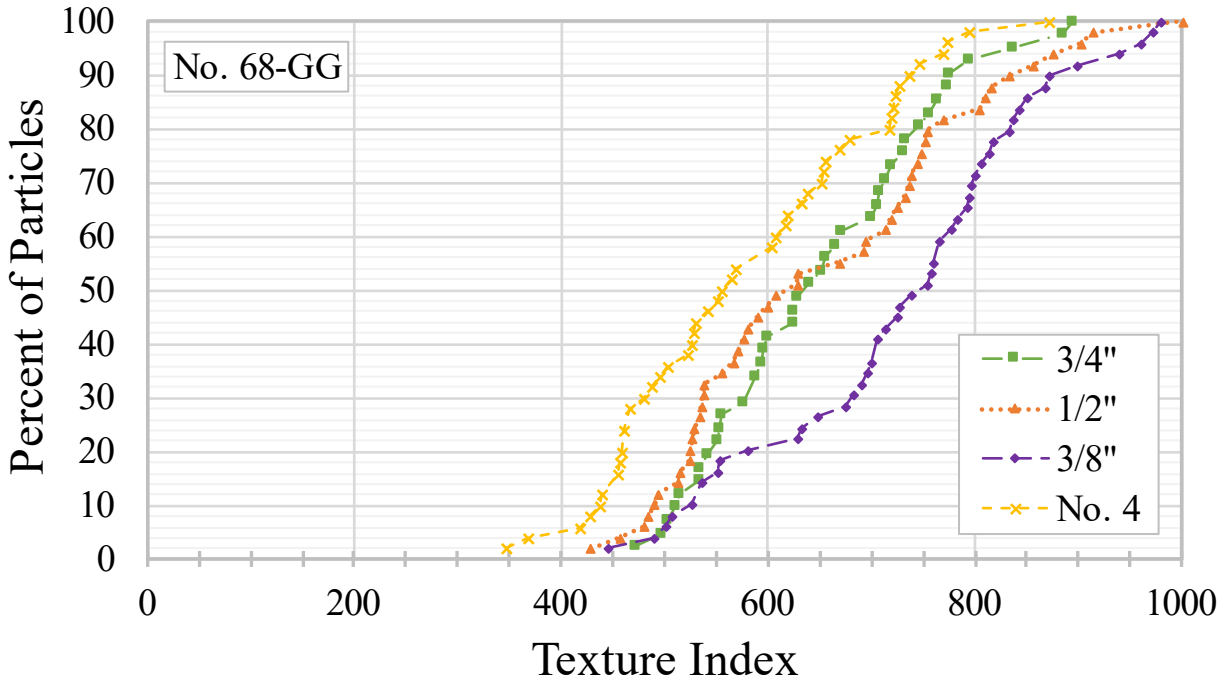

Source: FHWA.

B. TX.

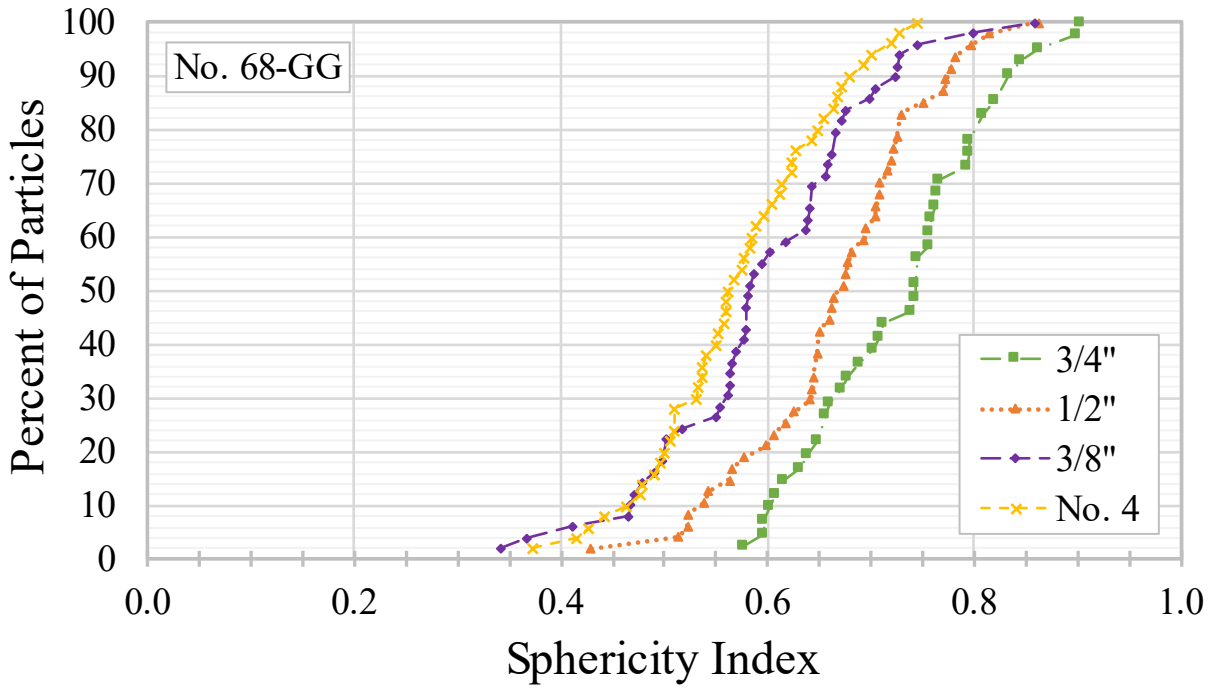

Source: FHWA.

C. SP.

Figure 65. Charts. AIMS2 cumulative distributions for No. 68-GG.

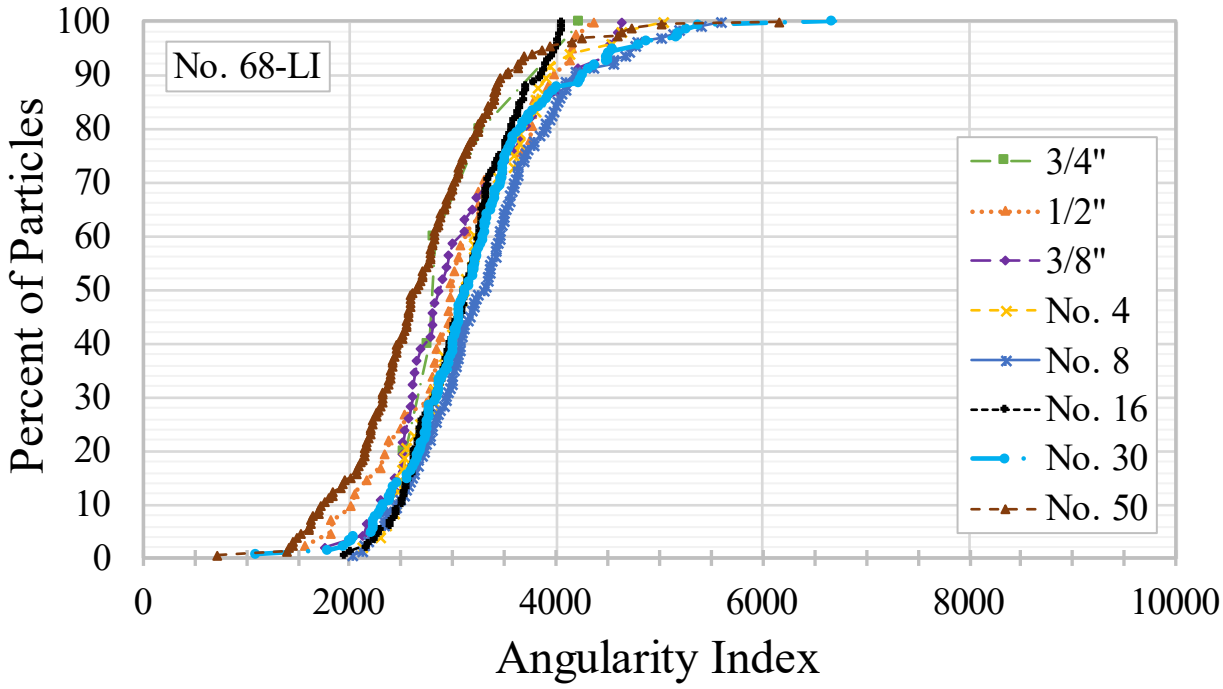

Source: FHWA.

A. Angularity.

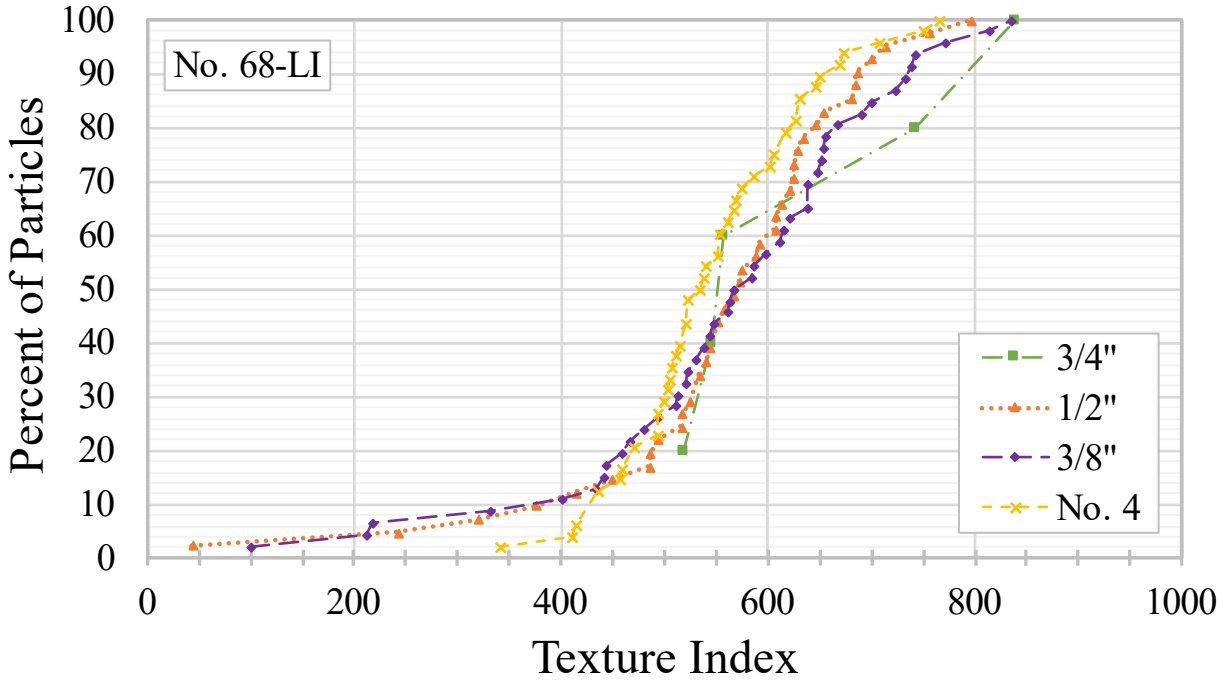

Source: FHWA.

B. TX.

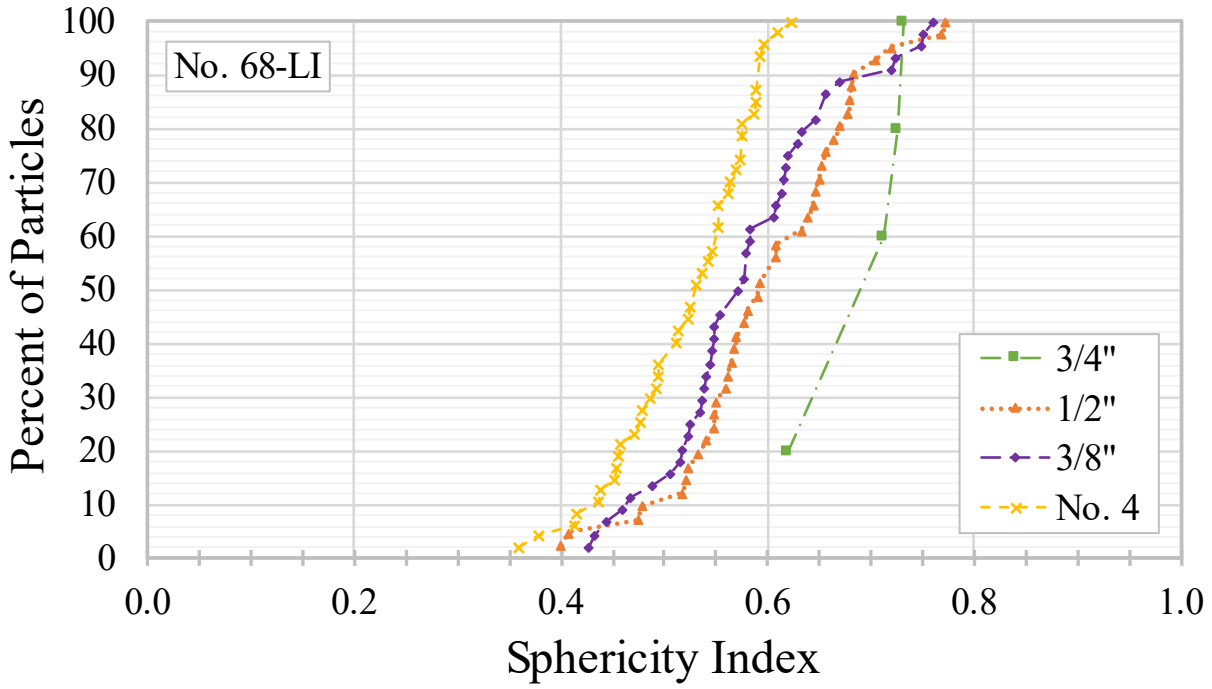

Source: FHWA.

C. SP.

Figure 66. Charts. AIMS2 cumulative distributions for No. 68-LI.

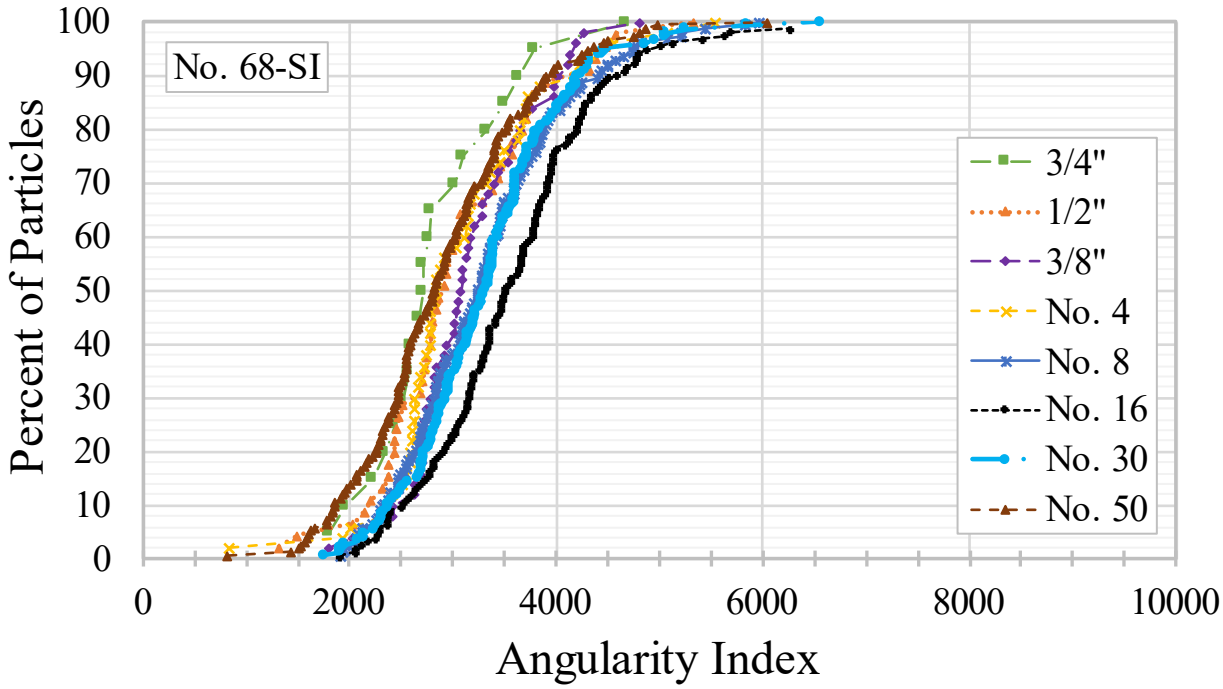

Source: FHWA.

A. Angularity.

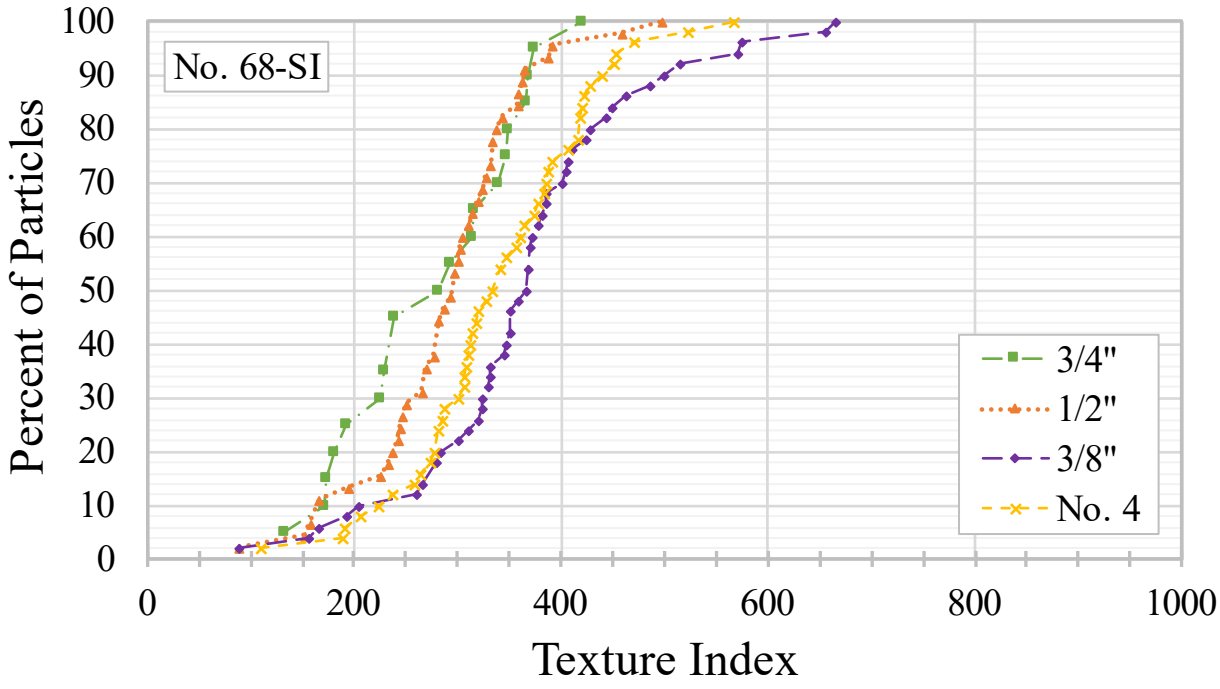

Source: FHWA.

B. TX.

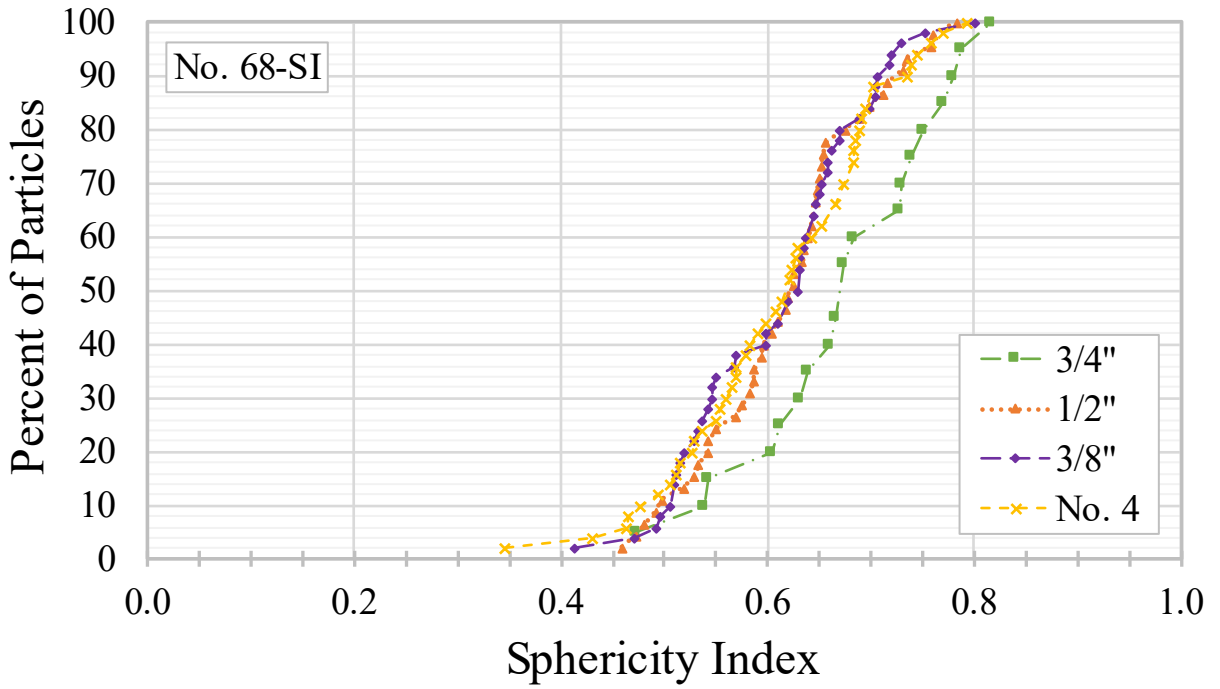

Source: FHWA.

C. SP.

Figure 67. Charts. AIMS2 cumulative distributions for No. 68-SI.

Summary tables with the weighted averages and F&E values are provided in table 54 and table 55, respectively.

Table 54. Summary of AIMS2 weighted averages for No. 68 OGAs.

Sample ID	Avg. GA Index	GA Classification	Avg. TX Index	TX Classification	Avg. SP Index	SP Classification
No. 68-BA	2956	Low	483	Medium	0.626	Medium
No. 68-DI	2936	Low	571	High	0.614	Medium
No. 68-GG	3158	Low	628	High	0.577	Medium
No. 68-LI	3185	Low	552	High	0.527	Medium
No. 68-SI	3147	Low	336	Medium	0.612	Medium
No. 68-avg.	3076	Low	514	Medium	0.591	Medium

Table 55. Summary of AIMS2 weighted average F&E values for No. 68 OGAs.

Sample ID	F&E Distribution (Percent)				
	L/S ≥ 1:1	L/S > 2:1	L/S > 3:1	L/S > 4:1	L/S > 5:1
No. 68-BA	86.4	67.8	30.1	12.0	6.3
No. 68-DI	94.2	85.6	43.8	16.8	4.7
No. 68-GG	95.9	81.5	46.0	18.1	7.5
No. 68-LI	90.1	87.6	66.5	32.9	11.6
No. 68-SI	92.0	82.6	45.7	20.3	9.4
No. 68-Avg.	91.7	81.0	46.4	20.0	7.9

NO. 8 OGAS

The cumulative angularity, TX, and SP results are presented for No. 8-BA (figure 68), No. 8-DI (figure 69), No. 8-GG (figure 70), No. 8-LI (figure 71), and No. 8-SI (figure 72).

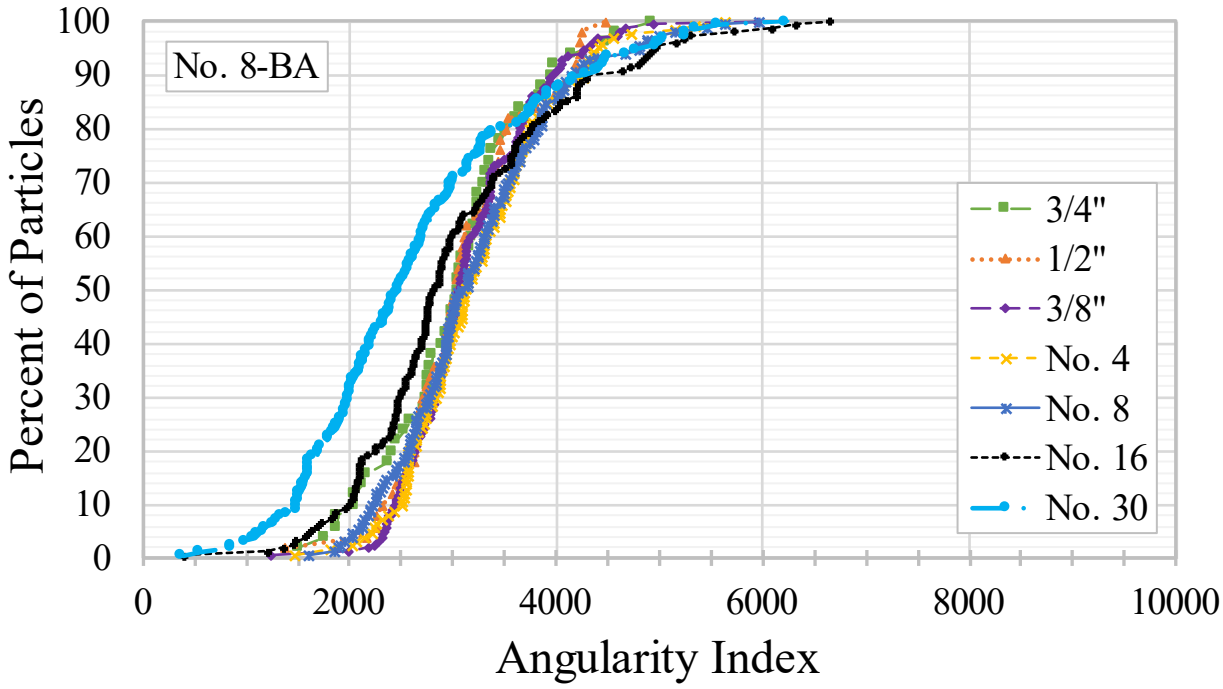

Source: FHWA.

A. Angularity.

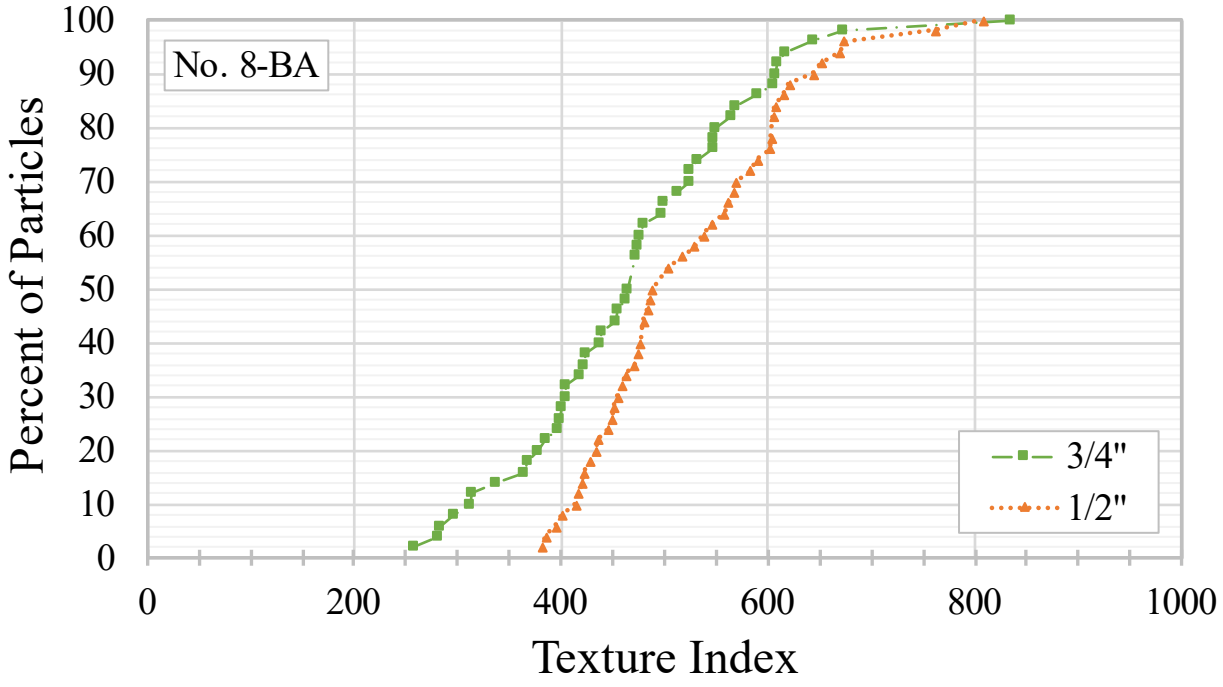

Source: FHWA.

B. TX.

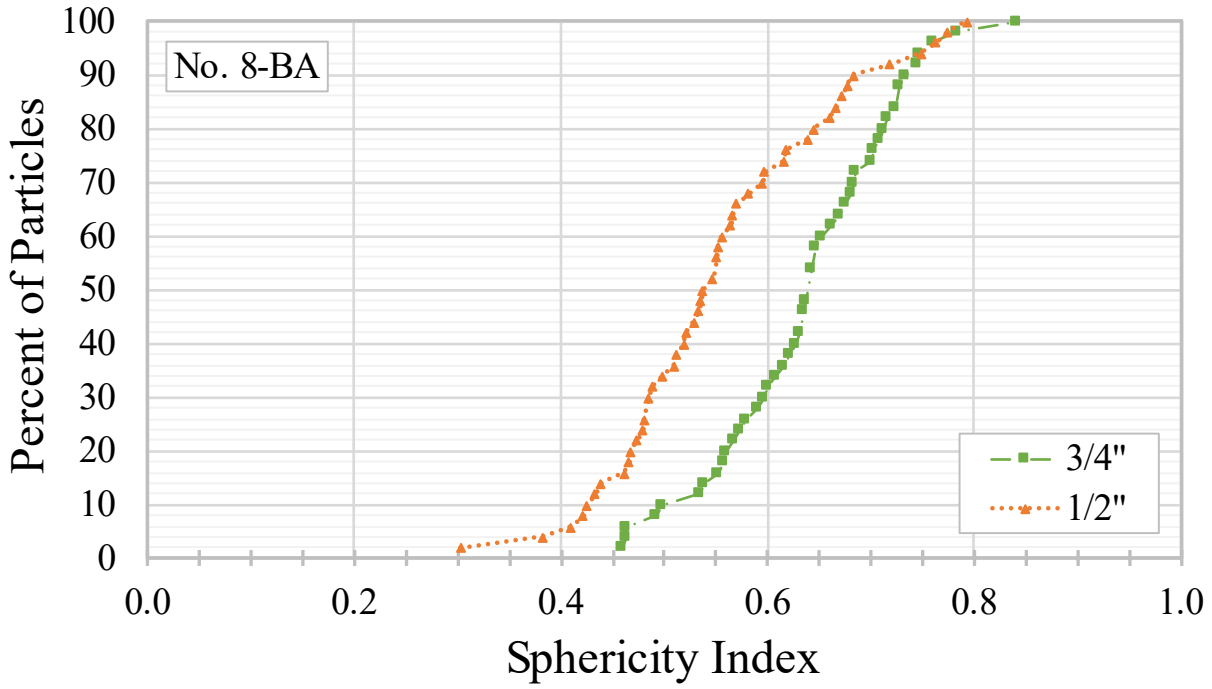

Source: FHWA.

C. SP.

Figure 68. Charts. AIMS2 cumulative distributions for No. 8-BA

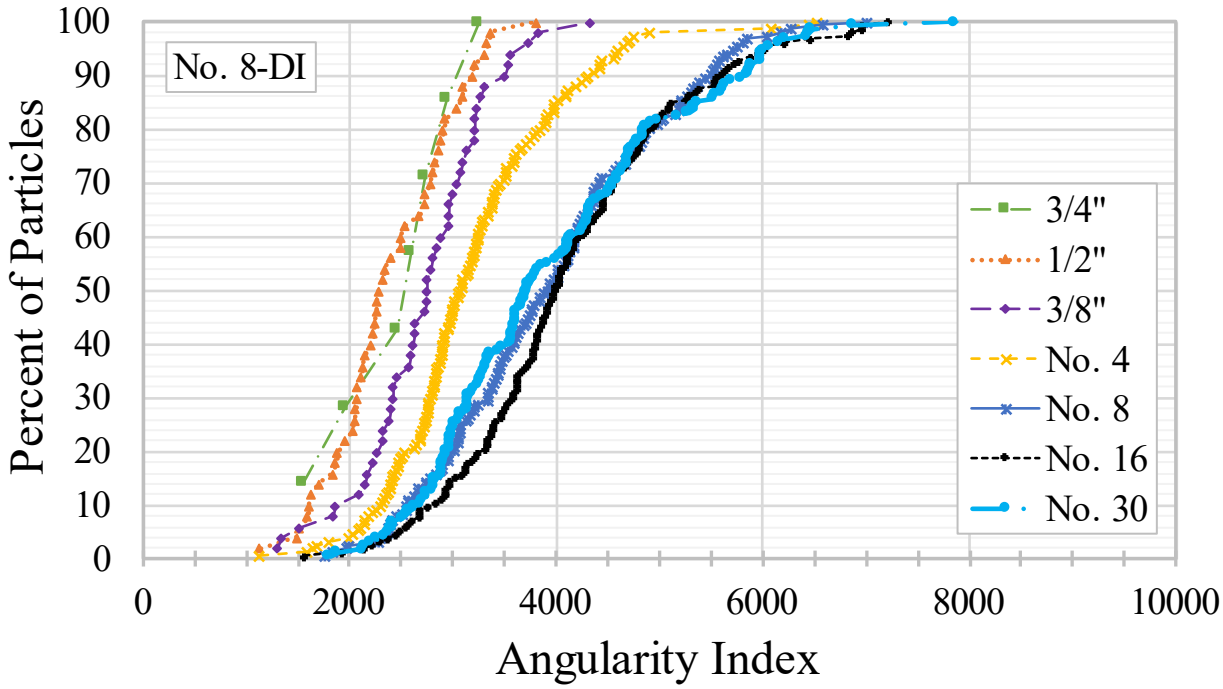

Source: FHWA.

A. Angularity.

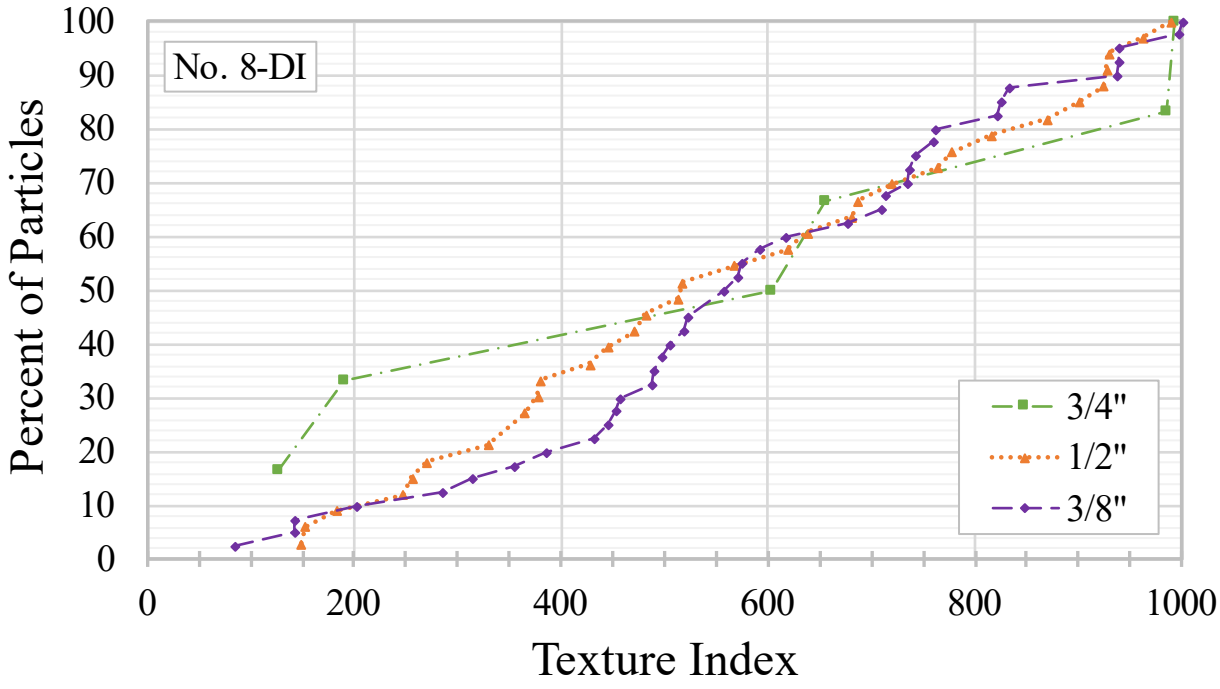

Source: FHWA.

B. TX.

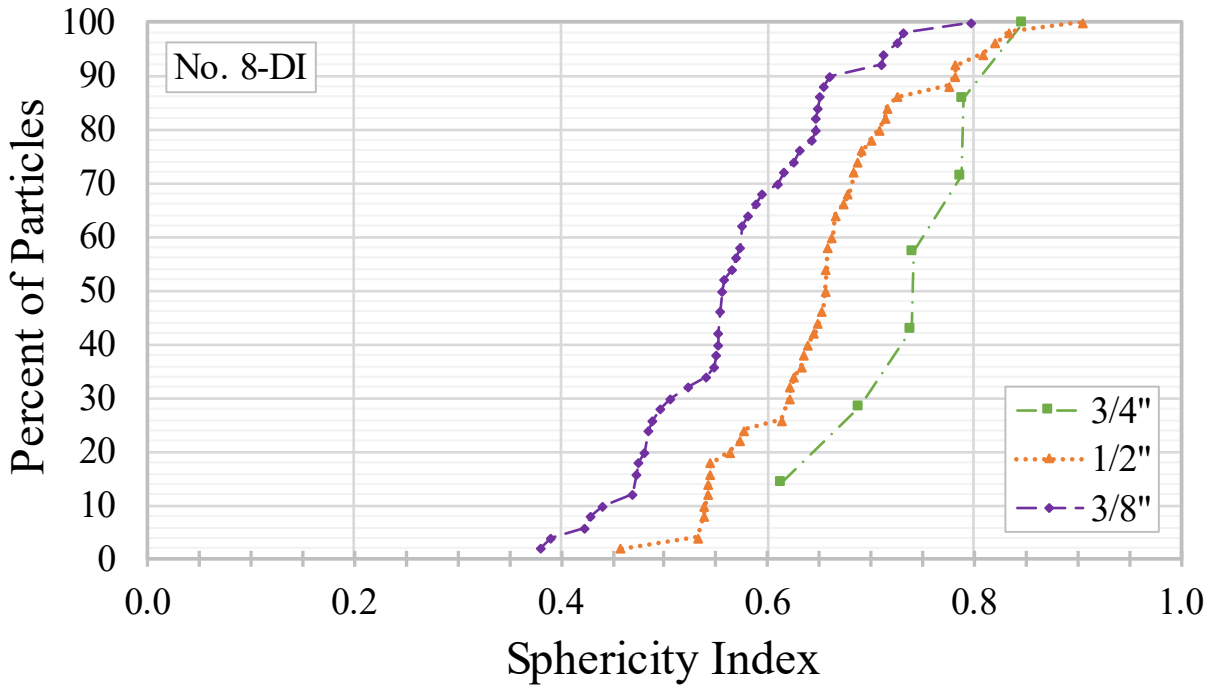

Source: FHWA.

C. SP.

Figure 69. Charts. AIMS2 cumulative distributions for No. 8-DI.

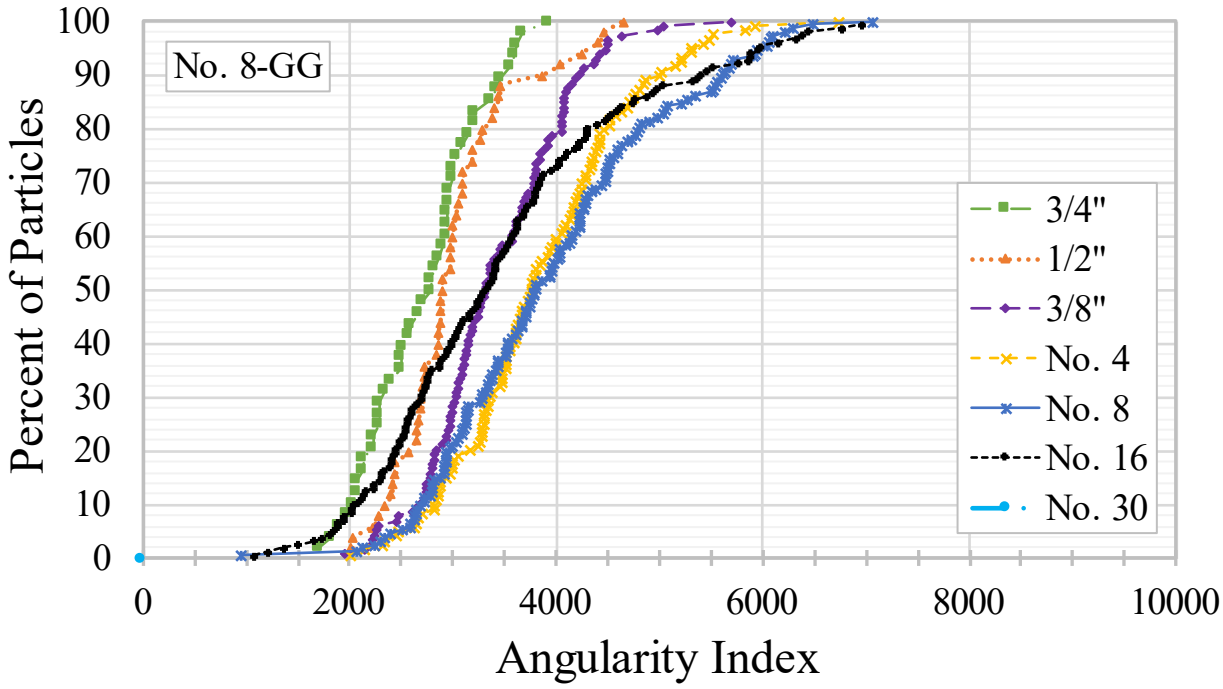

Source: FHWA.

A. Angularity.

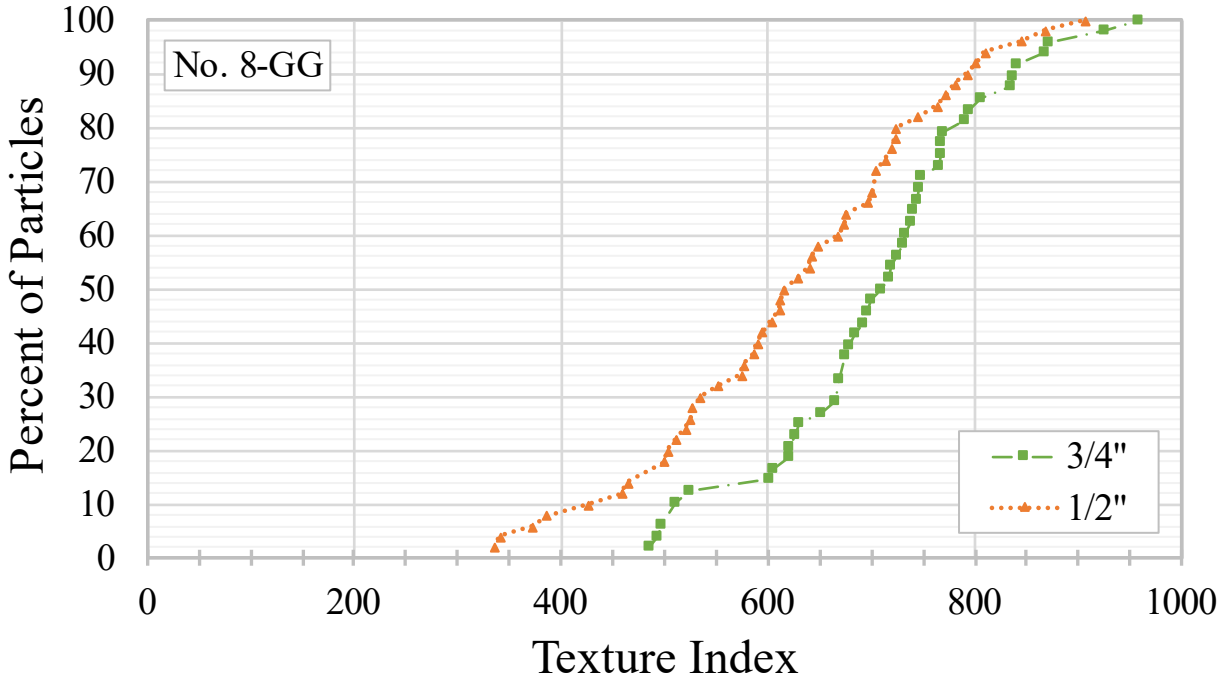

Source: FHWA.

B. TX.

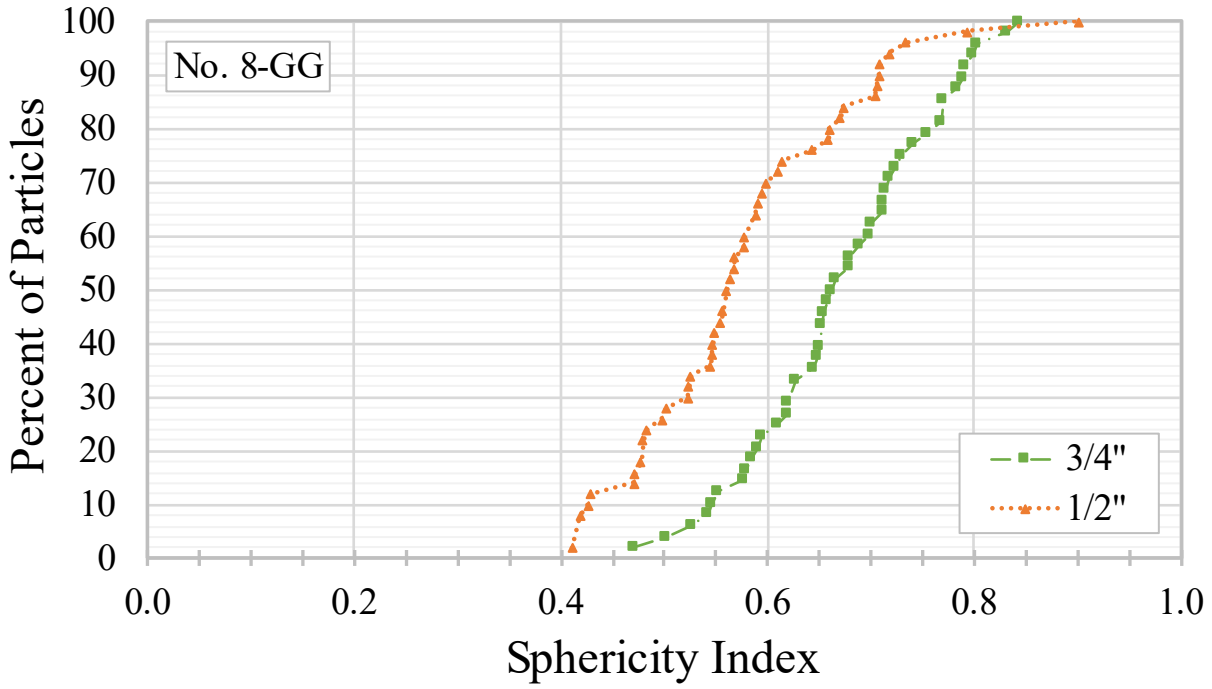

Source: FHWA.

C. SP.

Figure 70. Charts. AIMS2 cumulative distributions for No. 8-GG.

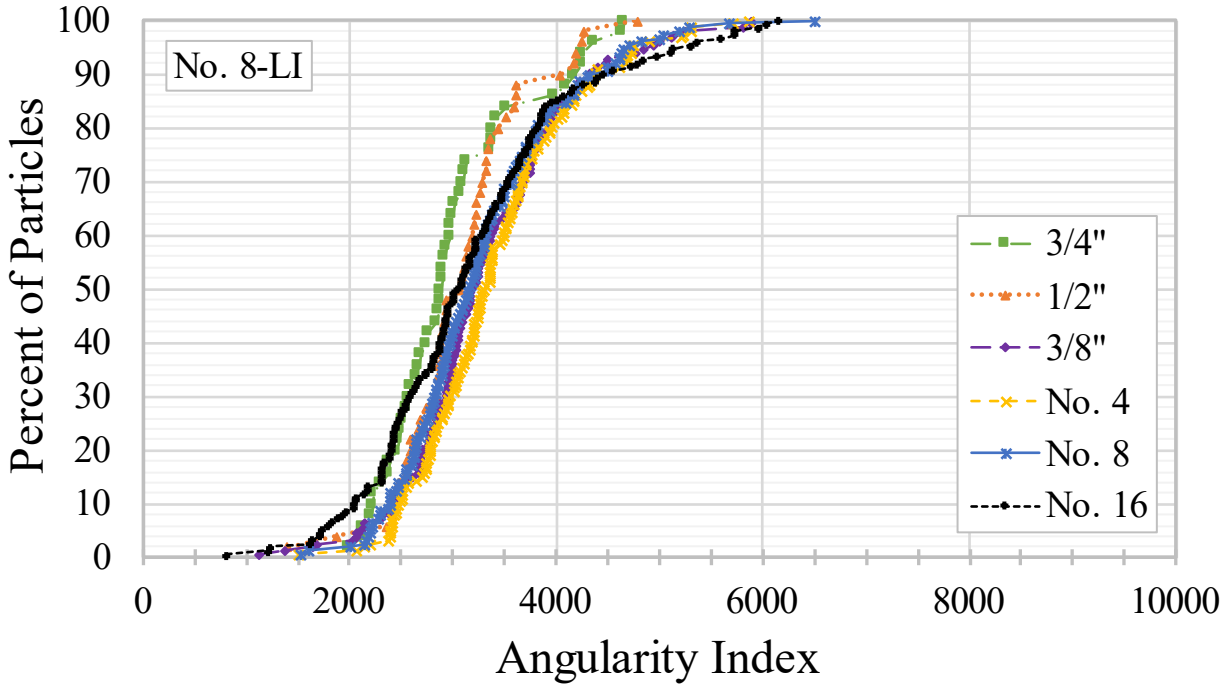

Source: FHWA.

A. Angularity.

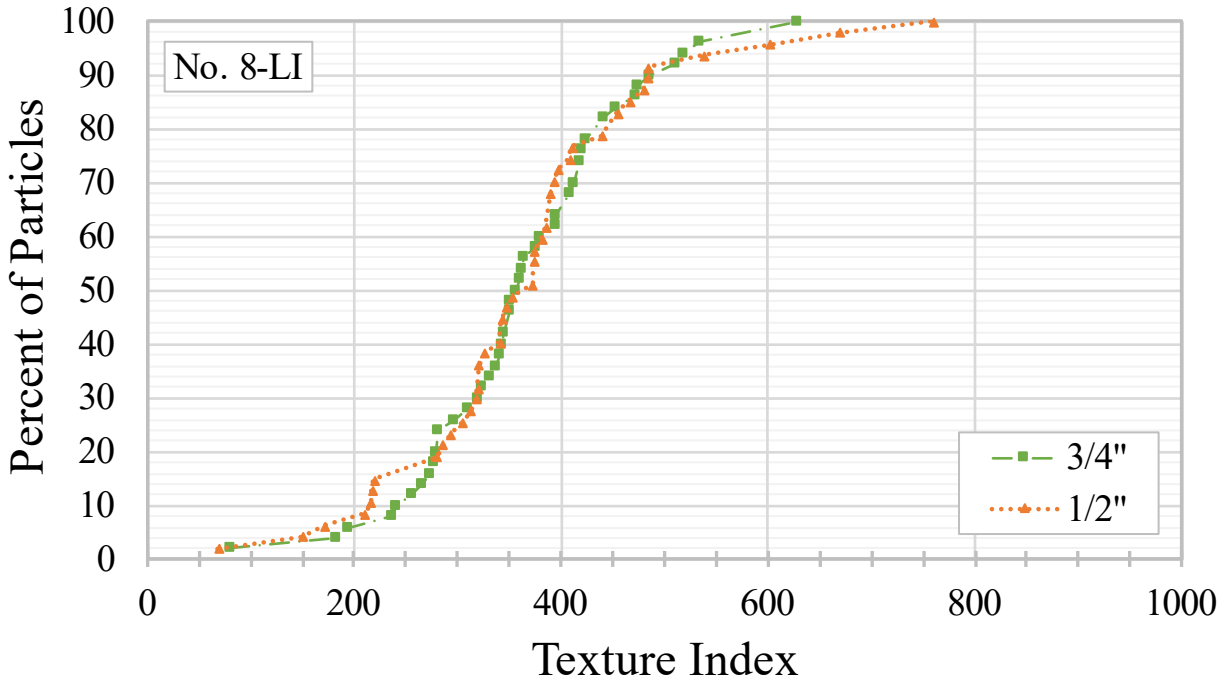

Source: FHWA.

B. TX.

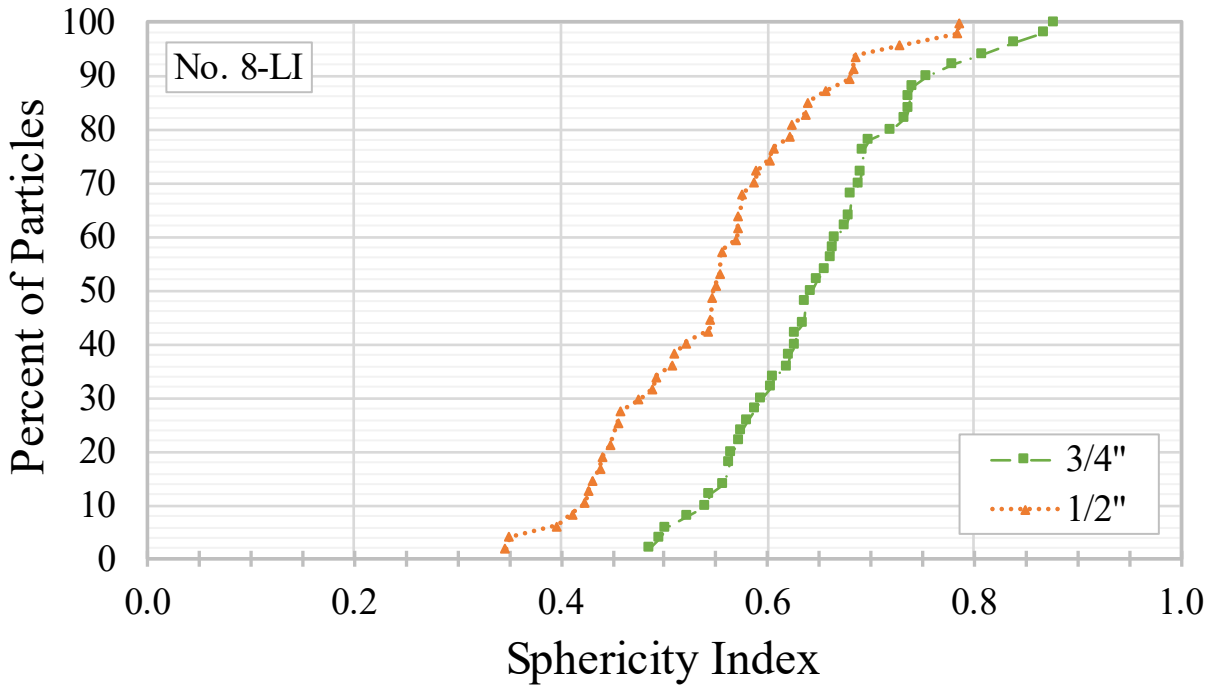

Source: FHWA.

C. SP.

Figure 71. Charts. AIMS2 cumulative distributions for No. 8-LI.

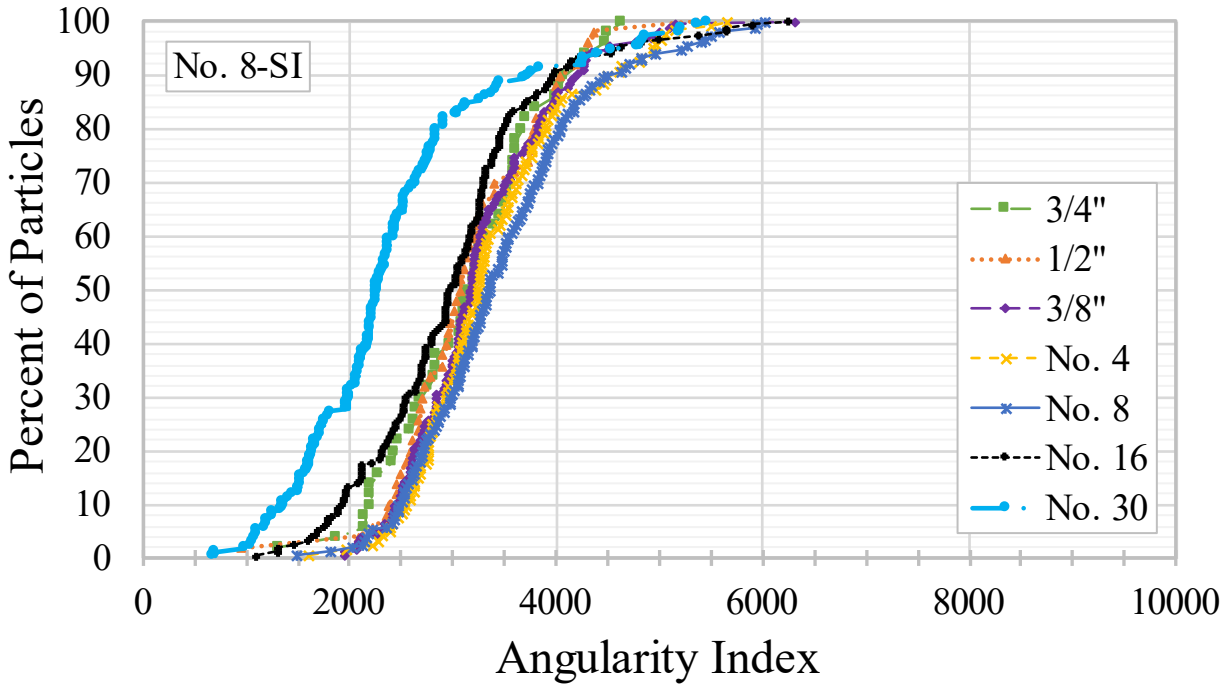

Source: FHWA.

A. Angularity.

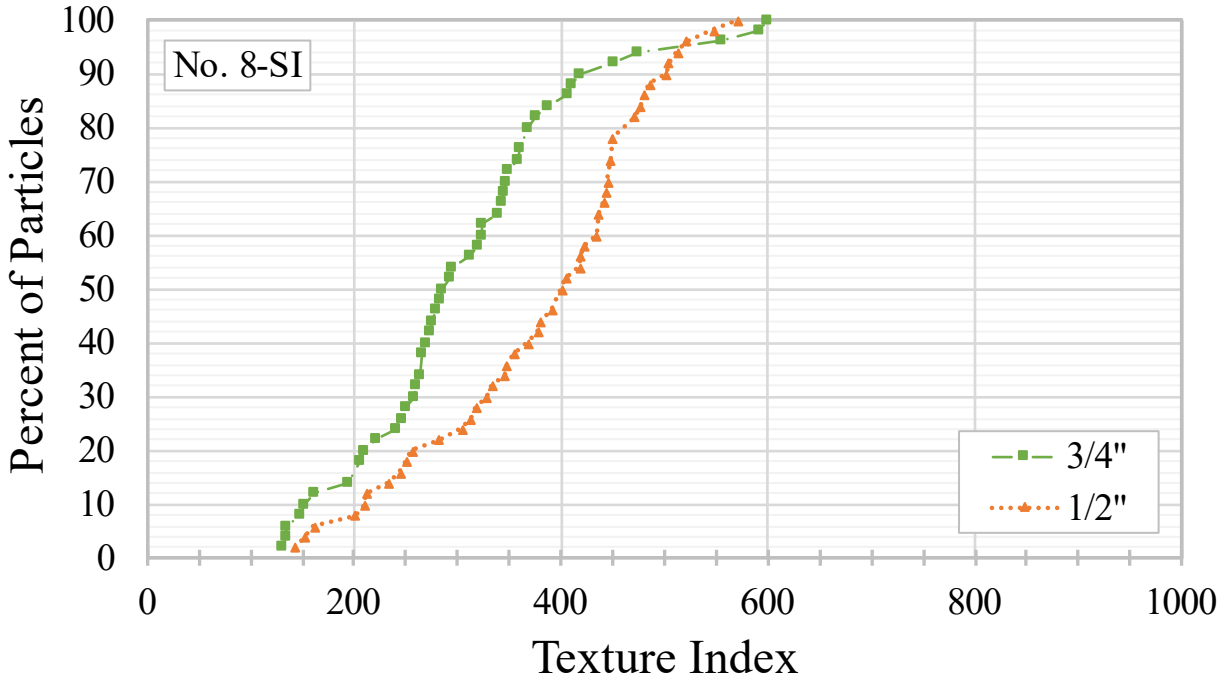

Source: FHWA.

B. TX.

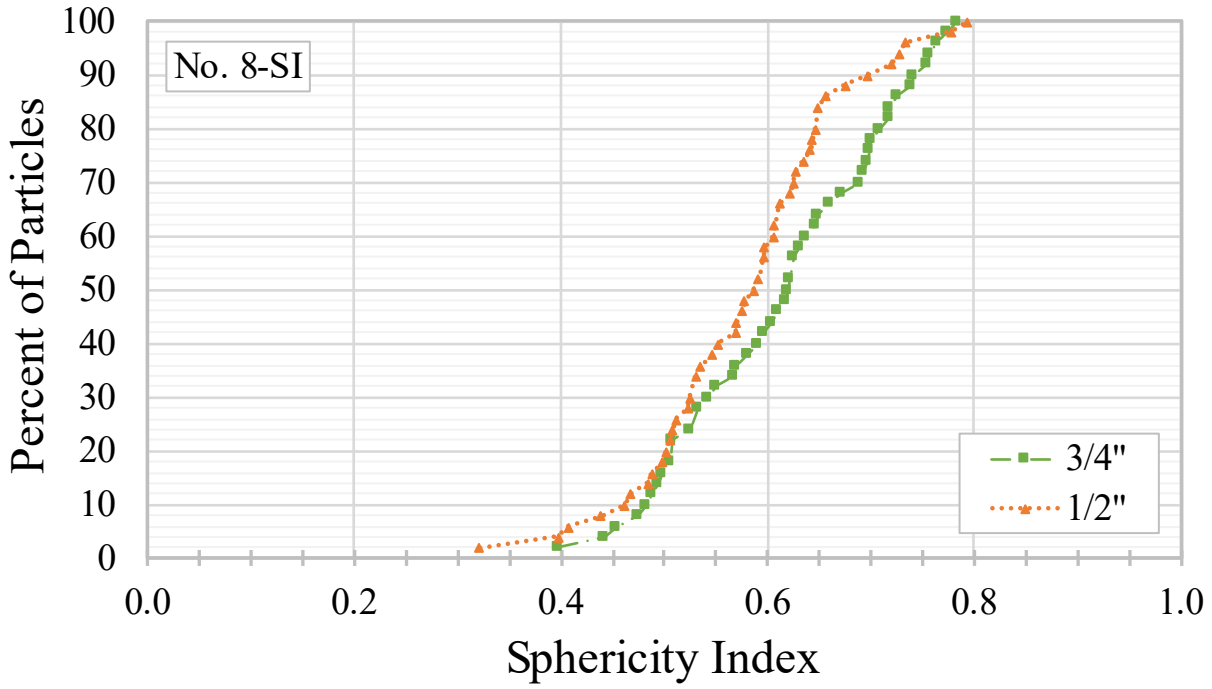

Source: FHWA.

C. SP.

Figure 72. Charts. AIMS2 cumulative distributions for No. 8-SI.

Summary tables with the weighted averages and F&E values are provided in table 56 and table 57, respectively.

Table 56. Summary of AIMS2 weighted averages for No. 8 OGAs.

Sample ID	Avg. GA Index	GA Classification	Avg. TX Index	TX Classification	Avg. SP Index	SP Classification
No. 8-BA	3131	Low	518	Medium	0.556	Medium
No. 8-DI	2922	Low	582	High	0.567	Medium
No. 8-GG	3147	Low	630	High	0.576	Medium
No. 8-LI	3209	Low	366	Medium	0.547	Medium
No. 8-SI	3192	Low	372	Medium	0.580	Medium
No. 8-Avg.	3120	Low	494	Medium	0.565	Medium

Table 57. Summary of AIMS2 weighted average F&E values for No. 8 OGAs.

Sample ID	F&E Distribution (Percent)				
	L/S ≥ 1:1	L/S > 2:1	L/S > 3:1	L/S > 4:1	L/S > 5:1
No. 8-BA	80.6	73.4	57.1	38.9	21.8
No. 8-DI	82.6	78.3	49.1	22.0	9.3
No. 8-GG	92.0	83.6	50.8	31.1	11.4
No. 8-LI	74.2	67.8	50.1	31.8	19.9
No. 8-SI	76.8	72.2	46.9	23.8	16.4
No. 8-Avg.	81.2	75.1	50.8	29.5	15.8

APPENDIX D. LSDS TEST RESULTS

This appendix contains the main results of LSDS testing by each laboratory for all tested materials, including shear stress versus horizontal strain, vertical strain versus horizontal strain, and linear Mohr-Coulomb failure envelopes. The plots shown in this appendix are followed by summary tables containing the initial shear stress before zeroing reported in each laboratory's raw data, normal stress at peak shear, peak and residual shear stresses, secant friction angles at peak and residual shear, and maximum dilation angle for each applied nominal normal stress alongside the tangent friction angle at peak, c_a, tangent friction angle at residual shear stress, and constant volume friction angle from each four-point test series.

OS-20-30

The shear stress versus horizontal strain curves for OS-20-30 are shown in figure 73. The vertical strain versus horizontal strain curves for OS-20-20 are shown in figure 74, with the linear Mohr-Coulomb failure envelopes shown in figure 75. A full summary of results can be found in table 58.

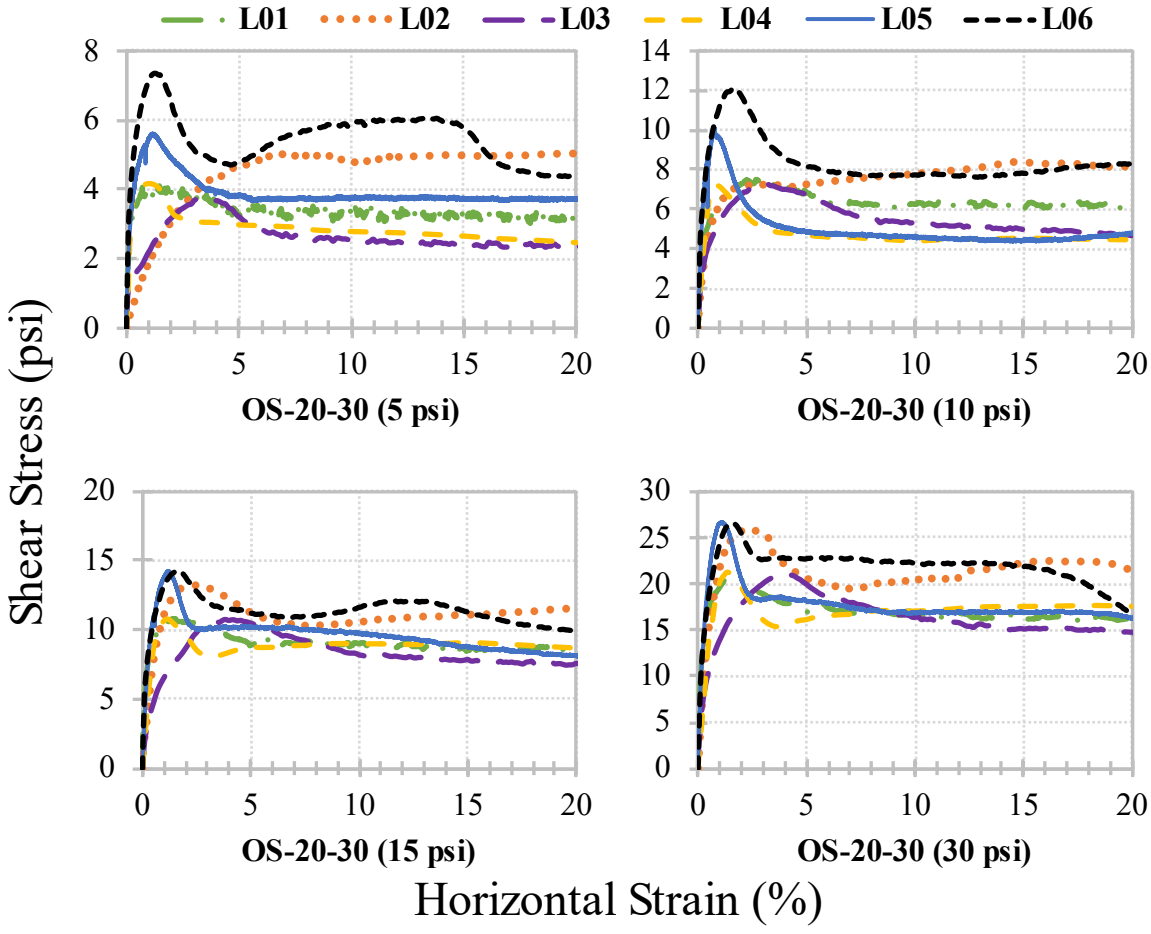

Source: FHWA.

Figure 73. Charts. Shear stress versus horizontal strain for OS-20-30.

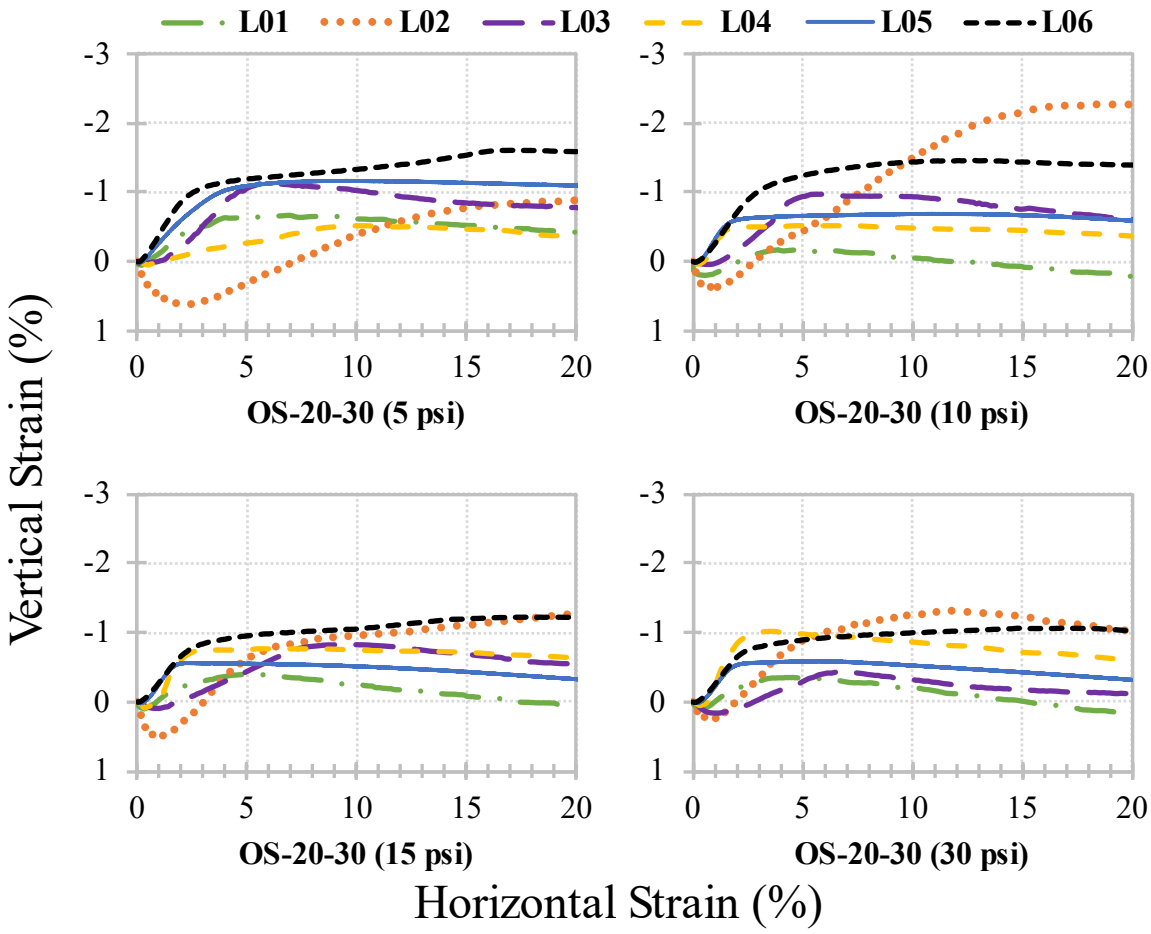

Source: FHWA.

Figure 74. Charts. Vertical strain versus horizontal strain for OS-20-30.

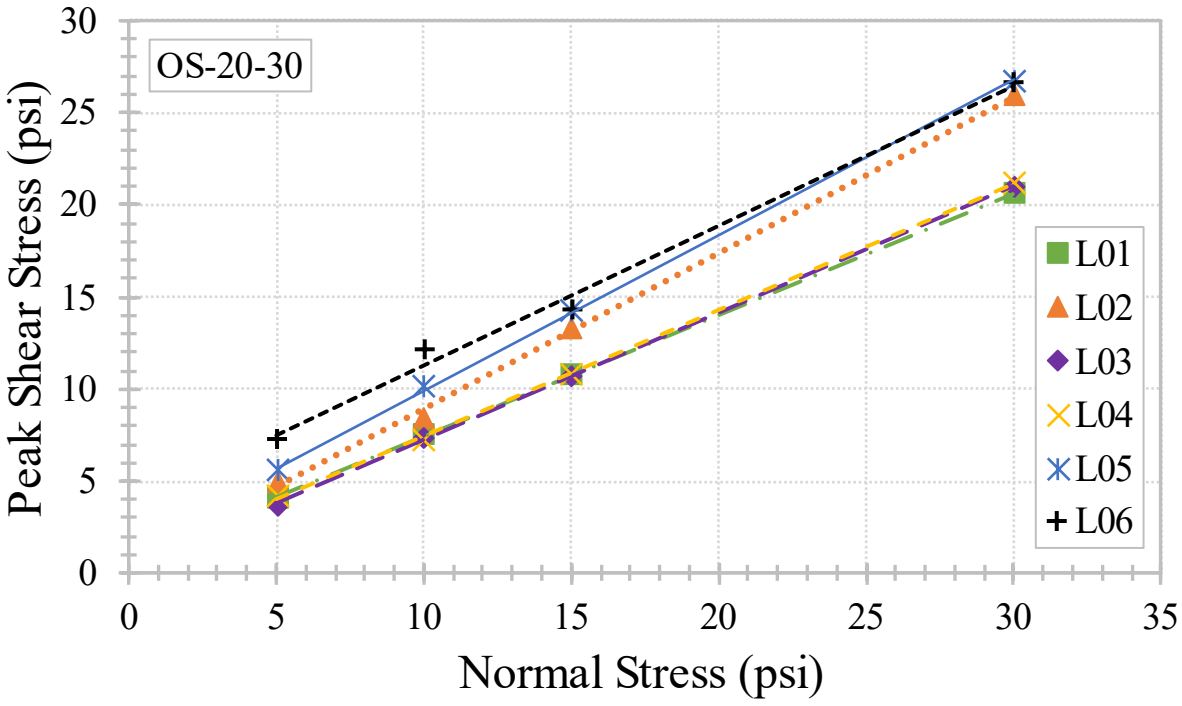

Source: FHWA.

Figure 75. Chart. Linear Mohr-Coulomb failure envelopes for OS-20-30.

Table 58. Summary of LSDS results for OS-20-30.

Lab ID	Target σ_n (psi)	$\tau_{initial}$ (psi)	σ_n at τ_{peak} (psi)	τ_{peak} (psi)	τ_r (psi)	ϕ_s (deg)	ϕ_r (deg)	ψ_{max} (deg)	ϕ_t (deg)	c_a (psi)	$\phi_{t,r}$ (deg)	ϕ_{cv} (deg)
L01	5	0.2	5.2	4.1	3.1	39.4	32.0	9.6	34.5	0.9	29.2	32.4
	10	0.1	10.1	7.5	6.1	36.9	31.3	5.9				
	15	0.1	15.1	10.8	8.7	35.8	30.0	8.7				
	30	0.1	30.1	20.6	16.4	34.5	28.7	7.7				
L02	5	0.0	5.0	5.0	5.0	45.3	45.2	10.6	40.0	0.5	36.5	48.4
	10	0.0	10.0	8.4	8.1	40.0	39.1	14.3				
	15	0.0	15.0	13.3	11.6	41.5	37.6	14.3				
	30	0.0	30.0	25.9	21.6	40.8	35.7	19.6				
L03	5	0.1	5.0	3.7	2.4	36.8	25.2	14.4	37.1	0.4	26.2	34.3
	10	0.2	10.0	7.3	4.7	36.0	25.0	15.6				
	15	0.0	14.9	10.7	7.5	35.6	26.7	9.6				
	30	0.1	30.0	21.0	14.7	35.0	26.2	4.9				
L04	5	0.0	5.0	4.2	2.5	39.8	26.2	5.7	36.7	0.5	29.7	41.1
	10	0.0	10.0	7.2	4.5	35.8	24.0	21.8				
	15	0.0	15.0	10.8	8.7	35.7	30.1	24.2				
	30	0.0	30.0	21.2	17.5	35.3	30.3	24.2				
L05	5	0.6	5.1	5.6	3.7	48.3	36.8	15.2	3.0	1.6	28.4	44.7
	10	0.1	10.0	10.1	4.8	45.4	25.5	18.4				
	15	0.1	15.1	14.2	8.1	43.5	28.5	16.9				
	30	1.2	30.2	26.7	16.2	41.6	28.4	15.3				
L06	5	0.0	5.1	7.3	4.4	55.8	41.1	19.3	8.2	3.7	31.1	−0.7
	10	−0.2	10.1	12.1	8.3	50.3	39.7	16.4				
	15	2.1	15.1	14.3	9.9	43.6	33.4	14.7				
	30	3.4	30.1	26.6	16.7	41.5	29.2	15.0				

NO. 57 OGAs

The shear stress versus horizontal strain, vertical strain versus horizontal strain, and linear Mohr-Coulomb failure envelopes for No. 57-BA are shown in figure 76, figure 77, and figure 78, respectively. The full summary of LSDS results is presented in table 59.

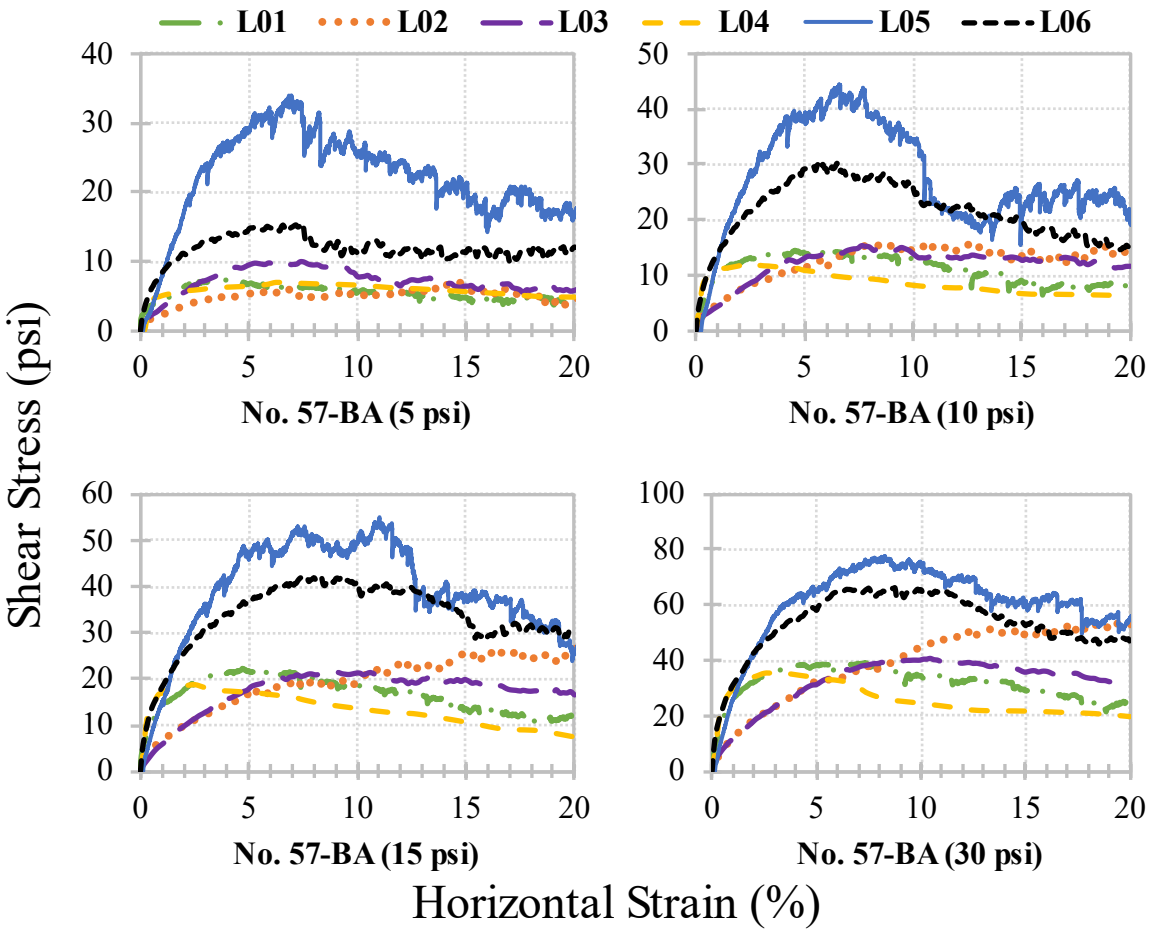

Source: FHWA.

Figure 76. Charts. Shear stress versus horizontal strain for No. 57-BA.

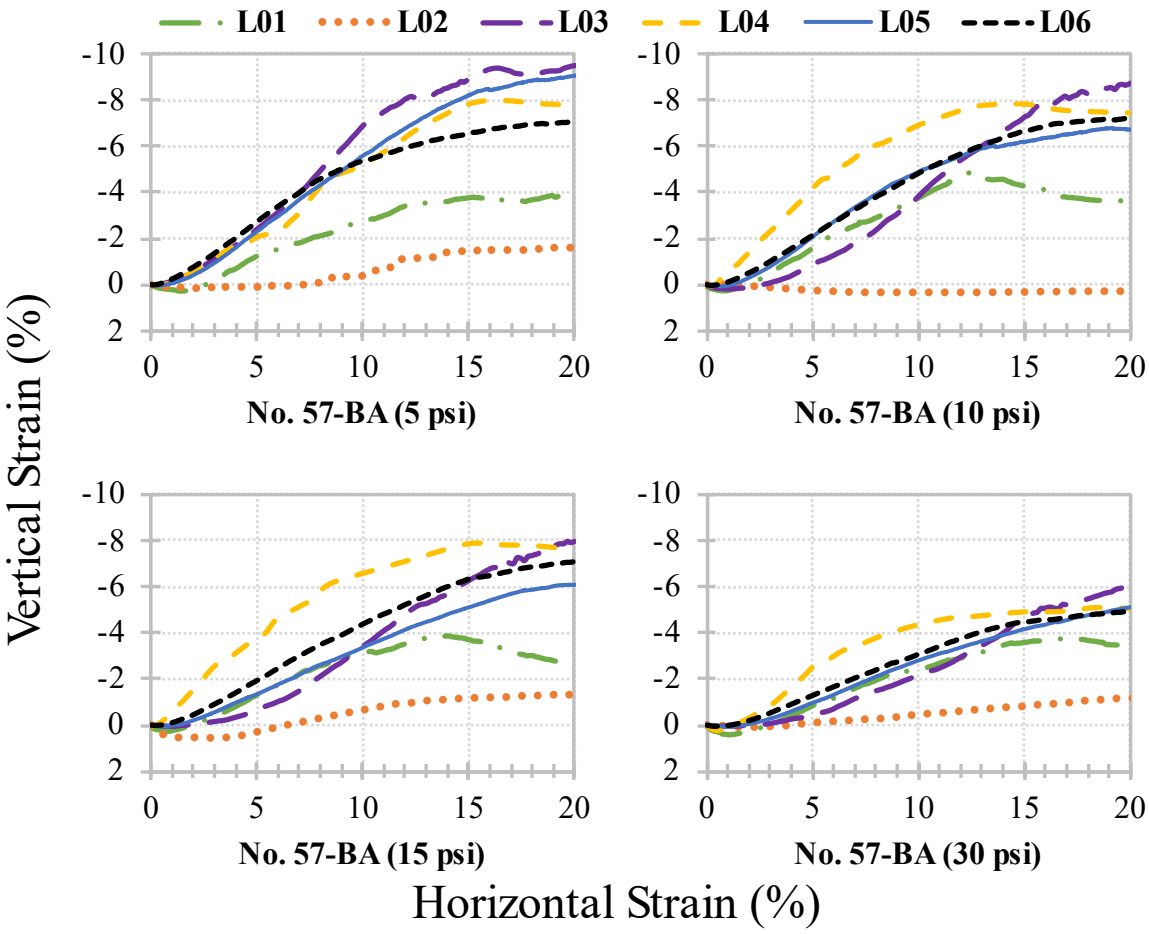

Source: FHWA.

Figure 77. Charts. Vertical strain versus horizontal strain for No. 57-BA.

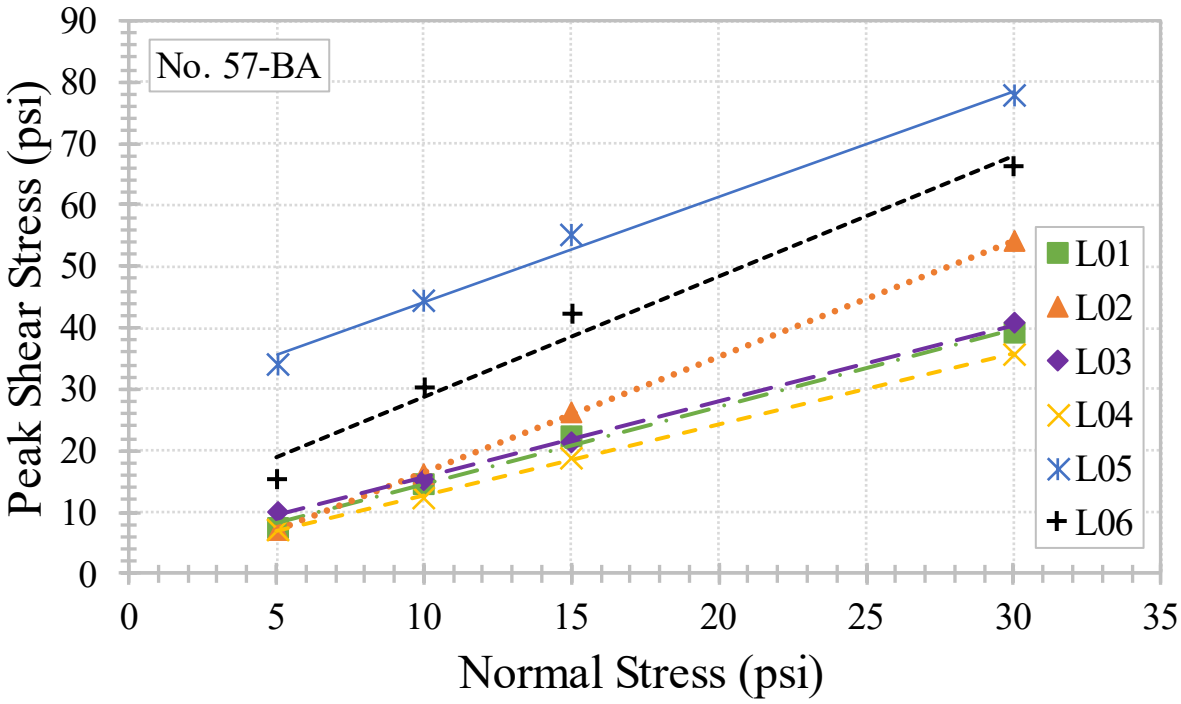

Source: FHWA.

Figure 78. Chart. Linear Mohr-Coulomb failure envelopes for No. 57-BA.

Table 59. Summary of LSDS results for No. 57-BA.

Lab ID	Target σ_n (psi)	$\tau_{initial}$ (psi)	σ_n at τ_{peak} (psi)	τ_{peak} (psi)	τ_r (psi)	ϕ_s (deg)	ϕ_r (deg)	ψ_{max} (deg)	ϕ_t (deg)	c_a (psi)	$\phi_{t,r}$ (deg)	ϕ_{cv} (deg)
L01	5	0.1	5.1	7.3	4.0	55.7	39.0	18.9	51.5	1.9	38.5	49.3
	10	0.1	10.3	14.5	7.9	55.5	38.4	23.3				
	15	−0.2	15.2	22.3	11.8	56.0	38.2	17.8				
	30	0.2	30.1	39.1	24.0	52.5	38.6	15.1				
L02	5	0.0	5.0	7.0	4.1	54.3	39.5	25.6	62.1	−2.5	59.9	61.3
	10	0.0	10.0	16.1	14.6	58.1	55.6	3.5				
	15	0.0	15.0	26.4	26.4	60.4	60.4	9.7				
	30	0.0	30.0	54.1	53.2	61.0	60.6	8.4				
L03	5	0.2	5.0	10.0	5.8	63.4	49.2	28.5	51.2	3.3	47.2	61.6
	10	0.2	10.0	15.3	11.6	56.9	49.3	28.5				
	15	0.2	15.1	21.5	16.5	55.1	47.8	38.3				
	30	0.2	30.0	40.7	31.8	53.6	46.7	26.1				
L04	5	0.0	5.0	7.0	4.9	54.4	44.3	32.6	49.2	1.1	32.3	37.7
	10	0.0	10.0	12.3	6.3	50.8	32.3	28.8				
	15	0.0	15.0	18.8	7.4	51.3	26.3	31.0				
	30	0.0	30.0	35.7	19.7	50.0	33.3	24.7				
L05	5	0.0	5.0	34.0	16.7	81.6	73.3	25.9	59.9	26.9	61.7	57.0
	10	0.0	10.1	44.5	19.7	77.3	63.1	25.0				
	15	0.0	15.0	55.0	25.6	74.7	59.7	17.0				
	30	0.0	30.1	77.7	55.3	68.9	61.5	15.6				
L06	5	0.1	5.1	15.3	11.9	71.9	67.2	25.1	63.1	8.9	59.2	56.8
	10	−1.6	10.1	30.2	15.3	71.7	56.8	20.8				
	15	−0.7	15.0	42.2	31.6	70.4	64.6	20.2				
	30	−3.0	30.0	66.2	47.0	65.6	57.5	15.0				

The shear stress versus horizontal strain, vertical strain versus horizontal strain, and linear Mohr-Coulomb failure envelopes for No. 57-DI are shown in figure 79, figure 80, and figure 81, respectively. The full summary of LSDS results is presented in table 60.

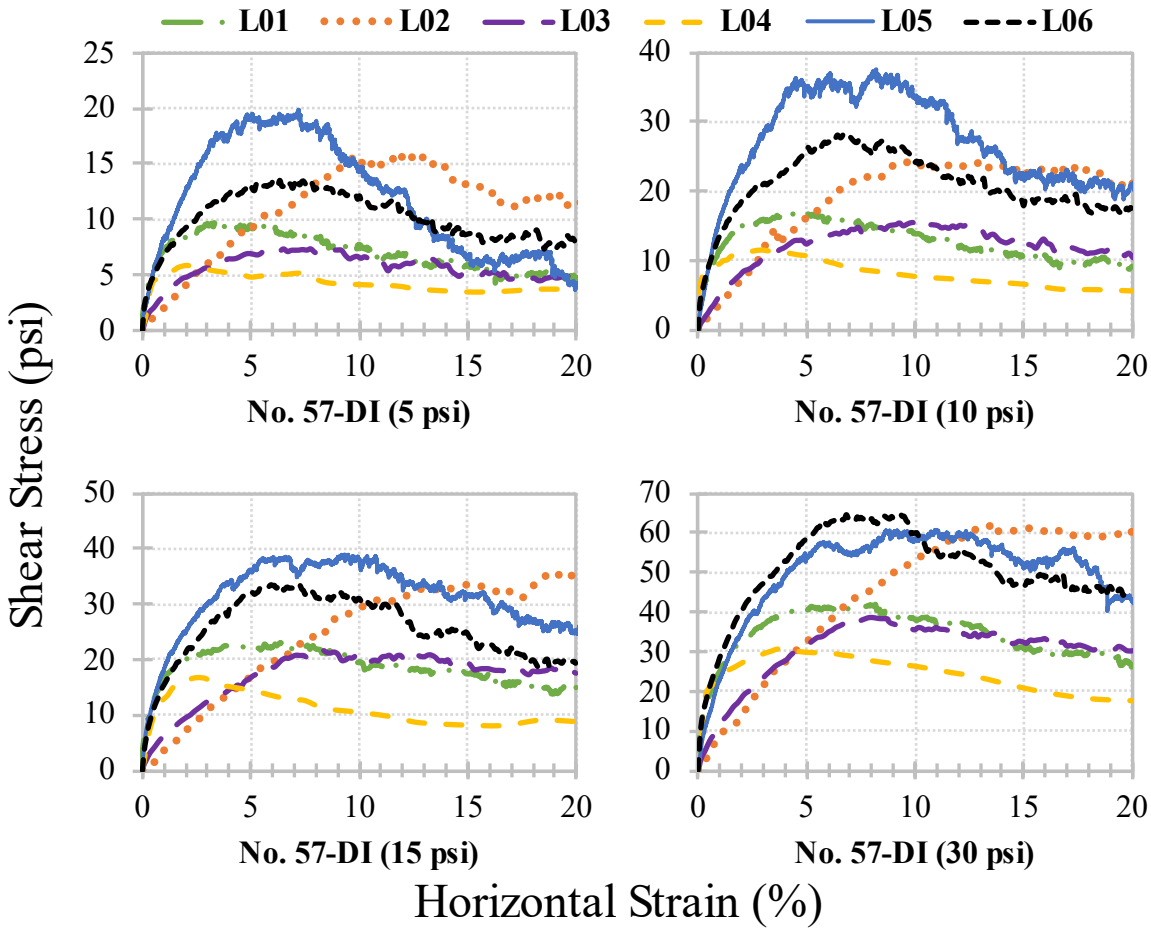

Source: FHWA.

Figure 79. Charts. Shear stress versus horizontal strain for No. 57-DI.

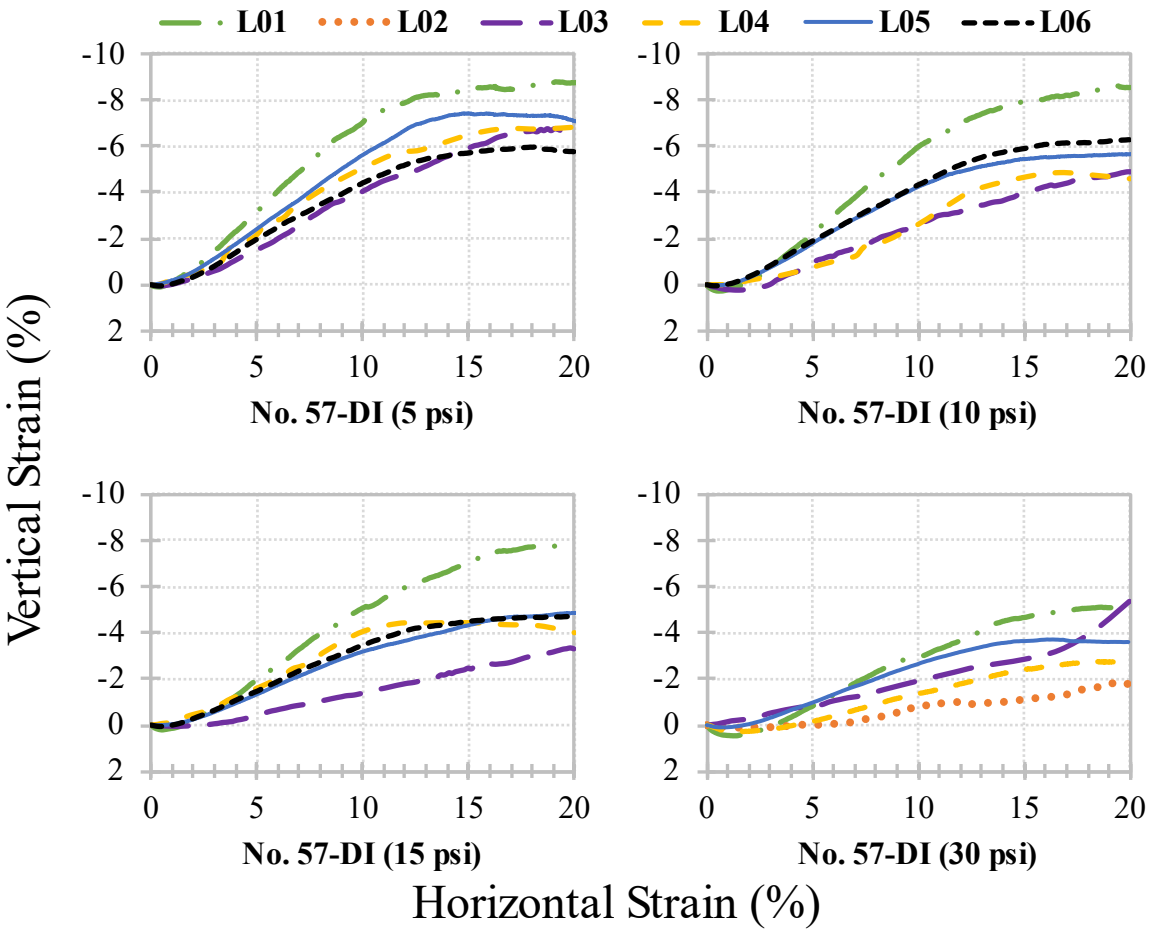

Source: FHWA.

Figure 80. Charts. Vertical strain versus horizontal strain for No. 57-DI.

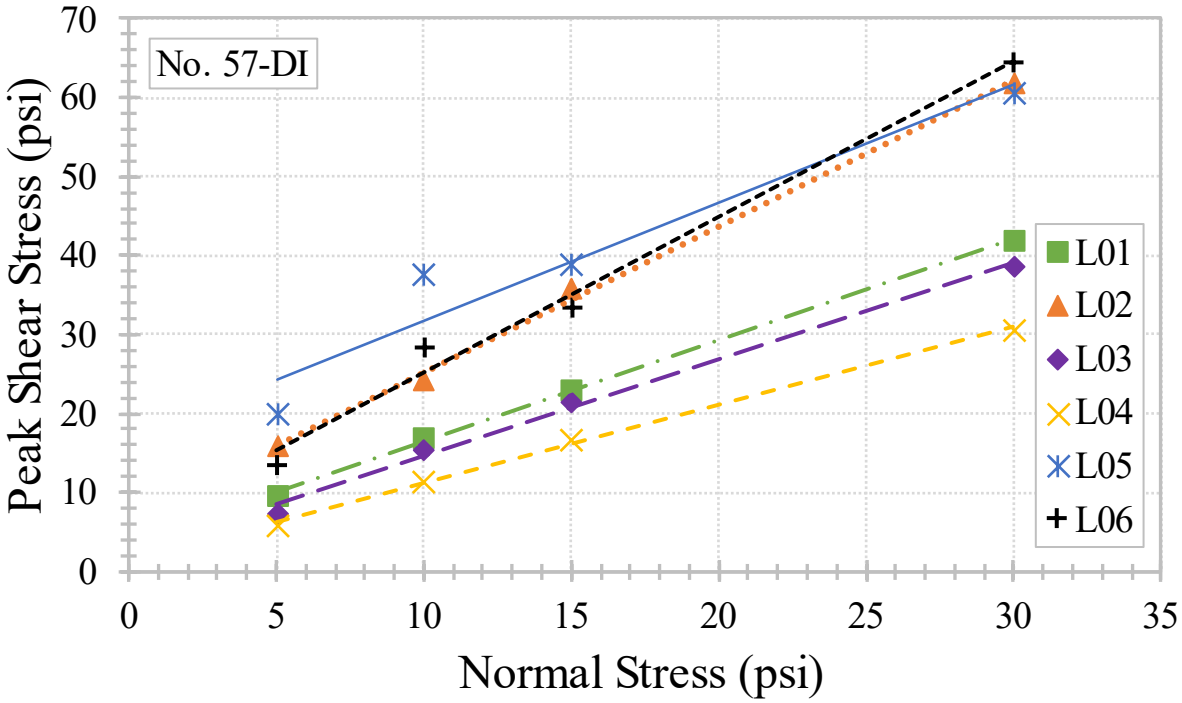

Source: FHWA.

Figure 81. Chart. Linear Mohr-Coulomb failure envelopes for No. 57-DI.

Table 60. Summary of LSDS results for No. 57-DI.

Lab ID	Target σ_n (psi)	$\tau_{initial}$ (psi)	σ_n at τ_{peak} (psi)	τ_{peak} (psi)	τ_r (psi)	ϕ_s (deg)	ϕ_r (deg)	ψ_{max} (deg)	ϕ_t (deg)	c_a (psi)	$\phi_{t,r}$ (deg)	ϕ_{cv} (deg)
L01	5	0.1	5.2	9.7	4.8	62.7	43.6	26.7	51.9	3.8	41.3	38.2
	10	0.1	10.3	16.9	9.2	59.5	42.5	24.6				
	15	0.1	15.3	23.0	14.2	56.9	43.4	23.2				
	30	0.0	30.1	41.9	25.7	54.4	40.6	17.7				
L02	5	0.0	5.0	16.1	11.6	72.7	66.6	—	61.5	6.9	64.5	—
	10	0.0	10.0	24.3	21.2	67.7	64.8	—				
	15	0.0	15.0	35.8	35.8	67.3	67.3	—				
	30	0.0	30.0	61.8	60.3	64.1	63.5	—				
L03	5	0.3	5.0	7.4	4.9	55.8	44.7	19.4	50.7	2.4	46.2	65.8
	10	0.2	10.0	15.5	11.1	57.2	47.9	22.4				
	15	0.2	14.9	21.6	17.5	55.3	49.4	23.8				
	30	0.2	29.7	38.6	30.1	52.1	45.1	24.0				
L04	5	0.0	5.0	5.8	3.7	49.4	36.3	35.8	44.5	1.5	30.4	44.2
	10	0.0	10.0	11.5	5.6	49.1	29.4	25.6				
	15	0.0	15.0	16.7	8.8	48.1	30.4	19.3				
	30	0.0	30.0	30.7	17.6	45.6	30.4	20.8				
L05	5	0.6	5.0	19.9	4.0	75.9	38.7	24.4	56.3	16.8	56.5	54.8
	10	−0.1	10.1	37.6	21.0	75.1	64.6	20.7				
	15	0.3	15.0	38.9	25.0	68.9	59.1	15.5				
	30	0.2	30.0	60.7	42.7	63.7	54.9	10.2				
L06	5	−1.4	5.1	13.7	7.7	69.9	56.9	21.2	63.1	5.4	55.7	55.0
	10	−3.1	10.1	28.4	17.6	70.6	60.3	19.8				
	15	−1.8	15.0	33.5	19.3	65.9	52.2	16.5				
	30	−5.5	30.0	64.6	44.4	65.1	55.9	13.2				

—Not measured/evaluated.

The shear stress versus horizontal strain, vertical strain versus horizontal strain, and linear Mohr-Coulomb failure envelopes for No. 57-GG are shown in figure 82, figure 83, and figure 84, respectively. The full summary of LSDS results is presented in table 61.

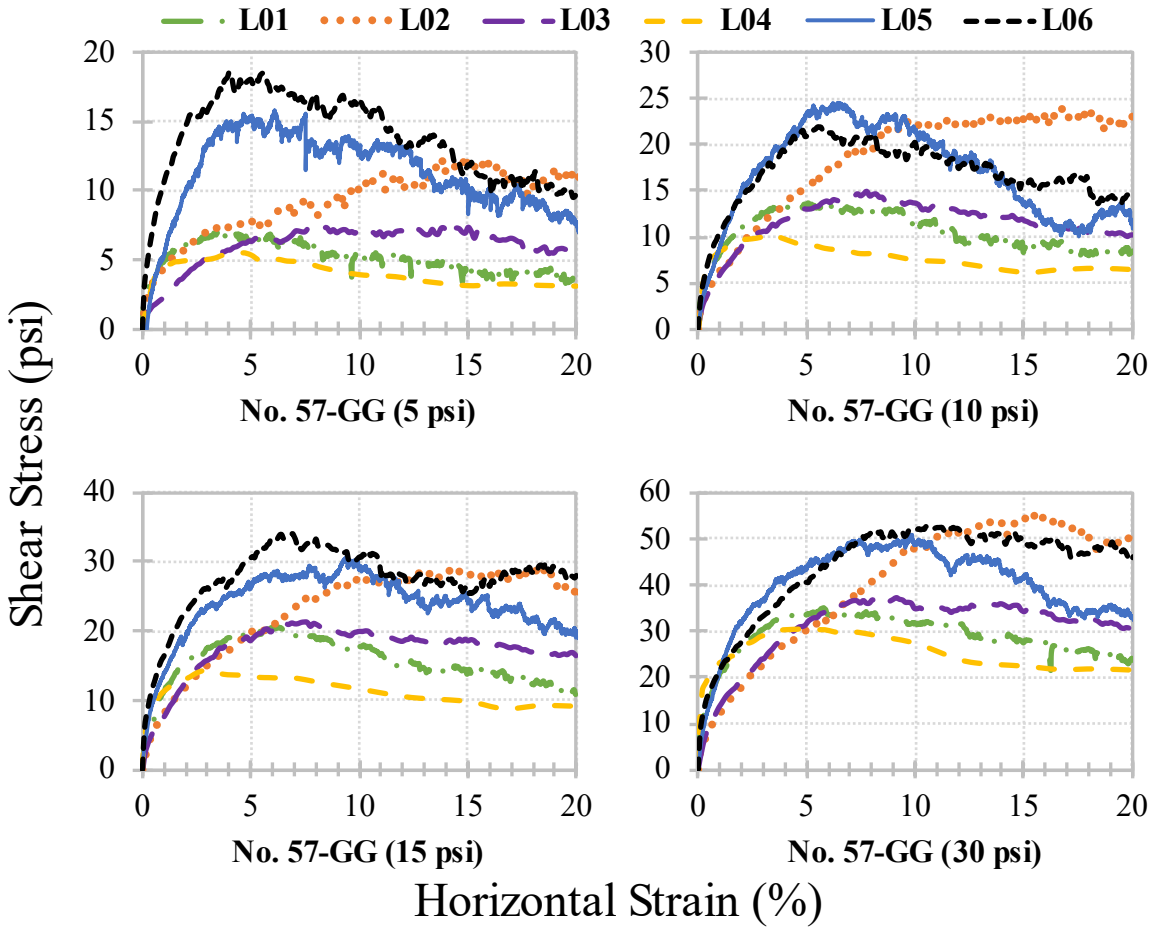

Source: FHWA.

Figure 82. Charts. Shear stress versus horizontal strain for No. 57-GG.

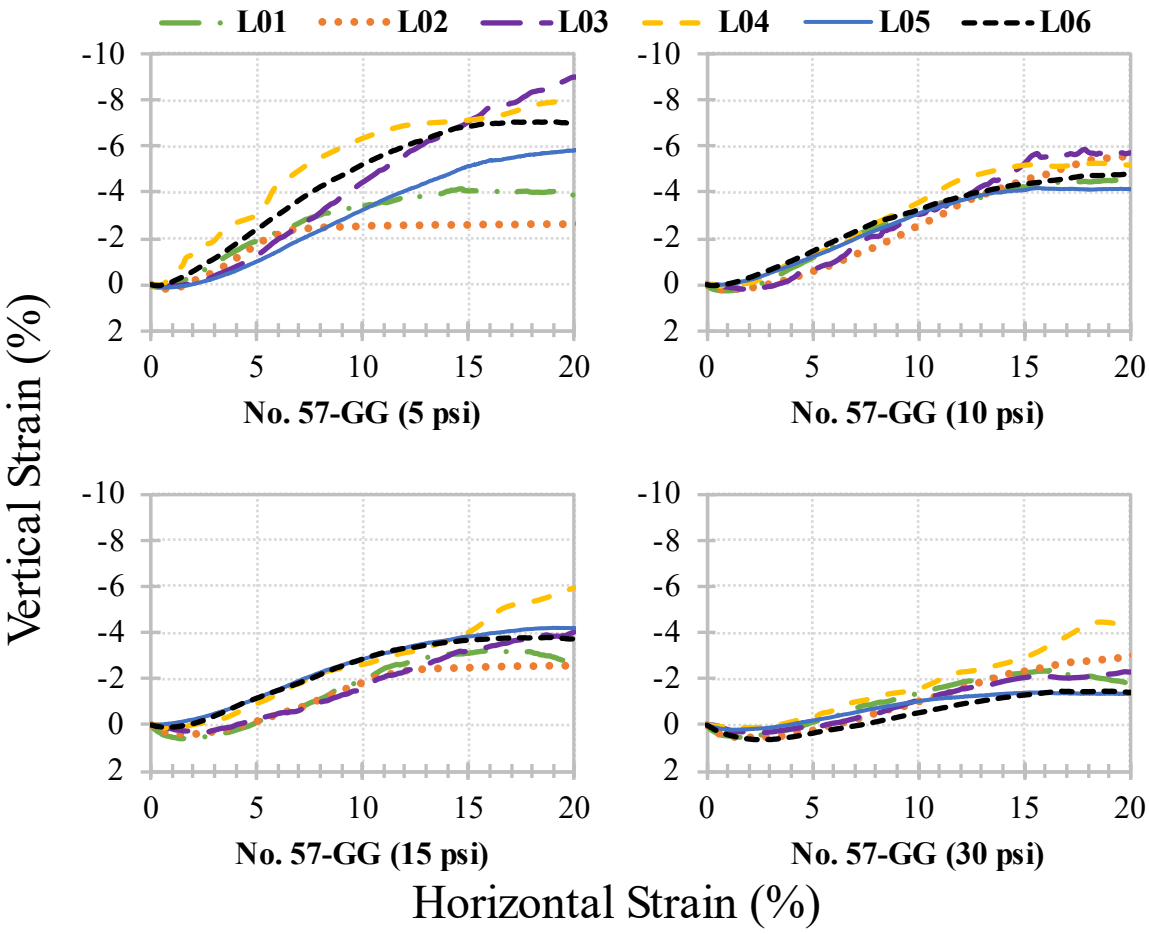

Source: FHWA.

Figure 83. Charts. Vertical strain versus horizontal strain for No. 57-GG.

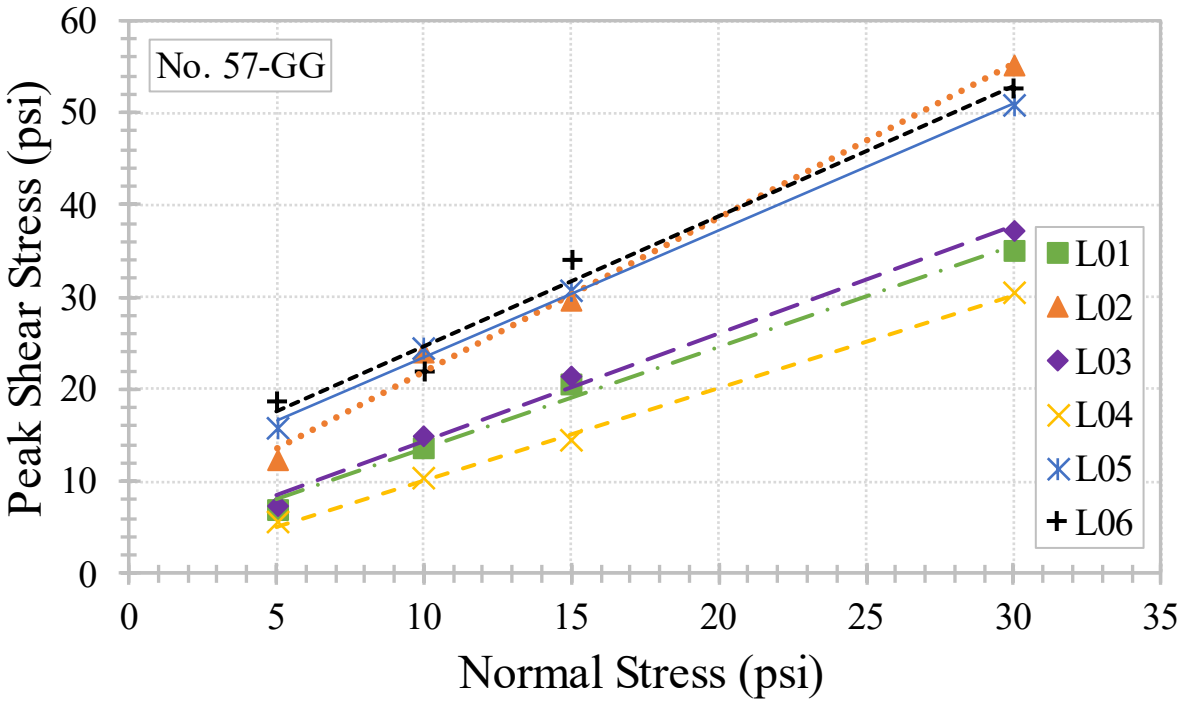

Source: FHWA.

Figure 84. Chart. Linear Mohr-Coulomb failure envelopes for No. 57-GG.

Table 61. Summary of LSDS results for No. 57-GG.

Lab ID	Target σ_n (psi)	$\tau_{initial}$ (psi)	σ_n at τ_{peak} (psi)	τ_{peak} (psi)	τ_r (psi)	ϕ_s (deg)	ϕ_r (deg)	ψ_{max} (deg)	ϕ_t (deg)	c_a (psi)	$\phi_{t,r}$ (deg)	ϕ_{cv} (deg)
L01	5	0.2	5.3	6.9	3.9	54.2	38.1	18.4	47.9	2.4	38.4	41.3
	10	0.2	10.2	13.7	8.4	53.8	40.0	16.4				
	15	−0.2	15.1	20.6	10.9	53.9	35.9	18.4				
	30	0.2	30.1	35.0	24.1	49.4	38.8	11.8				
L02	5	0.0	5.0	12.3	10.9	67.9	65.4	19.6	59.1	5.2	59.5	52.1
	10	0.0	10.0	23.9	22.9	67.3	66.4	18.4				
	15	0.0	15.0	29.6	24.7	63.1	58.7	13.8				
	30	0.0	30.0	55.2	49.1	61.5	58.6	11.4				
L03	5	0.1	5.0	7.4	5.5	56.1	47.6	23.7	49.5	2.7	46.0	50.4
	10	0.2	10.0	14.9	10.2	56.2	45.5	36.2				
	15	0.2	14.9	21.3	16.4	54.9	47.6	18.0				
	30	0.2	29.7	37.2	30.6	51.1	45.6	12.7				
L04	5	0.0	5.0	5.5	3.1	47.8	31.9	43.5	45.0	0.1	34.7	43.1
	10	0.0	10.0	10.3	6.5	45.7	32.9	24.7				
	15	0.0	15.0	14.4	9.2	43.8	31.4	19.8				
	30	0.0	30.0	30.5	21.6	45.4	35.7	13.5				
L05	5	−0.1	4.9	15.8	7.6	72.4	56.7	18.7	54.0	9.8	49.0	48.5
	10	1.0	10.0	24.5	11.8	67.8	49.7	15.9				
	15	1.2	15.0	30.7	19.4	63.9	52.3	15.1				
	30	1.9	30.0	50.8	33.0	59.5	47.7	8.4				
L06	5	−1.6	5.1	18.6	9.7	74.9	62.6	23.2	54.7	10.6	58.2	52.3
	10	0.0	10.1	21.9	14.9	65.5	56.2	17.2				
	15	−2.9	15.1	34.1	28.0	66.2	61.8	15.0				
	30	−9.9	30.0	52.6	46.5	60.3	57.2	7.8				

The shear stress versus horizontal strain, vertical strain versus horizontal strain, and linear Mohr-Coulomb failure envelopes for No. 57-LI are shown in figure 85, figure 86, and figure 87, respectively. The full summary of LSDS results is presented in table 62.

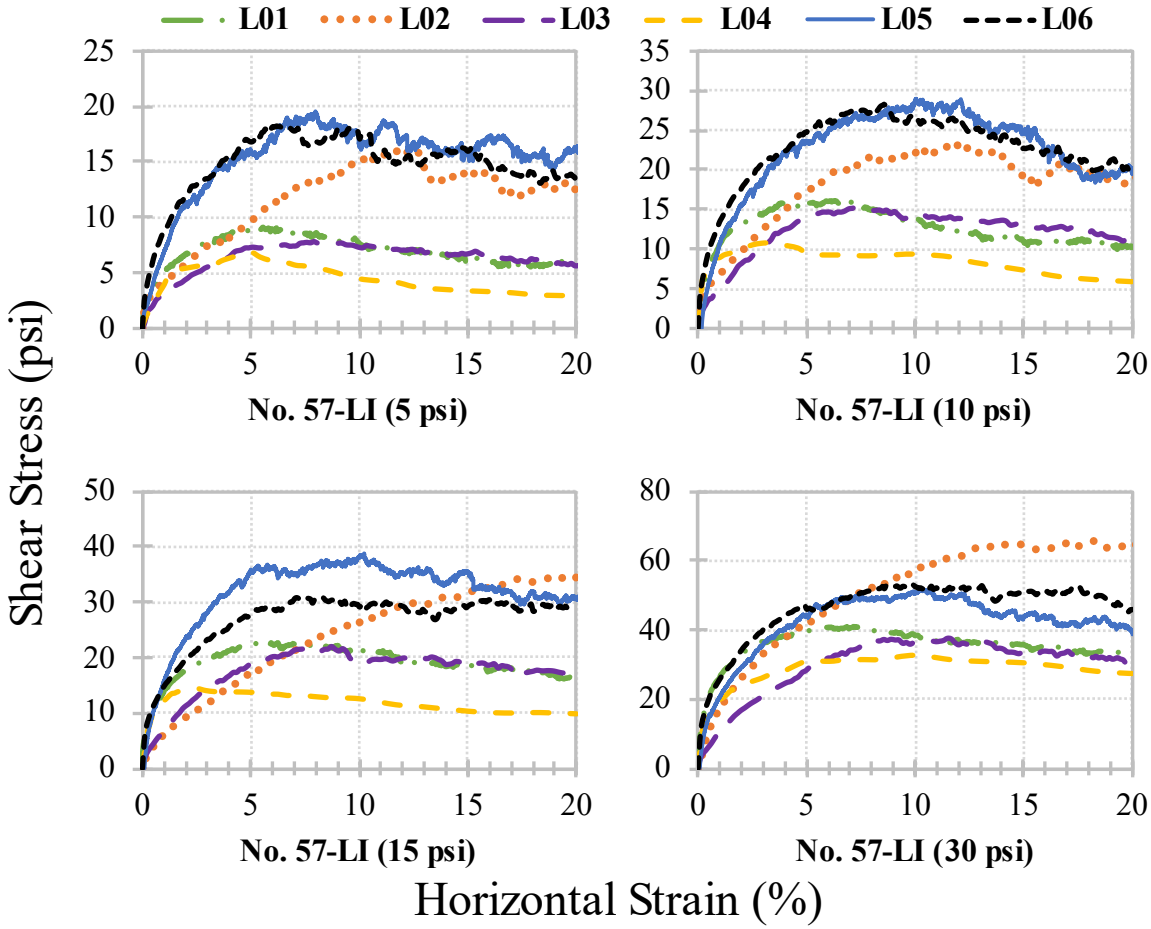

Source: FHWA.

Figure 85. Charts. Shear stress versus horizontal strain for No. 57-LI.

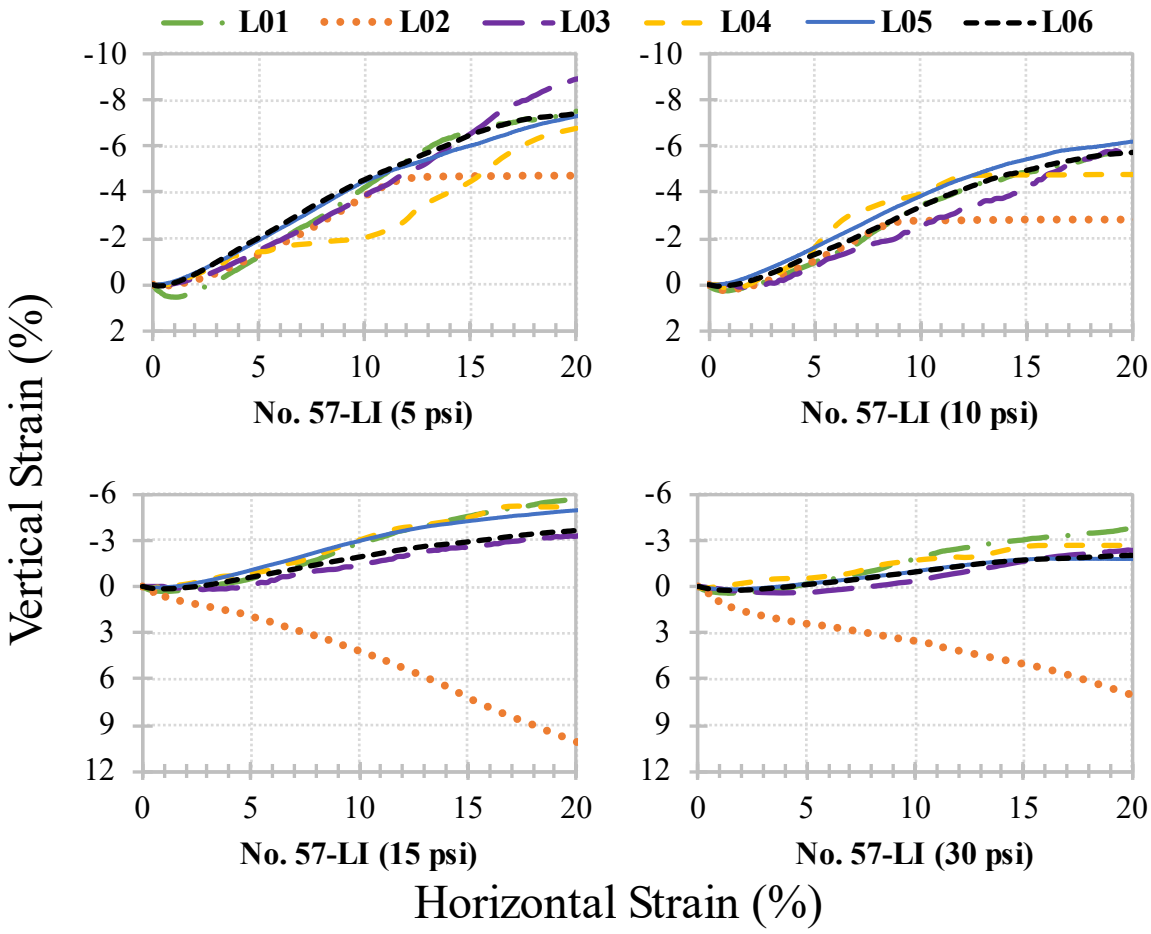

Source: FHWA.

Figure 86. Charts. Vertical strain versus horizontal strain for No. 57-LI.

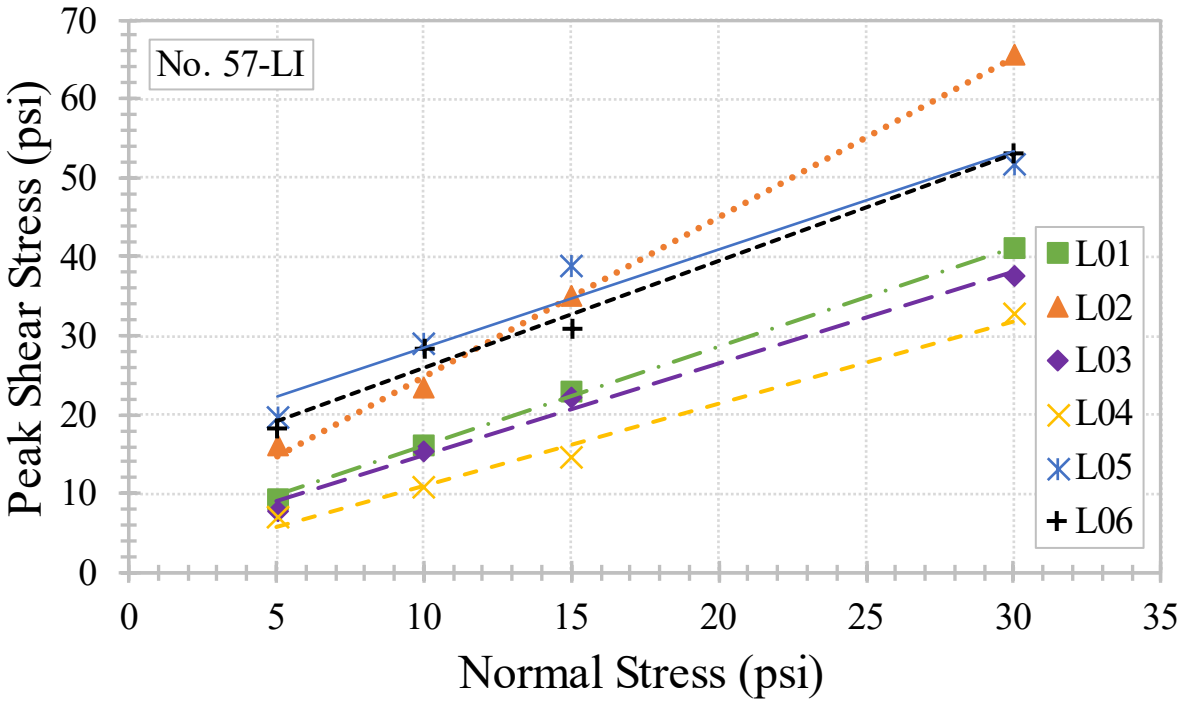

Source: FHWA.

Figure 87. Chart. Linear Mohr-Coulomb failure envelopes for No. 57-LI.

Table 62. Summary of LSDS results for No. 57-LI.

Lab ID	Target σ_n (psi)	$\tau_{initial}$ (psi)	σ_n at τ_{peak} (psi)	τ_{peak} (psi)	τ_r (psi)	ϕ_s (deg)	ϕ_r (deg)	ψ_{max} (deg)	ϕ_t (deg)	c_a (psi)	$\phi_{t,r}$ (deg)	ϕ_{cv} (deg)
L01	5	0.1	5.2	9.3	5.8	61.6	42.3	20.5	51.6	3.4	47.9	20.7
	10	0.0	10.1	16.1	10.2	58.1	38.6	19.7				
	15	0.0	15.1	22.9	16.6	56.8	38.2	19.3				
	30	−0.1	30.2	41.0	33.4	53.8	36.3	16.8				
L02	5	0.0	5.0	16.1	12.6	72.8	72.3	18.0	63.6	4.8	65.2	65.9
	10	0.0	10.0	23.4	18.7	66.8	62.4	15.3				
	15	0.0	15.0	34.9	34.9	66.7	68.2	0.0				
	30	0.0	30.0	65.6	64.6	65.4	60.2	0.0				
L03	5	0.0	5.0	7.8	5.6	57.4	46.9	21.1	49.4	3.1	46.6	46.8
	10	0.1	10.0	15.3	11.0	56.8	48.2	24.5				
	15	0.4	15.0	22.0	17.4	55.7	47.4	22.6				
	30	0.2	30.3	37.5	30.7	51.4	47.0	11.3				
L04	5	0.0	5.0	6.9	3.0	54.0	35.3	20.7	46.4	0.4	39.8	47.0
	10	0.0	10.0	10.8	5.9	47.1	23.6	30.1				
	15	0.0	15.0	14.4	9.8	43.8	24.8	17.7				
	30	0.0	30.0	32.6	27.4	47.4	36.9	11.3				
L05	5	0.0	5.0	19.6	16.3	75.7	62.4	19.4	51.2	16.1	56.9	47.0
	10	0.0	10.0	29.0	19.5	71.0	70.3	17.2				
	15	0.0	15.0	38.8	30.7	68.8	64.7	15.1				
	30	0.0	30.0	51.7	39.3	59.9	64.0	8.8				
L06	5	−2.0	5.1	18.2	13.5	74.7	70.3	20.0	53.5	12.3	59.0	51.7
	10	0.2	10.1	28.3	20.2	70.5	64.9	17.1				
	15	−3.3	15.0	30.8	29.1	64.0	58.2	10.8				
	30	−5.2	30.0	53.1	45.8	60.5	58.3	7.8				

The shear stress versus horizontal strain, vertical strain versus horizontal strain, and linear Mohr-Coulomb failure envelopes for No. 57-SI are shown in figure 88, figure 89, and figure 90, respectively. The full summary of LSDS results is presented in table 63.

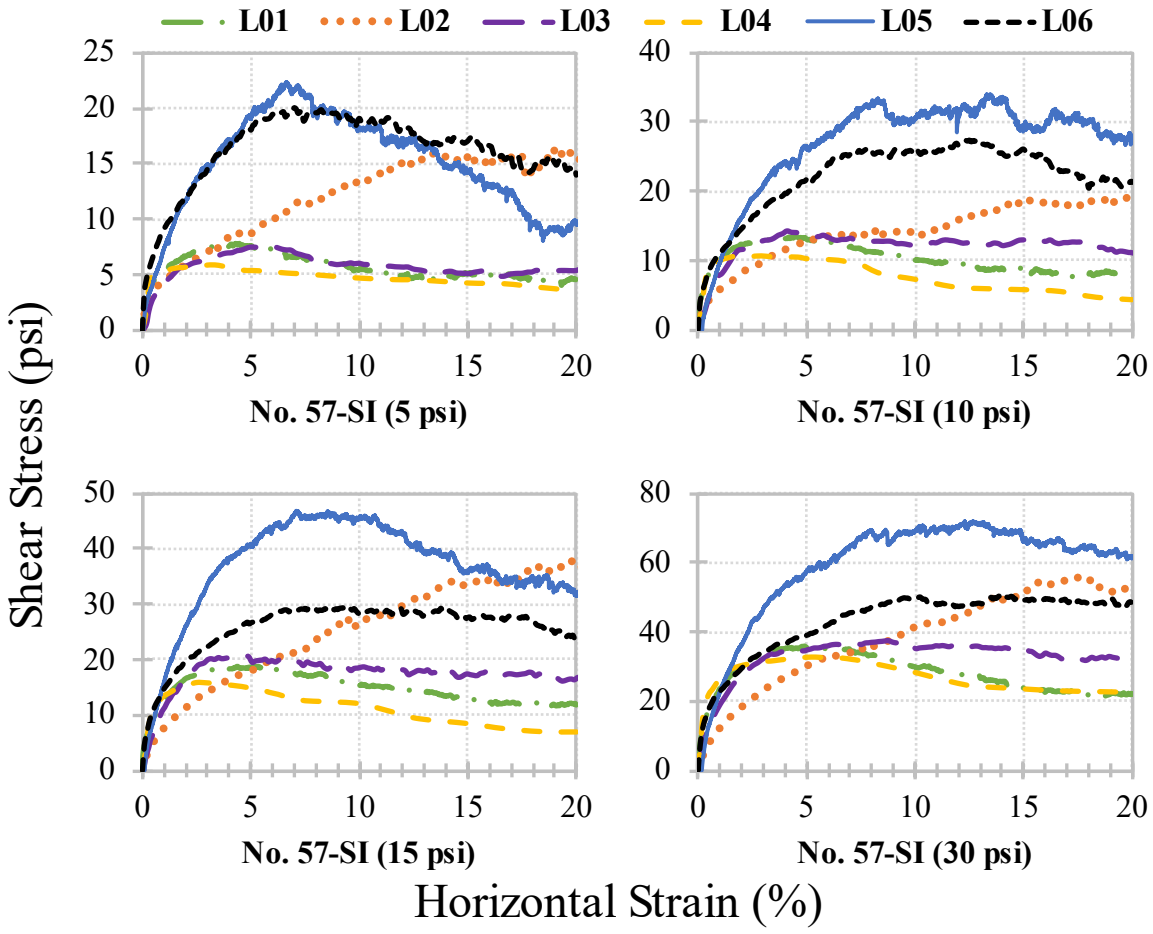

Source: FHWA.

Figure 88. Charts. Shear stress versus horizontal strain for No. 57-SI.

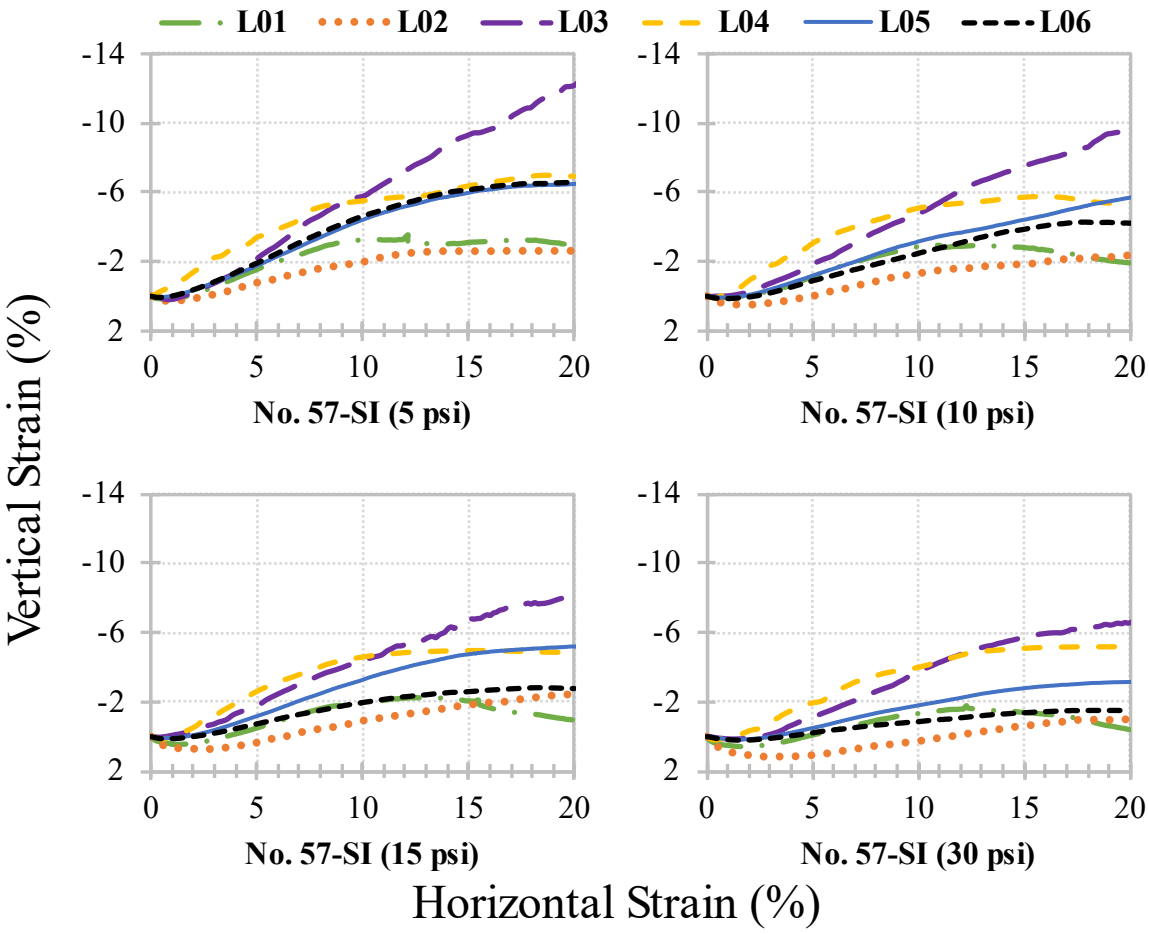

Source: FHWA.

Figure 89. Charts. Vertical strain versus horizontal strain for No. 57-SI.

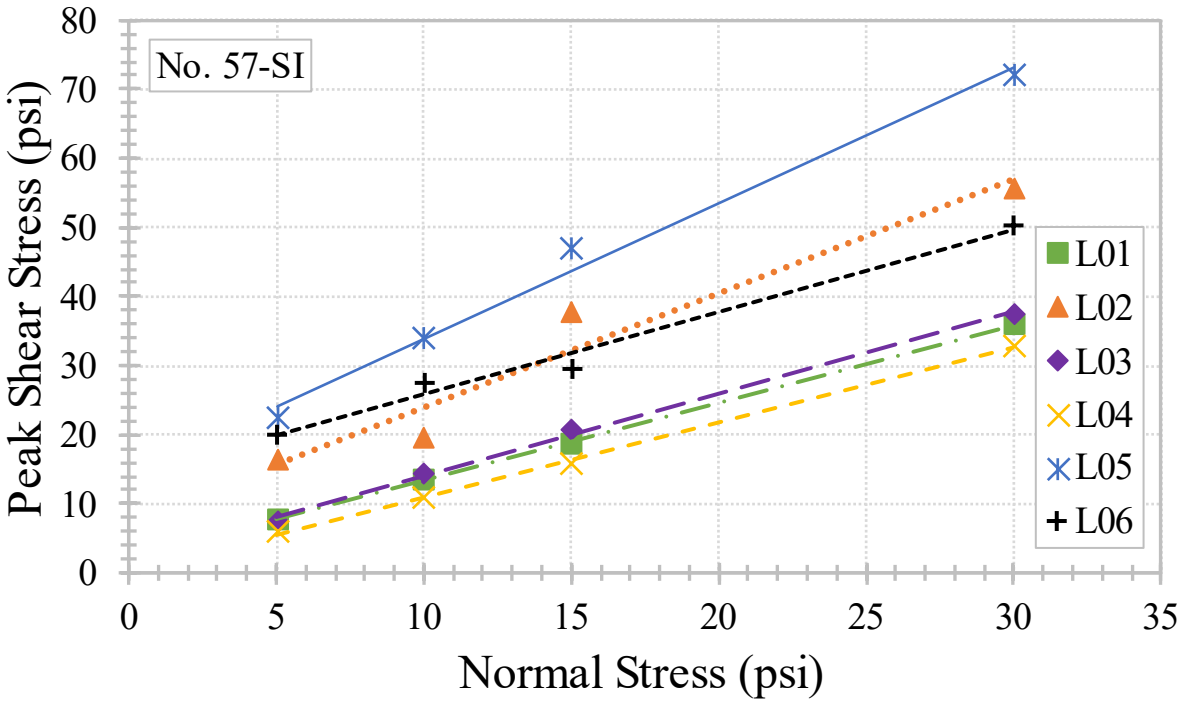

Source: FHWA.

Figure 90. Chart. Linear Mohr-Coulomb failure envelopes for No. 57-SI.

Table 63. Summary of LSDS results for No. 57-SI.

Lab ID	Target σ_n (psi)	$\tau_{initial}$ (psi)	σ_n at τ_{peak} (psi)	τ_{peak} (psi)	τ_r (psi)	ϕ_s (deg)	ϕ_r (deg)	ψ_{max} (deg)	ϕ_t (deg)	c_a (psi)	$\phi_{t,r}$ (deg)	ϕ_{cv} (deg)
L01	5	0.2	5.2	7.8	4.5	57.3	38.4	16.1	48.4	2.1	40.6	37.7
	10	0.1	10.1	13.5	8.0	53.4	38.2	15.2				
	15	0.0	15.1	18.7	11.8	51.3	38.6	12.3				
	30	−0.1	30.2	35.9	22.0	50.1	0.0	10.1				
L02	5	0.0	5.0	16.3	15.7	72.9	55.6	13.0	58.6	7.6	62.3	61.3
	10	0.0	10.0	19.4	19.1	62.8	60.4	15.2				
	15	0.0	15.0	37.7	37.6	68.3	60.6	12.5				
	30	0.0	30.0	55.6	52.4	61.7	0.0	11.0				
L03	5	0.0	5.0	7.5	5.4	56.4	49.3	28.3	49.8	2.2	46.6	55.1
	10	0.0	10.0	14.3	11.2	55.0	47.8	28.3				
	15	−0.1	14.8	20.6	16.3	53.9	46.7	39.2				
	30	−0.1	30.1	37.4	32.2	51.3	0.0	20.7				
L04	5	0.0	5.0	5.9	3.5	49.5	32.3	33.0	47.2	0.1	34.2	42.8
	10	0.0	10.0	10.7	4.4	46.9	26.3	29.2				
	15	0.0	15.0	15.8	6.9	46.6	33.3	24.7				
	30	0.0	30.0	32.7	22.5	47.5	0.0	22.8				
L05	5	0.0	5.0	22.3	9.6	77.4	63.1	20.3	63.0	14.4	57.8	52.3
	10	0.0	10.0	34.0	27.9	73.6	59.7	16.4				
	15	0.0	15.0	46.8	31.7	72.2	61.5	16.7				
	30	0.0	30.0	71.9	61.6	67.4	0.0	11.6				
L06	5	−2.6	5.1	20.0	14.0	76.0	56.8	21.3	50.0	14.0	58.3	53.3
	10	−1.9	10.0	27.5	21.4	70.0	64.6	13.4				
	15	−2.1	15.1	29.4	24.2	63.0	57.5	11.1				
	30	−4.6	30.0	50.3	48.5	59.2	0.0	7.4				

NO. 68 OGAs

The shear stress versus horizontal strain, vertical strain versus horizontal strain, and linear Mohr-Coulomb failure envelopes for No. 68-BA are shown in figure 91, figure 92, and figure 93, respectively. The full summary of LSDS results is presented in table 64.

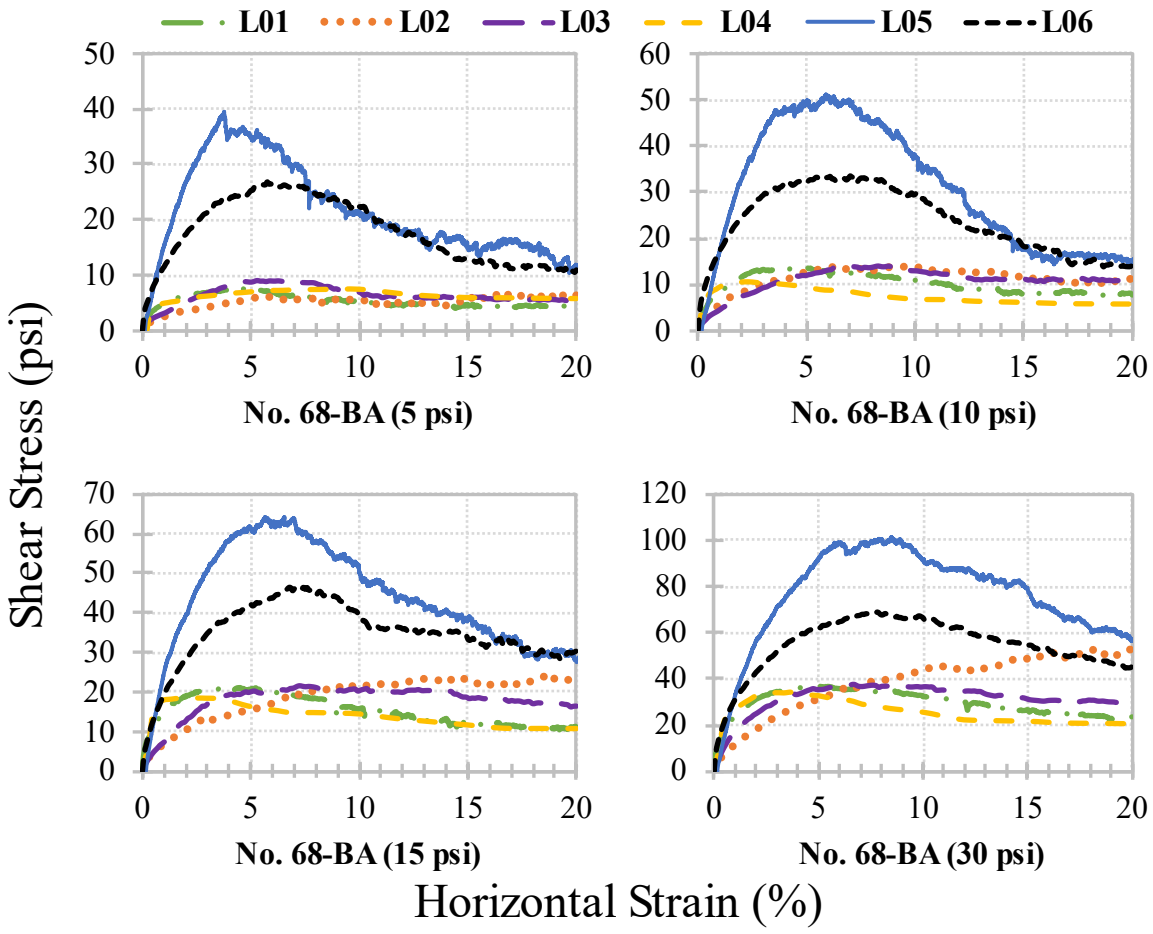

Source: FHWA.

Figure 91. Charts. Shear stress versus horizontal strain for No. 68-BA.

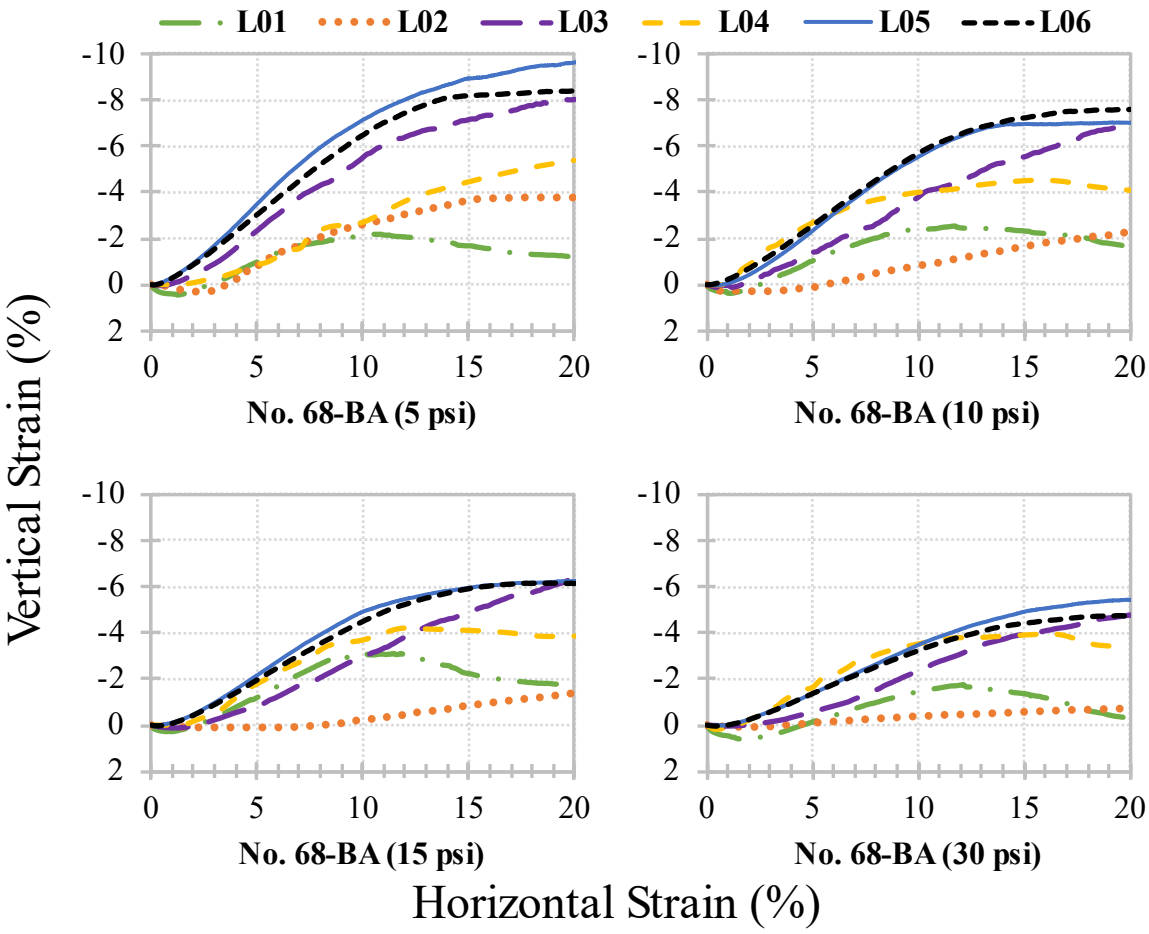

Source: FHWA.

Figure 92. Charts. Vertical strain versus horizontal strain for No. 68-BA.

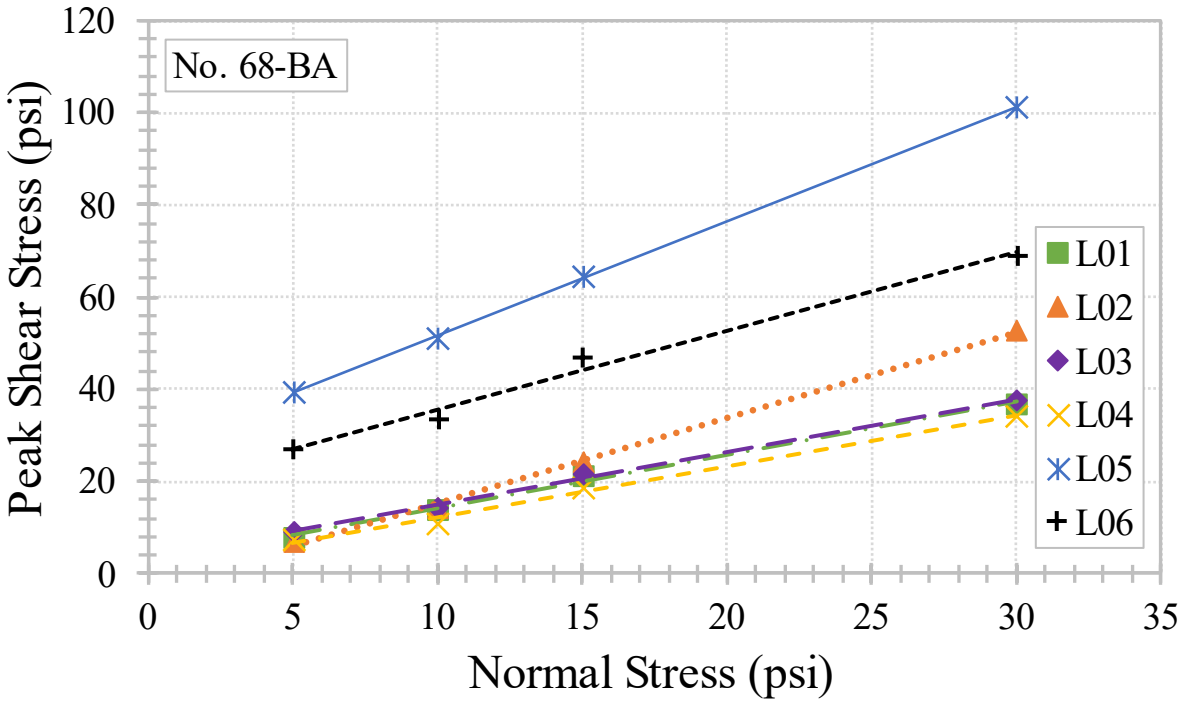

Source: FHWA.

Figure 93. Chart. Linear Mohr-Coulomb failure envelopes for No. 68-BA.

Table 64. Summary of LSDS results for No. 68-BA.

Lab ID	Target σ_n (psi)	$\tau_{initial}$ (psi)	σ_n at τ_{peak} (psi)	τ_{peak} (psi)	τ_r (psi)	ϕ_s (deg)	ϕ_r (deg)	ψ_{max} (deg)	ϕ_t (deg)	c_a (psi)	$\phi_{t,r}$ (deg)	ϕ_{cv} (deg)
L01	5	0.1	5.1	7.6	4.4	56.8	41.6	17.6	49.3	2.4	38.0	43.8
	10	0.1	10.2	13.8	7.7	54.0	37.7	15.1				
	15	−0.1	15.3	21.3	11.3	54.8	37.0	16.6				
	30	0.2	30.2	36.8	23.5	50.8	38.1	9.8				
L02	5	0.0	5.0	6.8	6.3	53.6	51.7	22.8	61.8	−3.5	58.8	60.0
	10	0.0	10.0	14.1	11.2	54.6	48.1	9.5				
	15	0.0	15.0	24.3	22.7	58.3	56.6	5.3				
	30	0.0	30.0	52.8	52.6	60.4	60.3	4.2				
L03	5	0.2	5.0	9.1	5.4	61.1	47.4	23.0	48.9	3.4	45.5	43.1
	10	0.6	10.0	14.2	11.1	54.8	47.9	23.6				
	15	0.2	15.1	21.6	16.4	55.2	47.5	16.6				
	30	0.3	30.5	37.6	29.6	51.4	44.6	15.4				
L04	5	0.0	5.0	7.5	5.8	56.2	49.2	30.1	47.7	1.2	34.6	50.8
	10	0.0	10.0	10.6	5.8	46.6	30.0	33.0				
	15	0.0	15.0	18.5	10.8	50.9	35.6	20.8				
	30	0.0	30.0	34.2	20.5	48.7	34.3	22.8				
L05	5	0.0	5.0	39.5	11.8	82.8	67.0	31.0	68.1	26.8	61.8	63.2
	10	0.0	10.0	51.2	15.0	78.9	56.3	26.5				
	15	0.0	15.0	64.2	27.9	76.8	61.7	22.0				
	30	0.0	30.0	101.3	56.7	73.5	62.1	16.4				
L06	5	−0.4	5.2	26.8	11.0	79.4	65.5	26.1	59.6	18.4	58.0	50.2
	10	1.1	10.0	33.6	14.1	73.4	54.7	23.6				
	15	−2.7	15.1	46.7	30.1	72.2	63.5	19.9				
	30	−0.3	30.1	68.9	45.1	66.5	56.3	15.1				

The shear stress versus horizontal strain, vertical strain versus horizontal strain, and linear Mohr-Coulomb failure envelopes for No. 68-DI are shown in figure 94, figure 95, and figure 96, respectively. The full summary of LSDS results is presented in table 65.

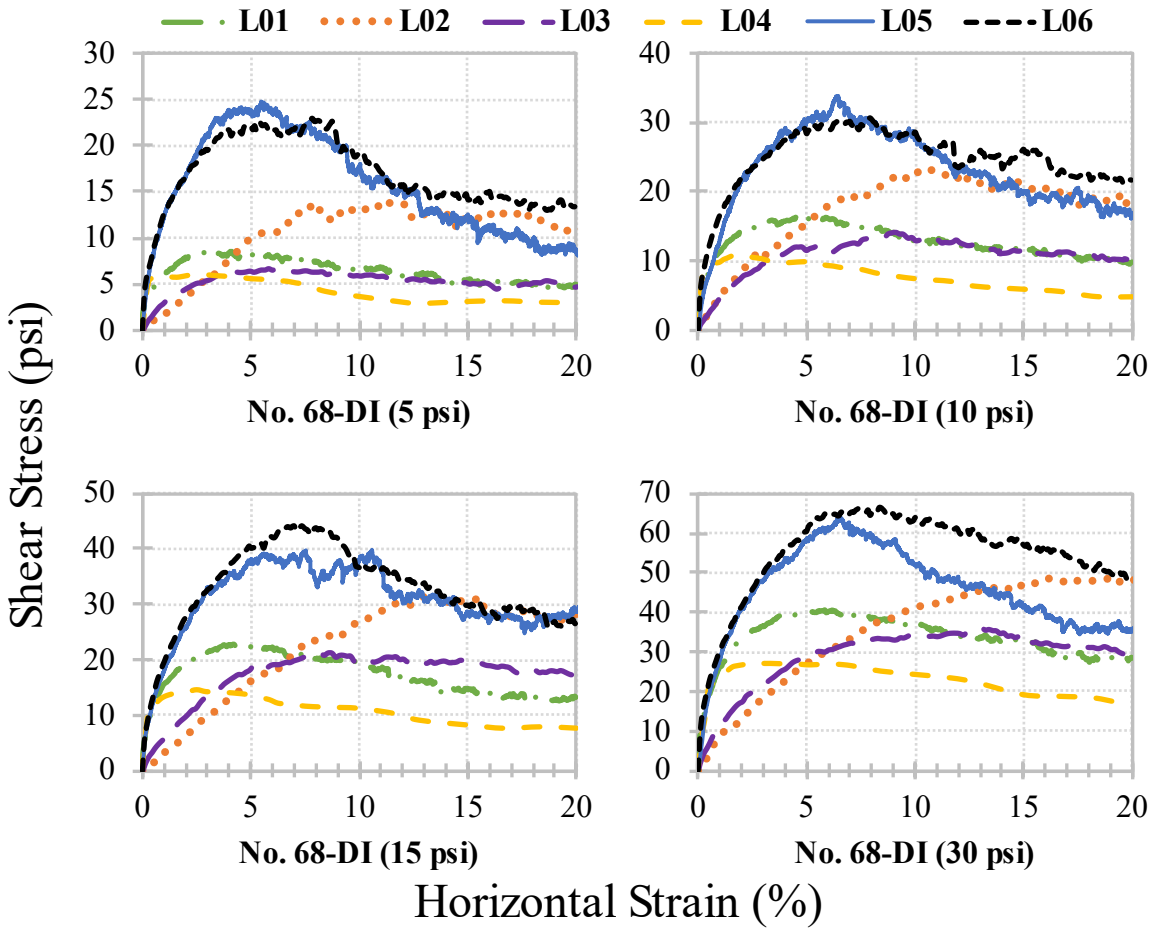

Source: FHWA.

Figure 94. Charts. Shear stress versus horizontal strain for No. 68-DI.

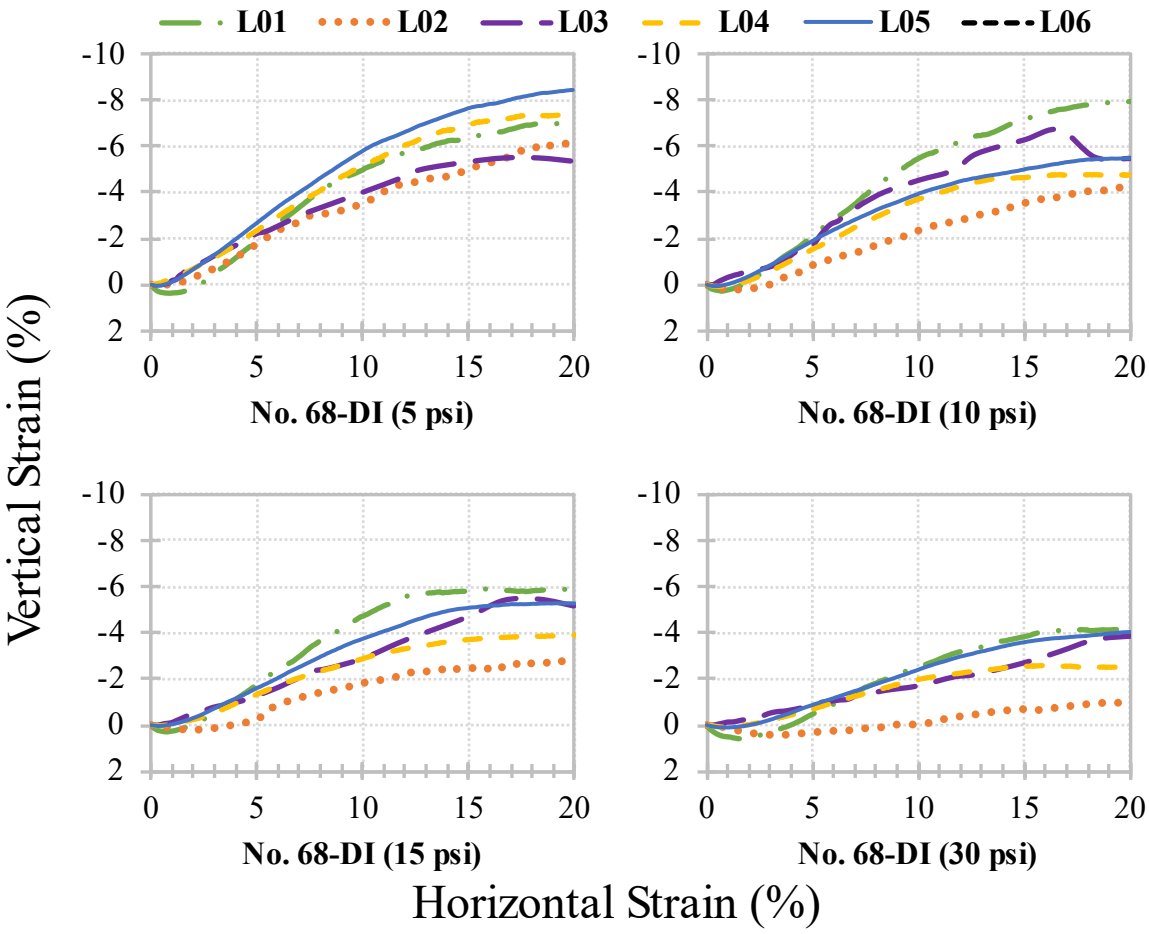

Source: FHWA.

Figure 95. Charts. Vertical strain versus horizontal strain for No. 68-DI.

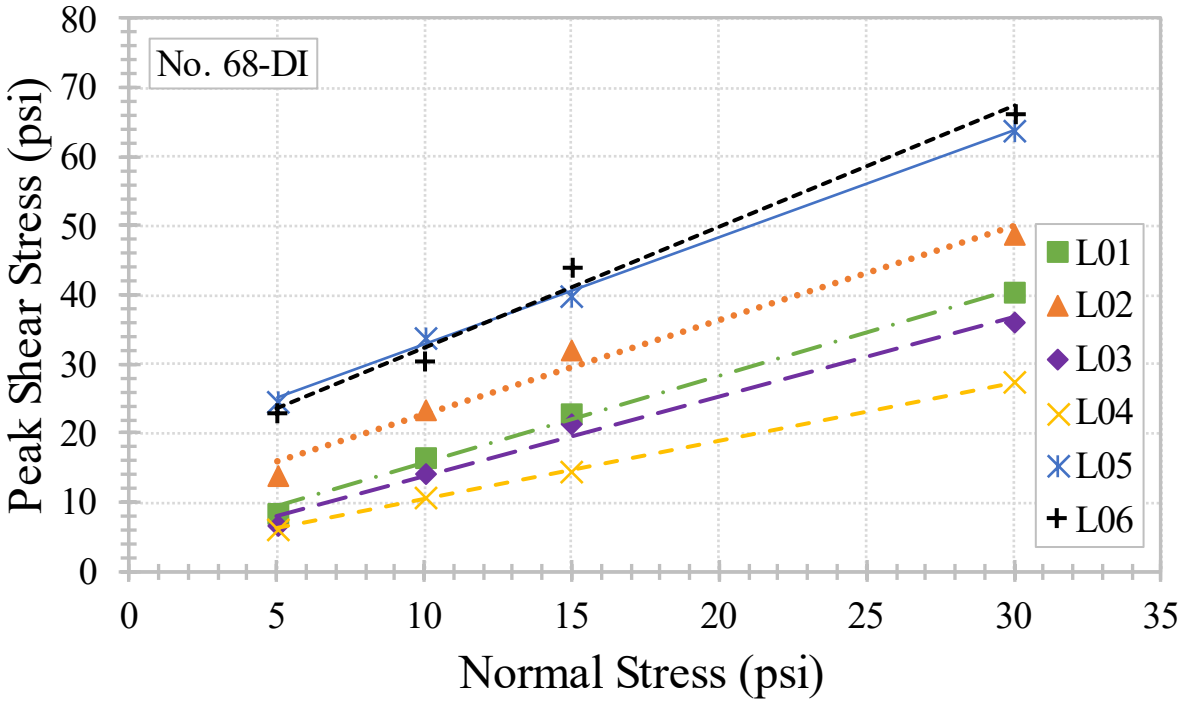

Source: FHWA.

Figure 96. Chart. Linear Mohr-Coulomb failure envelopes for No. 68-DI.

Table 65. Summary of LSDS results for No. 68-DI.

Lab ID	Target σ_n (psi)	$\tau_{initial}$ (psi)	σ_n at τ_{peak} (psi)	τ_{peak} (psi)	τ_r (psi)	ϕ_s (deg)	ϕ_r (deg)	ψ_{max} (deg)	ϕ_t (deg)	c_a (psi)	$\phi_{t,r}$ (deg)	ϕ_{cv} (deg)
L01	5	0.1	5.1	8.5	4.9	59.6	44.2	24.3	51.5	3.2	43.0	44.2
	10	0.1	10.1	16.6	9.8	58.9	44.5	25.3				
	15	0.1	15.3	22.8	12.7	56.7	40.2	21.9				
	30	0.0	30.3	40.6	28.4	53.5	43.5	15.4				
L02	5	0.0	5.0	13.8	10.7	70.0	64.9	—	53.7	9.1	58.9	—
	10	0.0	10.0	23.4	18.2	66.9	61.1	—				
	15	0.0	15.0	32.0	28.2	64.9	62.0	—				
	30	0.0	30.0	48.8	47.2	58.4	57.6	—				
L03	5	0.2	5.0	6.7	4.7	53.1	43.0	22.1	49.1	2.2	45.7	48.8
	10	0.2	10.0	14.1	10.2	54.7	45.4	20.0				
	15	0.2	15.1	21.3	17.3	54.8	49.1	32.3				
	30	0.2	30.3	36.0	29.9	50.2	44.9	11.7				
L04	5	0.0	5.0	6.1	3.0	50.6	30.9	26.6	40.2	2.1	28.1	38.9
	10	0.0	10.0	10.9	4.8	47.4	25.8	30.1				
	15	0.0	15.0	14.6	7.7	44.2	27.1	15.6				
	30	0.0	30.0	27.4	16.3	42.4	28.5	11.3				
L05	5	−0.1	5.0	24.7	8.5	78.6	59.7	22.4	57.2	17.3	53.7	51.1
	10	0.0	10.0	33.8	16.5	73.5	58.8	18.2				
	15	1.1	15.0	39.8	28.8	69.3	62.5	15.0				
	30	0.6	30.0	63.9	35.3	64.9	49.7	11.2				
L06	5	−3.6	5.1	22.9	13.4	77.7	69.5	24.3	60.3	14.7	59.6	51.8
	10	−4.4	10.1	30.6	21.7	71.9	65.2	19.4				
	15	−2.7	15.0	44.2	26.6	71.2	60.6	17.9				
	30	−7.6	30.1	66.4	48.4	65.7	58.2	13.1				

—Not measured/evaluated.

The shear stress versus horizontal strain, vertical strain versus horizontal strain, and linear Mohr-Coulomb failure envelopes for No. 68-GG are shown in figure 97, figure 98, and figure 99, respectively. The full summary of LSDS results is presented in table 66.

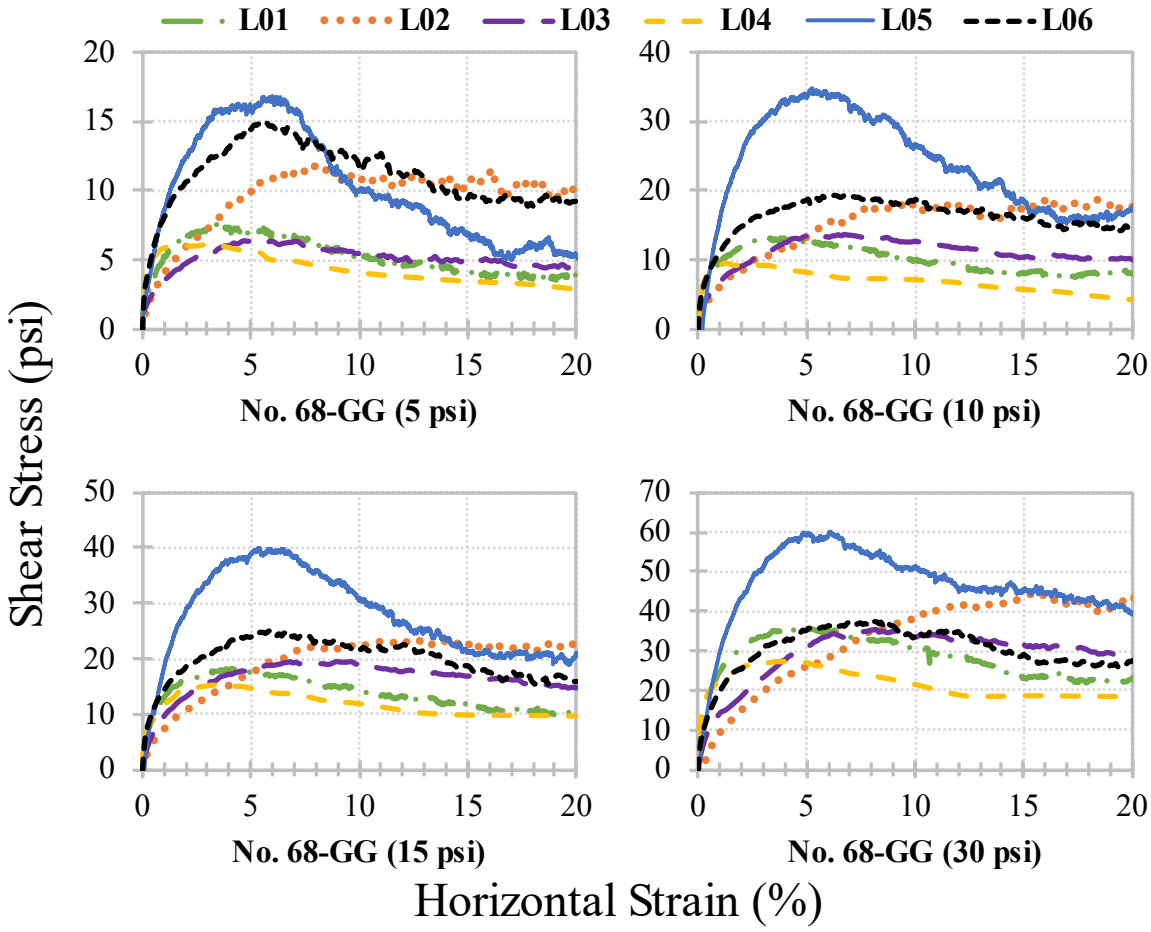

Source: FHWA.

Figure 97. Charts. Shear stress versus horizontal strain for No. 68-GG.

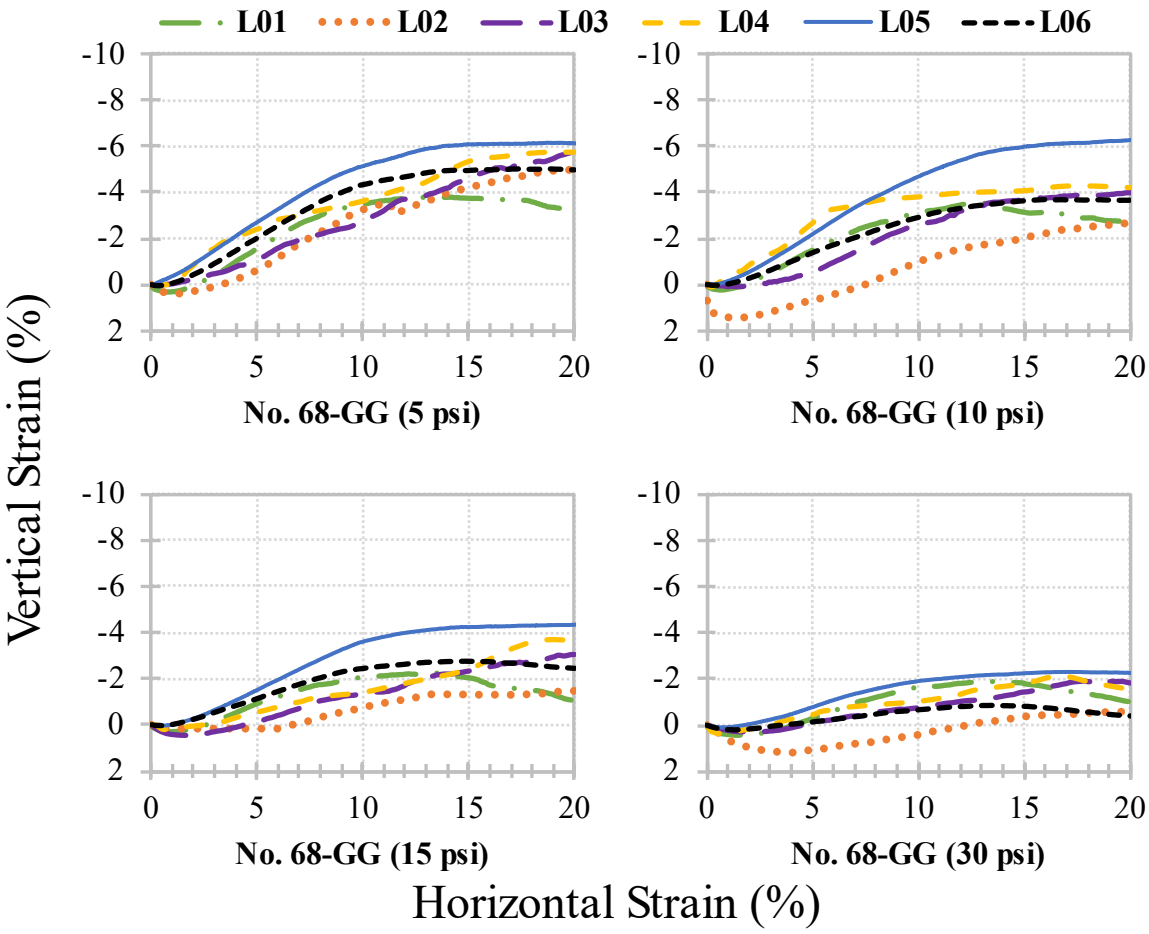

Source: FHWA.

Figure 98. Charts. Vertical strain versus horizontal strain for No. 68-GG.

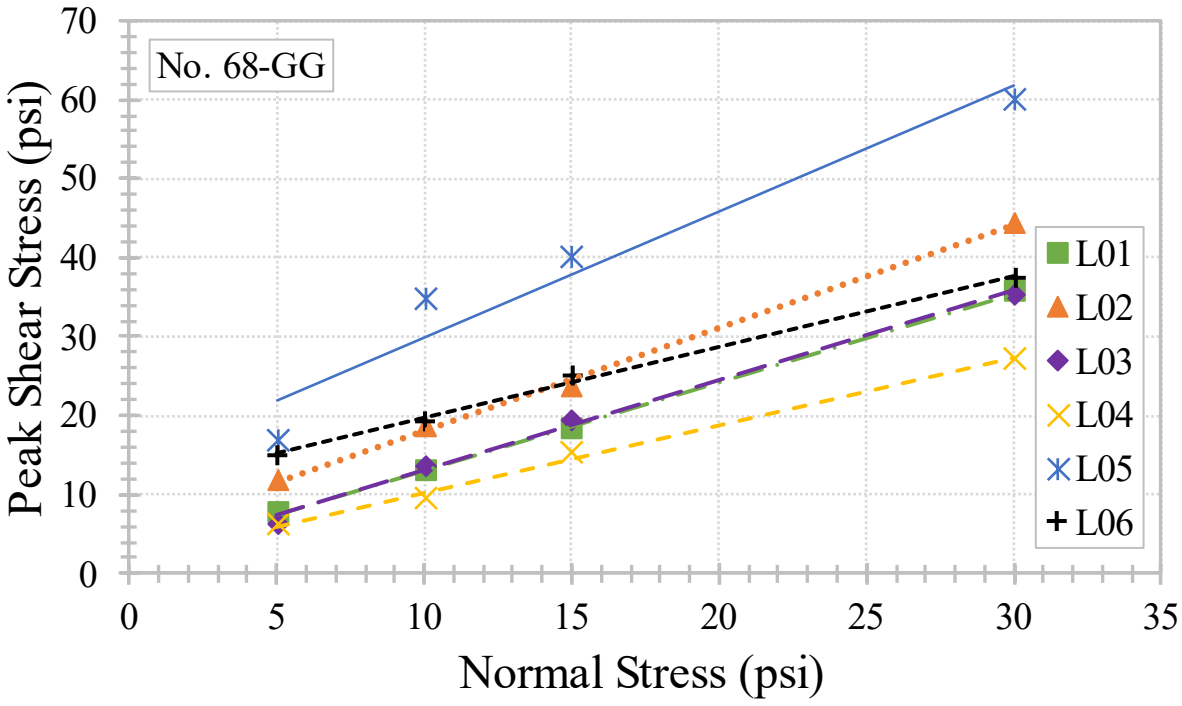

Source: FHWA.

Figure 99. Chart. Linear Mohr-Coulomb failure envelopes for No. 68-GG.

Table 66. Summary of LSDS results for No. 68-GG.

Lab ID	Target σ_n (psi)	$\tau_{initial}$ (psi)	σ_n at τ_{peak} (psi)	τ_{peak} (psi)	τ_r (psi)	ϕ_s (deg)	ϕ_r (deg)	ψ_{max} (deg)	ϕ_t (deg)	c_a (psi)	$\phi_{t,r}$ (deg)	ϕ_{cv} (deg)
L01	5	0.0	5.2	7.7	3.9	56.8	38.1	18.6	48.3	1.9	37.2	37.3
	10	−0.1	10.1	13.2	8.0	53.0	38.8	16.1				
	15	0.0	15.2	18.3	10.8	50.6	35.8	12.5				
	30	0.1	30.1	35.7	22.9	50.0	37.4	12.5				
L02	5	0.0	5.0	11.8	10.1	67.0	63.7	21.6	52.5	5.1	56.3	49.6
	10	0.0	10.0	18.7	17.7	61.8	60.5	14.1				
	15	0.0	15.0	23.6	22.6	57.5	56.4	9.3				
	30	0.0	30.0	44.4	43.5	56.0	55.4	8.6				
L03	5	0.2	5.0	6.4	4.6	52.0	42.7	19.9	48.7	1.7	44.1	45.8
	10	0.2	10.0	13.7	10.2	53.8	45.6	23.1				
	15	0.3	15.1	19.5	14.8	52.4	44.7	17.3				
	30	0.0	30.4	35.4	28.9	49.7	43.9	19.6				
L04	5	0.0	5.0	6.2	2.9	51.1	30.0	33.0	40.6	1.7	31.1	39.8
	10	0.0	10.0	9.5	4.3	43.6	23.2	23.7				
	15	0.0	15.0	15.3	9.7	45.5	32.8	12.7				
	30	0.0	30.0	27.3	18.4	42.3	31.5	10.2				
L05	5	1.0	5.0	16.8	5.2	73.4	46.3	22.1	57.9	14.0	53.7	51.9
	10	0.0	9.9	34.8	17.5	74.0	60.2	21.2				
	15	0.0	15.0	40.0	20.9	69.4	54.3	16.8				
	30	0.0	30.0	60.1	39.6	63.5	52.9	11.8				
L06	5	−2.3	5.1	14.9	9.2	71.4	61.6	20.4	42.1	10.6	45.0	43.9
	10	−1.3	10.0	19.3	14.7	62.6	55.7	14.5				
	15	−0.2	15.1	25.0	15.9	59.1	46.6	12.0				
	30	2.2	30.0	37.4	27.3	51.3	42.3	5.1				

The shear stress versus horizontal strain, vertical strain versus horizontal strain, and linear Mohr-Coulomb failure envelopes for No. 68-LI are shown in figure 100, figure 101, and figure 102, respectively. The full summary of LSDS results is presented in table 67.

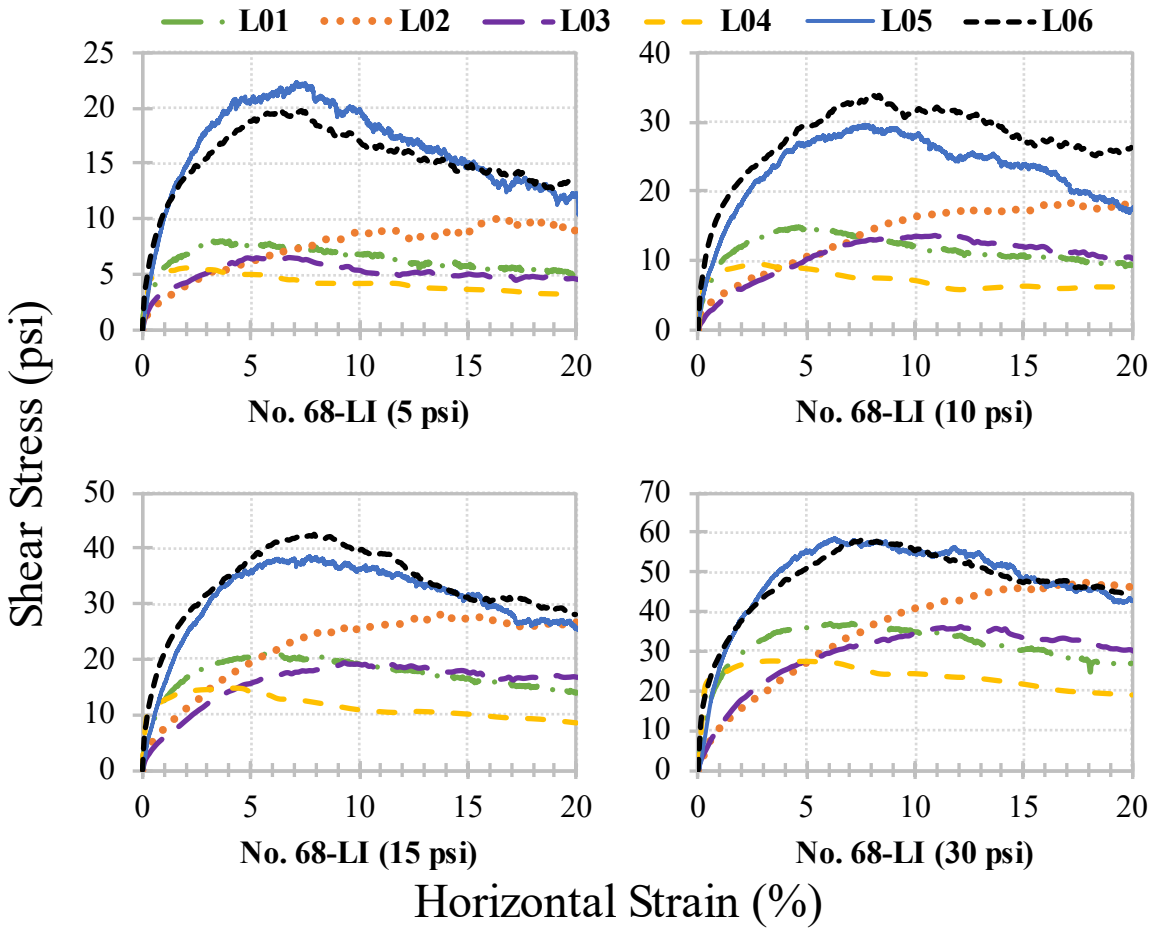

Source: FHWA.

Figure 100. Charts. Shear stress versus horizontal strain for No. 68-LI.

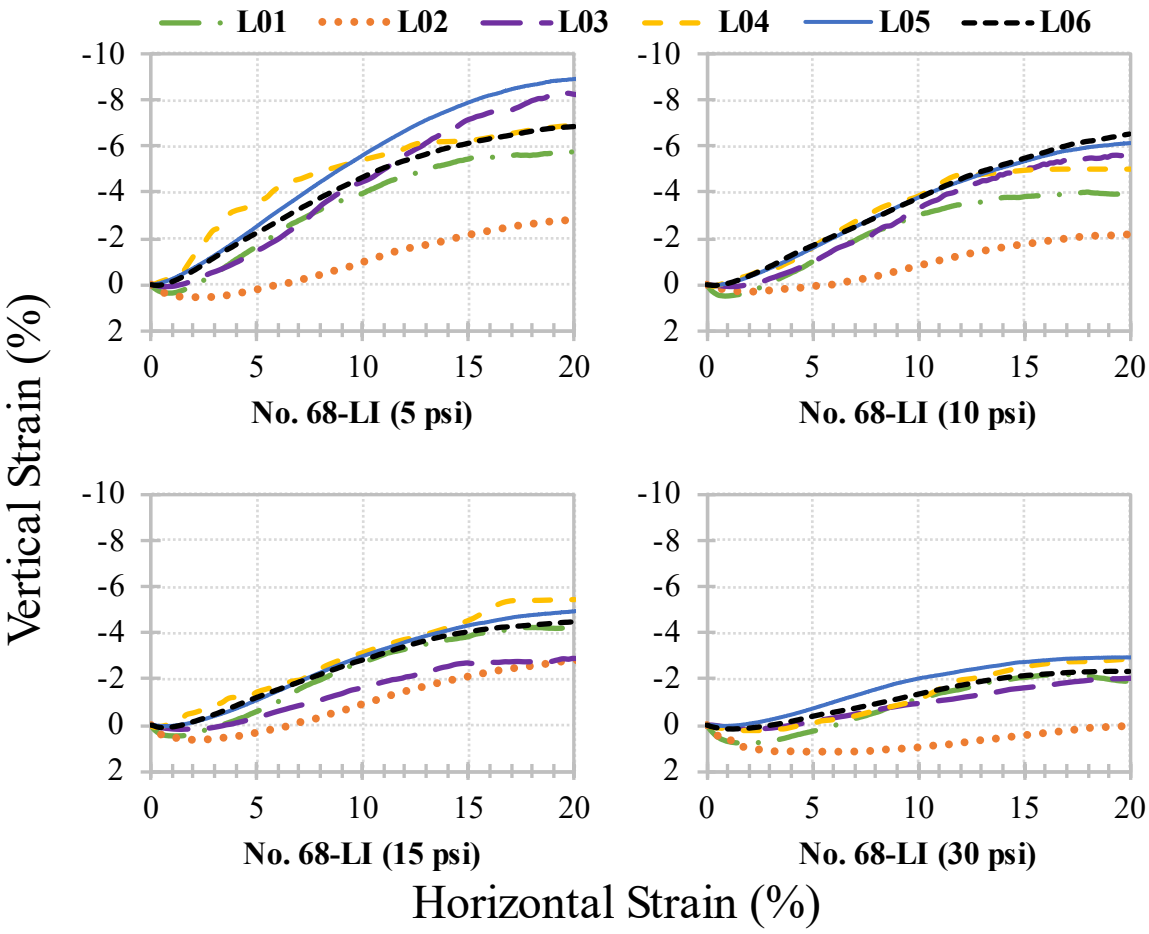

Source: FHWA.

Figure 101. Charts. Vertical strain versus horizontal strain for No. 68-LI.

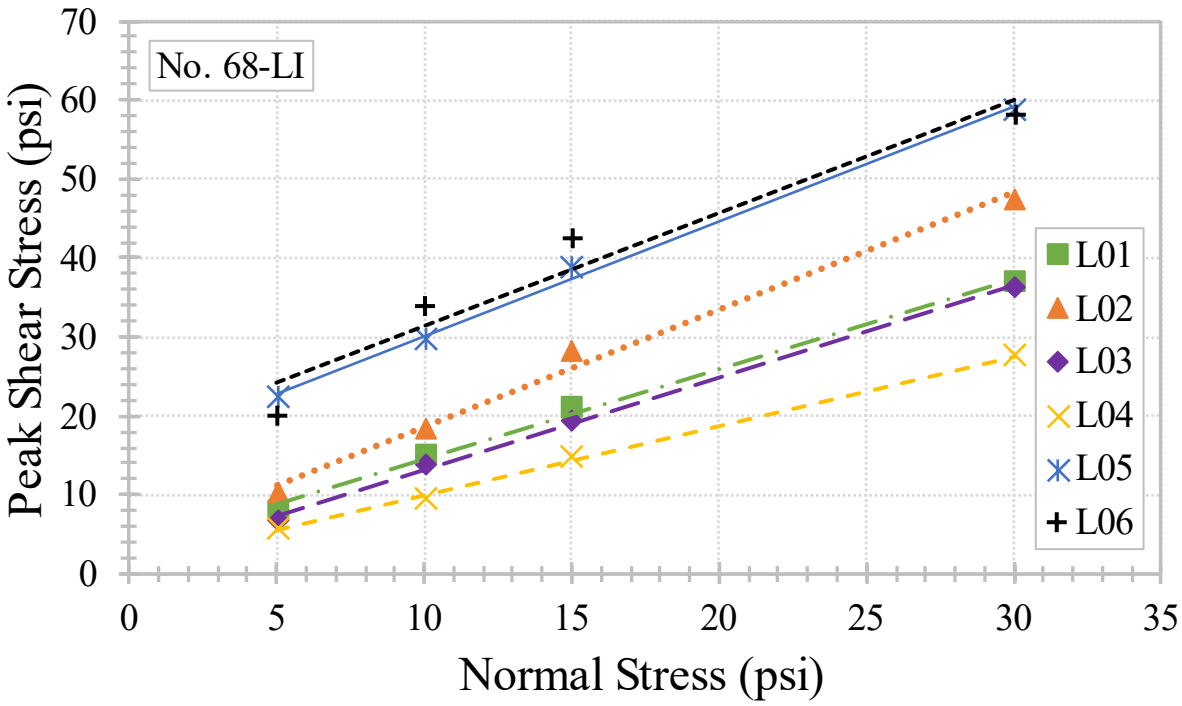

Source: FHWA.

Figure 102. Chart. Linear Mohr-Coulomb failure envelopes for No. 68-LI.

Table 67. Summary of LSDS results for No. 68-LI.

Lab ID	Target σ_n (psi)	$\tau_{initial}$ (psi)	σ_n at τ_{peak} (psi)	τ_{peak} (psi)	τ_r (psi)	ϕ_s (deg)	ϕ_r (deg)	ψ_{max} (deg)	ϕ_t (deg)	c_a (psi)	$\phi_{t,r}$ (deg)	ϕ_{cv} (deg)
L01	5	0.0	5.2	8.0	5.1	58.0	38.6	19.8	48.9	3.1	42.3	42.4
	10	0.0	10.2	14.9	9.3	56.1	36.8	16.3				
	15	−0.1	15.2	21.0	13.9	54.5	38.6	18.5				
	30	0.0	30.2	37.0	27.0	51.0	37.9	11.8				
L02	5	0.0	5.0	10.1	8.9	63.6	69.3	10.7	55.9	3.8	58.1	45.9
	10	0.0	10.0	18.4	17.7	61.5	65.1	10.0				
	15	0.0	15.0	28.1	26.7	61.9	65.8	11.8				
	30	0.0	30.0	47.4	46.2	57.6	61.5	8.5				
L03	5	0.1	5.0	6.6	4.6	52.8	43.6	25.5	49.4	1.5	45.9	50.2
	10	0.1	10.0	13.8	10.5	54.1	49.0	23.2				
	15	0.2	15.0	19.3	16.8	52.2	47.0	10.4				
	30	0.3	30.4	36.2	30.4	50.3	45.0	5.6				
L04	5	0.0	5.0	5.6	3.2	48.2	33.4	35.0	41.5	1.1	31.8	38.7
	10	0.0	10.0	9.5	6.1	43.5	29.5	21.8				
	15	0.0	15.0	14.8	8.5	44.5	30.8	26.6				
	30	0.0	30.0	27.5	19.0	42.5	34.5	12.7				
L05	5	0.0	5.0	22.3	12.2	77.4	66.0	23.3	55.4	15.5	56.7	50.8
	10	−0.1	10.0	29.6	17.4	71.3	64.6	16.9				
	15	0.0	15.0	38.6	25.6	68.8	62.0	15.3				
	30	0.3	30.0	58.6	42.8	62.9	61.6	10.9				
L06	5	−2.1	5.0	19.8	13.9	75.8	69.3	20.8	55.2	17.0	59.0	54.1
	10	−4.0	10.1	33.8	26.3	73.5	72.8	18.2				
	15	−3.6	15.0	42.5	28.1	70.6	61.1	14.8				
	30	−6.2	30.1	58.0	44.3	62.7	62.4	8.4				

The shear stress versus horizontal strain, vertical strain versus horizontal strain, and linear Mohr-Coulomb failure envelopes for No. 68-SI are shown in figure 103, figure 104, and figure 105, respectively. The full summary of LSDS results is presented in table 68.

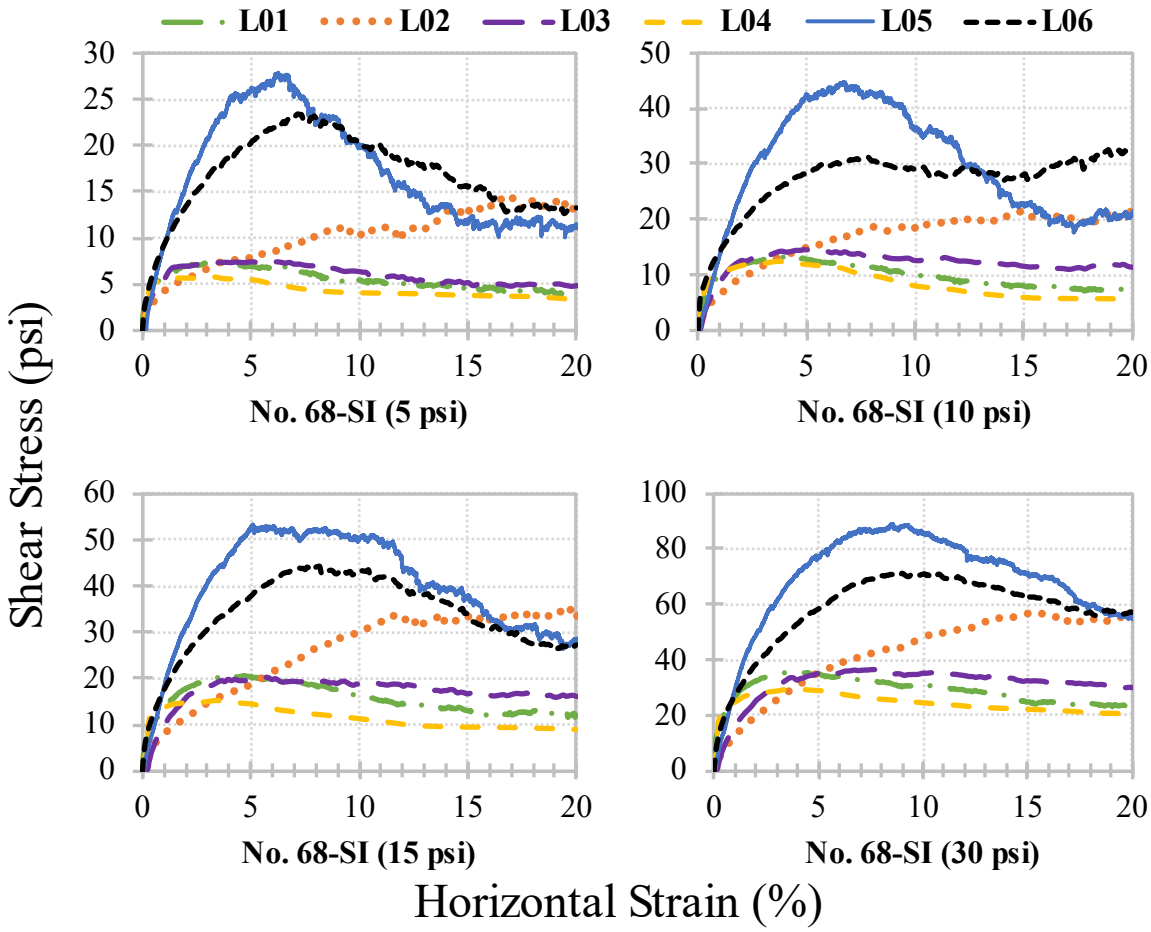

Source: FHWA.

Figure 103. Charts. Shear stress versus horizontal strain for No. 68-SI.

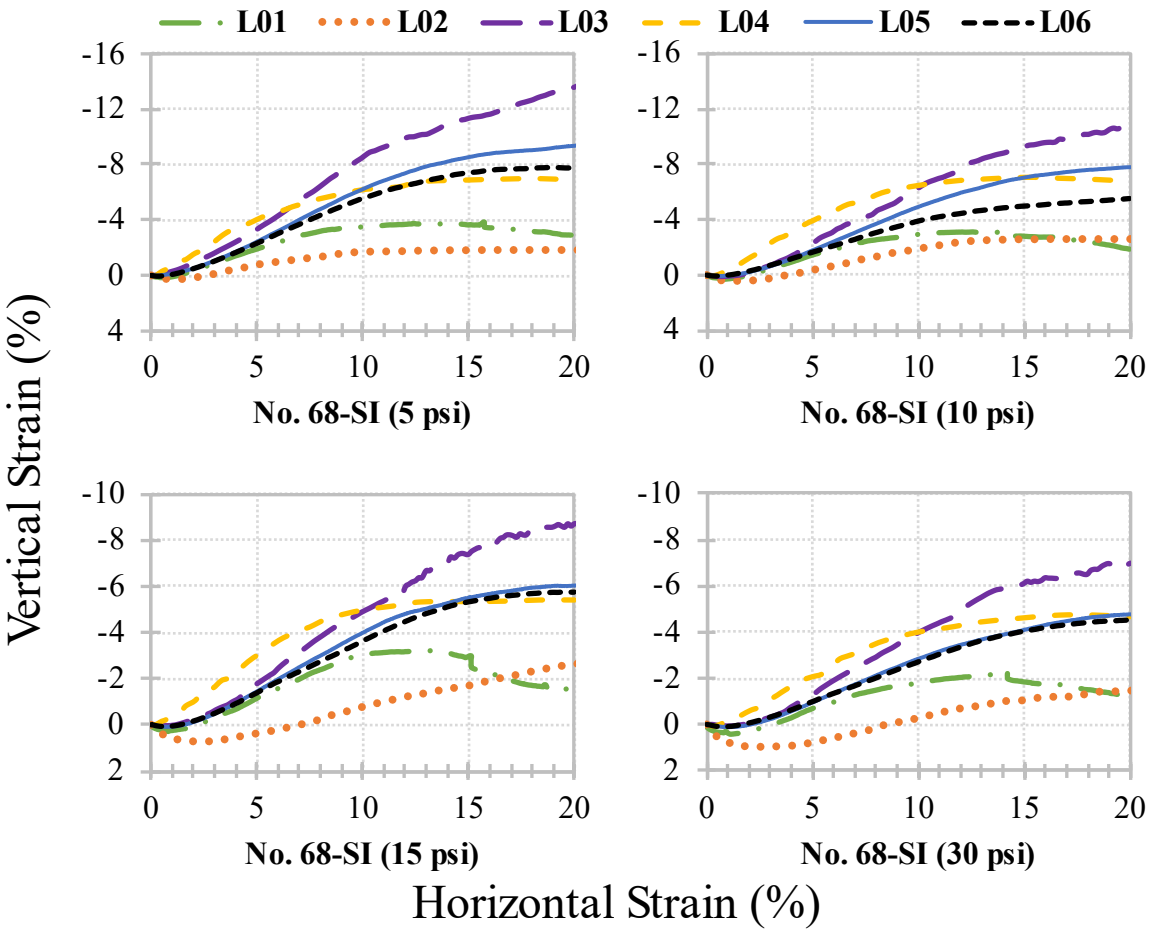

Source: FHWA.

Figure 104. Charts. Vertical strain versus horizontal strain for No. 68-SI.

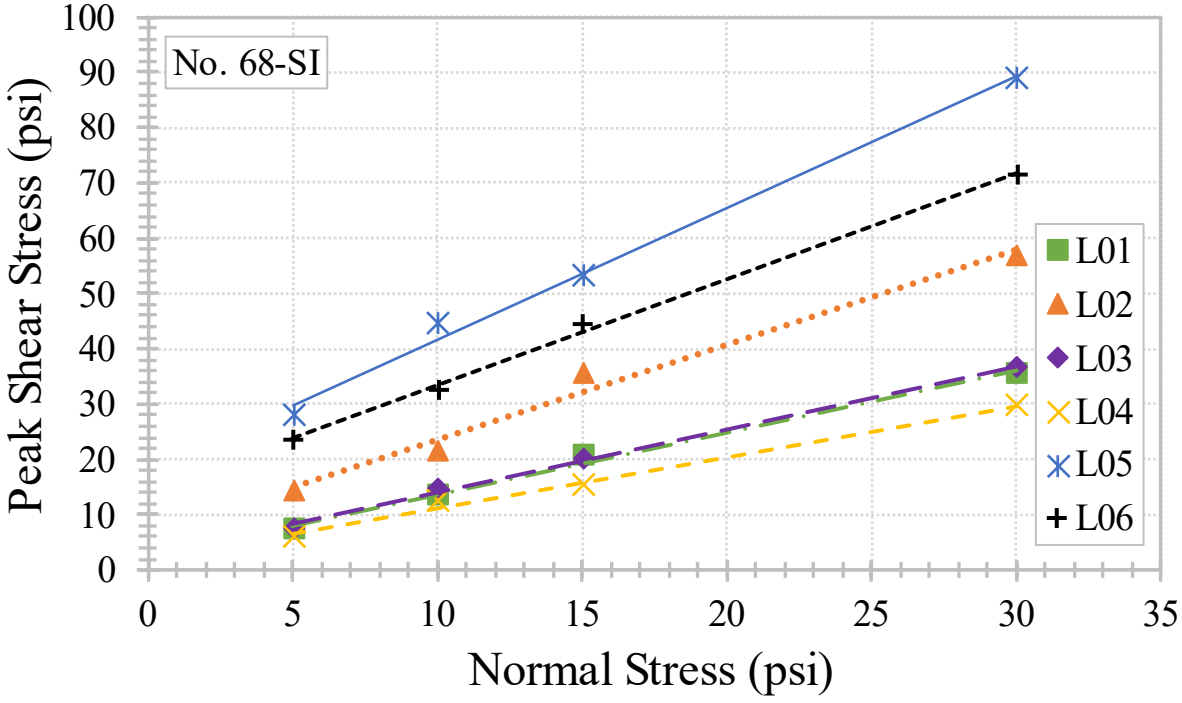

Source: FHWA.

Figure 105. Chart. Linear Mohr-Coulomb failure envelopes for No. 68-SI.

Table 68. Summary of LSDS results for No. 68-SI.

Lab ID	Target σ_n (psi)	$\tau_{initial}$ (psi)	σ_n at τ_{peak} (psi)	τ_{peak} (psi)	τ_r (psi)	ϕ_s (deg)	ϕ_r (deg)	ψ_{max} (deg)	ϕ_t (deg)	c_a (psi)	$\phi_{t,r}$ (deg)	ϕ_{cv} (deg)
L01	5	0.0	5.2	7.3	4.0	55.8	37.7	16.8	48.3	2.4	39.7	40.0
	10	−0.1	10.1	13.4	7.5	53.2	37.0	16.0				
	15	−0.1	15.2	20.6	12.0	53.9	38.1	14.6				
	30	−0.1	30.1	35.5	23.4	49.8	0.0	13.2				
L02	5	0.0	5.0	14.4	13.2	70.9	48.1	12.5	59.7	6.3	59.0	53.0
	10	0.0	10.0	21.5	21.5	65.1	56.6	13.0				
	15	0.0	15.0	35.5	33.4	67.1	60.3	11.0				
	30	0.0	30.0	56.8	55.3	62.2	0.0	11.7				
L03	5	−0.1	5.0	7.4	4.8	56.0	47.9	30.8	48.9	2.5	45.4	47.9
	10	−0.1	10.0	14.5	11.5	55.5	47.5	33.9				
	15	−0.1	15.1	20.2	16.1	53.4	44.6	45.6				
	30	−0.1	30.3	36.5	30.0	50.6	0.0	26.6				
L04	5	0.0	5.0	5.8	3.3	49.0	30.0	31.8	42.8	1.9	31.8	38.9
	10	0.0	10.0	12.4	5.7	51.2	35.6	33.4				
	15	0.0	15.0	15.2	8.9	45.4	34.3	26.6				
	30	0.0	30.0	29.6	20.6	44.6	0.0	24.7				
L05	5	0.0	4.9	27.9	11.2	79.8	56.3	28.3	67.2	18.0	57.6	55.9
	10	0.0	10.0	44.7	21.1	77.4	61.7	23.4				
	15	0.0	15.0	53.3	28.3	74.3	62.1	19.2				
	30	0.0	30.0	89.0	55.4	71.4	0.0	14.5				
L06	5	−1.0	5.2	23.4	13.2	77.9	54.7	24.6	62.6	14.0	57.0	50.8
	10	−4.6	10.0	32.6	32.3	72.9	63.5	18.2				
	15	−4.1	15.1	44.3	27.2	71.3	56.3	17.7				
	30	−3.9	30.1	71.4	57.3	67.2	0.0	13.7				

NO. 8 OGAs

The shear stress versus horizontal strain, vertical strain versus horizontal strain, and linear Mohr-Coulomb failure envelopes for No. 8-BA are shown in figure 106, figure 107, and figure 108, respectively. The full summary of LSDS results is presented in table 69.

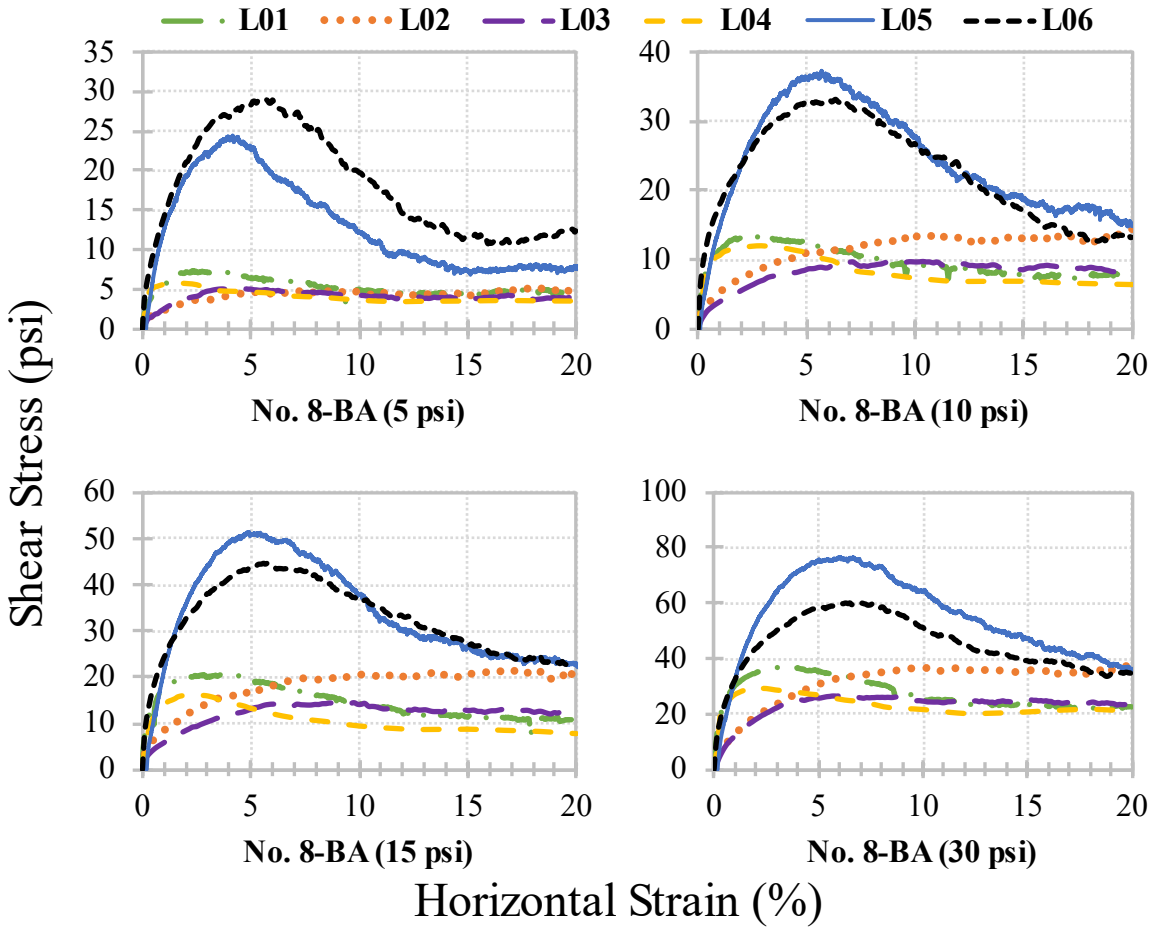

Source: FHWA.

Figure 106. Charts. Shear stress versus horizontal strain for No. 8-BA.

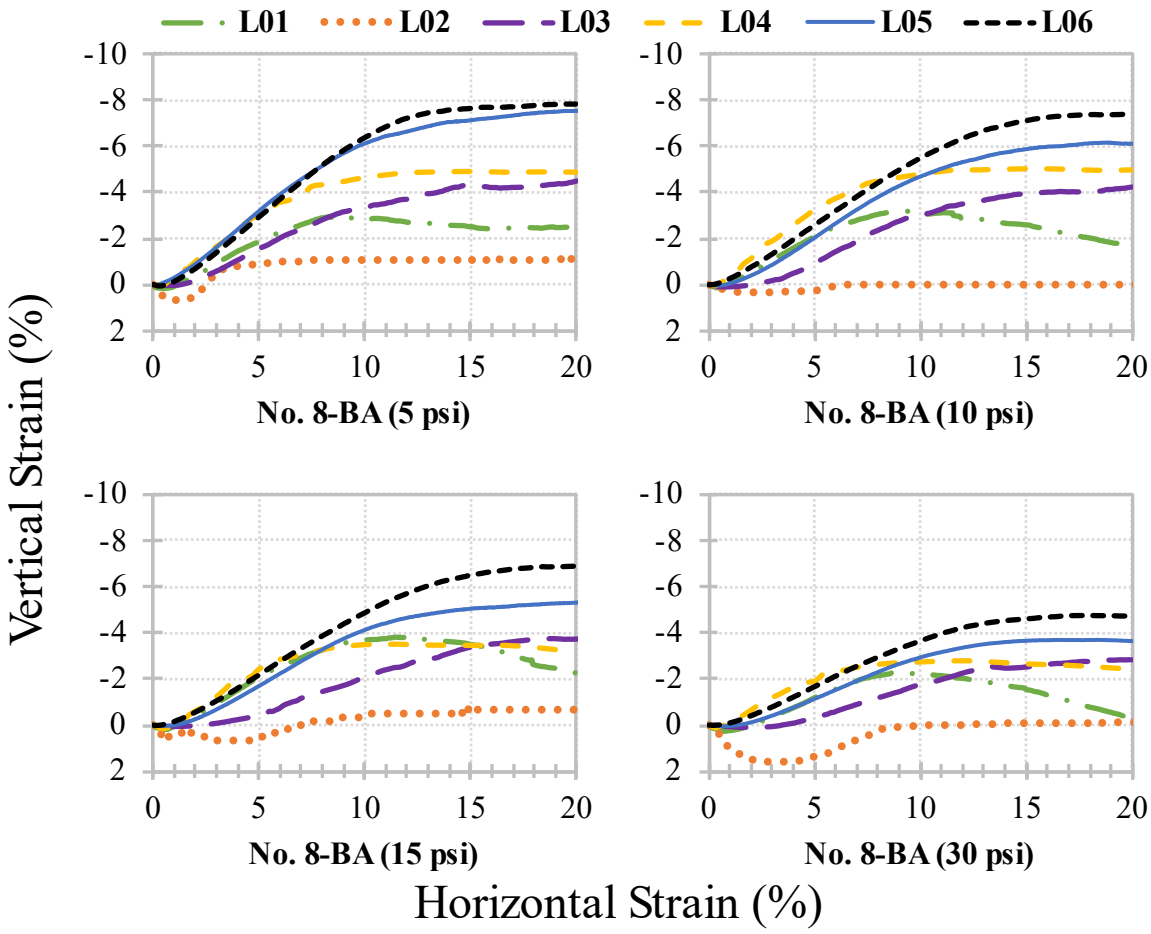

Source: FHWA.

Figure 107. Charts. Vertical strain versus horizontal strain for No. 8-BA.

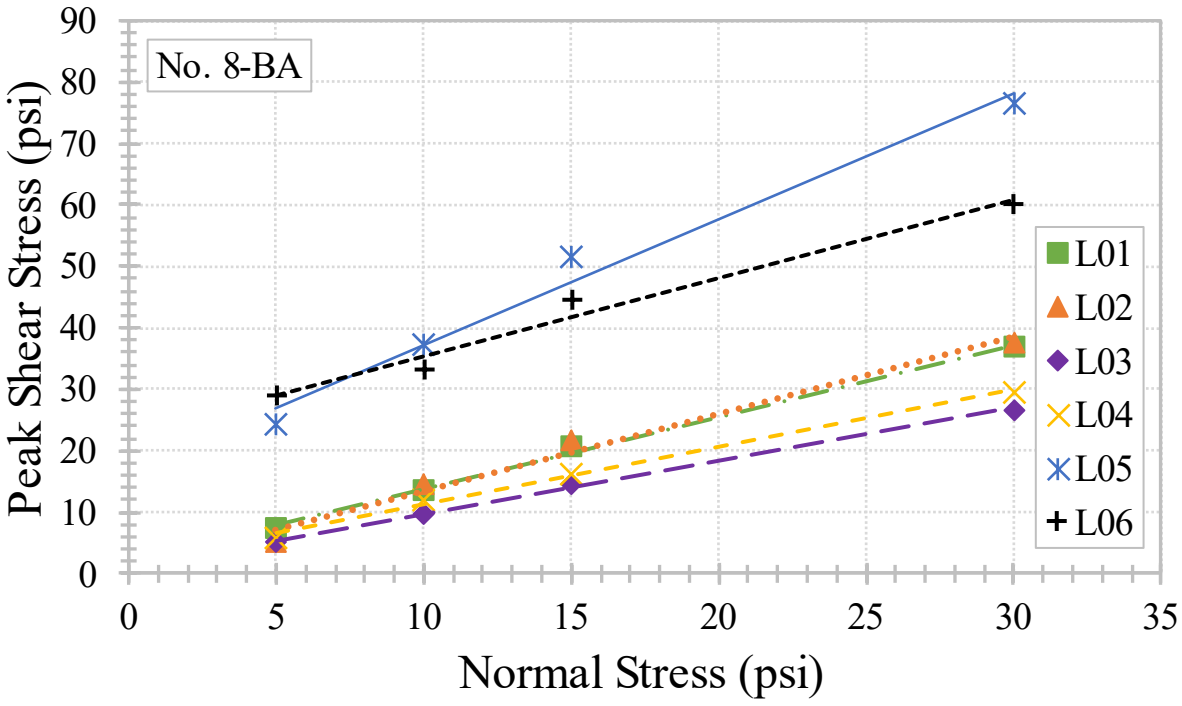

Source: FHWA.

Figure 108. Chart. Linear Mohr-Coulomb failure envelopes for No. 8-BA.

Table 69. Summary of LSDS results for No. 8-BA.

Lab ID	Target σ_n (psi)	$\tau_{initial}$ (psi)	σ_n at τ_{peak} (psi)	τ_{peak} (psi)	τ_r (psi)	ϕ_s (deg)	ϕ_r (deg)	ψ_{max} (deg)	ϕ_t (deg)	c_a (psi)	$\phi_{t,r}$ (deg)	ϕ_{cv} (deg)
L01	5	0.0	5.2	7.4	4.8	55.9	43.9	19.2	49.7	1.9	37.1	37.0
	10	0.0	10.1	13.5	8.1	53.4	38.9	16.6				
	15	−0.1	15.2	20.6	10.8	54.0	35.9	18.3				
	30	−0.1	30.2	36.9	22.6	50.9	36.9	14.5				
L02	5	0.0	5.0	5.3	5.2	46.6	46.3	35.7	51.4	0.9	52.0	59.1
	10	0.0	10.0	14.4	14.4	55.2	55.2	9.1				
	15	0.0	15.0	21.8	21.1	55.4	54.5	23.6				
	30	0.0	30.0	37.6	37.2	51.4	51.1	21.0				
L03	5	0.1	5.0	5.1	4.0	45.5	38.8	15.4	40.8	1.1	38.5	39.8
	10	0.1	10.0	9.7	8.3	44.3	39.6	18.3				
	15	0.1	14.9	14.5	12.5	44.1	39.9	18.8				
	30	0.2	30.0	26.7	23.4	41.7	38.0	14.9				
L04	5	0.0	5.0	5.8	3.5	49.3	35.3	25.6	42.9	1.9	33.4	34.3
	10	0.0	10.0	12.0	6.4	50.2	32.7	30.1				
	15	0.0	15.0	16.1	7.8	47.1	27.3	26.6				
	30	0.0	30.0	29.6	20.9	44.6	34.9	19.8				
L05	5	0.0	5.0	24.4	7.9	78.4	57.8	26.9	64.0	16.6	52.3	58.2
	10	0.0	10.0	37.3	15.0	75.0	56.3	21.9				
	15	0.0	15.1	51.4	22.9	73.7	56.8	19.4				
	30	0.0	30.0	76.6	36.2	68.6	50.4	14.3				
L06	5	−3.8	5.0	29.0	12.4	80.2	68.0	26.7	51.8	22.7	51.1	35.3
	10	−0.4	10.1	33.1	13.2	73.2	52.9	22.4				
	15	−1.6	15.2	44.6	22.4	71.4	56.2	20.8				
	30	2.2	30.1	60.1	34.1	63.5	48.6	16.9				

The shear stress versus horizontal strain, vertical strain versus horizontal strain, and linear Mohr-Coulomb failure envelopes for No. 8-DI are shown in figure 109, figure 110, and figure 111, respectively. The full summary of LSDS results is presented in table 70.

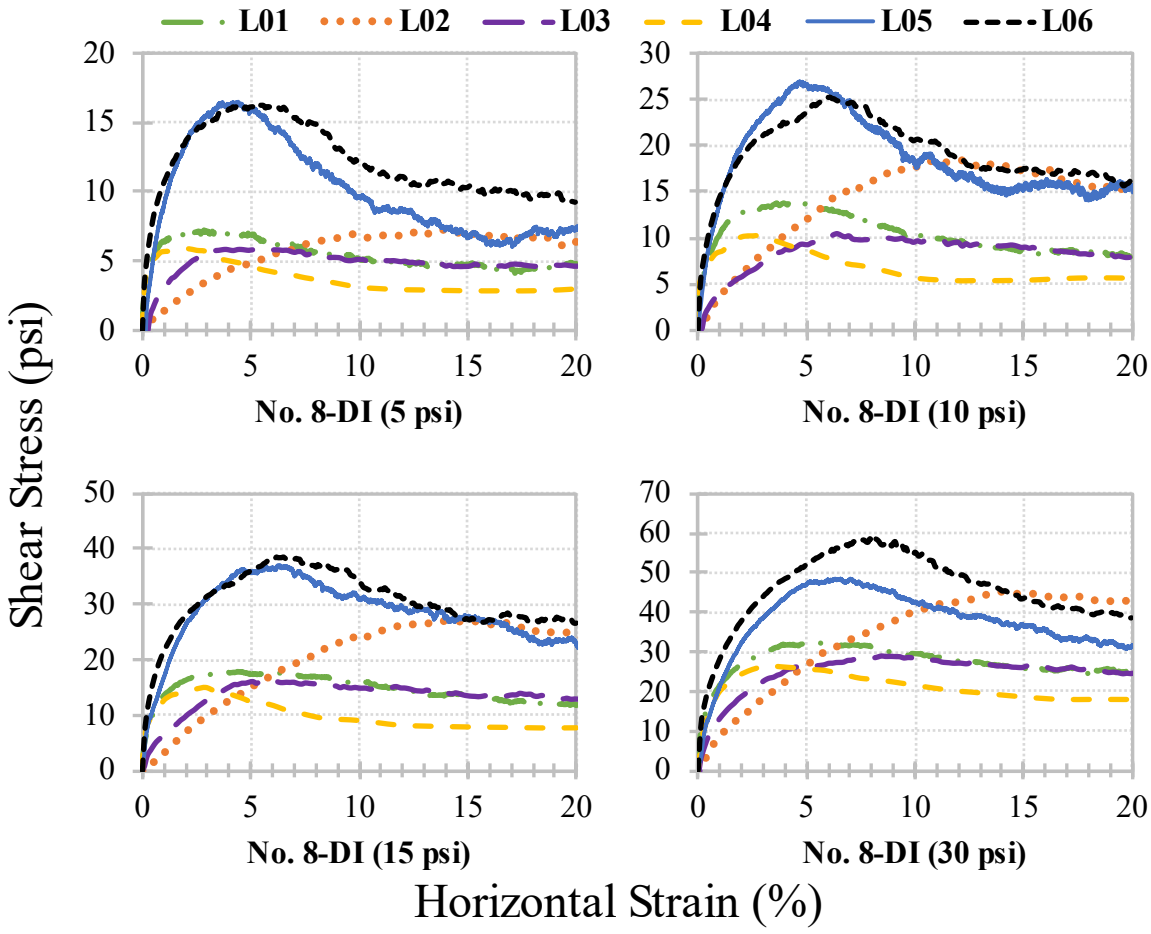

Source: FHWA.

Figure 109. Charts. Shear stress versus horizontal strain for No. 8-DI.

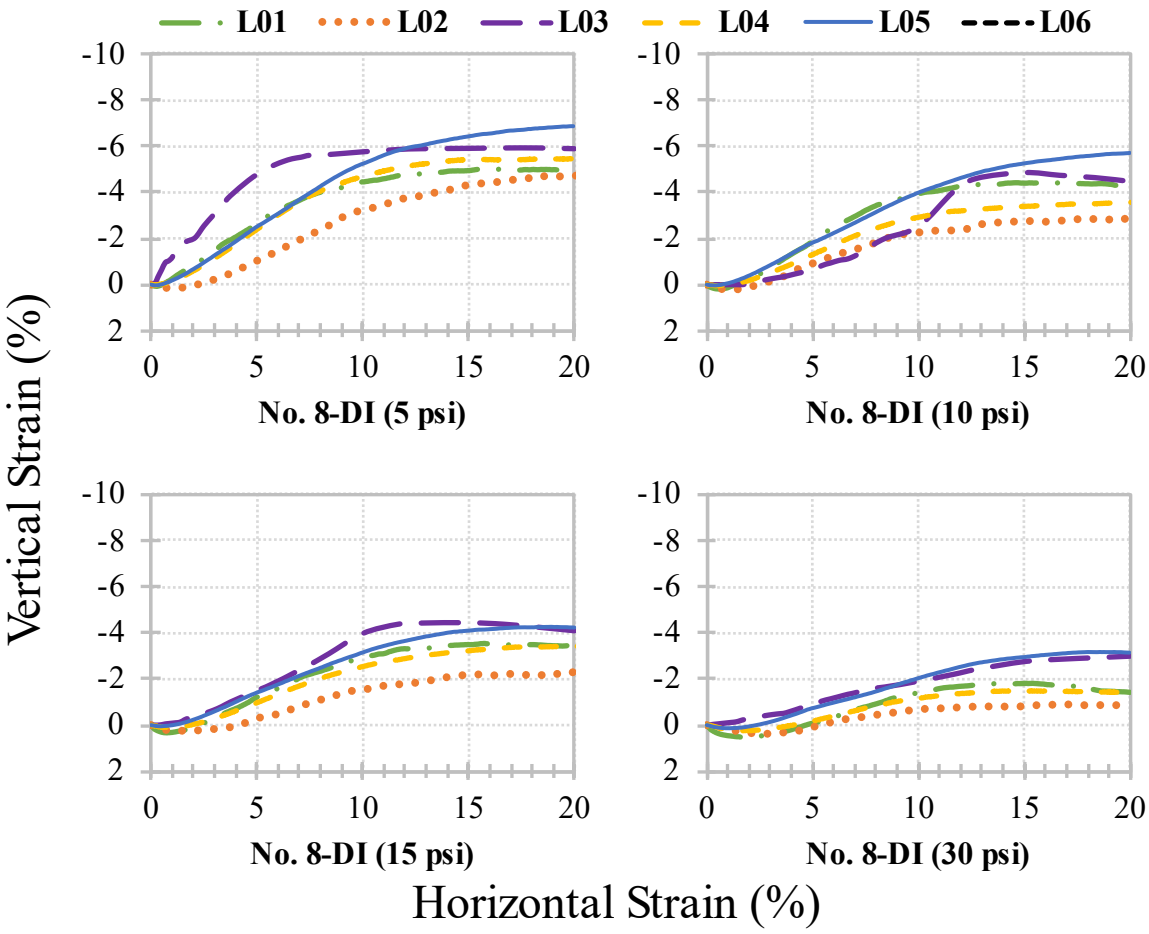

Source: FHWA.

Figure 110. Charts. Vertical strain versus horizontal strain for No. 8-DI.

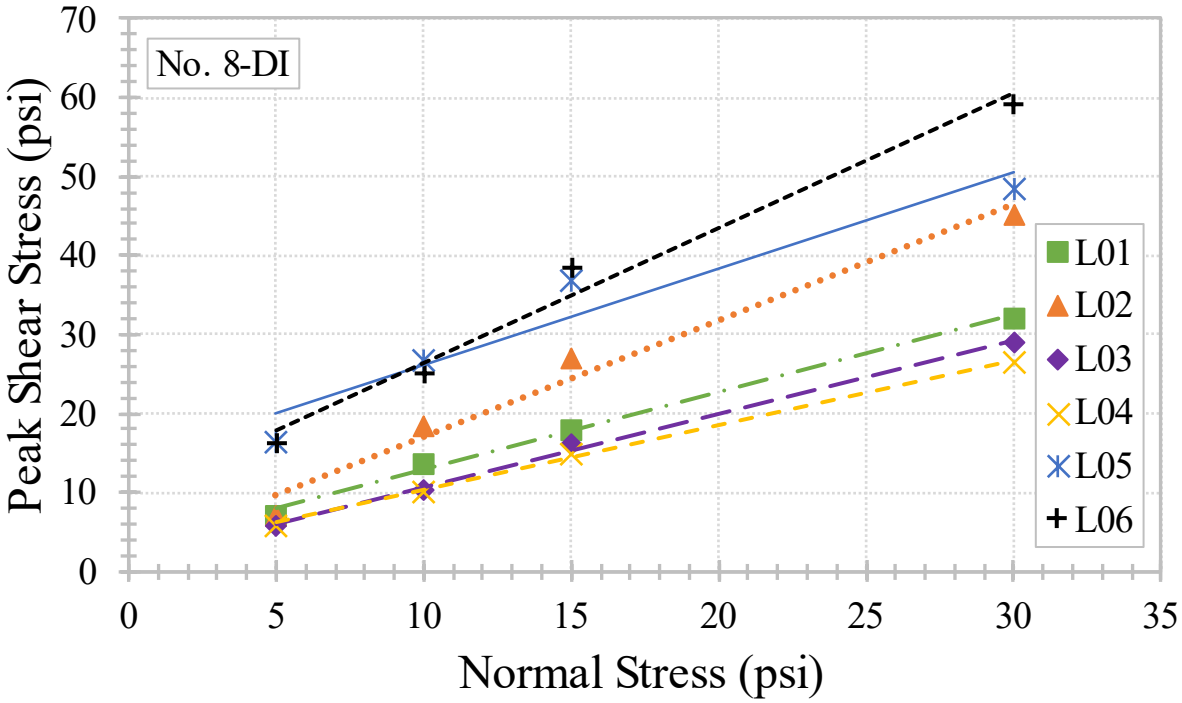

Source: FHWA.

Figure 111. Chart. Linear Mohr-Coulomb failure envelopes for No. 8-DI.

Table 70. Summary of LSDS results for No. 8-DI.

Lab ID	Target σ_n (psi)	$\tau_{initial}$ (psi)	σ_n at τ_{peak} (psi)	τ_{peak} (psi)	τ_r (psi)	ϕ_s (deg)	ϕ_r (deg)	ψ_{max} (deg)	ϕ_t (deg)	c_a (psi)	$\phi_{t,r}$ (deg)	ϕ_{cv} (deg)
L01	5	0.1	5.1	7.2	4.8	55.3	43.6	21.8	44.4	3.1	39.5	37.9
	10	0.0	10.2	13.8	7.9	54.0	38.5	19.8				
	15	0.0	15.1	17.9	11.9	50.0	38.5	17.1				
	30	0.2	30.0	32.2	24.9	47.1	39.7	11.1				
L02	5	0.0	5.0	7.2	6.3	55.4	51.7	—	55.8	2.5	55.9	—
	10	0.0	10.0	18.4	15.3	61.5	56.7	—				
	15	0.0	15.0	27.0	24.5	61.0	58.5	—				
	30	0.0	30.0	45.3	43.2	56.5	55.2	—				
L03	5	0.3	5.0	5.8	4.6	49.4	42.7	16.0	42.8	1.5	39.5	41.2
	10	0.0	10.0	10.5	7.9	46.3	38.3	17.5				
	15	0.0	15.0	16.3	12.9	47.5	40.8	13.6				
	30	0.0	30.1	29.0	24.5	44.0	39.3	8.7				
L04	5	0.0	5.0	5.9	3.0	49.7	30.8	45.0	39.4	2.1	30.2	40.4
	10	0.0	10.0	10.2	5.6	45.7	29.4	24.5				
	15	0.0	15.0	15.0	7.7	45.0	27.3	15.3				
	30	0.0	30.0	26.5	18.0	41.5	30.9	11.3				
L05	5	0.0	5.0	16.5	7.4	73.1	55.8	22.6	50.7	13.9	49.8	51.2
	10	−0.1	10.0	26.9	15.5	69.6	57.2	15.3				
	15	0.0	15.0	37.0	22.6	68.0	56.4	13.8				
	30	0.0	30.0	48.5	31.6	58.3	46.5	9.4				
L06	5	−2.1	5.1	16.4	9.2	73.0	61.6	22.6	59.6	9.2	54.7	52.4
	10	−2.9	10.1	25.3	16.1	68.4	58.1	18.1				
	15	−4.5	15.1	38.5	26.6	68.7	60.6	15.5				
	30	−5.4	30.1	59.2	38.6	63.1	52.1	13.0				

—Not measured/evaluated.

The shear stress versus horizontal strain, vertical strain versus horizontal strain, and linear Mohr-Coulomb failure envelopes for No. 8-GG are shown in figure 112, figure 113, and figure 114, respectively; the full summary of LSDS results is presented in table 71.

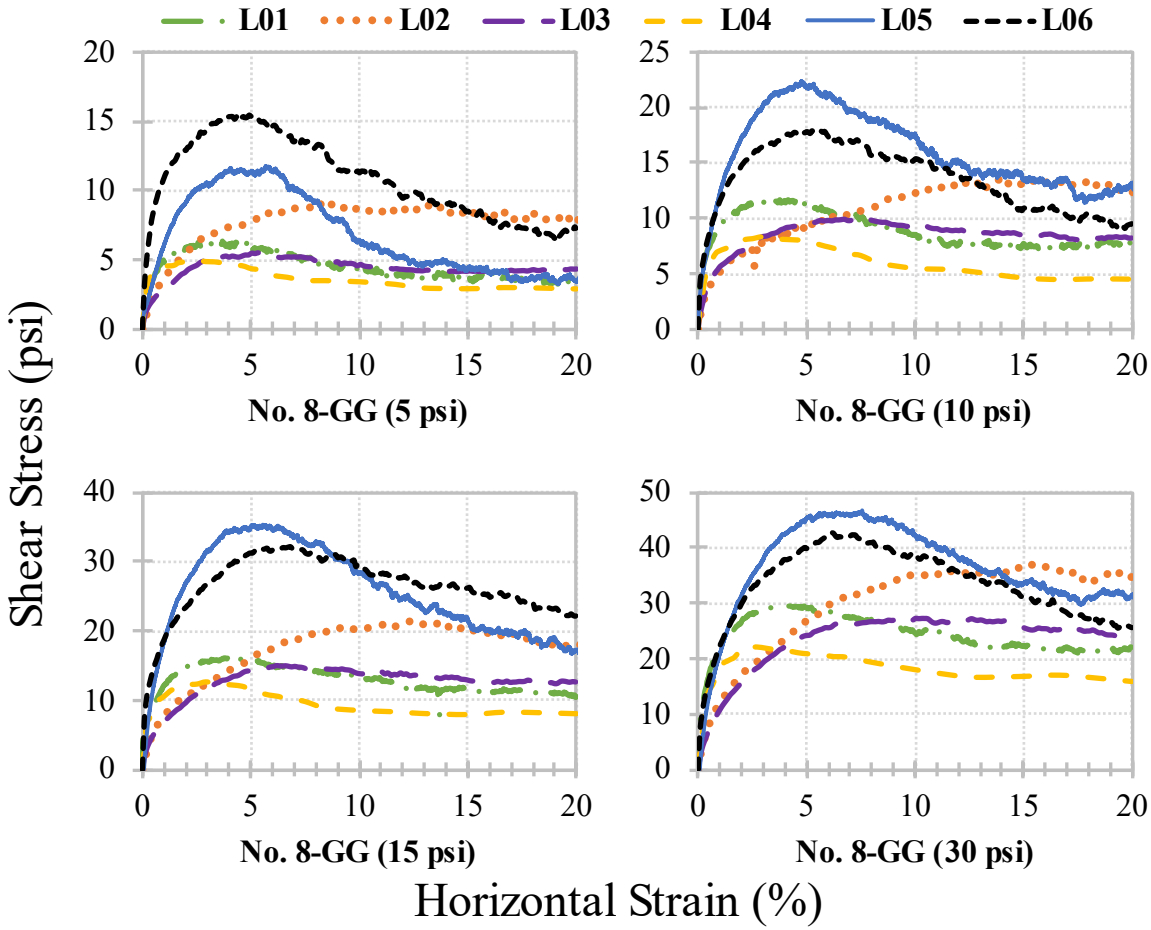

Source: FHWA.

Figure 112. Charts. Shear stress versus horizontal strain for No. 8-GG.

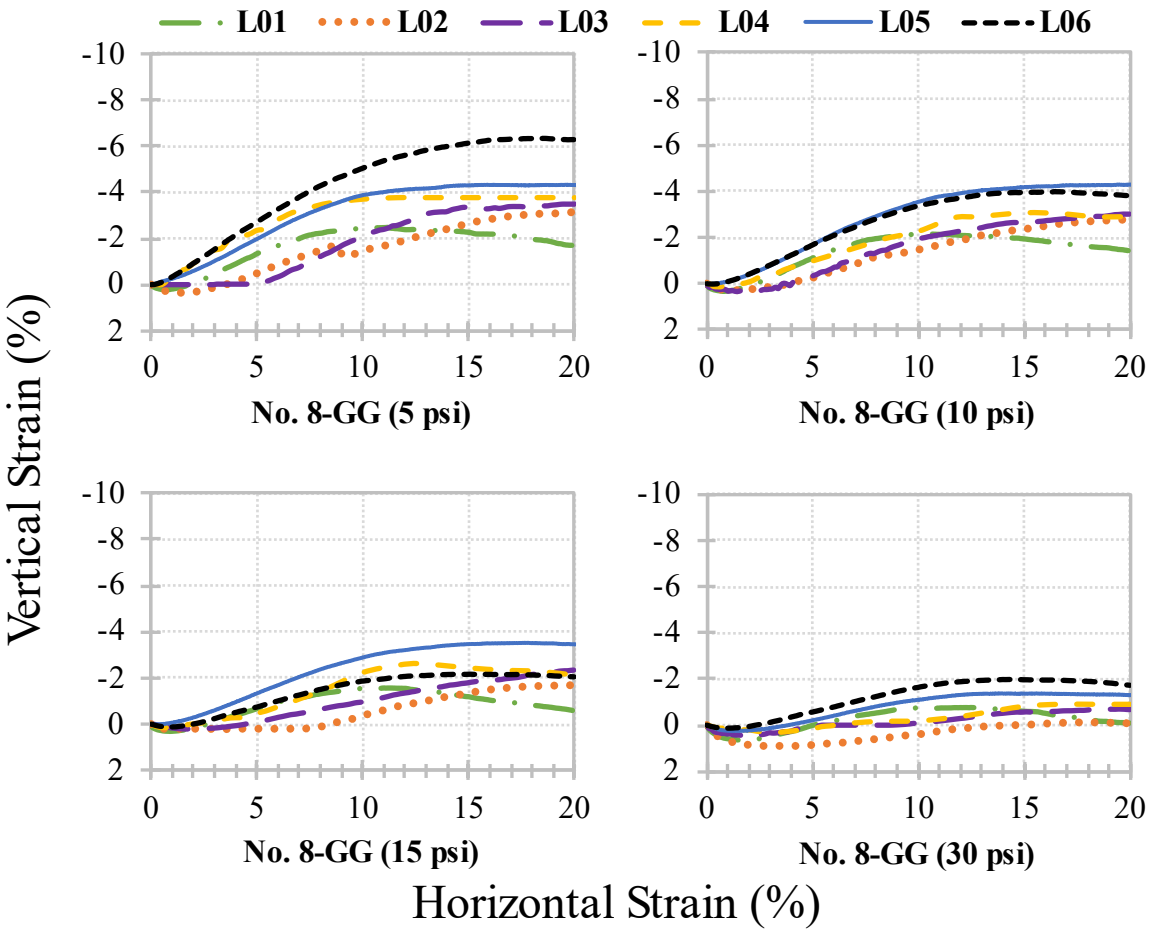

Source: FHWA.

Figure 113. Charts. Vertical strain versus horizontal strain for No. 8-GG.

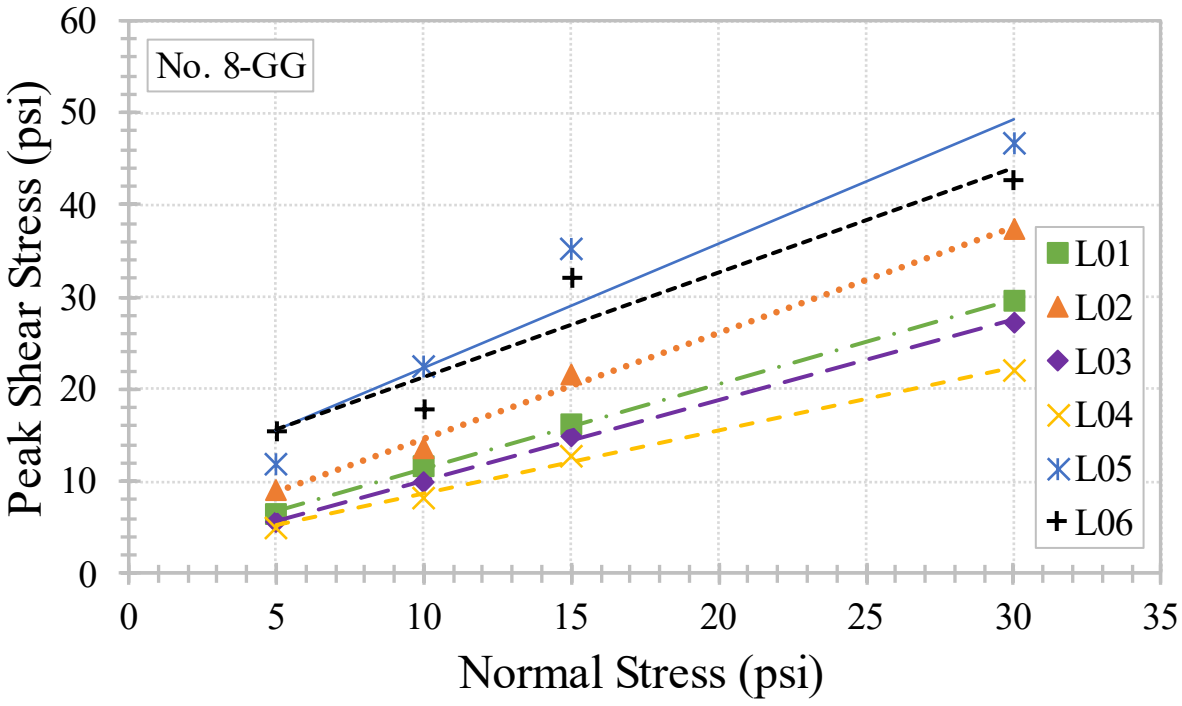

Source: FHWA.

Figure 114. Chart. Linear Mohr-Coulomb failure envelopes for No. 8-GG.

Table 71. Summary of LSDS results for No. 8-GG.

Lab ID	Target σ_n (psi)	$\tau_{initial}$ (psi)	σ_n at τ_{peak} (psi)	τ_{peak} (psi)	τ_r (psi)	ϕ_s (deg)	ϕ_r (deg)	ψ_{max} (deg)	ϕ_t (deg)	c_a (psi)	$\phi_{t,r}$ (deg)	ϕ_{cv} (deg)
L01	5	0.0	5.3	6.4	3.6	51.8	35.8	15.9	42.6	2.2	36.3	38.1
	10	−0.1	10.1	11.7	7.8	49.4	37.9	14.7				
	15	0.2	15.1	16.2	10.6	47.2	35.4	9.8				
	30	0.0	30.1	29.6	22.1	44.6	36.4	8.7				
L02	5	0.0	5.0	9.1	7.9	61.3	57.7	12.5	48.9	3.2	49.8	45.3
	10	0.0	10.0	13.5	12.4	53.5	51.2	12.5				
	15	0.0	15.0	21.5	18.1	55.1	50.3	10.8				
	30	0.0	30.0	37.3	34.9	51.2	49.3	6.0				
L03	5	0.1	5.0	5.5	4.3	47.8	40.9	17.1	41.0	1.4	38.8	44.3
	10	0.1	10.0	10.0	8.2	44.9	39.4	31.5				
	15	0.1	14.9	15.0	12.7	45.0	40.2	8.7				
	30	0.1	29.7	27.3	23.7	42.3	38.3	11.7				
L04	5	0.0	5.0	5.0	2.9	44.9	30.2	31.0	34.5	1.7	27.8	35.4
	10	0.0	10.0	8.3	4.5	39.8	24.3	12.4				
	15	0.0	15.0	12.7	8.1	40.2	28.3	11.6				
	30	0.0	30.0	22.1	15.9	36.4	27.9	6.8				
L05	5	2.3	5.1	11.8	3.4	67.0	34.4	18.3	53.4	8.8	47.2	50.1
	10	0.0	10.0	22.4	13.0	65.9	52.4	17.1				
	15	0.0	15.0	35.3	17.3	67.0	49.0	13.9				
	30	0.0	30.1	46.8	31.5	57.3	46.4	8.8				
L06	5	−0.2	5.1	15.5	7.3	72.2	55.5	22.3	48.5	10.1	44.6	49.4
	10	1.8	10.1	17.9	9.5	60.8	43.5	16.4				
	15	−3.1	15.1	32.2	22.2	65.0	55.9	10.5				
	30	2.3	30.0	42.7	25.6	54.9	40.5	9.3				

The shear stress versus horizontal strain, vertical strain versus horizontal strain, and linear Mohr-Coulomb failure envelopes for No. 8-LI are shown in figure 115, figure 116, and figure 117, respectively; the full summary of LSDS results is presented in table 72.

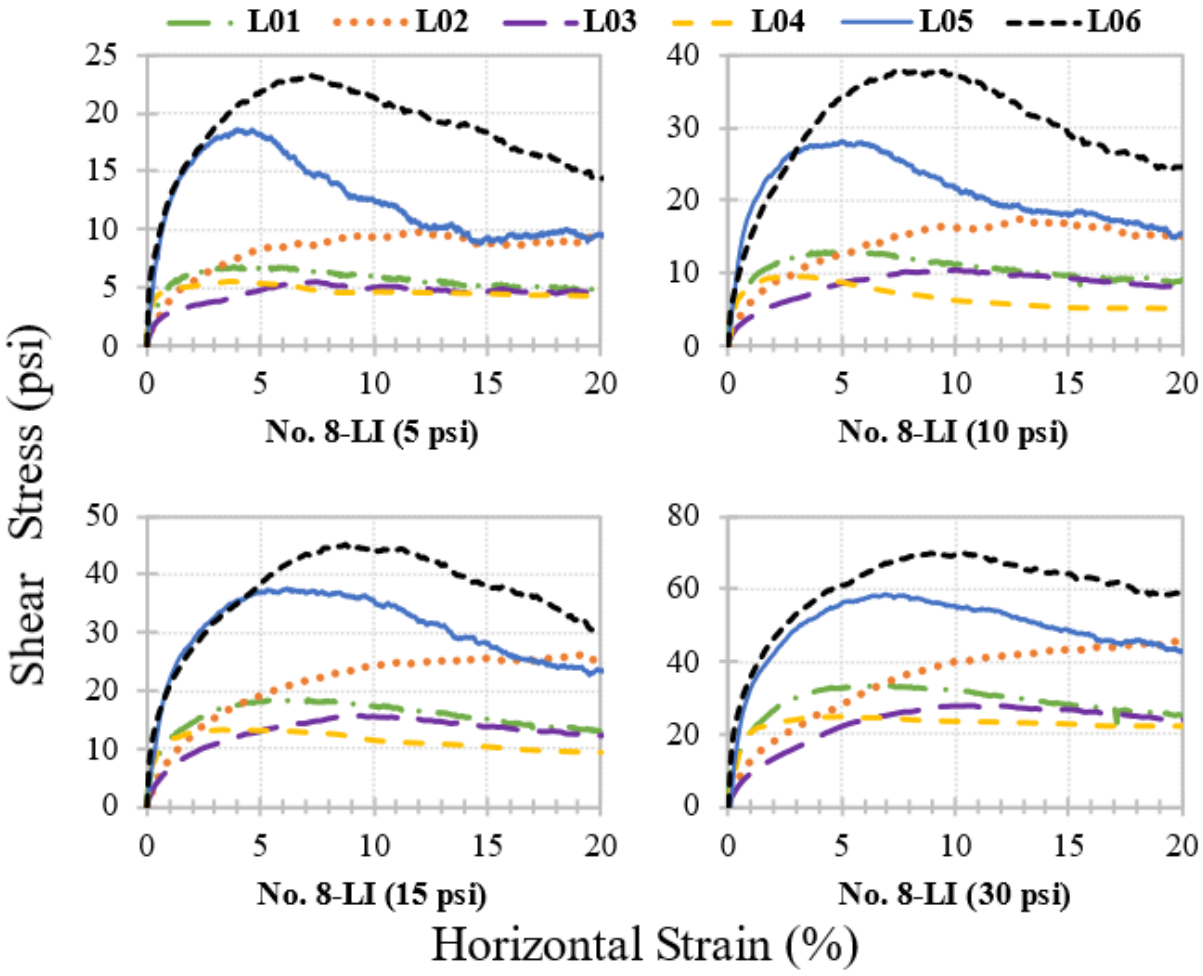

Source: FHWA.

Figure 115. Charts. Shear stress versus horizontal strain for No. 8-LI.

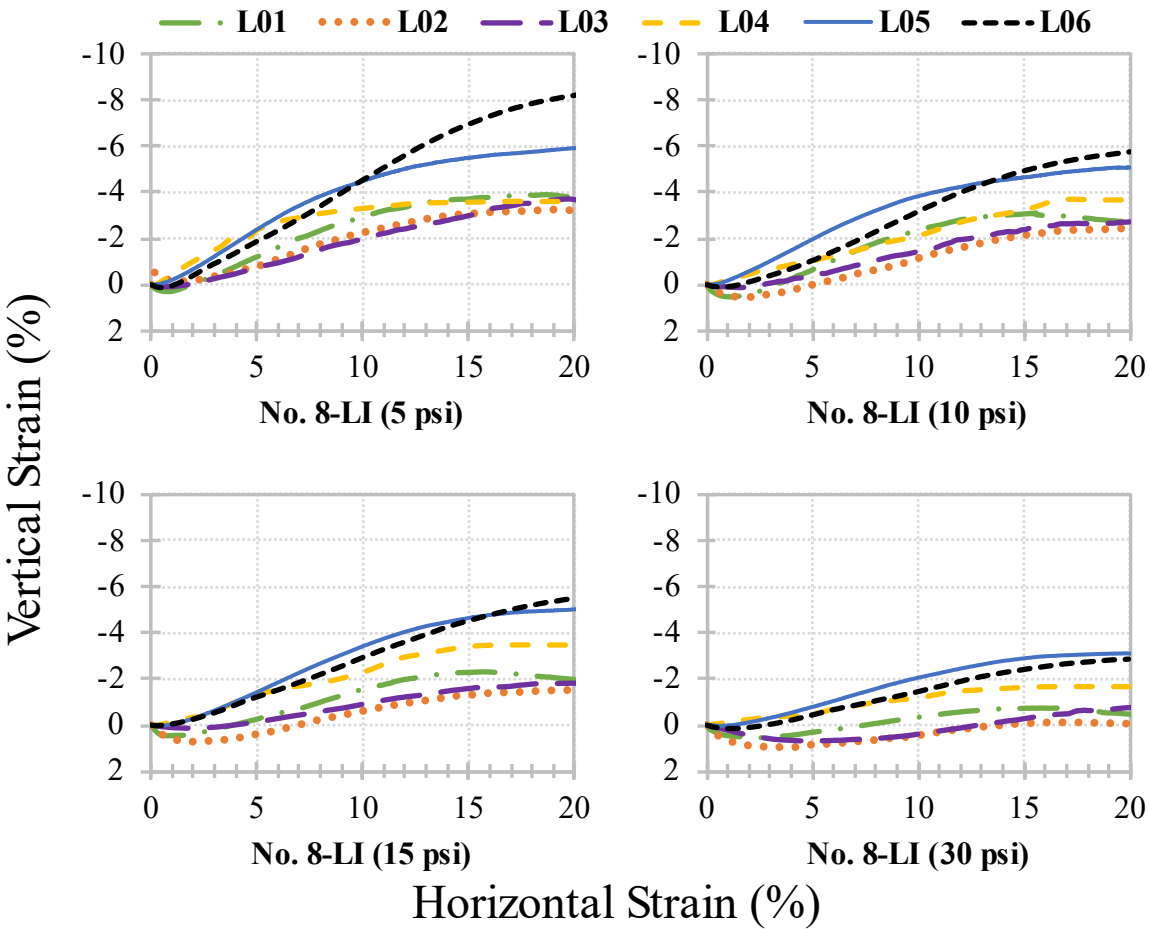

Source: FHWA.

Figure 116. Charts. Vertical strain versus horizontal strain for No. 8-LI.

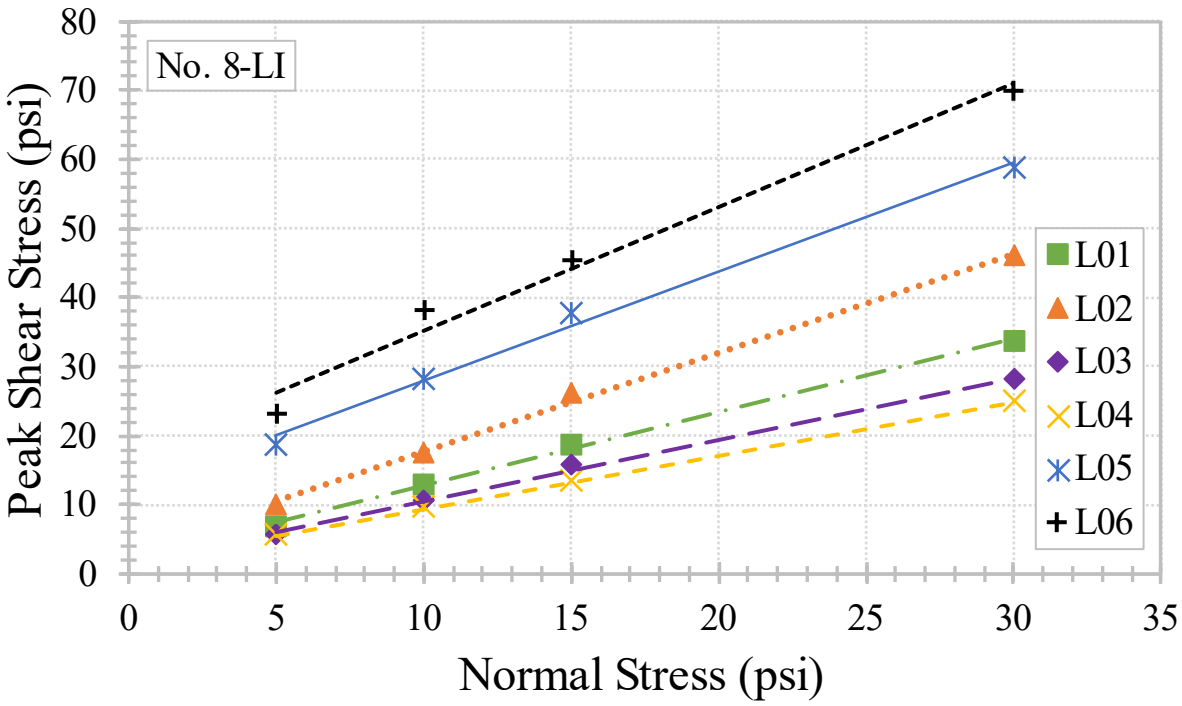

Source: FHWA.

Figure 117. Chart. Linear Mohr-Coulomb failure envelopes for No. 8-LI.

Table 72. Summary of LSDS results for No. 8-LI.

Lab ID	Target σ_n (psi)	$\tau_{initial}$ (psi)	σ_n at τ_{peak} (psi)	τ_{peak} (psi)	τ_r (psi)	ϕ_s (deg)	ϕ_r (deg)	ψ_{max} (deg)	ϕ_t (deg)	c_a (psi)	$\phi_{t,r}$ (deg)	ϕ_{cv} (deg)
L01	5	0.0	5.2	6.8	4.8	53.8	40.0	14.1	46.7	2.1	40.5	46.0
	10	−0.1	10.1	12.9	9.1	52.3	39.3	13.8				
	15	−0.2	15.2	18.6	13.1	51.2	36.9	9.5				
	30	−0.1	30.1	33.6	25.2	48.2	36.7	4.7				
L02	5	0.0	5.0	9.8	9.4	62.9	57.7	14.5	55.2	3.3	57.4	53.4
	10	0.0	10.0	17.5	15.1	60.2	61.2	11.6				
	15	0.0	15.0	26.2	25.3	60.2	59.7	8.9				
	30	0.0	30.0	45.9	45.9	56.8	58.9	6.0				
L03	5	0.2	5.0	5.5	4.6	47.6	40.0	10.7	41.8	1.5	38.9	45.9
	10	0.2	10.0	10.4	7.9	46.2	43.2	12.4				
	15	0.2	14.9	15.7	12.3	46.4	41.0	5.4				
	30	0.2	29.7	28.0	24.1	43.0	39.3	10.0				
L04	5	0.0	5.0	5.5	4.3	47.9	26.6	21.8	37.7	1.7	35.2	34.6
	10	0.0	10.0	9.6	5.1	43.8	28.0	11.3				
	15	0.0	15.0	13.3	9.4	41.6	26.7	13.5				
	30	0.0	30.0	24.9	22.3	39.7	32.7	11.3				
L05	5	−0.1	5.0	18.6	9.6	75.0	58.4	20.6	57.7	12.1	55.8	50.6
	10	0.2	10.0	28.2	15.5	70.5	58.4	16.9				
	15	0.0	15.1	37.7	23.5	68.3	55.4	15.3				
	30	−0.1	30.0	58.7	42.8	62.9	50.7	10.4				
L06	5	−4.0	5.1	23.2	14.5	77.9	51.7	21.5	60.8	17.3	63.7	58.8
	10	−1.8	10.1	38.0	24.6	75.3	60.3	16.4				
	15	1.2	15.1	45.2	30.6	71.7	60.6	14.2				
	30	−8.0	30.1	69.9	58.5	66.8	58.8	9.2				

The shear stress versus horizontal strain, vertical strain versus horizontal strain, and linear Mohr-Coulomb failure envelopes for No. 8-SI are shown in figure 118, figure 119, and figure 120, respectively. The full summary of LSDS results is presented in table 73.

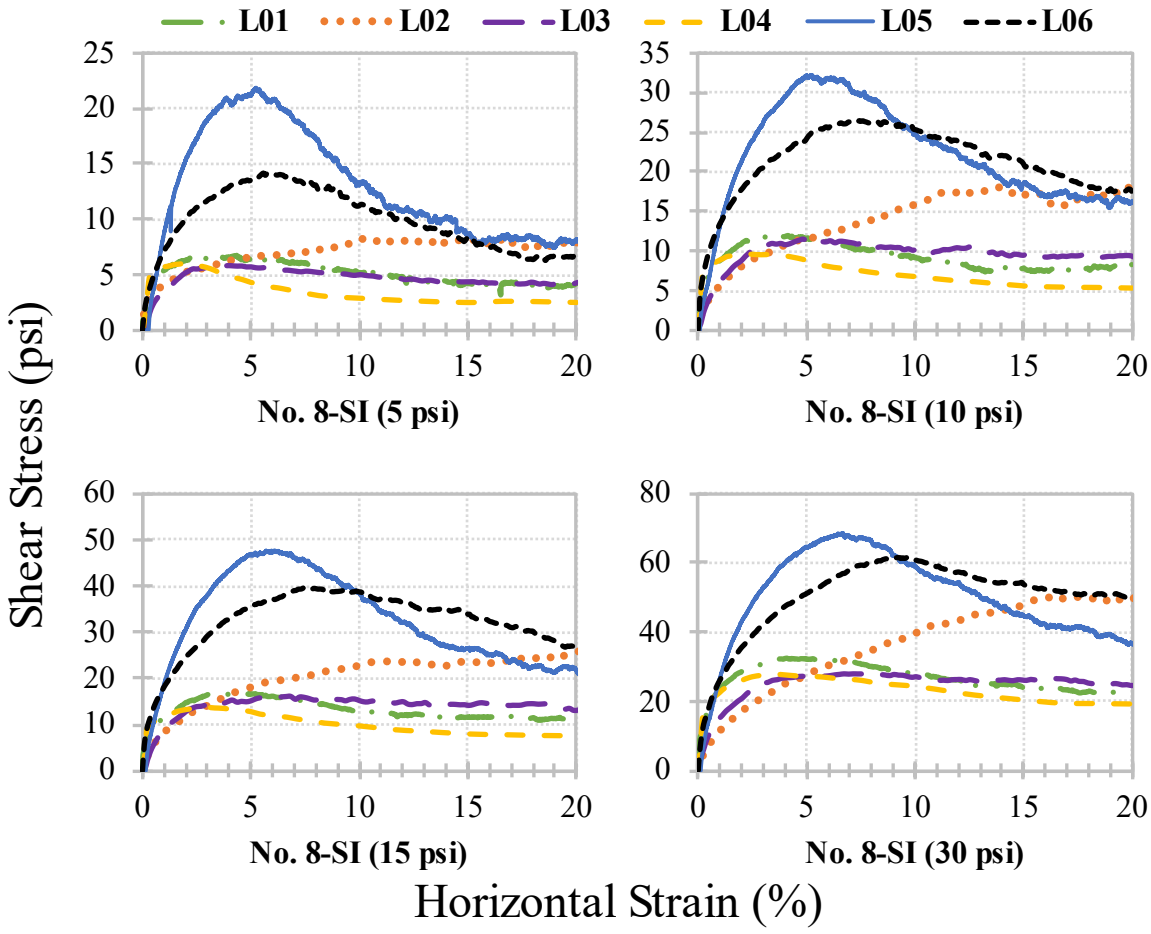

Source: FHWA.

Figure 118. Charts. Shear stress versus horizontal strain for No. 8-SI.

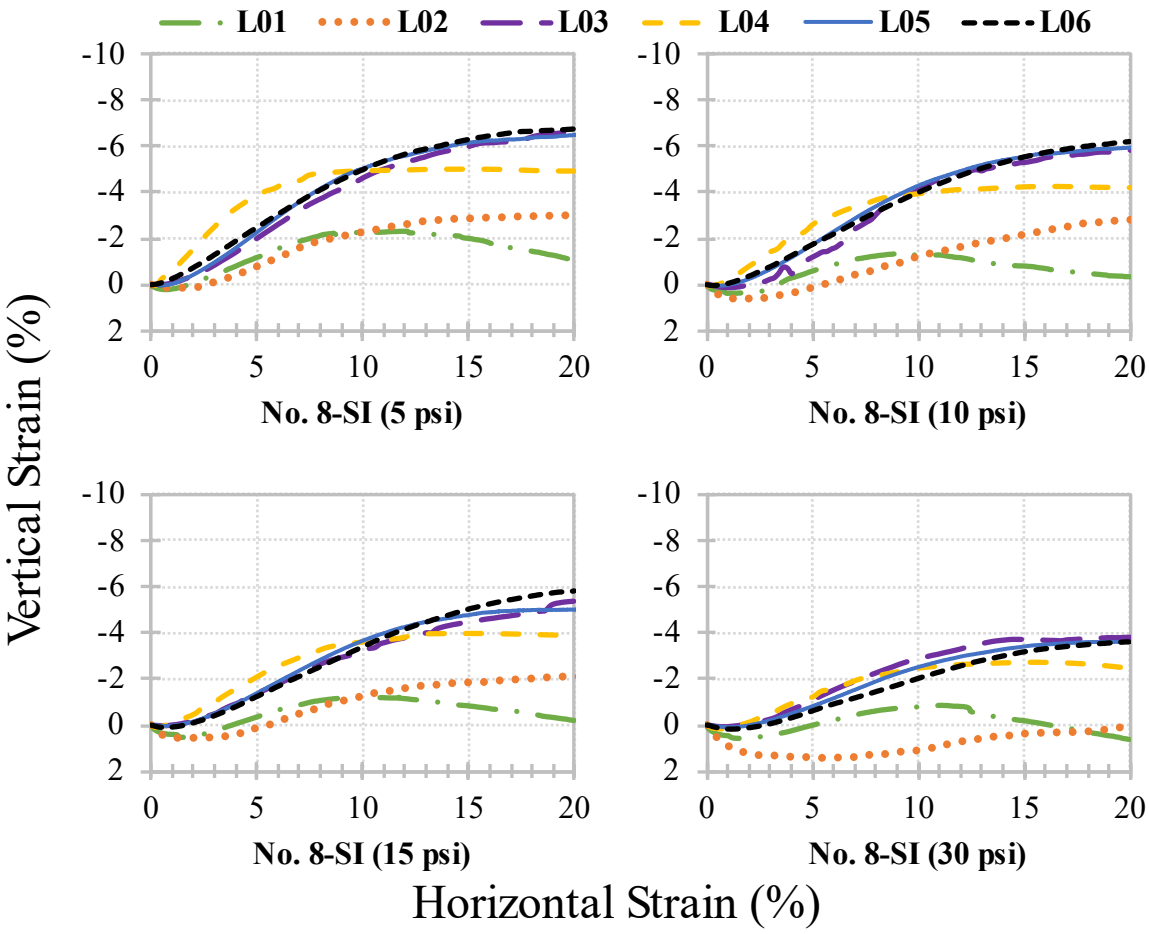

Source: FHWA.

Figure 119. Charts. Vertical strain versus horizontal strain for No. 8-SI.

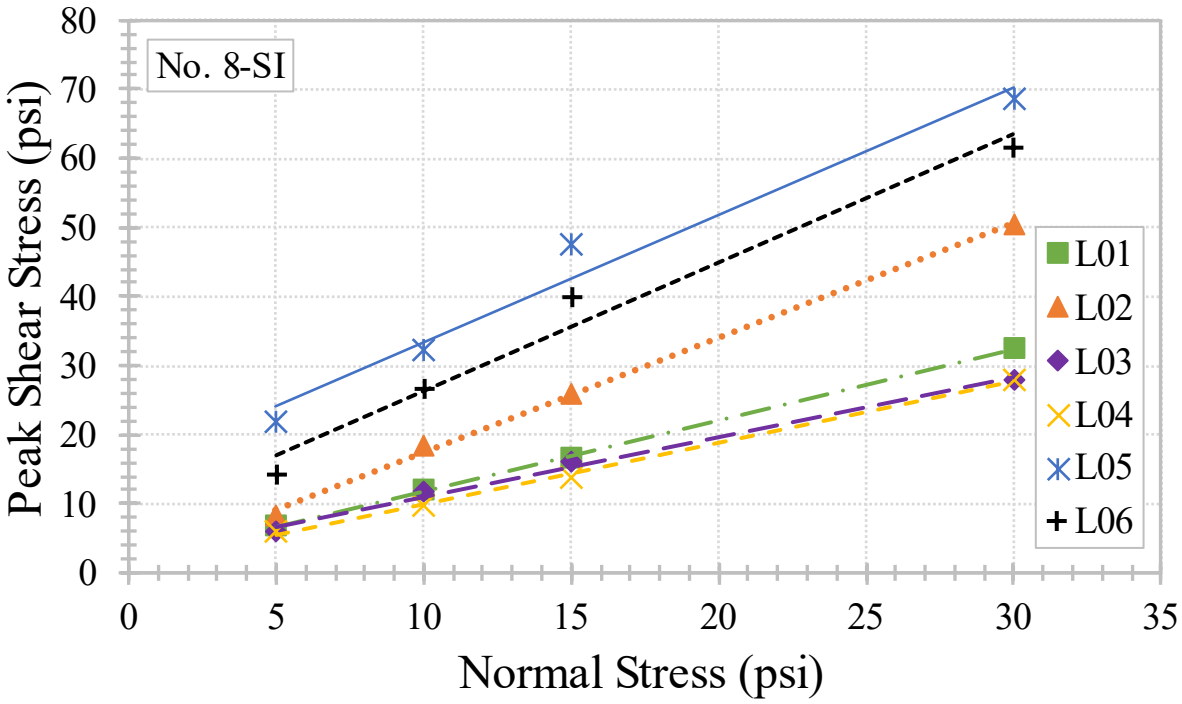

Source: FHWA.

Figure 120. Chart. Linear Mohr-Coulomb failure envelopes for No. 8-SI.

Table 73. Summary of LSDS results for No. 8-SI.

Lab ID	Target σ_n (psi)	$\tau_{initial}$ (psi)	σ_n at τ_{peak} (psi)	τ_{peak} (psi)	τ_r (psi)	ϕ_s (deg)	ϕ_r (deg)	ψ_{max} (deg)	ϕ_t (deg)	c_a (psi)	$\phi_{t,r}$ (deg)	ϕ_{cv} (deg)
L01	5	0.1	5.3	6.8	4.2	53.5	38.9	12.3	45.8	1.5	38.1	40.3
	10	0.1	10.1	11.9	8.2	50.1	35.9	14.3				
	15	−0.2	15.1	16.7	11.3	48.0	36.9	9.8				
	30	0.0	30.1	32.5	22.4	47.3	0.0	7.7				
L02	5	0.0	5.0	8.3	7.9	58.9	55.2	14.4	58.9	0.7	54.9	56.1
	10	0.0	10.0	18.2	18.2	61.2	54.5	12.5				
	15	0.0	15.0	25.7	25.7	59.7	51.1	12.7				
	30	0.0	30.0	50.4	49.7	59.2	0.0	12.3				
L03	5	0.0	5.0	5.8	4.2	49.4	39.6	17.4	40.9	2.4	39.1	42.9
	10	0.0	10.0	11.7	9.4	49.4	39.9	40.0				
	15	0.0	14.8	16.1	13.1	47.0	38.0	23.5				
	30	−0.1	30.0	28.0	24.6	43.0	0.0	14.8				
L04	5	0.0	5.0	6.0	2.5	50.3	32.7	30.6	41.5	1.0	31.6	35.3
	10	0.0	10.0	9.7	5.3	44.0	27.3	22.8				
	15	0.0	15.0	13.7	7.6	42.4	34.9	19.8				
	30	0.0	30.0	27.9	19.3	42.9	0.0	16.7				
L05	5	0.0	5.0	21.9	8.1	77.1	56.3	23.8	61.7	14.8	51.5	52.8
	10	0.0	10.0	32.2	16.2	72.8	56.8	20.2				
	15	0.0	15.0	47.6	21.7	72.5	50.4	17.7				
	30	0.0	30.0	68.6	36.7	66.4	0.0	13.3				
L06	5	1.7	5.1	14.2	6.3	70.6	52.9	21.1	61.7	7.6	54.6	50.5
	10	−0.4	10.1	26.5	17.6	69.3	56.2	17.5				
	15	−4.3	15.1	39.8	26.6	69.3	48.6	16.4				
	30	−6.1	30.1	61.6	49.5	64.0	0.0	11.5				

APPENDIX E. AD TEST AND ANOVA ANALYSIS

The sections included within this appendix are related to the summarized steps for the Anderson-Darling (AD) goodness-of-fit test and the two-way ANOVA analysis. The steps followed to evaluate the appropriate assumptions were satisfied for performing ANOVA analysis are also presented.

AD TEST

Besides computing mean, standard deviation, and COV, more advanced statistical analyses were performed to determine the frequency distribution types that would best suit the underlying data collected, namely dry unit weight and shear strength, as well as to determine the sensitivity of these data as a function of sample type and testing laboratory. Goodness-of-fit tests are methods used to evaluate how well a dataset fits a given distribution type (D'Agostino and Stephens 1986). A wide range of goodness-of-fit tests are available in the literature. As reported in Jäntschi and Bolboacă (2018), the most frequently used tests are AD, Kolmogorov-Smirnov (KS), Pearson's chi-square, Cramer-von Mises, Shapiro-Wilk, Jarque-Bera, D'Agostino-Pearson, and Lilliefors. In a comparison between AD and K-S tests conducted by Engmann and Cousineau (2011), the AD test was found to be superior because it detects small variations between two distributions and differences at the extreme ends of distributions more reliably, even for small sample sizes. Thus, the AD test gives weight to the tails of the data, where such phenomena could be critical in engineering design. Hence, the AD method is used in this study to perform normality tests for the unit weight and shear strength data collected from the OGA round-robin study.

The null hypothesis (H_0) of the AD test states that the data follow a specified distribution (e.g., normal distribution). Conversely, the alternative hypothesis (H_1) would be that the data depart significantly from the specified, theoretical distribution. The functional form for the AD test is provided in equation 8 (Stephens 1986).

$$AD = -n - \sum_{i=1}^{n} \frac{(2i-1)}{n} [\ln (F(x_i) + \ln (1 - F(x_{n-i+1})] \quad (8)$$

Where:

n = sample size.

$F(x_i)$ and $F(x_{N-i+1})$ = the cumulative probability for the parameter value at the i^{th} order and $N-i+1$ order.

AD = AD statistic.

To perform an AD test for normality, the data were first sorted in ascending order and then the cumulative probability of each data point was estimated based on the mean and standard deviation of the entire dataset. Using equation 8, the AD statistic was computed. The OGAs used for this study were considered representative but not exhaustive samples of their corresponding rock sources; accordingly, instead of directly using the AD statistic, an adjusted AD statistic (AD*) for testing normality was computed using equation 9 (Stephens 1986).The computed AD* was then used to estimate the p-value for each normality test, as shown in table 74 (Stephens 1986). The p-value is a statistical measure indicating the probability of producing results at least

as extreme as the observed outcome if the null hypothesis (H_0) is correct. An alpha of 0.05 was selected in this study, meaning H_0 would be accepted if the p-value were greater than 0.05 (i.e., a 5 percent probability that random chance could have produced the observed results). Alternatively, H_0 would be rejected if the p-value were less than 0.05. If normality was not found (i.e., H_0 was rejected), then lognormality was tested. To test for lognormality, the data were log-transformed before the basic AD* normality test was repeated (Romeu 2003). Additional groupings of data were evaluated if neither normality nor lognormality was found for a given parameter.

$$AD^* = AD \times \left(1 + \frac{0.75}{N} + \frac{2.25}{N^2}\right) \tag{9}$$

Table 74. AD* *p*-values for normal distributions.

AD*	*p*-value
≤ 0.2	$1 - e^{(-13.436+101.14AD^*-223.73AD^{*2})}$
$0.2 < AD^* < 0.34$	$1 - e^{(-8.318+42.796AD^*-59.938AD^{*2})}$
$0.34 < AD^* < 0.6$	$e^{(0.9177-4.279AD^*-1.38AD^{*2})}$
≥ 0.6	$e^{(1.2937-5.709AD^*+0.0186AD^{*2})}$

AD tests were performed based on the entire 90-point dataset, representing five rock types from each of the three stone sizes, with results from all six participating laboratories. Tests were performed for dry unit weight at *95RD* and for strength (i.e., ϕ_s, ϕ_t, $\phi_{t,r}$, and ϕ_{cv}) and dilatancy (ψ_{max}) parameters. Data across the range of σ_n values (i.e., 5 to 30 psi) were combined for the ϕ_s and ψ_{max} AD tests. The analysis based on the entire dataset (table 75) showed that only ϕ_t and ϕ_{cv} are normally distributed. The data for γ_{d95}, ϕ_s, $\phi_{t,r}$ and ψ_{max} followed neither normal nor lognormal distributions. The descriptive statistics of $\phi_{t,r}$ (table 33) suggest that $\phi_{t,r}$ follows a uniform distribution. Further evaluation of γ_{d95}, ϕ_s, and ψ_{max} (table 76) found that normality was present when the datasets were separated into groups based on OGA bulk dry specific gravity, LSDS device upper box fixity, and LSDS device data collection frequency and corresponding dilation data smoothing, respectively.

Table 75. AD test results for key parameters.

Parameter	*n*	Normal Distribution		Lognormal Distribution	
		p-value	Data Fitted	*p*-value	Data Fitted
γ_{d95}	90	0.00	No	0.01	No
ϕ_s	360	0.00	No	0.00	No
ϕ_t	90	0.08	Yes	0.10	Yes
$\phi_{t,r}$	90	0.00	No	0.00	No
ϕ_{cv}	86	0.70	Yes	0.04	No
ψ_{max}	346	0.00	No	0.02	No

Table 76. Grouped AD results for nonnormal key parameters.

Parameter	Group	*n*	Normal Distribution		Lognormal Distribution	
			***p*-Value**	**Data Fitted**	***p*-Value**	**Data Fitted**
γ_{d95}	Low Specific Gravity	54	0.30	Yes	0.25	Yes
	High Specific Gravity	36	0.40	Yes	0.37	Yes
ϕ_s	Fixed Box	180	0.16	Yes	0.01	No
	Mobile Box	180	0.03	No	0.01	No
ψ_{max}	Data Smoothing	226	0.62	Yes	0.00	No
	No Data Smoothing	120	0.25	Yes	0.00	No

ANOVA

ANOVA is a common type of statistical analysis employed for comparing the means of groups of measurement data (Casella and Berger 2002). The ANOVA technique was used to evaluate the sensitivity of the physical properties and shear strength to inherent variability (e.g., stone size and mineralogy) and measurement variability (e.g., device type, operator). For example, the data collected for ϕ_t, considered the dependent variable, can be grouped according to two categorical, independent variables, represented by factor A (i.e., sample type) and factor B (i.e., laboratory), as shown in table 77. Each value of one independent variable is therefore found in combination with each value of the other independent variable. In this case, a two-factor ANOVA without replicates (Zaiontz 2020) was selected.

Two null hypotheses to test using the adopted two-factor ANOVA without replicates exist. Taking table 77 as an example, the two null hypotheses will be that there is no difference in the mean of ϕ_t among the 15 sample types for factor A, and there is no difference in the mean of ϕ_t due to the laboratory for factor B. The approach to determine whether to accept or reject the null hypotheses is based on comparing a computed F-statistic to a critical value (i.e., F-critical). The F-statistic for factors A and B are computed using equations 10 and 11 (Zaiontz 2020).

Table 77. LSDS test results for tangent friction angle by factor.

Factor A—Sample Type	Factor B—Laboratory					
	L01	L02	L03	L04	L05	L06
No. 57-BA	51.5	62.1	51.2	49.2	59.9	63.1
No. 57-DI	51.9	61.5	50.7	44.5	56.3	63.1
No. 57-GG	47.9	59.1	49.5	45.0	54.0	54.7
No. 57-LI	51.6	63.6	49.4	46.4	51.2	53.5
No. 57-SI	48.4	58.6	49.8	47.2	63.0	50.0
No. 68-BA	49.3	61.8	48.9	47.7	68.1	59.6
No. 68-DI	51.5	53.7	49.1	40.2	57.2	60.3
No. 68-GG	48.3	52.5	48.7	40.6	57.9	42.1
No. 68-LI	48.9	55.9	49.4	41.5	55.4	55.2
No. 68-SI	48.3	59.7	48.9	42.8	67.2	62.6
No. 8-BA	49.7	51.4	40.8	42.9	64.0	51.8
No. 8-DI	44.4	55.8	42.8	39.4	50.7	59.6
No. 8-GG	42.6	48.9	41.0	34.5	53.4	48.5
No. 8-LI	46.7	55.2	41.8	37.7	57.7	60.8
No. 8-SI	45.8	58.9	40.9	41.5	61.7	61.7

$$F\text{–}Statistic\ for\ factor\ A = \frac{b(b-1)\sum_{i=1}^{a}(\bar{x}_i - \bar{x})^2}{\sum_{j=1}^{b}\sum_{i=1}^{a}\left(\bar{x}_{ij} - \bar{x}_i - \bar{x}_j + \bar{x}\right)^2} \quad (10)$$

$$F\text{–}Statistic\ for\ factor\ B = \frac{a(a-1)\sum_{j=1}^{b}\left(\bar{x}_j - \bar{x}\right)^2}{\sum_{j=1}^{b}\sum_{i=1}^{a}\left(\bar{x}_{ij} - \bar{x}_i - \bar{x}_j + \bar{x}\right)^2} \quad (11)$$

Where:

i and *j* refer to the i^{th} row (i.e., level) of factor A and j^{th} column (i.e., level) of factor B, respectively.

a and *b* refer to the total number of levels for factors A and B.

$\bar{x}_i$, $\bar{x}_j$, *and* $\bar{x}$ are the mean of the i^{th} row of factor A, the j^{th} column of factor B, and the grand mean of all data, respectively.

Step-by-step details for computing these values is provided by Zaiontz (2020).

F-critical values for both target factors (sample type or testing laboratory) were selected from established F-distribution tables based on Kanji (2010) using an alpha value of 0.05, the degrees of freedom for the target factor of interest (equal to one less than the number of levels within the target factor), and the product of both factors' degrees of freedom. The null hypotheses were accepted when the F-statistic was lower than F-critical, meaning that there was no statistically significant influence on the parameter due to the considered factor. Conversely, F-statistics

greater than the F-critical validate the alternative hypothesis, meaning the examined factor is significant enough to impact the parameter.

The ANOVA analysis results for all parameters are summarized in table 78. The F-statistics for all tests, except for one case, were greater than their paired F-critical values. Thus, the null hypotheses are rejected. The interpretation of these results is that the measured parameters were significantly sensitive to sample type and laboratory.

Table 78. Test results from the two-factor ANOVA without replicates analysis.

Parameter	Factor	Two-Factor ANOVA		
		***F*-statistic**	***F*-critical**	**Significant**
γ_{d95}	Sample type	86.00	1.84	Yes
	Laboratory	18.21	2.35	Yes
ϕ_s	Sample type	6.56	1.37	Yes
	Laboratory	442.58	2.24	Yes
ϕ_t	Sample type	4.00	1.84	Yes
	Laboratory	45.33	2.35	Yes
$\phi_{t,r}$	Sample type	5.81	1.84	Yes
	Laboratory	172.83	2.35	Yes
ϕ_{cv}	Sample type	1.94	2.03	No
	Laboratory	18.79	2.40	Yes
ψ_{max}	Sample type	5.29	1.43	Yes
	Laboratory	29.80	2.25	Yes

The major assumptions for two-factor ANOVA without replicates is that (a) the observations within each level are normally distributed, (b) the levels within each factor have equal variance and (c) there is no interaction between the factors (Zaiontz 2020). Since there were no replicates in this study, assumption (c) is valid for the entire dataset. To evaluate whether the assumptions for normality were satisfied (i.e., assumption (a)), AD tests were performed for each level (i.e., each individual testing laboratory and sample type) in the same manner discussed in the previous section.

A summary of the AD tests performed for normality testing of the levels within each factor are presented in table 79. In general, most of the levels within both factors passed the normality test, meeting assumption (a) of the two-factor ANOVA. Overall, it seems that a higher percentage of the levels within factor A (i.e., sample type) passed the normality test compared to the levels within factor B (i.e., laboratory).

Table 79. Summary of AD normality test results for datasets within each factor.

Parameter	Factor A—Sample Type			Factor B—Laboratory		
	No. of Levels	No. of Passing Levels	Percent Passing	No. of Levels	No. of Passing Levels	Percent Passing
γ_{d95}	15	14	93	6	5	83
ϕ_s	60	60	100	6	5	83
ϕ_t	15	15	100	6	5	83
$\phi_{t,r}$	15	15	100	6	3	50
ϕ_{cv}	11	10	91	6	5	83
ψ_{max}	46	38	83	6	5	83

Levene's test were employed to test assumption (b), or the equality of variance among the levels (Levene 1960). This test uses the absolute value of residuals (i.e., the difference between a given measured parameter and the mean for a given level). For example, in examining ϕ_t (table 77) when sample type (i.e., factor A) is considered, the level is represented by the rows, so there are 15 levels total each with a sample size of 6. The mean was calculated for each level, and the absolute value of the difference between ϕ_t and the mean of that level was found.

A one-factor ANOVA analysis was then performed to evaluate the homogeneity of variance among the levels. The null hypothesis (H_0) is that there is equality of variance among the columns. F-critical values were determined using an alpha of 0.05, the degrees of freedom of the factor (equal to the number of levels within the target factor minus one), and the remaining degrees of freedom within the dataset (equal to the number of samples minus the sample size of the tested factor). As before, H_0 is accepted when the F-statistic is lower than the F-critical, meaning that there is equal variance along the target factor of the given parameter.

The results from Levene's tests for all key parameters are presented in table 80. Except for ψ_{max}, a significant equality of variance was observed among the levels when sample type was the factor of interest, satisfying this assumption for ANOVA. However, only γ_{d95}, $\phi_{t,r}$, and ϕ_{cv} passed Levene's test when the considered factor was testing device.

Table 80. Levene's test for selected parameters by factor.

Parameter	Factor	Equality of Variance Test		
		F-statistic	F-critical	Equal Variance
γ_{d95}	Sample type	0.65	1.83	Yes
	Laboratory	0.08	2.32	Yes
ϕ_s	Sample type	0.80	1.37	Yes
	Laboratory	4.74	2.24	No
ϕ_t	Sample type	1.29	1.83	Yes
	Laboratory	3.11	2.32	No
$\phi_{t,r}$	Sample type	0.76	1.83	Yes
	Laboratory	1.70	2.32	Yes
ϕ_{cv}	Sample type	2.08	2.01	No
	Laboratory	0.56	2.37	Yes
ψ_{max}	Sample type	1.78	1.42	No
	Laboratory	8.39	2.25	No

In summary, the results from both the AD test and Levene's test showed that most of the data satisfied the ANOVA assumptions for normality and equal variance, yet there were some departures, namely for ϕ_t where there were deviations from both assumptions for factor B. A lack of consensus exists regarding the robustness of using an ANOVA analysis when the main assumptions are violated. In these cases, a Type 1 error (NIST 2012) in ANOVA can occur whereby H_0 is falsely rejected. However, many researchers have validated the method's robustness against moderate departures from nonnormality (Glass et al. 1972; Lix et al. 1996; Schmider et al. 2010). Thus, the chance of Type I errors is likely minimal using the data considered in this report.

ACKNOWLEDGMENTS

FHWA gratefully acknowledge the efforts and contributions of the following individuals:

- Rick Meininger (former Federal laboratory manager) and Mengesha Beyene (contract laboratory manager) of the FHWA Aggregate and Petrology Laboratory for performing petrographic analysis of the rock types to verify the mineralogy.

- Silas Nichols (FHWA Principal Geotechnical Engineer) and Justice Maswoswe (FHWA Senior Geotechnical Engineer) for their technical review of this report.

- Timothy Barrett (FHWA Concrete Materials Engineer) for his technical review and statistical analysis verification of the goodness-of-fit and ANOVA approaches employed.

- The five participating laboratories in this round-robin study. While their identities are held confidential, their participation and feedback throughout the course of the study led to many valuable insights and a better understanding of LSDS testing.

REFERENCES

AASHTO. 2005. *M 43: Standard Specification for Sizes of Aggregate for Road and Bridge Construction*. Washington, DC: American Association of State Highway and Transportation Officials.

AASHTO. 2014. *T 248: Standard Method of Test for Reducing Samples of Aggregate to Testing Size*. Washington, DC: American Association of State Highway and Transportation Officials.

AASHTO. 2018a. *M 43-05: Standard Specification for Sizes of Aggregate for Road and Bridge Construction*. Washington, DC: American Association of State Highway and Transportation Officials.

AASHTO. 2018b. *R 91: Standard Practice for Determining Aggregate Source Shape Values from Digital Image Analysis Shape Properties*. Washington, DC: American Association of State Highway and Transportation Officials.

AASHTO. 2018c. *T 99-18: Standard Method of Test for Moisture-Density Relations of Soils Using a 2.5-kg (5.5-lb) Rammer and a 305-mm (12-in.) Drop*, Washington, DC: American Association of State Highway and Transportation Officials.

AASHTO. 2018d. *T 180-18: Standard Method of Test for Moisture-Density Relations of Soils Using a 4.54-kg (10-lb) Rammer and a 457-mm (18-in.) Drop*, Washington, DC: American Association of State Highway and Transportation Officials.

AASHTO. 2018e. *T 381: Determining Aggregate Shape Properties by Means of Digital Image Analysis*. Washington, DC: American Association of State Highway and Transportation Officials.

AASHTO. 2020a. *AASHTO LRFD Bridge Design Specifications*, 9th ed. Washington, DC: American Association of State Highway and Transportation Officials.

AASHTO. 2020b. *T 327-12: Standard Method of Test for Resistance of Coarse Aggregate to Degradation by Abrasion in the Micro-Deval Apparatus*. Washington, DC: American Association of State Highway and Transportation Officials.

Abu-Farsakh, M., A. Ardah, and M. Saghebfar. 2020. *Monitoring of In-Service Geosynthetic Reinforced Soil (GRS) Bridge Abutments in Louisiana*. Report No. FHWA/La.18/614. Baton Rouge, LA: Louisiana Department of Transportation and Development.

Abu-Hejleh, N., T. Wang, and J. G. Zornberg. 2000. "Performance of Geosynthetic-Reinforced Walls Supporting Bridge and Approaching Roadway Structures" in *Advances in Transportation and Geoenvironmental Systems Using Geosynthetics, Geotechnical Special Publication 103,* 218–243.

Adams, M. T., and J. E. Nicks. 2018. *Design and Construction Guidelines for Geosynthetic Reinforced Soil Abutments and Integrated Bridge Systems*. Report No. FHWA-HRT-17-080. Washington, DC: FHWA.

Adams, M. T., J. E. Nicks, T. Stabile, J. T. H. Wu, W. Schlatter, and J. Hartmann. 2011. *Geosynthetic Reinforced Soil Integrated Bridge System, Interim Implementation Guide*. Report No. FHWA-HRT-11-026. Washington, DC: FHWA.

Allen, T. M., A. S. Nowak, R. J. Bathurst. 2005. *Transportation Research Circular No. E-C079: Calibration to Determine Load and Resistance Factors for Geotechnical and Structural Design*. Washington, DC: Transportation Research Board.

Altaf, O., A. Rehman, H. Mujtaba, and M. Ahmad. 2016. "Study of the Effects of Specimen Shape and Remoulding on Shear Strength Characteristics of Fine Alluvial Sand in Direct Shear Test." *Science International (Lahore)* 28, no. 2: 1115–1119.

Anderson, T. W., and D. A. Darling. 1954. "A Test of Goodness-of-Fit." *Journal of the American Statistical Association* 49, no. 268: 765–769.

ASTM. 2019. ASTM C136. *Standard Test Method for Sieve Analysis of Fine and Coarse Aggregates*. West Conshohocken, PA: ASTM International.

ASTM. 2018. ASTM C295. *Standard Guide for Petrographic Examination of Aggregates for Concrete*. West Conshohocken, PA: ASTM International.

ASTM. 2017. ASTM C778. *Standard Specification for Standard Sand.* West Conshohocken, PA: ASTM International.

ASTM. 2016a. ASTM C535. *Standard Test Method for Resistance to Degradation of Large-Size Coarse Aggregate by Abrasion and Impact in the Los Angeles Machine*. West Conshohocken, PA: ASTM International.

ASTM. 2016b. ASTM D4253. *Standard Test Methods for Maximum Index Density and Unit Weight of Soils Using a Vibratory Table.* D4253. West Conshohocken, PA: ASTM International.

ASTM. 2016c. ASTM D4254. *Standard Test Methods for Minimum Index Density and Unit Weight of Soils and Calculation of Relative Density.* D4254. West Conshohocken, PA: ASTM International.

ASTM. 2014. ASTM C802. *Standard Practice for Conducting an Interlaboratory Test Program To Determine the Precision of Test Methods for Construction Materials*. West Conshohocken, PA: ASTM International.

ASTM. 2011a. ASTM D3080. *Standard Test Method for Direct Shear Test of Soils Under Consolidated Drained Conditions.* West Conshohocken, PA: ASTM International.

ASTM. 2011b. ASTM D7181. *Standard Test Method for Consolidated Drained Triaxial Compression Test for Soils.* West Conshohocken, PA: ASTM International.

Bareither, C. A., C. H. Benson, and T. B. Edil. 2008a. "Comparison of Shear Strength of Sand Backfills Measured in Small-Scale and Large-Scale Direct Shear Tests." *Canadian Geotechnical Journal* 45, no. 9: 1224–1236.

Bareither, C. A., C. H. Benson, and T. B. Edil. 2008b. "Reproducibility of Direct Shear Tests Conducted on Granular Backfill Materials." *ASTM Geotechnical Testing Journal* 31, no. 1: 84–94.

Baecher, G. B., and J. T. Christian. 2003. *Reliability and Statistics in Geotechnical Engineering.* New York: John Wiley & Sons, Ltd. p. 618.

Berg, R. R., B. R. Christopher, and N. C. Samtani. 2009. *Design of Mechanically Stabilized Earth Walls and Reinforced Soil Slopes—Volume 1*. Report No. FHWA-NHI-10-024. Washington, DC: FHWA.

Bolton, M. D. 1986. "The Strength and Dilatancy of Sands." *Geotechnique* 36, no. 1: 65–78.

Borowicka, H. 1961. "The Mechanical Properties of Soil" in *Proceedings of the 5th International Conference on Soil Mechanics and Foundation Engineering*. Paris, France: International Society for Soil Mechanics and Geotechnical Engineering, https://www.issmge.org/uploads/publications/1/40/1961_01_0006.pdf, last accessed July 7, 2021.

Casella, G., and R. L. Berger. 2002. *Statistical Inference*, 2nd ed. Belmont, CA: Brooks/Cole, Cengage Learning.

Cerato, A. B, and A. J. Lutenegger. 2006. "Specimen Size and Scale Effects of Direct Shear Box Tests of Sands." *ASTM Geotechnical Testing Journal* 29, no. 6: 1–10.

Converse, F. J. 1952. "The Use of the Direct Shear Testing Machine in Foundation Engineering Practice" in *Symposium on Direct Shear Testing of Soils*, ASTM STP 131. Philadelphia, PA: ASTM, p. 75–80.

Cuelho, E., R. Mokwa, and K. Obert. 2007. *Comparative Analysis of Coarse Surfacing Aggregate Using Micro-Deval, L.A. Abrasion and Sodium Sulfate Soundness Tests*. Report no. FHWA/MR-06-016/8117-27. Washington, DC: FHWA.

Dadkhah, R., M. Ghafoori, R. Ajalloeian, and G. R. Lashkaripour. 2010. "The Effect of Scale Direct Shear Test on the Strength Parameters of Clayey Sand in Isfahan City, Iran." *Journal of Applied Sciences* 10, no. 18: 2027–2033.

D'Agostino, R.B. and Stephens, M. A. 1986. "Overview" in *Goodness-of-Fit Techniques*, ed. R. B. D'Agostino and M. A. Stephens. New York: CRC Press, p. 1–5.

Engmann, S., and D. Cousineau. 2011. "Comparing Distributions: the Two-Sample Anderson-Darling Test as an Alternative to the Kolmogorov-Smirnoff Test." *Journal of Applied Quantitative Methods* 6, no. 3: 1–17.

FHWA. N.d.. "FHWA InfoMaterials" (web page). https://infomaterials.fhwa.dot.gov/, last accessed December 19, 2022.

Ganji, H. 2019. "Evaluation of New Methods for Determining the Minimum and Maximum Index Densities of Sand." Master's thesis. University of Massachusetts, Amherst.

Gates, L., E. Masad, R. Pyle, and D. Bushee. 2011. *Aggregate Imaging Measurement System 2 (AIMS2)*. Report No. FHWA-HIF-11-030. Washington, DC: FHWA.

Gebrenegus, T., J. E. Nicks, and M. T. Adams. 2015. "Large Diameter Triaxial Testing of AASHTO Open Graded Aggregates and the Effect of Relative Density on Strength." *Proceedings of the 2015 International Foundations Congress and Equipment Expo*, San Antonio, TX: American Society of Civil Engineers.

Gebrenegus, T., J. E. Nicks, and M. T. Adams. 2017. "Strain Rate Effect on Shear Behavior of Open-Graded Aggregates." *Transportation Research Record* 2655: 64–70.

Glass, G. V., P. D. Peckham, and J. R. Sanders. 1972. "Consequences of Failure To Meet Assumptions Underlying the Fixed Effects Analyses of Variance and Covariance." *Review of Educational Research* 42, no. 3: 237–288.

Gomez, B. W., M. M. Dewoolkar, J. E. Lens, and C. C. Benda. 2014. "Effects of Fines Content on Hydraulic Conductivity and Shear Strength of Granular Structural Backfill." *Transportation Research Record* 2462: 1–6.

Greco, V. R. 2016. "Variability and Correlation of Strength Parameters Inferred From Direct Shear Tests." *Geotechnical and Geological Engineering* 34, no. 2: 585–603.

Guo, P., and X. Su. 2007. "Shear Strength, Interparticle Locking, and Dilatancy of Granular Materials." *Canadian Geotechnical Journal* 44, no. 5: 579-591.

Hamidi, B., S. Varaksin, and H. Nikraz. 2013. "Relative Density Concept Is Not a Reliable Criterion." *Proceedings of the Institution of Civil Engineers: Ground Improvement* 166, no. G12: 78–85.

Holtz, R. D., and W. D. Kovacs. 1981. *An Introduction to Geotechnical Engineering*. Englewood Cliffs, NJ: Prentice-Hall.

Hossain, M. S., and D. S. Lane. 2015. *Development of a Catalog of Resilient Modulus Values for Aggregate Base for Use with the Mechanistic-Empirical Pavement Design Guide (MEPDG)*. Report No. FHWA/VCTIR 15-R13. Richmond, VA: Virginia Department of Transportation.

Hossain, M. S., D. S. Lane, and B. N. Schmidt. 2007. *Use of the Micro-Deval Test for Assessing the Durability of Virginia Aggregates*. Report No. VTRC 07-R29. Richmond, VA: Virginia Department of Transportation.

Jäntschi, L., and S. D. Bolboacă. 2018. "Computation of Probability Associated with Anderson-Darling Statistic." *Mathematics* 6: 88.

Jewell, R. A., and C. P. Wroth. 1987. "Direct Shear Tests on Reinforced Sand." *Geotechnique* 37, no. 1: 53–68.

Kandhal, P. S., and R. B. Mallick. 1999. *Design of New-Generation Open-Graded Friction Courses*. Report No. 99-03. Auburn, AL: National Center for Asphalt Technology.

Kanji, G. K. 2010. *100 Statistical Tests*, 3rd ed. Thousand Oaks, CA: SAGE Publications, Ltd.

Kim, B., S. Shibuya, S. Park, and S. Kato. 2012. "Effect of Opening on the Shear Behavior of Granular Materials in Direct Shear Test." *KSCE Journal of Civil Engineering* 16, no. 17: 1132–1142.

Kittu, A., and M. L. Bernhardt. 2017. "Effects of Common Boundary Types in Direct Shear Tests." Presented at *Geotechnical Frontiers 2017*. Orlando, FL: Industrial Fabrics Association International and the Geo-Institute of the American Society of Civil Engineers.

Levene, H. 1960. "Robust Tests for Equality of Variances" in *Contributions to Probability and Statistics: Essays in Honor of Harold Hotelling*, ed. Olkin et al. Redwood City, CA: Stanford University Press, p. 278-292.

Lings, M. L., and M. S. Dietz. 2004. "An Improved Direct Shear Apparatus for Sand." *Geotechnique* 54, no. 4: 245–256.

Liu, S. H., D. Sun, and H. Matsuoka. 2005. "On the Interface Friction in Direct Shear Test." *Computers and Geotechnics* 32(5): 317–325.

Lix, L. M., J. C. Keselman, and H. J. Keselman. 1996. "Consequences of Assumption Violations Revisited: A Quantitative Review of Alternatives to the One-Way Analysis of Variance of Variance F Test." *Review of Educational Research* 66, no. 4: 579–619.

Mallick, R. B., P. S. Kandhal, L. A. Cooley, and D. E. Watson. 2000. *Design, Construction, and Performance of New-Generation Open-Graded Friction Courses*. Report No. 2000-01. Auburn, AL: National Center for Asphalt Technology.

Mamo, G. G., and A. Dey. 2014. "Critical Overview of the Effect of Strain Rate on Direct Shear Test Results." Presented at the *North East Students Geo-Congress on Advances in Geotechnical Engineering.* Guwahati, India: North East Students Geo-Congress on Advances in Geotechnical Engineering.

Marsal, R. J. 1967. “Large-Scale Testing of Rockfill Materials.” *Journal of the Soil Mechanics and Foundations Division* 93, no. 2: 27–43.

Matthews, M. C. 1988. “The Engineering Application of Direct and Simple Shear Testing.” *Ground Engineering* 21, no. 2: 13–21.

Nicks, J. E., and M. T. Adams. 2013. *TechBrief: Friction Angles of Open-Graded Aggregates From Large-Scale Direct Shear Testing*. Report No. FHWA-HRT-13-068. Washington, DC: FHWA.

Nicks, J. E., M. T. Adams, and T. Gebrenegus. 2018. *TechBrief: Impact of Initial Density on Strength-Deformation Characteristics of Open-Graded Aggregates*. Report No. FHWA-HRT-18-048. Washington, DC: FHWA.

Nicks, J. E., T. Gebrenegus, and M. T. Adams. 2015. *Strength Characterization of Open-Graded Aggregates for Structural Backfills*. Report No. FHWA-HRT-15-034. Washington, DC: FHWA.

Nicks, J. E., T. Gebrenegus, and M. T. Adams. 2021. “Interlaboratory Large-Scale Direct Shear Testing of Open-Graded Aggregates: Round One.” Presented at *Proceedings of the 2021 International Foundations Congress and Equipment Exposition*, Dallas, TX: International Foundations Congress and Equipment Exposition.

National Institute of Standards and Technology (NIST). 2012. “NIST/SEMATECH e-Handbook of Statistical Methods” (web page). http://www.itl.nist.gov/div898/handbook/, last accessed March 18, 2022.

Phoon, K. K., and F. H. Kulhawy. 1999. “Characterization of Geotechnical Variability,” *Canadian Geotechnical Journal* 36, no. 4: 612–624.

Romeu, J. L. 2003. “Anderson-Darling: A Goodness of Fit Test for Small Samples Assumptions.” *RAC START* 10: 1–6.

Rowe, P.W. 1962. “The Stress Dilatancy Relation for Static Equilibrium of an Assembly of Particles in Contact.” *Proceedings of the Royal Society of London* 269, no. 1339: 500–527.

Schmider, E., M. Ziegler, E. Danay, L. Beyer, and M. Bühner. 2010. “Is It Really Robust? Reinvestigating the Robustness of ANOVA Against Violations of the Normal Distribution Assumption.” *Methodology* 6: 147–151.

Scott, D.W. 1979. “On Optimal and Data-Based Histograms.” *Biometrika* 66: 605–610.

Selezneva, O.I., Y. J. Jiang, and G. Mladenovic. 2002. *Evaluation and Analysis of LTPP Pavement Layer Thickness Data*. Report No. FHWA-RD-03-041. Washington, DC: FHWA.

Shibuya, S., T. Mitachi, and S. Tamate. 1997. “Interpretation of Direct Shear Box Testing of Sands as Quasi-Simple Shear.” *Geotechnique* 47, no 4: 769–790.

Skempton, A. W., and A. W. Bishop. 1950. “The Measurement of the Shear Strength of Soils.” *Geotechnique* 2, no. 2: 188–192.

Sobol, E., W. Sas, and A. Szymanski. 2015. “Scale Effect in Direct Shear Tests on Recycled Concrete Aggregate.” *Studia Geotechnica et Mechanica* 37, no. 2: 45–49.

Stallings, J. A. 2020. “Implementation of Geosynthetic Reinforced Soil—Integrated Bridge System (GRS-IBS) Technology in Alabama.” Master’s thesis. Auburn University.

Stephens, M. A. 1986. “Tests Based on EDF Statistics” in *Goodness-of-Fit Techniques*, ed. R. B. D’Agostino and M. A. Stephens. New York: CRC Press, p. 97–193.

Tao, M., and M. Y. Abu-Farsakh. 2008. *Effect of Drainage in Unbound Aggregate Bases on Flexible Pavement Performance*. Report No. FHWA/LA.07/429. Baton Rouge, LA: Louisiana Transportation Research Center.

Taylor, D. W. 1953. “A Direct Shear Test with Drainage Control.” Presented at the *Symposium on Shear Testing of Soils*. Philadelphia, PA: ASTM.

Tyson, S., and S. Tayabji. 2012. *TechBrief: Pervious Concrete*. Report No. FHWA-HIF-13-006. Washington, D.C: FHWA.

Uzielli, M., S. Lacasse, F. Nadim, and K. K. Phoon. 2007. “*Soil Variability Analysis for Geotechnical Practice*” in *Characterisation and Engineering Properties of Natural Soils*, ed. Tan, Phoon, Hight, and Lerueil. London: Taylor & Francis Group, p. 1653–1752.

Weyers, R. E., G. S. Williamson, D. W. Mokarem, D. S. Lane, and P. D. Cady. 2005. *Testing Methods To Determine Long Term Durability of Wisconsin Aggregate Resources*. Report No. WHRP 06-07. Madison, WI: Wisconsin Department of Transportation.

Wu, P., K. Matsushima, and F. Tatsuoka. 2008. “Effects of Specimen Size and Some Other Factors on the Strength and Deformation of Granular Soil in Direct Shear Tests.” *ASTM Geotechnical Testing Journal* 31, no. 1: 45–64.

Yoshimi, Y., and I. Tohno. 1973. “Statistical Significance of the Relative Density” in *Evaluation of Relative Density and Its Role in Geotechnical Projects Involving Cohesionless Soils*, *ASTM STP 523*, ASTM, pp. 74-84.

Younger, K., R. G. Hicks, and M. Partl. 1994. *Evaluation of Porous Pavements for Road Surfaces*. Report No. FHWA-OR-RD-95-03. Salem, OR: Oregon Department of Transportation.

Zaiontz. 2020. “Real Statistics Using Excel” (web page). http://www.real-statistics.com/, last accessed March 22, 2022.

Recycled
Recyclable

Recommended citation: Federal Highway Administration,
Variability in the Engineering Properties of Open-Graded Aggregate Backfills: A Large-Scale Direct Shear Round-Robin Study
(Washington, DC: 2023) https://doi.org/10.21949/1521990

HRDI-40/07-23(WEB)E